Chemical Vapor Deposition of Molecular Thiolates of Bismuth, Tin and Lead & Multinuclear Solution NMR Studies on Lead Halide Perovskites

Ufuk Atamtürk
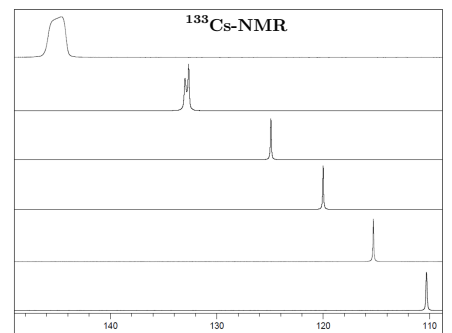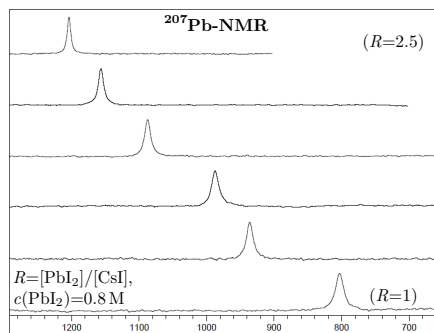
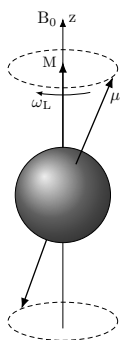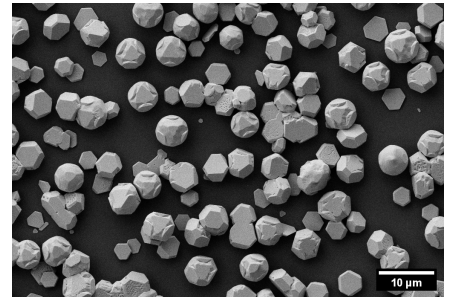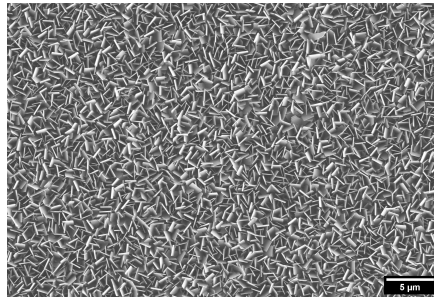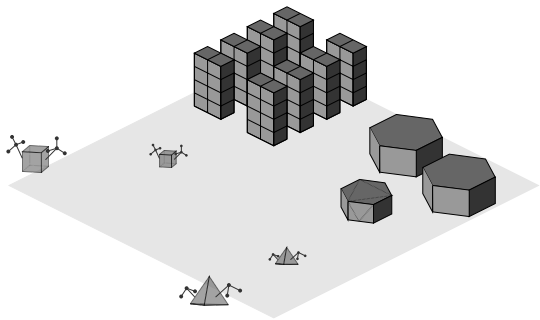# Chemical Vapor Deposition of Molecular Thiolates of Bismuth, Tin and Lead
& Multinuclear Solution NMR Studies on Lead Halide Perovskites

Inaugural-Dissertation
zur Erlangung des Doktorgrades
der Mathematisch-Naturwissenschaftlichen Fakultät
der Universität zu Köln

vorgelegt von

Diplom-Chemiker
Ufuk Atamtürk
aus
Stuttgart

Acknowledgment

♉ ♃ ♄ 🜍

Bismut	Zinn	Blei	Schwefel

Abstract

The first part of this thesis (Chapters 3 to 5) describes the investigation on molecular single-source precursor and their successful application in the chemical vapor deposition (CVD) of Bi_2S_3, SnS and PbS. In the second part (Chapter 6) light was shed on the dynamics existent in the precursor solutions used for the fabrication of APbI$_3$ ($A^+ = CH_3NH_3^+$, Cs^+) lead halide perovskites.

Chapter 3   Bismuth(III) alkylthiolates, $Bi(SR)_3$ ($R = -Bu^t$ (**1a**); $-Pr^i$ (**1b**)) were applied in the chemical vapor deposition (CVD) process as single-source precursors for both Bi_2S_3 and Bi. Whereas the CVD of $Bi(SBu^t)_3$ (**1a**) produced single-crystalline Bi_2S_3, elemental Bi was obtained from $Bi(SPr^i)_3$ (**1b**). The CVD deposits in both cases were unambiguously identified as Bi_2S_3 and Bi as verified by X-ray diffraction analysis (XRD), high-resolution X-Ray photoelectron spectroscopy (XPS) and scanning electron microscopy (SEM). The highly oriented and uniformly shaped 2D Bi_2S_3 platelets were found to be single-crystalline by selected area electron diffraction (SAED) performed during high-resolution transmission electron microscopy (HR-TEM), and correlative 2D-SEM-Raman spectroscopy. The photoconductivity of Bi_2S_3 deposited on FTO was characterized. The growth of Bi_2S_3 by CVD of (**1a**) was additionally investigated on different substrates (FTO, SiO_2/Si and glass, 250 °C) and elevated temperatures (Si, 300 °C). The unprecedented morphologies of the deposition product by $Bi(SPr^i)_3$ (**1b**) displayed the intrinsic crystal symmetry of Bi on micrometer sized particles, as the first example of elemental bismuth by non-classical crystallization. Moreover, was the crystal structure of $Bi(SBu^t)_3$ (**1a**) determined.

Chapter 4   The synthesis of a new heteroleptic tin(II) molecular precursor of is reported containing (i) a thiolate ligand forming a direct Sn-S bond, and (ii) a chelating O^N^N-donor ligand introducing a 'launch vehicle'-effect into the synthesized compound, thus remarkably increasing its volatility. The newly synthesized tin compound [$Sn(SBu^t)(tfb\text{-}dmeda)$] (**2a**) was characterized by single crystal X-ray diffraction analysis that verified the desired Sn:S ratio in the molecule, which was demonstrated in the direct conversion of the molecular complex into SnS thin films. The multinuclear (^{1}H, ^{13}C, ^{19}F and ^{119}Sn) and variable-temperature 1D and 2D NMR studies indicate retention of the overall solid-state structure of (**2a**) in the solution and suggest the presence of a dynamic conformational equilibrium. The fragmentation behavior of (**2a**) was analyzed by mass spectrometry and compared with those of homoleptic tin(II) and tin(IV) alkylthiolates $Sn(SBu^t)_2$ and $Sn(SBu^t)_4$. The precursor (**2a**) was then used to deposit SnS thin films on different substrates (FTO, Mo-coated soda-lime glass) by CVD and film growth rates at different temperatures (300 °C–450 °C) and times (15 min–60 min), film thickness, crystalline quality, and surface morphology were investigated.

Chapter 5   The crystal structure of lead(II) alkylthiolates $Pb(SBu^t)_2$ (**3a**) which showed a trimeric arrangement $[Pb_3(\mu\text{-}SBu^t)_6]$ in the solid-state and $Pb(SBu^i)_2$ (**3c**) which is a 1D coordination polymer of pentameric $[Pb_5(\mu\text{-}SBu^i)_4(SBu^i)_6]$ units, is presented. The application of $Pb(SPr^i)_2$ (**3b**) as single-source precursor for the CVD (chemical vapor deposition) of PbS is reported. The electron-ionization mass-spectrometric (EI-MS) analysis of (**3b**) and (**3c**) is presented, which revealed the molecules as monomeric in the gas phase and (**3c**) also as dinuclear species. The chemical shifts $\delta^{207}Pb$ of $Pb(SBu^t)_2$ (**3a**) and $Pb(SBu^i)_2$ (**3c**) are reported. Additionally, the new Pb^{II} oxygen thiolato cluster are presented $[Pb_{12}O_6(SPr^i)_{12}\cdot(C_6H_6)]$ (**3d**) and $[Pb_{12}O_6(SBu^t)_{12}\cdot 6\,(NC_5H_5)]$ (**3e**).

Chapter 6   The fundamental solution chemistry of PbI_2 and $PbI_2 + AI$ ($A^+ = Cs^+$, $CH_3NH_3^+$) in DMSO and DMF was elucidated, by means of multinuclear ^{207}Pb-, ^{133}Cs- and ^1H-NMR Spectroscopy. This was accomplished by NMR titration and dilution experiments, which describe the measurement and interpretation of the chemical shifts $\delta^{207}Pb$-, $\delta^{133}Cs$- and δ^1H as function of varying the ratio of precursor $R = [AI]/[PbI_2]$, ($A^+ = Cs^+$, $CH_3NH_3^+$) and varying the concentration of the precursor in constant ratio ($R = 1$). By establishing the link between solution and solid-state ^{207}Pb-NMR spectroscopy it could be shown that PbI_2 and $PbI_2 + AI$ exist in dynamic equilibria in DMSO and DMF solution ($c_{solute} \geq 0.4\,M$) as polynuclear species in the form of edge- and corner-sharing condensed PbI_6-octahedra. Hereby the acceptor property of the solvents, in terms of their iodide stabilizing capability was identified as key feature that governs the solute-solvent interactions in the investigated high concentration regime ($c_{solute} \geq 0.4\,M$). The correlation between solution and solid-state ^{207}Pb-NMR chemical shifts, was mirrored in the linewidths of the ^{133}Cs- and ^1H-NMR resonances, thus affecting the exchange rates on the NMR time-scale.

Contents

1 Introduction

In times of growing demand for renewable and environment-friendly energy sources increased research effort is being invested in the quest for new technologies and materials. In this context, chalkogenide based main-group semiconductor materials Bi_2X_3, SnX_2 and PbX_2 (X = S, Se, Te) and the perovskite structure related materials such as APbI$_3$ (A^+ = $CH_3NH_3^+$, Cs^+) have become promising candidates to fulfill the demands on future technologies.[1–9] Compounds comprising the heavier main-group elements in their lower oxidation state, i.e., Ge^{II}, Sn^{II}, Pb^{II} and Sb^{III}, Bi^{III} were associated with an increased likelihood for highly efficient and defect-tolerant photovoltaics, whereby their large potential as solar absorber material was inferred from the ns^2 lone pair's implications on the electronic structure and thereof following properties, such as a high absorption coefficient and charge carrier mobilities.[5,10–12] In layered structures such as Bi_2S_3 and SnS charge carrier related properties are generally anisotropic, which describes for example significantly increased conductivity along covalent bonds, when compared to between layers held together by van der Waals forces.[3,13,14] Considering these materials for future applications the ability to synthesize these in preferred orientation as well as crystallinity and purity is therefore fundamentally important. For this the chemical vapor deposition (CVD) is the method of choice and in order to exploit the full capabilities the CVD technique has to offer, are the properties of the single-source precursor (SSP) crucial.[15–19] The synthesis, characterization and application of new molecular SSP for the CVD of Bi_2S_3, SnS and PbS is presented in the first part of this thesis, of which the crystal structures shall be introduced briefly.

Bismuth(III) sulfide Bi_2S_3 occurs naturally as bismuthinite and crystallizes in the space group Pnma, isotypic to stibnite Sb_2S_3.[20–22] The structure of Bi_2S_3 consists of (Bi_4S_6) units extending covalently bonded to columnar structures also described as ribbons, which interact with adjacent ribbons by van der Waals forces. Two (Bi_4S_6)$_\infty$ ribbons of the crystal structure are shown in (Figure 1.1a) and as extended view on the unit cell in (Figure 1.1b). The bismuth atoms are five-coordinate by the sulfur atoms in distorted square-pyramidal geometry, forming edge-sharing condensed (BiS_5) coordination pyramids alongside (Bi_4S_6)$_\infty$ (Figure 1.3a). The bond lengths in the basal plane of the inner pyramids are (Bi-S: 273.80(98) pm and 297.53(108) pm) and to the vertex (Bi-S: 258.97(175)), and for the outer pyramids (Bi-S: 264.40(109) pm and 302.89(99) pm) and (Bi-S: 269.37(169)) respectively. The stereochemically active Bi^{III} $6s^2$ lone pair is located in the voids between the ribbons, which are separated by distances ranging between 304.81(153) pm to 338.59(182) pm.

Tin(II) sulfide SnS occurs naturally as the mineral herzenbergite and crystallizes in the space group Pbnm (Figure 1.2a) which as the most stable phase at room temperature, and is often referred to as α-SnS. The stereochemically active Sn^{II} $5s^2$ lone pair is accommodated in the interlayer voids of the structure. Within the layers two different Sn-S bond lengths in the basal plane (Sn-S: 278.36 pm and 312.84 pm) and one shorter bond lengths to the vertex (Sn-S: 259.57 pm) is present, making the Sn^{II} central atom three-coordinate.[23,24] Hereby, when considering longer interlayer Sn-S distances up to 360 pm the structure was described as double-layers consisting of condensed (SnS_5) coordination pyramids (Figure 1.3b).[22]

Lead(II) sulfide PbS occurs naturally as the mineral galena and crystallizes in the rock-salt structure (Figure 1.2b), whereby each Pb^{II} central atom is six-coordinate by the sulfur atoms in ideal octahedral geometry and therefore only one bond length (Pb-S: 296.58 pm) is present.[25,26] Considering the role of the ns^2 lone pair ($n = 5, 6$) from a chemical point of view,
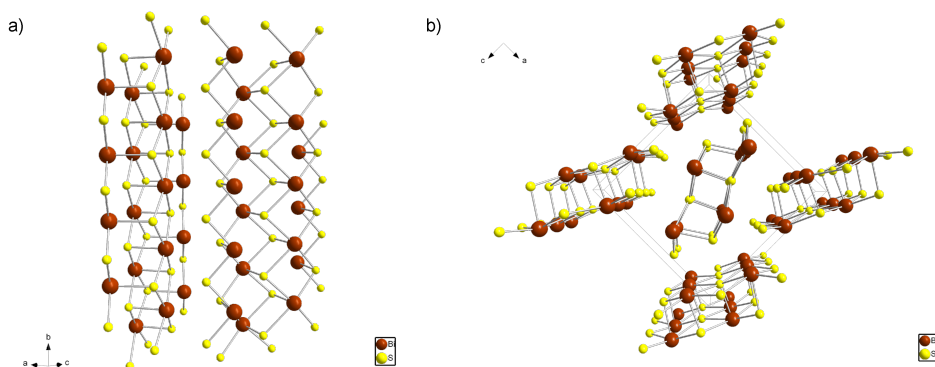
Figure 1.1: The crystal structure of Bi_2S_3 a) Two $(Bi_4S_6)_\infty$ ribbons in projection along the *ac*-plane b) view on the extended unit cell in projection along the covalently bonded axis (This is for the different settings of space group No. (62) in P*nma* the *b*-axis, and in P*bnm* the *c*-axis). The asymmetric unit was complemented to visualize the (Bi_4S_6) coordination units. The cif-file for the structure was obtained from the Crystallography Open Database (COD): Bi_2S_3 #9003472.[21]

in terms of its structural implications, is the lone pair in general stereochemically active for lower coordination numbers (c.n.< 6) and subject of interest for higher coordination numbers (c.n. $\geq$ 6).[27] In (Figure 1.3) the crystal structures of Bi_2S_3, SnS and PbS are presented with the corresponding coordination polyhedra surrounding the central atoms, which visualizes the stereochemically inactive lone pair on the Pb^{II} central atom and formation of the higher symmetry rock-salt structure. Whether the lone pair will be stereochemically active or not is especially for the sixth row elements not predictable by the VSEPR rules and is basically an orbital overlap phenomenon, which is mostly about to which extend the metal-metal (6s-6p) or metal-ligand orbitals mix.[27–29] Hereby it is worth mentioning that the $6s^2$ electrons as present in Bi^{III} and Pb^{II} is by no aspect 'inert', hence this term is avoided.[27,29,30]
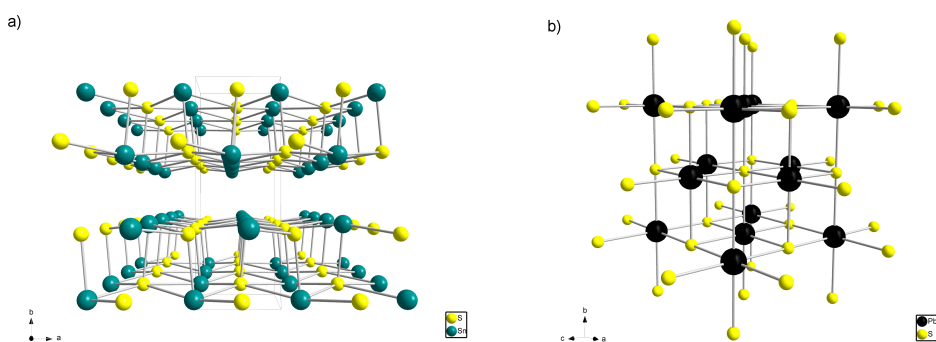
Figure 1.2: The crystal structures of a) SnS and b) PbS. The cif-files for the structures were obtained from the Crystallography Open Database (COD): SnS #1527226[24] and PbS #9013403.[25]

Compounds of the perovskite structure family such as $MAPbI_3$ and $CsPbI_3$ are in the focus of interest as photovoltaic materials due to their facile synthesis and remarkable high solar energy conversion efficiency.[31–33] There are extensive research efforts to gain more insight on
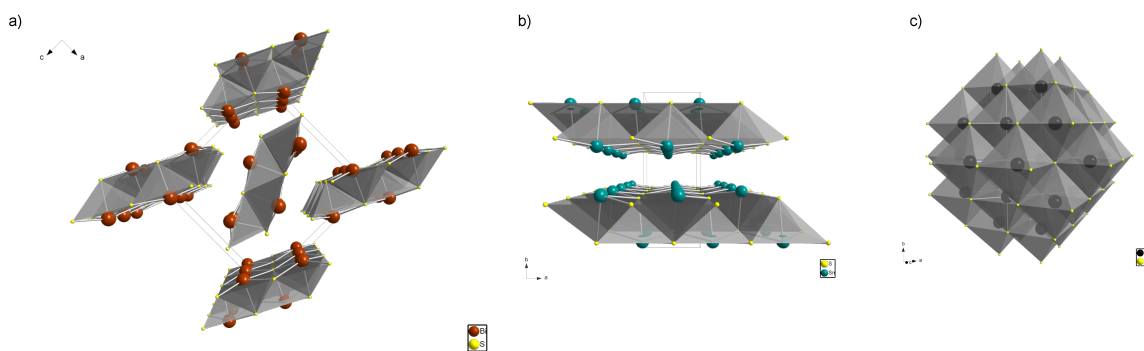
Figure 1.3: Visualization of the coordination polyhedra surrounding the cationic central atoms in the crystal structures of a) Bi_2S_3 b) SnS c) PbS from (Figure 1.2).

the solution dynamics and species, which is mainly being investigated by UV-Vis accompanied by DFT calculations,[34–36] whereas the former is restricted to very low-concentrated solutions (μM–mM) and the latter empirically of rather low diagnostic value in terms of solution chemistry. Generally are the solutions in the solar-cell material preparation by one to two orders of magnitude more concentrated ($\sim 1.0 \pm 0.5\,\mathrm{M}$). For this NMR spectroscopy is the method of choice, enabling the investigation on higher concentrated solutions by measuring the local electronic environment of the given nuclei on the atomic scale. The application of ^{13}C- and especially ^{1}H-NMR spectroscopy is, also beyond chemistry in various fields of natural sciences an analytical method of fundamental importance. Whereas, also in view of the large number of available isotopes and elements which are of potential diagnostic value, are investigations including NMR-active nuclei different than ^{13}C and ^{1}H, termed as *multinuclear* NMR spectroscopy, noticeable less present and explored.[37–41] In the first part of this thesis ^{119}Sn-, ^{19}F-, ^{29}Si-, ^{13}C-, ^{7}Li- and ^{1}H-NMR was applied in varying combinations for characterization and investigation on the solution structure and dynamics of the molecular precursor compounds. The second part describes the purely ^{207}Pb-, ^{133}Cs- and ^{1}H-NMR based investigation on the PbI_2 (methylammonium iodide, CH_3NH_3I) MAI and CsI solute-solvent interactions in DMSO and DMF.

The constituent elements of the here investigated materials tin, lead and sulfur can be categorized as earth-abundant and hereby including bismuth as low-cost elements, in varying individual contributions.[42] Whereas environmental and health related issues shall be shortly evaluated in view of the contrasting toxicity between the elements bismuth and lead.[43,44] For example is the bismuth subsalicylate as an over-the-counter medical product under the brand name Pepto-Bismol® commercially available. Bismuth based compounds were shown to be effective agents in the tumor therapy[45,46] and bismuth thiolates are well-known and investigated for their antimicrobial activity.[47] Bismuth was also referred to as *green* heavy-metal,[47] whereas the toxicity of lead was alongside its utility well-known for at least centuries.[48] Despite increasing research efforts finding a suitable substitute,[49,50] remains the popularity of lead based materials constant, which is due to the versatility in the elements unique inherent properties, displayed also in its compounds such as PbS.[5] Hereby the focus may be put more on for example, the extra-ordinary recycling rate over 99 % of lead acid batteries, which is by far not achieved for any other element.[51–53] When reducing its energy costs, such efficient and established industrial recycling processes may serve as a role model for a sustainable and responsible handling of the planets resources.

2 Scientific Objective of this Work

(I) Synthesis, Characterization and Application of Single-Source Precursors for the CVD of Bi_2S_3, SnS and PbS. There are several requirements for the molecular single-source precursor
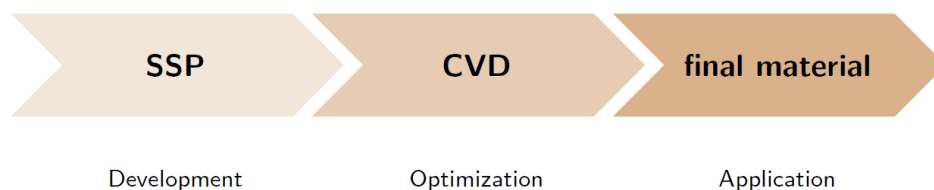
Scheme 1: Scheme illustrating the workflow for the molecular precursor and CVD related objective in a wider sense.

(SSP) such as: (i) volatility, that is a sufficiently large vapor pressure to ensure acceptable growth rates and generally decreases with increasing molecular weight and amount of polar bonds due to electrostatic forces. (ii) stability, to provide sufficiently large temperature window between sublimation and decomposition, including sublimation without decomposition and side reactions. (iii) well-defined thermal decomposition behavior, to ensure a reproducible CVD process and to avoid the incorporation of impurities in the final material and by releasing volatile by-products e.g., low molecular weight alkanes and alkenes. The synthesis route and handling of the SSP should proceed via readily available chemicals, an up-scalable reaction and reliable purification methods. Also is it desirable for the SSP not to be extra-ordinary air and moisture sensitive and to have a long shelf-life.

Hereby, more than the physical properties (e.g., vapor pressure, thermodynamic stability) is the chemical constitution of the precursor molecule a key parameter. This entity shall act as building block for the later material bearing the *bonding scheme*, here the metal-sulfur bond ($M-S$, M=Bi, Sn and Pb) already within, which then is transported via the gas phase onto the substrate surface. The complexity that arises from the suitable combination of different (physical) parameter stands against the comparable rather 'simple' demands on the (chemical) molecular framework. Hereby is 'simplicity' the limitations imposed on the molecular constitution arising from the general trend of decreasing volatility with increasing molecular weight and number of different elements present in the molecule.

The synthesis of molecular chalcogenolate complexes of Bi^{III}, Sn^{II} and Pb^{II} should not involve ionic components, thereby excluding e.g., salt metathesis reactions and should also not involve fluorine containing chemicals, thereby excluding fluorotrimethylsilane $(CH_3)_3SiF$ elimination. Therefore the 'silylamido' (= *bis*(trimethylsilyl)amido) complexes $M[N(SiMe_3)_2]_n$ were to be used for the synthesis of the metal chalcogenolates $M(SR)_n$ ($M = Sn^{II}$, Pb^{II} n=2; $M = Bi^{III}$, n=3.). The ligand exchange reaction at the Sn^{II} central atom was intended to proceed via protolysis by the corresponding alkylthiols HSR ($R = -Bu^t$, $-Pr^i$ and $-Bu^i$) thereby liberating volatile and readily removable $H[N(SiMe_3)_2]$ molecules. The characterization of molecular SSP for CVD and of en route earlier synthesis steps was to be done including the following main aspects: (i) solid-state structure: growth of single-crystals and characterization

4

by X-ray diffraction, elemental analysis (CHNS) (ii) gas phase species: (electron ionization mass spectrometry) EI-MS to investigate the constitution of gas phase species and establish a decomposition pathway (iii) solution structure and dynamics by NMR spectroscopy: 1D and 2D multinuclear NMR experiments including the nuclei ^{207}Pb, ^{119}Sn, ^{19}F, ^{29}Si, ^{13}C, ^{7}Li and ^{1}H in varying combinations and (variable temperature) VT-NMR experiments of relevant nuclei. (iv) thermal decomposition profile: (thermogravimetry) TG in combination with (difference thermal analysis) DTA to reveal phase transition(s), evaluation of decomposition steps, phase and purity assessment of the final residue. For the CVD process the choice of substrate is a key parameter for the deposition and desired preferred oriented growth of the final material. The substrate properties which have to be taken into consideration, in varying combinations, were (i) amorphous and crystalline substrate (exploring match in lattice parameter for epitaxial growth) (ii) smooth and rough surface (iii) conductivity and resistivity. These were to be further investigated by balancing and tuning the (iv) substrate and (v) sublimation temperature of the SSP and in combination with the latter the (vi) process time and (vii) precursor loading, which describes the amount of SSP introduced in the CVD process in order to control the mass flux. The characterization of layers obtained from a CVD process was to be done including the following aspects and methods: (i) phase identification and purity assessment by powder (X-Ray diffraction) XRD, Raman-spectroscopy and (energy dispersive X-Ray) EDX analysis. (ii) morphology and film thickness by (scanning electron microscopy) SEM and cross-sectional analysis by SEM (iii) microstructure and crystallinity by high-resolution (transmission electron microscopy) TEM and (selected area electron diffraction) SAED (iv) surface analysis by (X-Ray photoelectron spectroscopy) XPS (v) Application potential by conductivity measurements without and under light illumination and chronoamperometry.

(II) Investigations on the PbI_2, PbI_2+CH_3NH_3I and PbI_2+CsI solution dynamics and species and the solute-solvent system in DMSO and DMF by means of multinuclear ^{207}Pb-, ^{133}Cs-, ^{13}C- and ^{1}H-NMR spectroscopy.

Generally occur nuclei different than ^{1}H in lower natural abundance and have a lower receptivity, which is generally referenced to the ^{1}H isotope. These issues may only partially be addressed by the capabilities of modern spectrometer, and have to be considered for the specific nuclei of interest since the resonance frequencies are spread over a wider range which are not always accessible by the spectrometer hardware. For this is in the field of multinuclear NMR a deeper understanding necessary of how a signal is measured and generated under the given instrumental conditions, which goes beyond the standard knowledge acquired in chemistry classes. The availability of spectrometer operating at different frequencies equipped variable temperature units provided the practical frame for the multinuclear NMR investigations. Although routine NMR experiments are available for ^{207}Pb and ^{133}Cs nuclei, there is no 'routine' or general method for an investigation or interpretation of the hereby obtained results, as it is custom in^{1}H-NMR. The vast chemical shift range of ^{207}Pb-NMR spectroscopy ($\sim$ 17000 ppm) is the consequence of the ^{207}Pb nuclei's pronounced sensitivity towards subtle changes in its coordination environment, which in return shows the high potential in diagnostic value.

Considering the fundamentally different (than ^{1}H or ^{13}C) relaxation mechanism of the ^{133}Cs and ^{207}Pb nuclei, often pronounced concentration and temperature dependence in δ^{207}Pb chemical shifts, does the absence or presence of one (or more than one) resonance

within the measured range, require a reasonable and case-dependent verification. Further measurement parameter have to be taken into account and adjusted, such as the spectral window (sw), time domain (td), number of scans (ns) and decoupling frequency. Especially, for the likely case when extending the duration of measurements hardware and instrumental conditions have to be considered, such as variations in field and shimming homogeneity over time. These parameters are tunable only in relation to each other and have to be considered for each experiment and solution parameter in view of the resonance intensity and shape or its potential absence. To increase the resolution and intensity of a given signal additionally the processing parameter (apodization) have to investigated. Nevertheless, is the complexity expected to be also displayed in the variety and richness of obtained information by these experimental investigations. Since in NMR spectroscopy is the 'true' information obtained generally from coupling between either same or different nuclei the main overall goal was to resolve ^{207}Pb-^{207}Pb coupling (in viable cases also to other nuclei) and from there to obtain a conclusive picture of the chemical environment of ^{207}Pb nuclei. Given the ^{133}Cs nuclei's quadrupolar properties ($I = \frac{7}{2}$) the likelihood to observe coupling will be reduced, although not impossible.

Investigating the chemical shifts δ^{207}Pb and δ^{133}Cs depending on (i) solvent (ii) concentration (iii) temperature and (iv) spectrometer frequency, then interpreting these in the context of literature reported NMR studies and the general (coordination-) chemistry of the given elements was the basis for planning further steps in this pioneer investigation.
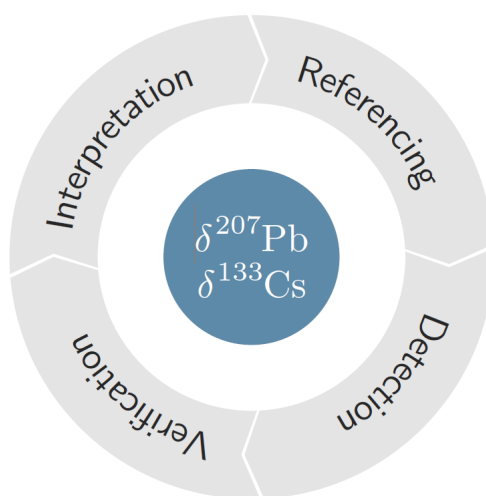
Scheme 2: Scheme illustrating the general aspects to be considered in this multinuclear NMR investigation, in a wider sense. Hereby means "Referencing" the interpretation of the results in the context of literature reports and the general as well as coordination chemistry of the given elements.

Part I

Chemical Vapor Deposition of Molecular Thiolates of Bismuth, Tin and Lead

3 Bismuth(III) Alkylthiolates as Single-Source Precursor for CVD

This chapter contains the reformatted manuscript published in the journal *Chemistry of Materials*. Reprinted with permission from

U. Atamtürk, E. Jung, T. Fischer, S. Mathur, *Chem. Mater.* **2022**, *34*(16), 7344–7356.

The investigation on the synthesis, characterization and CVD application and the fundamental

different thermal decomposition results from $Bi(SBu^t)_3$ (**1a**) and $Bi(SPr^i)_3$ (**1b**), differing by only one methyl moiety, were in the focus of this work. The experimental work was extended by DFT calculations in cooperation with Dr. Eunhwan Jung, who performed the DFT calculations.
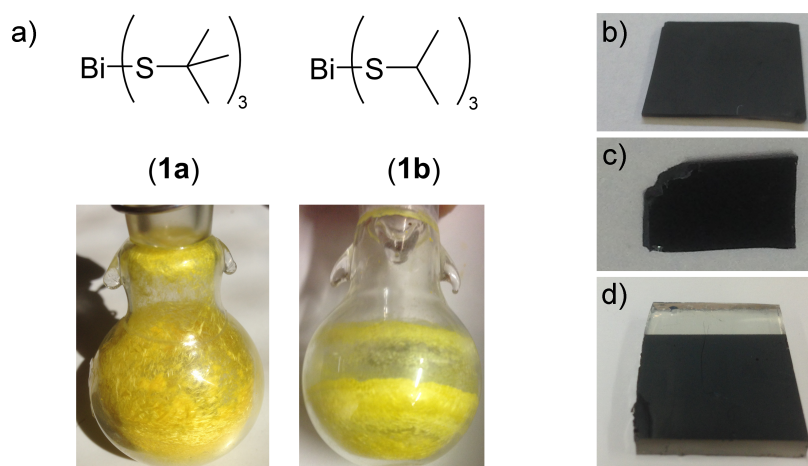
Figure 3.1: a) Schematic drawing of bismuth(III) alkylthiolates and corresponding images of the compounds in the solid state. The images on the right-hand side show the deposited Bi_2S_3 after CVD with (**1a**) on various substrates b) Si (250 °C) c) SiO_2/Si (250 °C) d) FTO (250 °C), hereby the surface was partially covered by Kapton® during the CVD process and removed afterwards.

3.1 Introduction

Bismuth(III) alkylthiolates such as $Bi(SEt)_3$[54,55] and $Bi(SMe)_3$[56] are potential precursors to much sought Bi_2S_3, which is an intrinsic n-type semiconductor with direct bandgap $E_g = 1.3\,eV$ to $1.7\,eV$ and high absorption coefficient of $\sim10^5\,cm^{-1}$ in the visible region[57,58] making it a promising candidate as absorber material in photovoltaic hetero-junctions.[12] When compared to other metal thiolates, bismuth derivatives are scarcely investigated. For instance, $Bi(SBu^t)_3$ (**1a**) was firstly synthesized via a solvent-less reaction between BiF_3 with $Me_3Si-SBu^t$[59] and described to be stable only in an evacuated tube, an observation that was not shared based on own investigation. The here reported bismuth(III) *iso*-propylthiolate $Bi(SPr^i)_3$ (**1b**) was not reported previously to the best of the author's knowledge. Bismuth sulfide (Bi_2S_3) has attracted significant attention due to its functional applications in thermoelectrics,[60] photo- and electrocatalysis,[61–64] supercapacitors,[65,66] lithium-ion[67,68] and sodium-ion[69] batteries, gas sensors,[70,71] photodetectors and superconductors.[62,63,72–75] However, techniques for simple and direct synthesis of Bi_2S_3 on substrates are not sufficiently developed. This work demonstrates the potential of molecular compounds with pre-organized Bi-S bonds in their conversion into solid-state bismuth sulfide, which also highlights the role of bond polarity in initiating the thermal decomposition cascade to influence the fate of the resulting materials. Previous studies on the thermolysis of long-chain dodecane thiolate (DDT) bismuth complex $Bi(DDT)_3$ showed the formation of elemental bismuth, at lower temperatures ($150\,°C$), whereas Bi_2S_3 nanowires were obtained at elevated temperatures ($225\,°C$).[76,77] While a variety of bismuth arylthiolates $Bi(SAr)_3$ have been reported and their structural characterization is reported, studies on their thermal decomposition are elusive.[78] Within this work the structural analysis of $Bi(SBu^t)_3$ (**1a**) is present and its potential as molecular single-source precursor to Bi_2S_3 in the chemical vapor deposition (CVD) evaluated.

3.2 Results and Discussion

3.2.1 Synthesis of $Bi(SBu^t)_3$ (1a) and $Bi(SPr^i)_3$ (1b)

The molecular Bi^{III} alkylthiolates $Bi(SBu^t)_3$ (**1a**) and $Bi(SPr^i)_3$ (**1b**) were synthesized in high yields by protolysis of $Bi[N(SiMe_3)_3]_3$ in THF as outlined in (Scheme 3). $Bi(SPr^i)_3$ (**1b**) is

$$Bi[N(SiMe_3)_2]_3 \quad + \quad 3\ HSR \quad \xrightarrow[\text{- 3 HN(SiMe}_3)_2]{\text{0 °C, 0.5 h, THF}} \quad Bi(SR)_3$$

$$R = \text{-Bu}^t\ (\textbf{1a}),\ \text{-Pr}^i\ (\textbf{1b}).$$
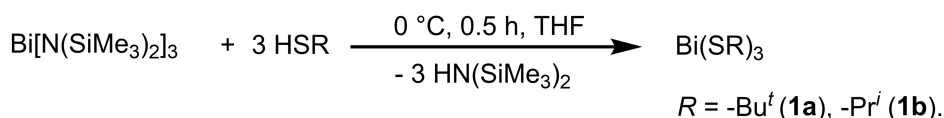
Scheme 3: Synthesis route of the bismuth alkylthiolates $Bi(SBu^t)_3$ (**1a**) and $Bi(SPr^i)_3$ (**1b**)

stable under ambient laboratory conditions and light for prolonged time without any detectable decomposition neither by visible inspection nor ^1H NMR spectroscopy, whereas $Bi(SBu^t)_3$ (**1a**) degrades upon exposure to ambient daylight within short time directly detectable by a color change from yellow to black. Both (**1a**) and (**1b**) undergo reduction to elemental bismuth in common organic solvents accompanied by the formation of the corresponding dialkyl disulfide, which can be followed by discoloration of the solution, and was confirmed by powder XRD data of the precipitate. The higher stability of the tertiary ($-Bu^t$) compared to the secondary ($-Pr^i$) radical possibly accounts for the higher photosensitivity of $Bi(SBu^t)_3$. Comparable Pb^{II}

alkylthiolates were reported to show a reverse stability $(Pb(SBu^t)_2 > Pb(SBu^i)_2 > Pb(SBu^n)_2)$ than expected for the alkyl radicals in both solid state and solution, which was associated with the availability of a proton at the α-carbon.[79]

3.2.2 Crystal Structure of Bismuth Alkylthiolates

Crystals of (**1a**) used in structure determination were grown from a THF solution, which crystallize in the space group $P6_3$ (173) with $Z = 6$ molecules in the unit cell. The crystal symmetry and structural motif (Figure 3.2) is analogous to $Bi(OBu^t)_3$.[80] In one molecular
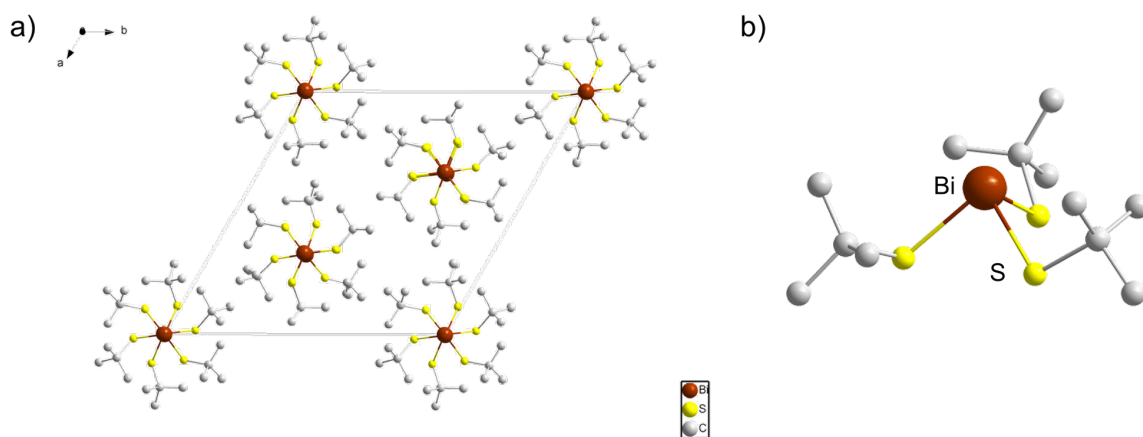
Figure 3.2: a) View on the unit cell along the crystallographic c-axis. b) One molecular unit $Bi(SBu^t)_3$. As the unit cell contains one-third of each molecule, the whole molecule was generated by symmetry. The hydrogen atoms are omitted for clarity

unit $Bi(SBu^t)_3$ the bismuth atoms at the apex of a trigonal pyramid are coordinated by three sulfur atoms which occupy the corners of the basal plane. The experimental Bi-S bond lengths range between (Bi-S: 252.4(6)–253.7(6) pm) and are comparable to reported Bi-S bond lengths in Bi^{III} arylthiolates.[81–83] The S-Bi-S bond angles (S-Bi-S: 88.2(2)°–88.7(2)°) indicate the high s-character of the bismuth lone pair and the high p-orbital contribution to the Bi-S bonding orbitals. The $Bi(SBu^t)_3$ units are stacked up in two different columns parallel to the crystallographic *c*-axis. In one column a three-fold rotational axis runs through the bismuth atoms, along which the orientation of the 'Bi-S$_3$' pyramid is inverted with respect to those span by the sulfur atoms bonded to the bismuth atoms, occupying the six-fold rotational symmetry axis located at the edges of the unit cell. Extended crystallographic data tables for (**1a**) are assembled in (Tables C.1– C.4) and details on the refinement are presented in the experimental part in (Section 9.2.3). The intermolecular distances between the sulfur and the bismuth atoms of the adjacent $Bi(SBu^t)_3$ unit is (Bi-S: 366.2 pm–385.5 pm). These values, when compared to the sum of the Van der Waals radii ($\Sigma_{VdW}(Bi,S)$: 389 pm),[84] shows the presence of discrete monomeric $Bi(SBu^t)_3$ units with weak intermolecular contacts in the solid state, as these intermolecular distances are significantly larger than in $Bi(SPh)_3$[82] (Bi-S: 347.0(1) pm–358.3(1) pm) for which a distorted-octahedral (3+3) coordination environment was suggested.

The application of Bi^{III} alkylthiolates as single-source precursors in the CVD process is not reported so far. The only comparable example for V-VI thin film deposition deals with antimony as the lighter congener of bismuth, where the molecular precursor complex

Sb(SBu^t)$_3$ was used in CVD process for the deposition of Sb$_2$S$_3$.[85] In another study, bismuth dithiocarbamates Bi(S$_2$CNRR')$_3$ where *R,R'* can be organic (alkyl or benzyl) substituents were used to grow fibers of Bi$_2$S$_3$ via low pressure CVD in the temperature range between 400 °C–450 °C.[86] Recently, heterocyclic dithiocarbamato bismuth complexes were reported as potential precursors that were however used in an aerosol-assisted CVD process due to relatively high sublimation temperatures of the precursor molecules (250 °C).[87] By changing the ligand to xanthate [Bi(S$_2$COR$_2$)$_3$] lower deposition temperatures became accessible, resulting in the formation of Bi$_2$S$_3$ nanorods, which however suffer from contamination by elemental sulfide (S$_8$).[88] In analogy, dichalcogenoimidodiphosphato complexes Bi[(SPR$_2$)$_2$N]$_3$ (*R* = alkyl) were also proposed as potential precursors to bismuth sulfides, however they required relatively high sublimation temperatures (230 °C–350 °C), and could not be vaporized intact into the gas phase.[89] A common feature of the above mentioned ligand classes is the presence of multiple elements in the ligand moiety that introduces a high ionic character in the bonds, which together with the high molecular weight limits the volatility and desired clean and defined decomposition behavior essential for a CVD process.

3.2.3 CVD Experiments with (1a) and (1b)

The CVD experiments performed with Bi(SBu^t)$_3$ (**1a**) and Bi(SPr^i)$_3$ (**1b**) on Si showed different outcomes despite similar CVD parameters and substrate temperature (250 °C). While the decomposition of Bi(SBu^t)$_3$ (**1a**) resulted in the formation of single-phase Bi$_2$S$_3$ (ICDD #17-320), Bi(SPr^i)$_3$ (**1b**) yielded elemental bismuth (ICDD #44-1246) at the same experimental conditions. The phase identification was confirmed by the XRD patterns of the CVD deposits (Figure 3.3).
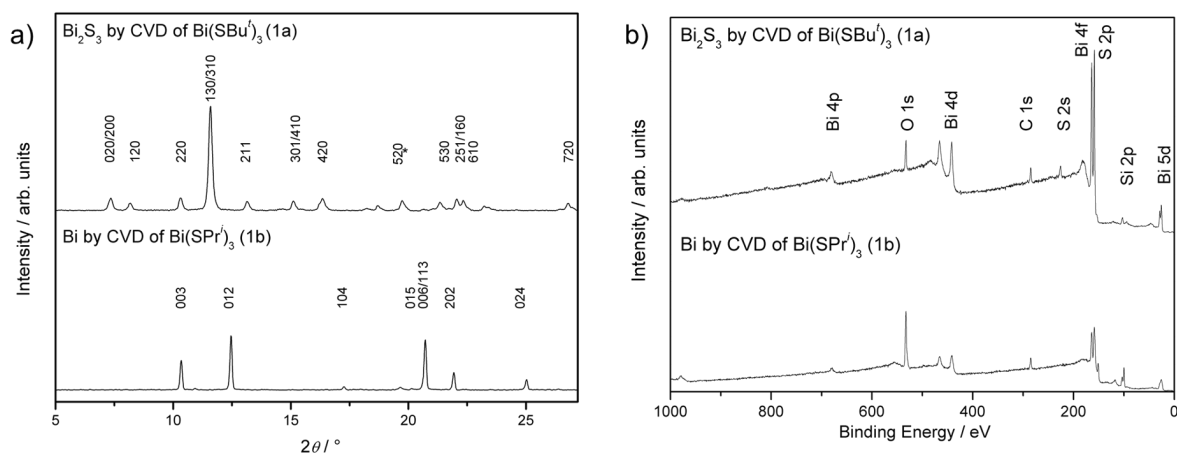
Figure 3.3: XRD pattern of a) (top) Bi$_2$S$_3$ via CVD of Bi(SBu^t)$_3$ (**1a**) b) (bottom) Bi via CVD of Bi(SPr^i)$_3$ (**1b**). Referenced according to a) (top) Bi$_2$S$_3$ (ICDD #17-320) b) (bottom) Bismuth (ICDD #44-1246) b) Survey XPS of the layers obtained by CVD with the molecules (**1a**) and (**1b**) summarized in one plot.

For Bi$_2$S$_3$ obtained from Bi(SBu^t)$_3$ (**1a**) the diffraction peak positions match well with the reference pattern of bulk Bi$_2$S$_3$ (ICDD #17-320). The predominant nature of (*hk*0) indexed planes in the pattern showed the material growth along a preferred orientation given by the horizontal stacking of *ab*-planes in the Bi$_2$S$_3$ material, with the *c*-axis being parallel to the substrate surface. The XRD pattern of the CVD deposit obtained using Bi(SPr^i)$_3$ (**1b**)

corresponded unambiguously with the reference pattern of bulk bismuth (ICDD #44-1246). When comparing the experimental diffraction pattern (Figure 3.3, top) to that of bulk bismuth, the peaks that arise from the (003) and (006)/(113) indexed planes were measured at a noticeable 10- and 15-fold increased relative intensity. The XRD patterns are discussed in more detail in section 3.4.

The morphology of the material as obtained by CVD of $Bi(SBu^t)_3$ (**1a**) and $Bi(SPr^i)_3$ (**1b**) at 250 °C, investigated by SEM (scanning electron microscopy) showed uniform 2D Bi_2S_3 platelets growing vertically out of the substrate plane, as evident in the top-view SEM image (Figure 3.4a) over an area of $50\,\mu m^2$. A closer inspection of the platelets, as shown in the inset
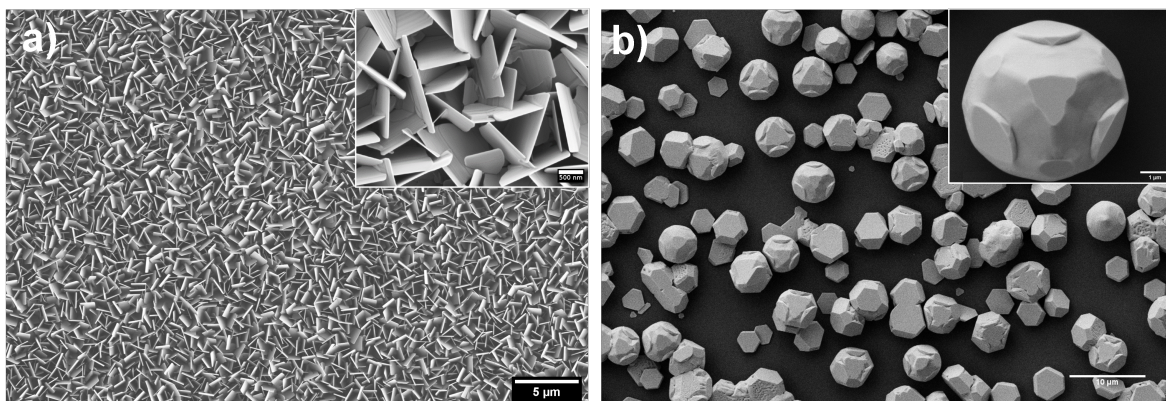
Figure 3.4: SEM top-view images of the layers obtained from the CVD: a) Bi_2S_3 via CVD of $Bi(SBu^t)_3$ of (**1a**). b) Bi by CVD of $Bi(SPr^i)_3$ (**1b**).

of (Figure 3.4a) and in (Figure 3.19) indicated each individual unit to be an assembly of thinner layers stacked up along their largest surface, which is accessible when vertically standing out of the substrate plane. Further analysis of individual 2D platelets of Bi_2S_3 by high-resolution transmission electron spectroscopy (Figure 3.5) confirmed their single-crystalline nature as verified by the selected area electron diffraction (SAED) pattern (inset of Figure 3.5a) and (Figure 3.5b) along the [531] zone axis of Bi_2S_3 (ICSD #153946). The high-resolution TEM image further reveals the internal structure of the sheets, which consist of individual single crystalline domains (Figure 3.5c); together with the single-crystalline appearance in SAED, a quasi-single-crystalline domain orientation is proposed. The overall morphology of Bi_2S_3 by CVD is typically described as 1D nanofibers-/rods or irregular sized plates.[73,88–90] In literature reports on comparable 2D shapes of Bi_2S_3 are limited to few wet-chemical synthesis methods, which highlights the importance of molecular precursors, containing all phase-forming elements in a single compound, in precisely controlling the morphology of the resulting material.[61,91]

A correlative 2D-SEM-Raman analysis of the Bi_2S_3 platelets is presented in (Figure 3.6), which shows the corresponding Raman spectra of the color-coded areas in the SEM top-view images. The blue colored areas in the SEM image (Figure 3.6a) correspond to the Bi_2S_3 plates that were vertically standing out of the substrate plane with the peaks measured as $97\,cm^{-1}$, $186\,cm^{-1}$ and $237\,cm^{-1}$, whereas the red color was assigned to the plates aligned horizontally on the substrate plane $100\,cm^{-1}$, $186\,cm^{-1}$, $237\,cm^{-1}$ and $257\,cm^{-1}$. The peak at $257\,cm^{-1}$ in (Figure 3.6b) is present only with the horizontally aligned Bi_2S_3 plates, and belongs to the set of longitudinal optical phonons B_{1g}, whereas the remaining modes belong to transverse optical phonons A_g (97, 100, 186 and $237\,cm^{-1}$).[92] This distinction by one peak
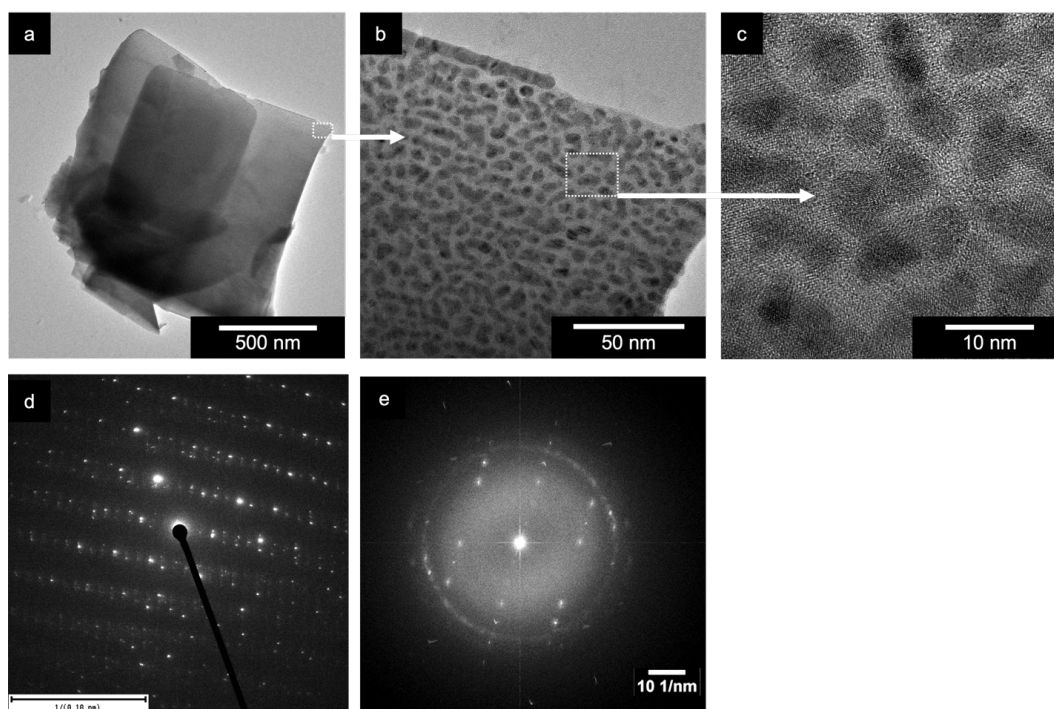
Figure 3.5: a) Large area TEM view of separated Bi$_2$S$_3$ flake that was obtained from (**1a**) and d) the corresponding SAED pattern. b) Magnified view of rectangular selection and e) its corresponding SAED diffraction. c) High magnification of selection illustrates the formation of singe crystalline oriented particles with a diameter of around 10 nm.

was further confirmed measuring a larger area of upright platelets (Figure 3.6c+d) whereby no peak at 257 cm^{-1} is apparent. The experimentally observed Raman modes (Figure 3.6b+d) reveal the phase purity of the Bi$_2$S$_3$ that was obtained by CVD from (**1a**), in accordance with literature reported values.[93,94] The energy dispersive X-Ray (EDX) measurements confirmed the elemental composition Bi:S (1:1.5) as in the sum formula of Bi$_2$S$_3$, which is shown in (Figure A.1) and tabulated in (Table A.1).

The elemental bismuth that was obtained when using (**1b**) as the molecular precursor revealed two types of morphologies consisting of hexagonal plates and spherical nodules. These are most probably expressions of a fluent transition between these morphologies and not distinctive. Both particle types are between 2–6 μm large and display on the micrometer scale the symmetry elements present in the unit cell of the rhombohedral space group $R - 3$m, which elemental bismuth crystallizes in. The magnified view of a spherical structure (inset, Figure 3.4b) showed a faceted geometry with visible triangular planes, which cap the overall spherical form of the particle. The SEM top-view (Figure 3.4b) manifested the three-fold rotational symmetry to be present throughout each formed plane on the surface of the bismuth particles. This is also displayed in the XRD pattern, in form of the largely increased intensities of (003) and (006) planes, which represent the largest surface area of the hexagonal shape. These morphologies are unprecedented for elemental bismuth obtained by CVD.

The XPS (X-Ray Photoelectron spectra) survey scan of the CVD deposits (Figure 3.3b) confirmed the chemical composition to be Bi$_2$S$_3$ and Bi for precursor (**1a**) and (**1b**), respectively. The elemental bismuth films showed no signs of any sulfur-bearing species within the detection limit of XPS, as supported by the absence of the sulfur 2s core level (Figure 3.3b, bottom)
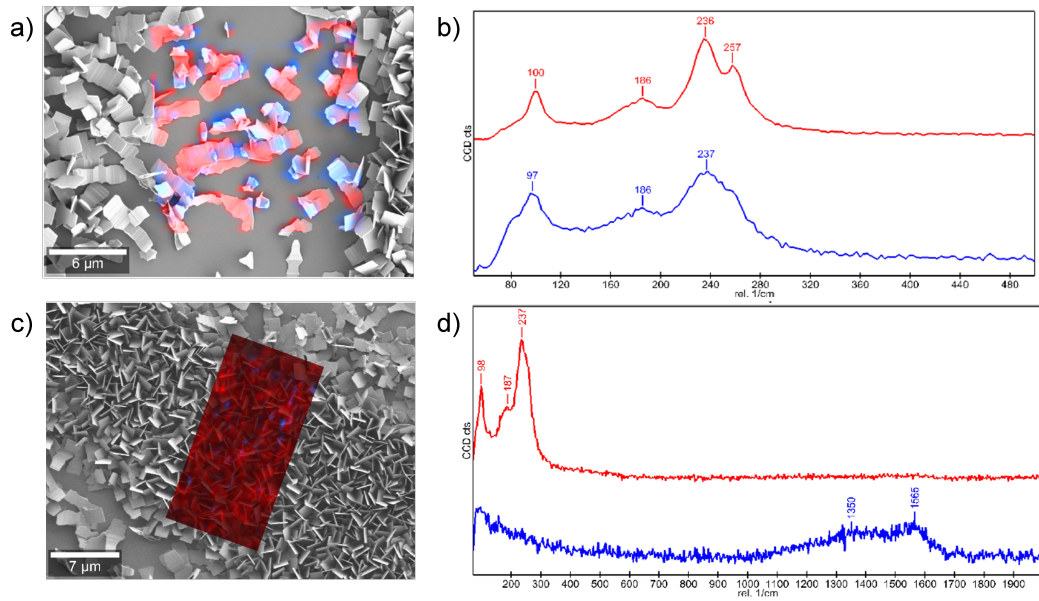
Figure 3.6: Color-coded 2D-RAMAN-SEM Measurement at an excitation wavelength $\lambda_{ex} = 532\,\text{nm}$, and power of $0.5\,\text{mW}$. a+b) SEM image and the corresponding Raman spectra of vertically (blue) and horizontally (red) oriented Bi_2S_3 plates on the substrate. c+d) SEM image and the corresponding RAMAN spectra (red) of vertically oriented Bi_2S_3 plates on the substrate. The blue spectrum in d) was assigned to adventitious amorphous carbon

and the $S\,2p_{3/2}$ and $2p_{1/2}$ spin-orbit doublet. The absence of the latter was confirmed by measuring the high-resolution spectra in the region of expected $S\,2p$ energy levels in case these signals were obscured below the broad $Bi\,4f$ spin-orbit doublet. The binding energies from the high-resolution (Figure A.3 and A.4) and survey scan spectra (Figure 3.3b) are summarized in (Table A.2). The binding energies (BE) of the Bi orbitals in Bi_2S_3 obtained by CVD of $Bi(SBu^t)_3$ are shifted to higher energies by $+\Delta BE = 1.0\text{--}1.8\,\text{eV}$ compared to elemental bismuth, whereas those of sulfur (S_8: $S\,2p_{1/2} = 165\,\text{eV}$ and $S\,2p_{3/2} = 164\,\text{eV}$) are shifted to lower energies by $-\Delta BE = 2.0\text{--}3.0\,\text{eV}$ and are in good agreement with reported values.[95–97] For example, when comparing the BE in the high-resolution spectra of the $Bi\,5d$ core levels, $Bi\,5d_{5/2}$ ($23.9\,\text{eV}$) and $5d_{3/2}$ ($26.9\,\text{eV}$) of elemental bismuth to those of Bi_2S_3 $Bi\,5d_{5/2}$ ($25.7\,\text{eV}$) and $5d_{3/2}$ ($28.7\,\text{eV}$). The sulfur core levels $S\,2s$ ($225.8\,\text{eV}$), $S\,2p_{3/2}$ ($161.5\,\text{eV}$) and $S\,2p_{1/2}$ ($162.7\,\text{eV}$) match with previously reported values for Bi_2S_3.[97] The binding energies of the Bi orbitals in Bi_2O_3, as result of surface oxidation, are shifted to higher energies by $+\Delta BE = 1.7\text{--}2.6\,\text{eV}$.[95]

In additional CVD experiments, the growth of Bi_2S_3 platelets from precursor (**1a**) was investigated on various substrates. The XRD patterns of Bi_2S_3 grown on FTO, glass and SiO_2/Si ($250\,°C$) are assembled in (Figure 3.7). For Bi_2S_3 preferred orientation growth was observed on SiO_2/Si and glass as substrate in a similar fashion as observed for Si as substrate (Figure 3.3, bottom). The SEM top-view images of Bi_2S_3 grown on SiO_2/Si (Figure 3.8b) and glass (Figure 3.8c) showed Bi_2S_3 platelets growing vertically out of the substrate plane with comparable morphology and crystallite dimensions to those grown on Si. On FTO substrate (Figure 3.7, bottom) no indication for oriented growth of Bi_2S_3 was noticed. The SEM images of Bi_2S_3 grown on FTO (Figure 3.8a) showed 2D Bi_2S_3 platelets in comparable morphology
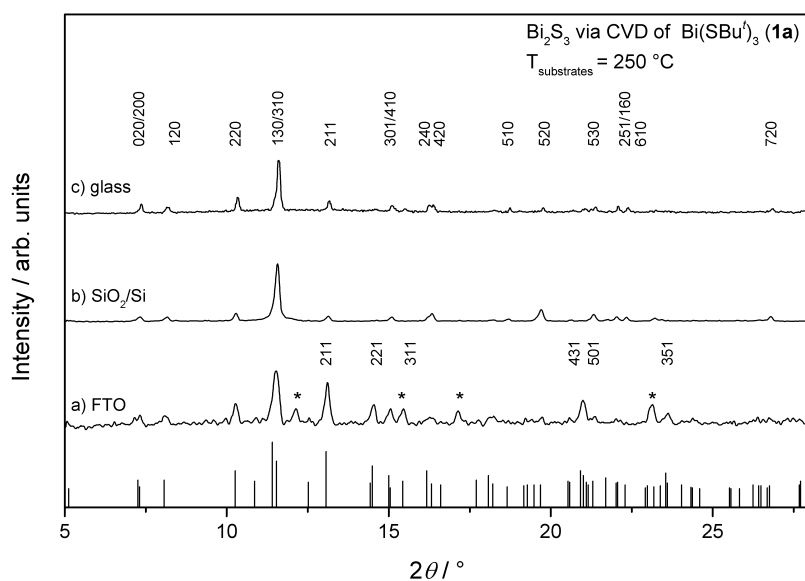
Figure 3.7: XRD patterns (rescaled to normalized peak intensities) of Bi_2S_3 via CVD of (**1a**) grown on a) FTO, b) SiO_2/Si and c) glass at the same temperature (250 °C). The (*hkl*) indices in a) FTO (bottom) indicate peaks from the reference card (Bi_2S_3 ICDD #17-320) observed either only from Bi_2S_3 grown on FTO or in noticeable increased intensity, e.g., (211), when compared to Bi_2S_3 on SiO_2/Si and glass. The asterix (*) in a) marks peaks of the FTO substrate.

and dimension, which consisted of randomly vertically oriented and horizontally aligned platelets on the substrate surface. These observations suggest that the precursor chemistry and gas phase species substantially affect the nucleation and crystal growth processes, which simplifies thin film growth and morphology control on various substrates.At elevated substrate temperature (325 °C) horizontal 2D Bi_2S_3 platelets were obtained, with their apparent largest surface area oriented parallel to the substrate plane. The SEM top-view image (Figure 3.9b) shows the substrate surface coverage by horizontal platelets, which is passed through by columns of vertically aligned Bi_2S_3 platelets. The simultaneous occurrence of perpendicular oriented platelets as showed in (Figure 3.9b) was observed in a series of CVD experiments and is possibly due to irregularity of the substrate surface (mechanical defects).
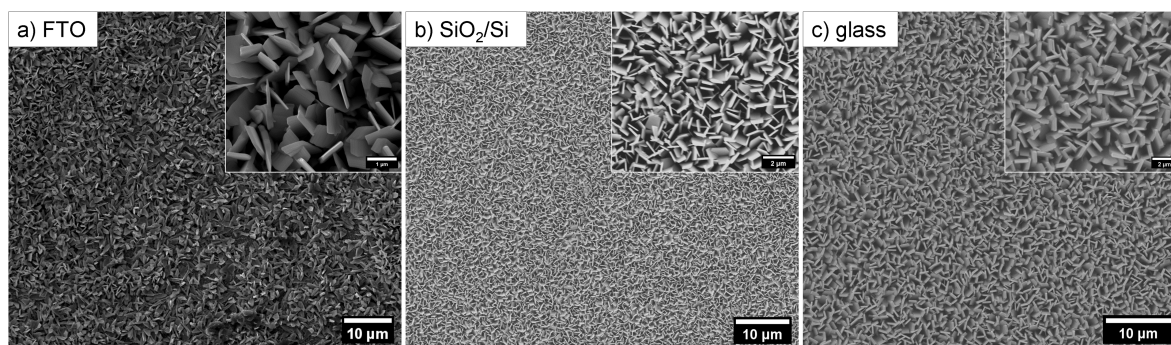
Figure 3.8: SEM top-view images of Bi_2S_3 via CVD of (**1a**) on a) FTO b) SiO_2/Si c) glass at the same temperature (250 °C).
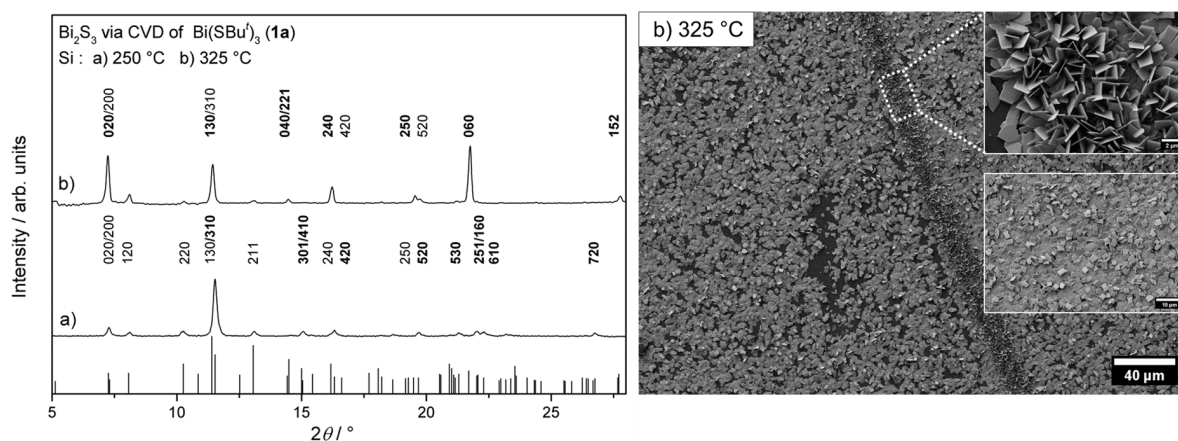
Figure 3.9: XRD patterns (normalized peak intensities) of Bi_2S_3 grown on Si, at two different substrate temperatures (top: 325 °C; bottom: 250 °C). The (hkl) indices printed in bold indicate noticeable increased intensity of the corresponding peak in the pattern. The diffraction pattern of Bi_2S_3 on Si (250 °C) (bottom) was replotted from (Figure 3.3a). Referenced according to Bi_2S_3 (ICDD #17-320). b) SEM top-view images of Bi_2S_3 by CVD of (**1a**) on Si (325 °C), of the sample the XRD pattern (top) was recorded from.

In view of the well-defined morphology of rest of the sample this is not likely a purely thermal effect, rather provides a hint towards electrostatic interactions that may for example arise from the difference in conductivity or surface defects as result of varying surface roughness in either of the two growth regimes.[98]

The plot in (Figure 3.9a) compares the diffraction pattern of horizontally oriented platelets (Si, 325 °C) and vertically oriented Bi_2S_3 platelets (Si, 250 °C) previously shown in (Figure 3.4a), of which the XRD pattern (Figure 3.3, bottom) was replotted in (Figure 3.9a). The striking difference observed from the XRD pattern of horizontally oriented Bi_2S_3 plates (Figure 3.9a, top) is the dominant presence of ($0k0$) indexed planes on the scale of relative intensities. The largest relative peak intensity ($I_{rel.,exp.} = 100$) is observed with the (060) indexed planes, which is four-fold of the intensity ($I_{rel.} = 25$) listed in the reference card (ICDD #17-320). A closer inspection of the diffraction pattern obtained from vertically oriented platelets (Figure 3.9a, bottom) shows practically no sign of diffraction from the (060) indexed planes. Following this approach reveals further intensity deviations within the frame of ($hk0$) and ($0k0$) indexed planes, which can be assigned to vertical or horizontal orientations. These are listed above each diffraction pattern in (Figure 3.9), whereas those printed in bold have noticeable increased intensity in correspondingly oriented Bi_2S_3 platelets.

3.2.4 Thermogravimetric Analysis of (1a) and (1b)

The analysis of $Bi(SBu^t)_3$ (**1a**) and $Bi(SPr^i)_3$ (**1b**) by thermogravimetry (Figure 3.10) provided insights into the formation of Bi or Bi_2S_3 despite similar chemical features of the two precursors. In both cases, significantly different mass loss values (Δm) were recorded. In addition, a prominent endothermic feature corresponding to the melting of elemental bismuth at 271 °C was observed in the TG-DTA profile of (**1b**) that was completely absent in (**1a**).

The decomposition occurs in a narrow temperature range between 85 °C to 235 °C, which is evident from the sudden and steep mass loss and as an endothermic event centered around 200 °C. Beyond the temperature 240 °C, no further mass loss was registered, which indicated
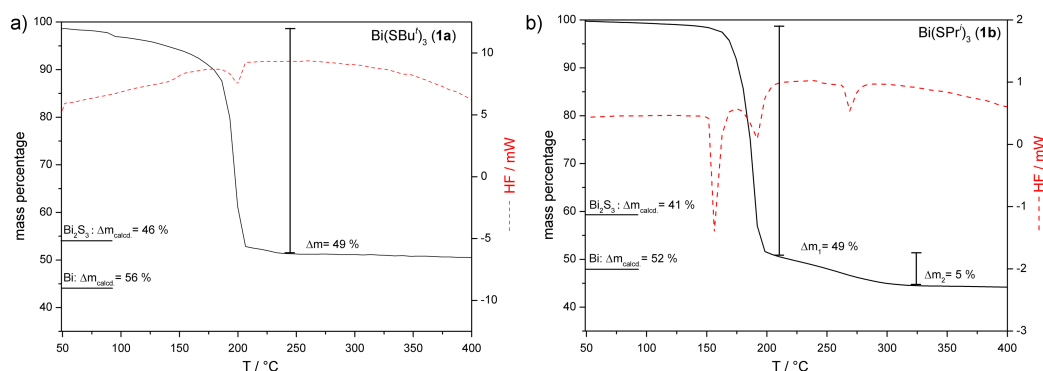
Figure 3.10: TG-DTA plots of the molecules (**1a**):*left-hand side* and (**1b**): *right-hand side.* The thermogravi-
metric curve is shown in solid black, and the DTA curve in solid red. The inset horizontal lines
at the left-hand mass percentage axis, denote the corresponding calculated $\Delta m_{calcd.}$ value for
full conversion to either Bi or Bi_2S_3 as guide for the eye.

the formation of a solid-state material with a definite composition. In the case of (**1a**), the
experimentally determined mass loss of $\Delta m = 49\%$ is in accordance with the theoretical
value ($\Delta m_{calcd.} = 46\%$) expected for the formation of Bi_2S_3. The slight deviation between the
calculated and observed mass loss values is attributed to a partial sublimation event occurring
prior to the incipient decomposition. For (**1b**) the two distinctive mass loss events were
recorded at 200 °C ($\Delta m = 49\%$) and at 300 °C ($\Delta m = 54\%$). The endothermic event at 200 °C
marks the single-step decomposition visible as steep mass loss between 170 °C to 200 °C whereas
the endothermic event at 271 °C coincides with the melting point of elemental bismuth, for
which full conversion was calculated as $\Delta m_{calcd.} = 52\%$, which is close to the above-mentioned
experimental values. The distinctive differences in the decomposition profiles of the two
precursors explain the differential fate of the CVD deposits for experiments performed under
similar conditions. This observation underscores the role of precursor chemistry in determining
the chemical composition and morphology of the final material.

3.2.5 Mass spectrometry of (1a) and (1b)

The distinctive decomposition behavior of (**1a**) and (**1b**) can be corroborated by the molecular
gas phase fragmentation patterns during mass spectrometrical analysis. Using EI-MS it
was shown the fragmentation pattern of Bi(SBu^t)$_3$ (**1a**) is dominated by the cleavage of the
carbon-sulfur 'C-S' bond, whereas the fragmentation of Bi(SPr^i)$_3$ (**1b**) results in molecular
species from the cleavage of the bismuth-sulfur 'Bi-S' bond. The molecular peak $[M]^+$ is
present for both compounds and dimeric (or *n*-meric) aggregates were not observed, even in
an extended measurement range $m/z = 1200$. The m/z range covering all bismuth containing
species is reproduced in (Figure 3.11) while the full patterns are shown in (Figure A.5 and
A.6). In the EI-MS fragmentation pattern of Bi(SBu^t)$_3$ (**1a**) the four most intensive signals,
in decreasing order, were detected for $[Bi(S)(SC_4H_9)]^+$ (38, m/z 330), Bi(SC$_4$H$_9$)$_3$]$^+$ (22, m/z
476), $[Bi(SH)_2]^+$ (22, m/z 275) and $[Bi(S)(SH)_2]^+$(10, m/z 307). Apart from the molecular
peak $[Bi(SC_4H_9)_3]^+$, these fragments represent the dominating fragmentation pathway for
Bi(SBu^t)$_3$, which initiates with the loss of an alkyl group through the cleavage of the C-S bond,
while the Bi-S bond is retained. The presence of the labile C-S bond generates a larger number
of fragments from the ionic series $[Bi(SC_4H_9)_{3-n}]^+$ ($n = 3, 2, 1$), which corresponded to the
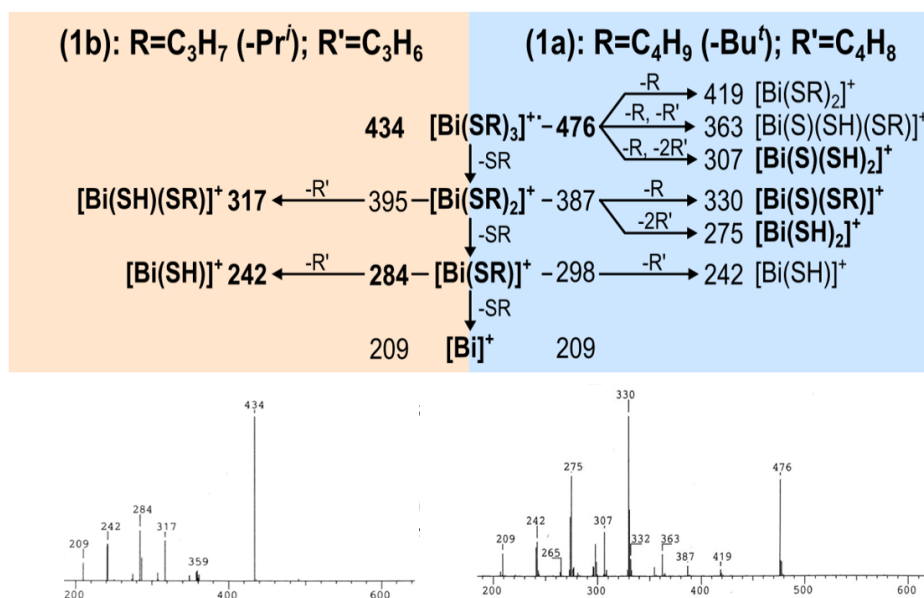
Figure 3.11: Comparison of mass spectrometrical fragmentation patterns of $Bi(SPr^i)_3$ (**1b**;*left*) and $Bi(SBu^t)_3$ (**1a**;*right*). Detected m/z values and assigned fragment ions were summarized in a suggested fragmentation pathway. The four most intensive fragment ions are presented in bold. Complete mass spectrometric data is presented in (Figure A.5 and A.6).

fragment molecular formulae $[Bi(S)(SC_4H_9)_{3-n}]^+$ and $[Bi(SH)(SC_4H_9)_{3-n}]^+$ with $(n = 2, 1, 0)$ or combination thereof. Signals arising from species, which do not comprise a cleaved 'C-S' bonds in the ligand sphere of bismuth were detected at low intensities, e.g., $[Bi(SC_4H_9)_2]^+$ (3, m/z 387) and $[Bi(SC_4H_9)]^+$ (8, m/z 298). The fragmentation pathway shown in (Figure 3.11) is a plausible suggestion based on the experimentally observed fragment species.

In the fragmentation pattern of $Bi(SPr^i)_3$ (**1b**) the highest relative intensity was observed for the molecular peak $[Bi(SC_3H_7)_3]^+$(38, m/z 434) followed by $[Bi(SC_3H_7)]^+$ (14, m/z 284) $[Bi(SH)(SC_3H_7)]^+$ (11, m/z 317) and $[Bi(SH)]^+$ (10, m/z 242). Together with $[Bi(SC_3H_7)_2]^+$ (2, m/z 359) and $[Bi]^+$ (6, m/z 209) these are all bismuth containing fragment ions from the EI-MS pattern (Figure 3.11), which lead to a comparable simple picture in terms of fragmentation, in which species containing an intact 'S-C' bond such as $[Bi(SC_3H_7)_{3-n}]^+$ $(n = 2, 1, 0)$ are observed as major fragments. The noticeable high relative intensity of the peak corresponding to dithiol $[H_7C_3S-SC_3H_7]^+$ (30, m/z 150), compared with $[M]^+$ peak indicated the loss of the H_7C_3S-group to be the dominating fragmentation mechanism. The corresponding R_2S_2 dithiol obtained from $Bi(SBu^t)_3$ is in contrast detected in almost negligible low intensity $[H_9C_4S-SC_4H_9]^+$ (5, m/z 178). On the other hand, the $[RSH]^+$ fragment is largely present in the pattern of $Bi(SBu^t)_3$ $[H_9C_4SH]^+$ (35, m/z 90) and merely detected for $Bi(SPr^i)_3$ $[H_3C_7SH]^+$ (5, m/z 76). This observation is possibly related to an inter- or intramolecular β-Hydrogen elimination mechanism, as reported for the metal complexes $Ti(SBu^t)_4$, $Mo(SBu^t)_4$[99] and $[R_2In(\mu\text{-}SBu^t)]_2$ $(R = \text{alkyl})$,[100] where all these molecules were successfully applied for the deposition of the corresponding metal sulfides by CVD.
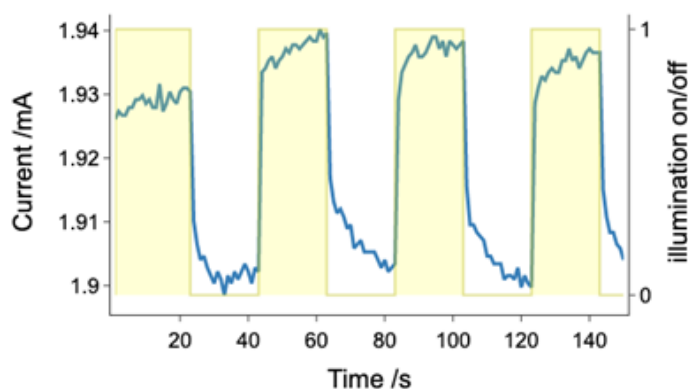
Figure 3.12: Photoresponse (blue line) of Bi_2S_3 deposited using (**1a**) at 300 °C on FTO under white light irradiation from a 150 W Xe-Lamp with AM1.5G filter, which follows the sequential illumination pattern (yellow).

3.2.6 Photoresponse measurements of Bi_2S_3 by CVD of (1a)

Chronoamperometric studies using a bias voltage of 20 mV under time varying white light illumination (irradiance: 100 mWcm^{-2}) reveal the directly proportional photoresponse of Bi_2S_3 deposited on FTO using (**1a**) at 300 °C substrate temperature, where a photocurrent of around 30 µA is observed repeatedly. In the selected sample geometry, where Bi_2S_3 was sandwiched between two FTO layers, signal rise times ($t_{90\%}$) of < 4 s and fall times ($t_{10\%}$) of < 9 s are observed (Figure 3.12). While the intensity as well as repeatability of observed photoresponse are intrinsic material properties, which are in accordance with published data,[73,74,101] the signal response times are highly dependent on device configuration, where the vertically oriented platelet like Bi_2S_3 film has only intermittent contact to the counter top-electrode geometry.

3.2.7 DFT calculations

For a better understanding of the different thermal behavior of the molecules (**1a**) and (**1b**) DFT calculations were performed to determine the highest occupied molecular orbital (HOMO) and lowest unoccupied molecular orbital (LUMO) energies for the optimized structures of $Bi(SBu^t)_3$ and $Bi(SPr^i)_3$. All the structural optimization was confirmed to be minimum-energy structures with the absence of imaginary frequency. This is implemented in the GAUSSIAN 16 suite of program package which was employed for all the calculations.[102] The HOMO and LUMO of $Bi(SBu^t)_3$ were found to be evenly distributed throughout the Bi and the three S atoms (Figure 3.13). The HOMO energy levels of $Bi(SBu^t)_3$ were estimated to be -5.99 eV. Moreover, for the $Bi(SBu^t)_3$, the HOMO, HOMO-1, and HOMO-2 energies were close to each other due to rather symmetrical structure. The LUMO energy levels of $Bi(SBu^t)_3$ is -1.77 eV. The HOMO was found to be localized on three S atoms, and the LUMO was delocalized on the Bi and the three S atoms. However, for the $Bi(SPr^i)_3$, the energy levels are more complicated when compared to $Bi(SBu^t)_3$. The HOMO and HOMO-1 energy levels are localized on the Bi and two S atoms with -6.12 eV and -6.17 eV , respectively. The HOMO-2 is mainly concentrated on the other S with a different energy level of -6.34 eV. For the LUMO, LUMO-1, and LUMO-2, their energy levels also indicated significant differences with values of -1.71, -1.67, and -1.50 eV, respectively. The calculation results indicated that the $Bi(SPr^i)_3$
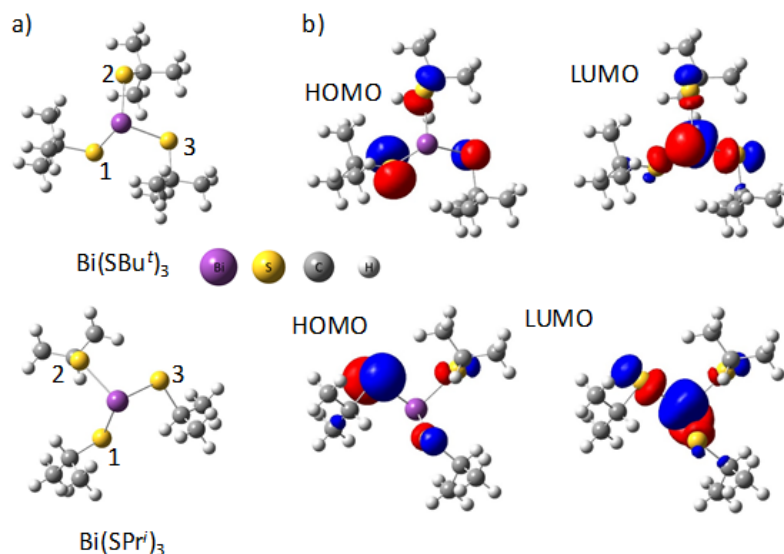
Figure 3.13: a) Optimized structure of $Bi(SBu^t)_3$ and $Bi(SPr^i)_3$ compounds and b) frontier molecular orbital plots of HOMO and LUMO (isoval: 0.02 a.u.) at the DFT B3LYP 6-311G(d,p) level of theory. Bi, S, C, and H atoms are shown as purple, yellow, gray, and white, respectively. The colored region represents the phase of the HOMO and LUMO molecular orbital wave function, and the red and blue represent the positive and negative values of the phase

may have complex atomic charge distribution, because the introduction of an isopropyl group lowers the molecular symmetry.
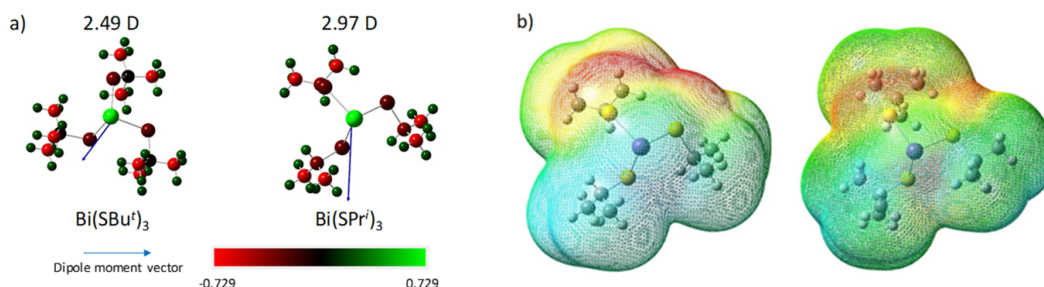
Figure 3.14: The structures of atomic charges of $Bi(SBu^t)_3$ and $Bi(SPr^i)_3$ compounds with display charge distribution and calculated dipole moment vector. b) Molecular electrostatic potential (MEP) maps from total SCF density. The electrostatic potential increase in the following order: red < green < blue.

The atomic charge calculation shows the deterministic influence of the dipole moment of the molecular system in the observed decomposition behavior. The atomic charge distributions (Figure 3.14) for $Bi(SPr^i)_3$ shows that the C atom attached to the S atom has a higher partial negative charge ($-0.327\,e$) compared to that calculated for $Bi(SBu^t)_3$ (0.012 e). This directly affects the charge density on S atom in $Bi(SPr^i)_3$ which has a slightly higher partial negative charge ($-0.299\,e$) compared to that of $Bi(SBu^t)_3$ ($-0.246\,e$). The S-C bond dipole moment of the $Bi(SPr^i)_3$ was found to be 0.38 D that is oriented along the S-C bond axis towards the carbon atom. However, the S-C bond dipole moment of $Bi(SBu^t)_3$ was 1.36 D, and the bond dipole moment vector is oriented towards the sulfur atom, which is in the opposite

Table 3.1: Bond angles and bond lengths of optimized Bi(SBu^t)$_3$ and Bi(SPr^i)$_3$ compounds.

Compound	n	(Bi-S$_n$-C) Bond Angle /°	(Bi-S$_n$) bond length / Å	(S$_n$-C) bond length / Å
Bi(SBu^t)$_3$	1	105.7	2.627	1.960
	2	115.6	2.583	1.971
	3	109.7	2.601	1.967
Bi(SPr^i)$_3$	1	102.2	2.617	1.940
	2	106.7	2.582	1.945
	3	103.7	2.603	1.942

direction, when compared to Bi(SPr^i)$_3$. As a result, even though the Bi-S bond length of each compound was comparatively similar (2.58 Å for Bi(SBu^t)$_3$; 2.6 Å for Bi(SPr^i)$_3$), the Bi-S bond dipole moment for the Bi(SBu^t)$_3$ was 6.34 D which is stronger compared to Bi(SPr^i)$_3$ (6.01 D). However, the net dipole moment of Bi(SBu^t)$_3$ was 2.49 D, which is significantly weaker when compared to Bi(SPr^i)$_3$ (3.28 D) due to their orientation of the S-C bond dipole moment vector. The concept of polarity reversal' so-called *umpolung* is suggested to explain this phenomenon.,[103,104] The molecular electrostatic potential (MEP) maps corroborates the above hypothesis in the intramolecular charge distribution evident in the MEP plotted for Bi(SBu^t)$_3$ and Bi(SPr^i)$_3$ (Figure 3.14). The selected bond angles and the bond lengths are summarized in (Table 3.1). For the Bi(SPr^i)$_3$ compound, due to the lone pair repulsion, Bi-S-C bond angles are reduced from the theoretical angle of 109.2°. However, Bi-S-C bond angle of the Bi(SBu^t)$_3$ increases from the 109.2° to maximum 115.6°. The bond lengths between Bi and S of each compound are similar to each other, however, S-C bond lengths of Bi(SBu^t)$_3$ are expectedly longer compared to the S-C bond lengths of Bi(SPr^i)$_3$ compound, which is shown in (Table 3.1). It is assumed that this possibly results from the steric hindrance of the $-$Bu^t group. The bond dissociation energy between S-C bond calculation is, therefore, carried out to confirm these results.

ΔH_f = -6.38 eV ΔH_f = -7.35 eV
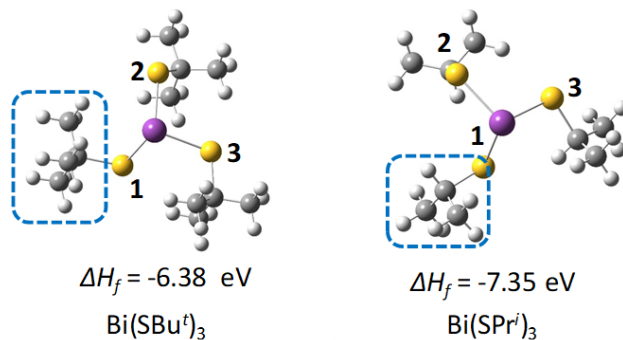
Bi(SBu^t)$_3$ Bi(SPr^i)$_3$

Figure 3.15: The S–C bond dissociation energies of Bi(SBu^t)$_3$ and Bi(SPr^i)$_3$ compounds.

As shown in (Figure 3.15) the calculated S-C bond dissociation energy for the Bi(SBu^t)$_3$ is -6.38 eV. In the case of the Bi(SPr^i)$_3$, the calculated value of ΔH_f is -7.35 eV. The more negative value of ΔH_f in Bi(SPr^i)$_3$ with respect to the Bi(SBu^t)$_3$ indicates that S-C bond of the Bi(SPr^i)$_3$ is thermodynamically more stable than that of Bi(SBu^t)$_3$.

3.3 Conclusion

The differential thermal decomposition behavior of two new single-source molecules, $Bi(SBu^t)_3$ and $Bi(SPr^i)_3$ in the CVD process as discussed in this study demonstrates the potential of preorganized molecular units in precursor compounds but it also reveals the limitations of precursor design due to the intrinsic bond strengths of peripheral moieties that can act as potential 'break points' for an uncontrolled and premature decomposition of the precursors. This study demonstrates with the aid of DFT calculations that the steric hindrance induced by one additional methyl group in $Bi(SBu^t)_3$ when compared to $Bi(SPr^i)_3$ results in elongation and weakening of the 'S-C' sulfur-carbon bond, so that the thermolysis during CVD results in phase pure Bi_2S_3 as the final material. Their experimental mass spectrometric gas phase fragmentation patterns were in accordance with these findings. On the other hand, elemental Bi that was obtained by CVD of $Bi(SPr^i)_3$ containing thermolabile 'Bi-S' units provided the first example of bismuth mesocrystal formation by non-classical crystallization in the CVD process.

3.4 Additional Information on the Experimental Data

XRD of Bi₂S₃ and Bi by CVD at 250 °C. In (Figure 3.16) the XRD pattern of Bi deposited from (**1b**) on Si is presented. Relative intensities were referenced to the peak at $2\theta = 12.41°$ from the (012) plane ($I_{\mathrm{rel.,exp.}} = 100$), in accordance with the reference card ($I_{\mathrm{rel.}} = 100$). The
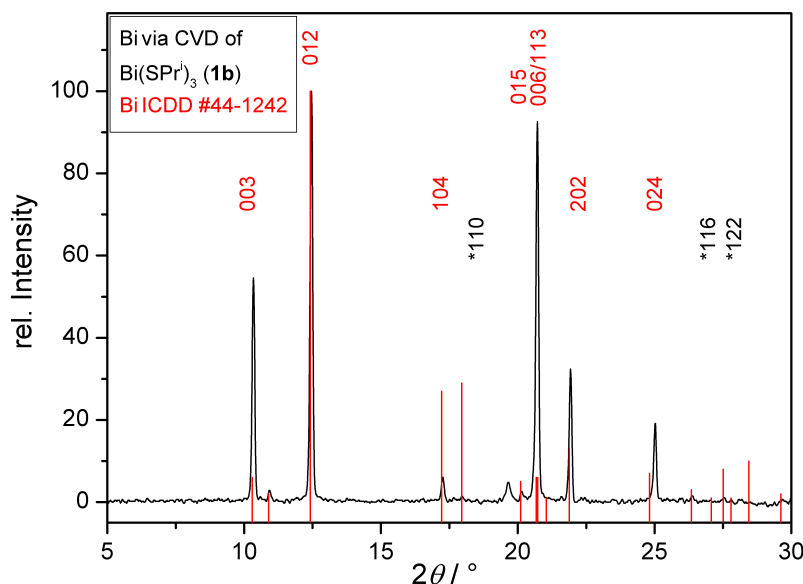
Figure 3.16: XRD pattern of Bi obtained from CVD of (**1b**) at 250 °C, normalized to relative Intensities. The planes from the reference card (ICDD # 44-1246) that have been assigned in the experimental pattern are held in red (hkl), and those not observed in black with an asterix in front (*hkl).

2ⁿᵈ largest peak listed in the reference ($I_{\mathrm{rel.}} = 29$) at $2\theta = 17.95°$ from the (110) plane, was not observed experimentally. Whereas the peak from the (104) plane at $2\theta = 17.22°$ as the 3ʳᵈ highest by relative intensity ($I_{\mathrm{rel.}} = 27$), was detected in lower intensity ($I_{\mathrm{rel.,exp.}} = 5$). The signal from the (003) plane ($I_{\mathrm{rel.,exp.}} = 55$) and the overlapping peak by the (006)/(113) planes (each $I_{\mathrm{rel.}} = 6$) were measured in largely increased rel. intensities ($I_{\mathrm{rel.,exp.}} = 90$). Less pronounced, yet also increased in their Intensities ($I_{\mathrm{rel.,exp.}}$) were the following (202) and (024) diffraction peaks. The (116) and (112) planes listed for bulk bismuth were not detected from Bi deposited by CVD of (**1b**).

In (Figure 3.17) and the following text the XRD pattern from Bi₂S₃ deposited on Si (250 °C) is compared en detail to the reference pattern of bulk Bi₂S₃ (ICDD # 17-320) is presented. The large part of $(hkl), (0kl), (0k0)$ and $(h0k)$ indexed planes in the reference card were either not detected or measured below their expected relative intensities, when comparing $2\theta = 11.41°$ as the (130) plane to the reference pattern, followed by the (310) plane at $2\theta = 11.53°$ ($I_{\mathrm{rel.}} = 50$). There is a higher likelihood to assign the experimental peak at this position to the (310) plane yet given the linewidth of the signal and the close 2θ values of the (130) and (310) planes in the reference pattern, no exclusive assignment to one of these two planes was possible for this peak. Comparing the experimental diffraction pattern by its relative intensities reveals that apart from the 'base' peak assigned as (130)/(310) only the (020)/(200) peak is close to the relative intensity that was given in the reference card. For example, the (211)-plane as the second highest by relative intensity in the reference card ($I_{\mathrm{rel.}} = 80$), was detected by ten-fold
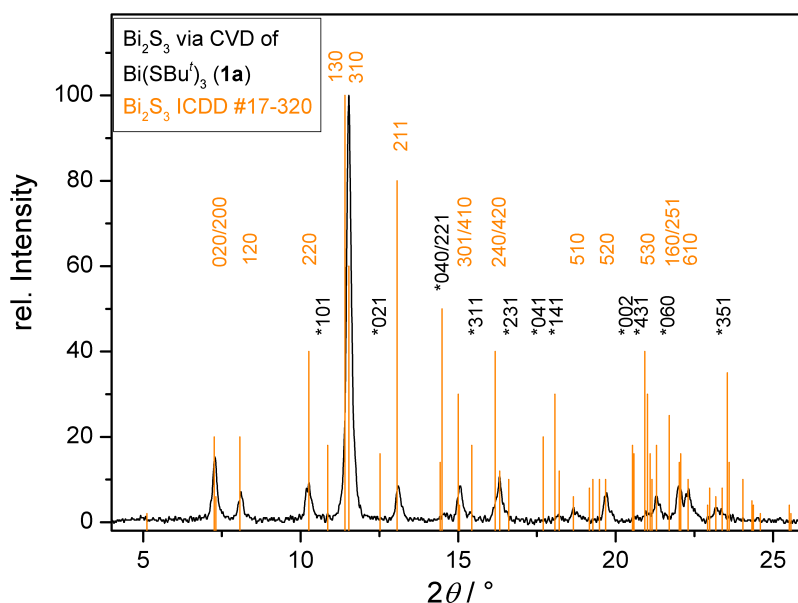
Figure 3.17: XRD pattern of Bi_2S_3 obtained from CVD of (**1a**) at 250 °C, normalized to relative Intensities. The planes from the reference card (ICDD # 17-320) that have been assigned in the experimental pattern are held in orange (hkl), and those not observed in black with an asterix in front (*hkl).

lower intensity ($I_{rel.,exp.} \sim 8$). In all remaining cases the peaks were noticeable similar in their reduced intensities ($I_{rel.,exp.} \sim 10 \pm 5$) than listed in the reference pattern.

Bi from CVD of (1b) at 250 °C and 300 °C   In (Figure 3.18a) the SEM top-view image recorded at enlarged magnification of bismuth deposited by (**1b**) on Si at (250 °C) is shown, in addition to (Figure 3.4). Hereby the porous interior structure of the material became apparent.In (Figure 3.18b) the SEM top-view image of bismuth deposited by (**1b**) on Si is shown, when the substrate temperature was adjusted to 325 °C. Here nanometer sized platelets
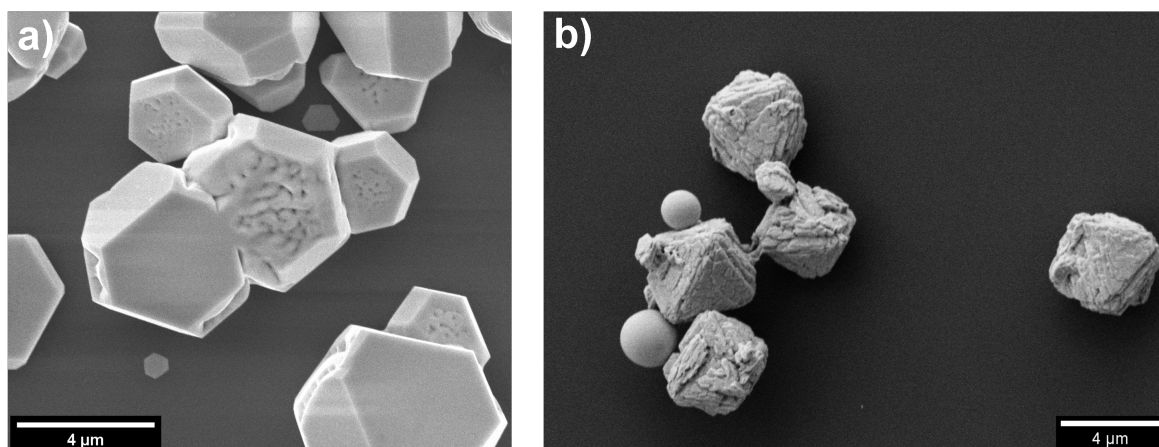
Figure 3.18: SEM top-view image of elemental bismuth Bi as deposition product of (**1b**) by CVD on Si at the substrate temperature a) 250 °C and b) 325 °C.

of irregular shape are stacked on their largest surface and act as building blocks for individual structures on the micrometer scale, which display the three-fold rotational symmetry present in the unit cell of bismuth, apparent as triangular shaped surfaces in (Figure 3.18). It is suggested these are mesocrystals formed by oriented attachment of the irregular shaped nanoplates along their high energy surface.[105,106] On a speculative basis, these nanoplates would possibly be formed by charged particles (in size below the resolution capabilities of the SEM technique) formed in the gas phase by the molecular precursor (**1b**), as an example of non-classical crystallization of bismuth by CVD.[98] Being aware that a porous structure and outer shape is not alone sufficient to draw this conclusion and also were the above particles not characterized by HR-TEM in order to determine the long-range crystallographic order.[107] The suggestion does not substitute the necessity of *in-situ* mechanistic studies, which is in general a difficult task in CVD. Nevertheless this is regarded as a strong hint, in view of the apparent similarity to reported mesocrystal structures[105,106,108] and for plausibility reasons as discussed in the following text. The SEM top-view (Figure 3.18) on the right-hand side shows the simultaneous presence of round spheres, which is considered as the result of melting, due to the adjusted temperature of the Si substrate (325 °C) which is above the melting point of bismuth (271 °C) at STP. The co-existence with the micrometer sized particles beyond the melting point of bismuth can either be the result of inhomogeneous temperature coverage of the substrate or increased temperature stability of the micrometer-sized structures. In either case the re-formation of irregular plates out of a melt that stack up to a particle that displays symmetry elements of the unit cell is regarded as not likely. Therefore, it is suggested the individual platelets visible in (Figure 3.18) are the result preformed gas phase particles. These are subject to further investigation.
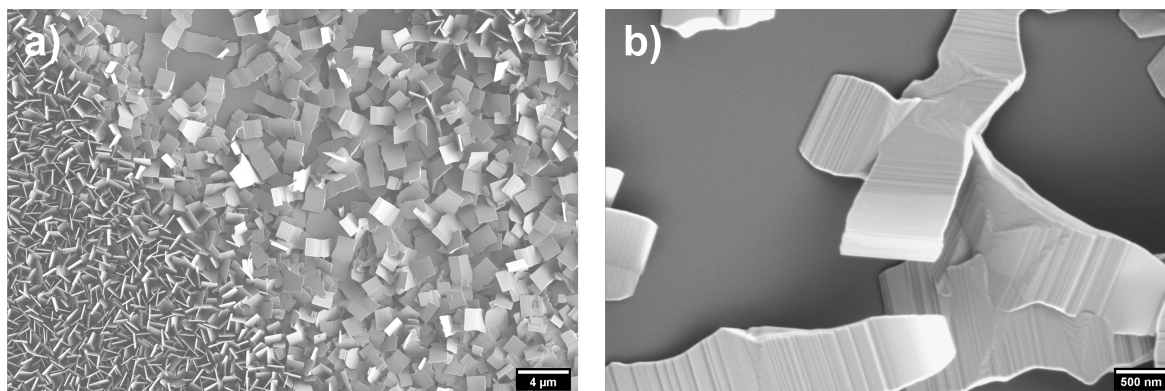
Figure 3.19: SEM top-view image of Bi_2S_3 as deposition product of (**1a**) by CVD on Si at the substrate temperature 250 °C.

SEM of Bi_2S_3 from CVD of (1a) at 250 °C In (Figure 3.19) additional SEM images of Bi_2S_3 that was obtained by CVD of (**1a**) are shown. The right-hand side image in (Figure 3.19) shows an area of the deposition product that experienced mechanical damage after the deposition, which enabled closer inspection of the larger surface of the individual plates, that are otherwise perpendicular to the substrate surface. The images in (Figure 3.19) show the incremental increase in dimension towards the middle of the plate-like structure.

4 Tin Alkylthiolates as CVD Precursor to SnS

This chapter contains the reformatted manuscript published in the journal *Molecules*:

The synthesis, characterization and application for CVD of the molecular single-source precursor [Sn(SBu^t)(*tfb-dmeda*)] (**2a**) is presented. The fact that the tin(II) alkylthiolates Sn(SPr^i)$_2$ (2b) and Sn(SBu^i)$_2$ (2c) (including Sn(SBu^t)$_2$) were not applicable as single-source precursor molecules in the CVD process, compound (**2a**) was introduced, which enabled the deposition of SnS by CVD. The CVD study includes the investigation on different substrates and deposition parameter. The solution structure and fluxional dynamics of (**2a**) were investigated by 1D and 2D multinuclear NMR experiments involving the ^{1}H, ^{13}C, ^{19}F and ^{119}Sn nuclei and by variable-temperature NMR experiments involving the ^{1}H and ^{119}Sn nuclei.

(2a)
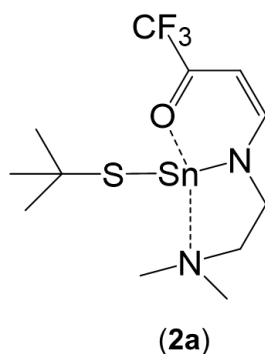
Figure 4.1: Schematic drawing of the heteroleptic tin(II) precursor molecule (**2a**) investigated in this chapter.

4.1 Introduction

The monochalcogenide material SnS, which is isostructural to black phosphorous,[109] has recently gained much attention due to its unique semiconductor and optoelectronic properties, as well as its low toxicity and the earth-abundant character of tin and sulfur.[110–113] Two-dimensional (2D) layered monochalcogenides like SnS exhibit a puckered lattice structure with reduced crystal symmetry (orthorhombic)[114] and display structural resemblance to the classical 2D van der Waals material graphene and most of the transition metal dichalcogenides (TMDCs).[115,116] Their layer-dependent tunable bandgap, high carrier mobility, and strong in-plane anisotropy make these materials promising for emerging next-generation electronic[117] and photonic applications.[118,119] SnS has been actively studied due to its p-type semiconductor characteristics and remarkable optoelectronic properties[120] due to the reported direct bandgap of about 1.3 eV and indirect bandgap of about 1.0 eV.[121] Various crystal structures are known for SnS, such as orthorhombic,[111] zinc blende like,[122] or a highly distorted rock salt (NaCl) structure,[123] among which the orthorhombic is the most commonly found structure in SnS films reported so far.[124]

Molecular Precursor for CVD of SnS
Thin films of SnS have been obtained using various techniques such as thermal evaporation, chemical vapor deposition, electro-deposition, spray pyrolysis,[125] and sulfurization of metallic precursors.[126] To achieve a stoichiometrically pure phase with desired material characteristics (morphology, grain size, etc.), carefully designed and optimized synthesis of the materials is necessary. Phase deposition processes like chemical vapor deposition (CVD) enable the growth of high-quality 2D materials with mono- or few-layer thickness control.[127] The preparation of SnS by CVD using multi-source precursors (MSP) has been reported previously, for instance, by reacting $SnCl_4$ with H_2S[128] or $Sn(SPh)_4$ with H_2S.[129] However, the MSP approach requires at least two components possessing different properties like vapor pressure and stability in the gas phase and often uses hazardous co-reagent like H_2S. Some of these drawbacks can be over-come by the single-source precursor (SSP) approach, which enables a predefined stoichiometry and phase control already at the molecular level. For instance, the Sn^{II} aminothiolate single-source precursor $Sn[SCH(Me)_2CH_2CH_2N(Me)_2]$ was used for the deposition of SnS films with preferred crystal orientation along the (040) planes at temperatures as low as 300–350 °C.[130] The Sn^{II} dithiolate $Sn(SCH_2CH_2CH_2S)_2$ has been used for phase-pure SnS deposition, obtained in CVD at temperatures between 300 and 400 °C.[131] The alkyltin chalcogenolate precursors $[SnBu^n_2(SBu^n)_2]$ and $[SnBu^n_3(SBu^n)]$ were employed in low pressure (LP)-CVD for the deposition of phase pure SnS in the temperature range between 375 and 530 °C.[132] Aerosol-assisted chemical vapor deposition (AA-CVD) of Sn^{II} thioamidates,[133] Sn^{II} thioureide, Sn^{II} dithiocarbamates $[Sn(S_2CNRR')_2]$ (R,R' = alkyl),[134] Sn^{IV} dialkyldithiocarbamates as single-source precursor $[Sn(C_4H_9)(S_2CNRR')_2]$, $[Sn(C_6H_9)(S_2CNRR')_2]$[135] and heteroleptic molecular tribenzyl Sn^{IV} thiosemicarbazones $[Bz_3SnCl(L)]$[136] (L = thiosemicarbazone) resulted in temperature-dependent polymorphs of SnS.[137,138] Using (atmospheric pressure) AP-CVD and H_2S with the Sn^{IV} dithiocarbamate $Sn(R)_2(S_2CNRR')_2$, a mixture of SnS and Sn_2S_3 was obtained.[139] Similarly, were the compound $Sn(SCH_2CF_3)_4$ and $Sn(SCH_2CH_2S)_2$ employed for the deposition of SnS at temperatures of 550 °C and 600 °C, respectively.[140,141]

In many of the above-mentioned compounds, the presence of various element combinations introduces higher ionicity in the bonds, which often leads to higher sublimation temperatures that affect the thermal decomposition profile, leading to multi-step decomposition processes and concomitant formation of secondary phases. Further approaches to circumvent limited volatility include the application of a carrier gas, which is challenging for process engineering and reproducibility. Difficulties may also arise from a mismatch in oxidation states of the central atom (Sn^{II} vs. Sn^{IV}) in the precursor and the final material.

Herein, the direct synthesis of phase-pure SnS by CVD experiments performed at extraordinary low precursor temperatures (T$_s$) using the SSP approach is presented. By introducing a tridentate OˆNˆN ligand *Htfb-dmeda* [(3Z)-4-[2- (dimethylamino)ethyl]amino-1,1,1-trifluorobut-3-en-2-one] in pre-synthesized Sn(SBu^t)$_2$, a monomeric and highly volatile Sn^{II} complex [Sn(SBu^t)(*tfb-dmeda*)] (**2a**) was obtained, which shows a clean and well-defined decomposition profile and sublimes without leaving any residue. The oxidation state of the Sn^{II} central atom remains unaltered and the element ratio Sn:S 1:1 is the same in the precursor molecule and in the desired final material SnS. The neutral role of the tridentate ligand (tfb-dmeda)$^-$ in the steric stabilization of the complex and its non-participating nature in the thermal decomposition process (no incorporation of N or O in the final products) makes it an ideal 'launch vehicle' to deliver Sn and S atoms on the substrate surface during the CVD process.

4.2 Results and discussion

4.2.1 Synthesis and Characterization of New Molecular Precursor

The motivation of this work was to generate single-phase, nanostructured tin monosulfide SnS by CVD method using an extraordinary volatile molecular precursor. The monoanionic,
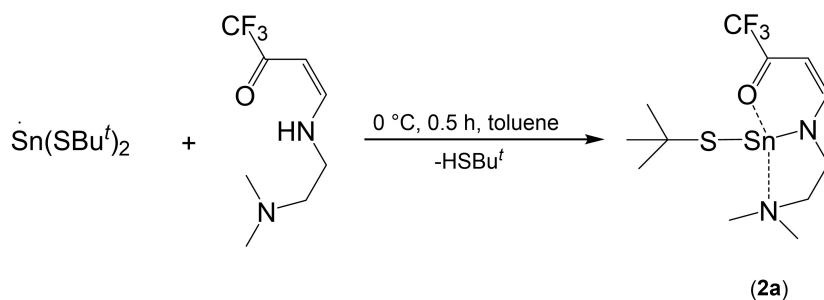
Scheme 4: Synthesis of (**2a**) via ligand exchange reaction.

tridentate coordinating *Htfb-dmeda* ligand was synthesized following the literature,[142] whereas Sn(SBu^t)$_2$ was synthesized using a simple protolysis reaction between Sn[N(SiMe$_3$)]$_2$[143] and commercially available HSBu^t (2-methyl-2-propanethiol). An equivalent amount of the ligand *Htfb-dmeda* was added to a toluene solution of Sn(SBu^t)$_2$ under daylight exclusion, resulting in an orange solution. Removal of volatile compounds and purification of the orange product by sublimation enabled the isolation of the pure compound [Sn(SBu^t)(*tfb-dmeda*)] (**2a**) (Scheme 4).

4.2.2 Single Crystal X-Ray Analysis of (2a)

Crystals of (**2a**) suitable for single-crystal X-ray diffraction were obtained by sublimation. Compound (**2a**) crystallized in the triclinic space group $P\bar{1}$ with four identical molecules [Sn(SBu^t)(*tfb-dmeda*)] present in the asymmetric unit. Since there are no significant inter-
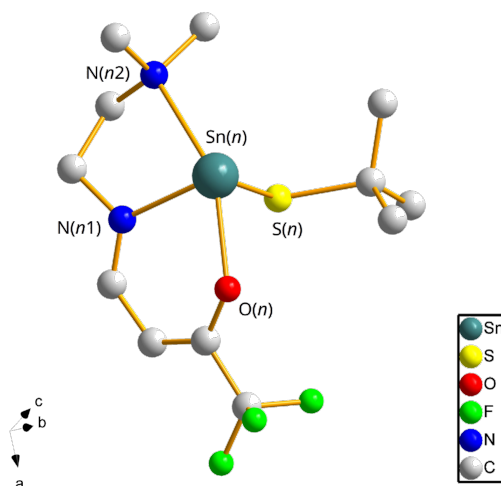
Figure 4.2: Molecular structure of [Sn(SBu^t)(*tfb-dmeda*)] (**2a**)

actions present among these four independent molecules to form a pseudotetramer, only one such molecule is shown in (Figure 4.2). The central Sn^{II} atom in (**2a**) is coordinated by one monodentate (SBu^t)$^-$ and one tridentate (tfb-dmeda)$^-$ unit, resulting in a distorted (pseudo)trigonal-bipyramidal coordination geometry for it (Figure 4.2). Three equatorial positions are occupied by sulfur S(1), amine nitrogen N(11) and the lone pair of the Sn^{II} central atom. The axial positions are occupied by the carbonyl oxygen O(1) and the nitrogen atoms N(12) of the terminal $-$NMe$_2$ group. Some selected bond lengths and angles are listed in (Tables 4.1 and A.3), respectively.

Table 4.1: Selected bond lengths of (**2a**).

Atom-Atom	Bond length / pm	Atom-Atom	Bond length / pm
Sn(1)-S(11)	248.61(8)	Sn(1)-O(11)	226.9(2)
Sn(2)-S(21)	249.25(8)	Sn(2)-O(21)	224.8(2)
Sn(3)-S(31)	248.89(8)	Sn(3)-O(31)	223.7(2)
Sn(4)-S(41)	249.27(8)	Sn(4)-O(41)	225.4(2)
Sn(1)-N(11)	224.9(2)	Sn(3)-N(31)	226.0(2)
Sn(1)-N(12)	254.2(3)	Sn(3)-N(32)	254.1(3)
Sn(2)-N(21)	224.6(3)	Sn(4)-N(41)	224.2(2)
Sn(2)-N(22)	254.5(3)	Sn(4)-N(42)	255.7(3)

In the basal plane, the N(11)-Sn(1)-S(1) bond angles (83.12(6)°–84.93(7)°) are more compressed, as compared to the bond angles between the equatorial and apical positions, e.g., N(12)-Sn(1)-S(1) (86.47(7)°–88.26(7)°) and O(1)-Sn(1)-S(1) (90.77(6)°–92.53(6)°). The (tfb-dmeda)$^-$ ligand framework enforces a bent arrangement of the moiety with the bipyramidal axis O(1)-Sn(1)-N(12) (153.01(8)°–154.04(8)°) deviating significantly from the ideal linear

geometry. All the Sn-S, Sn-N, and Sn-O distances in (**2a**) are well within the sum of their Van der Waals radii,[84] and on the other hand, exceed the sum of the covalent radii for the corresponding element combinations (r_{cov}(Sn) = 140 pm, r_{cov}(N) = 71 pm, r_{cov}(O) = 63 pm, r_{cov}(S) = 103 pm).[144] The Sn-S distances in (**2a**) (Sn-S: 248.61(8) pm–249.27(8) pm) are only slightly above their corresponding covalent radii sum Σ_{cov}(Sn-S = 243 pm) bearing a high tendency towards covalency in their bonds. These tin-sulfur Sn-S bond lengths in (**2a**) are shorter than those reported for the homoleptic Sn^{II} alkylthiolates.[145–150] Compound $Sn(SBu^t)_2$[145] possesses two shorter Sn-S bonds (Sn-S: 252.7(2) pm and 252.9(2) pm) and two longer Sn←S intermolecular coordinative bonds (Sn-S: 303.4(2) pm and 303.3(2) pm), resulting in a network of interlinked molecular units with four-fold coordinated Sn^{II} atoms in pseudo-trigonal bipyramidal geometry. The just mentioned structural motif is also present in the crystal structures of $Sn(SPr^i)_2$ (**2b**) (Figure C.2) and $Sn(SBu^i)_2$ (**2c**) (Figure C.1), whereby the shortest tin-sulfur bond length is (Sn-S: 253.33(11) pm) (Table C.14) and (Sn-S: 252.77(9) pm) (Table C.14) respectively. Similarly, in the 1D coordination polymer $[Sn(SPh)_2]_n$, the central Sn^{II} atom adopts a distorted trigonal pyramidal coordination geometry, with two shorter Sn-S bonds (Sn-S: 251.8(2) pm and 257.7(2) pm) and two longer Sn←S coordinative bonds (Sn-S: 273.1(2) pm).[149] With bulkier substituents, lower degrees of oligomerization were realized as observed in the monomeric compounds $Sn(SMes^*)_2$ (Sn-S: 243.56(3) pm)[150] and $[Sn\{S-2,4,6-(Bu^t)_3C_6H_2\}_2]$[146] (Sn-S: 243.5(1) pm), similarly also in the trimeric compound $[Sn\{S-2,6-(Pr^i)_2C_6H_3\}_2]_3$ with (Sn-S: 247.1(5) pm–283.8(4) pm).[146] In anionic molecular Sn^{II} compounds, the Sn-S bond lengths show minor differences as compared to those in the coordination polymers, such as $[(Me_3Si)_3CSn(\mu\text{-}SBu)_2]^-$[148] (Sn-S: 256.8(1) pm–257.4(1) pm) or $[Sn(SPh)_3]^-$[151] (Sn-S: 253.2(1) pm and 255.2(1) pm). In analogous Sn^{IV} compounds, the tendency to form coordination polymers is absent. For example, $Sn(SBu^t)_4$ (Sn–S: 239.7(2) pm)[151] and $Sn(SPh)_4$ (Sn-S: 237.9(4) pm and 240.1(4) pm)[152] exist in their solid-state structures as monomeric units with distorted tetrahedral geometry around the Sn^{IV} central atom.

The Sn^{II} central atom interacts with both the N(11) and N(12) nitrogen atoms in (**2a**) by Sn←N coordinative bonds. One set of larger Sn(1)-N(12) distances in (**2a**) (Sn-N: 254.1(3) pm–255.7(3) pm) arises from weak intramolecular Sn←N coordination of the terminal $-NMe_2$ group. The second set of significantly shorter Sn-N distances Sn(1)-N(11) (Sn-N: 224.2(2) pm–226.0(2) pm) can be categorized as stronger Sn←N coordinative interaction, which are comparable to the bonding strength displayed by μ-bridging monoanionic nitrogen donor atoms, as found in the dimeric $[Sn(NMe_2)_2]_2$ with two terminal Sn-N single bonds (Sn-N: 206.7(4) pm) and two bridging Sn–μ-N (Sn-N: 226.5(4) pm and 226.6(5) pm).[153] For comparison, the Sn(1)-N(12) distances in (**2a**) are longer than in the monomeric $Sn(OCH_2CH_2NMe_2)_2$ (Sn-N: 245.8(2) pm),[154] yet shorter than in the dimeric $[\{(Me_3Si)_2N\}Sn(OCH_2CH_2NMe_2)]_2$[147] with weaker Sn←N coordinative interaction between the Sn^{II} center and the $-NMe_2$ moieties (Sn-N: 261.5(3) pm and 261.7(3) pm). Similarly, a Sn^{II}←O coordinative bonding interaction between the central Sn^{II} atom and the carbonyl oxygen atom is present in (**2a**), with Sn-O distances typically observed between Sn^{II} central atoms and neutral oxygen donor atoms.[155,156] The experimental Sn-O distances in (**2a**) (Sn-O: 223.7(2) pm–226.9(2) pm) fall in the region of bond lengths measured for μ-bridging anionic oxygen donor atoms or intermolecular contacts. Corresponding Sn-O single bond lengths between Sn^{II} and an anionic oxygen donor atom are significantly shorter. For example, the Sn-O bond lengths lie in the range 212.8(4) pm–216.5(4) pm in $[Sn(OBu^t)_2]_2$, having an archetypical 'Sn$_2$O$_2$' core as a structural motif.[145] One Sn-O single bond length is reported for $Sn(OCH_2CH_2NMe_2)_2$ (Sn-O: 205.6(2) pm),[154] and in $[\{(Me_3Si)_2N\}Sn(OCH_2CH_2NMe_2)]_2$, two Sn-O single bonds (Sn-O: 213.3(2) pm and

213.7(2) pm) and two Sn←O coordinative bonds (Sn-O = 226.7(2) pm and 229.9(2) pm) are observed.[147] In Sn[SCH(Me)$_2$CH$_2$CH$_2$NMe$_2$]$_2$[130] is the Sn-S bond (Sn-S = 252.63(4) pm) elongated, whereas the Sn-N distance arising from the −NMe$_2$ moiety (Sn-N = 247.13(12) pm) is shorter in comparison to (**2a**). Similar observations were made in Sn[SC(Pr^i)N(Bu^t)]$_2$, where two bidentate thioimidates, each coordinated through sulfur and nitrogen atoms, form a distorted square-pyramid with the central Sn^{II} atom (Sn-N: 237.91(12) pm and Sn-S: 254.67(4) pm).[133] The comparative observations above reveal the shortest nature of the Sn-S bond length in (**2a**) among all the Sn^{II} alkylthiolates Sn(SR)$_2$ reported so far.

4.2.3 Spectroscopic Characterization of (2a)

The structure of (**2a**) in solution was analyzed by a combination of 1D and 2D NMR experiments of ^{1}H, ^{13}C, ^{19}F, and ^{119}Sn nuclei. The ^{1}H-NMR spectrum of (**2a**) in C$_6$D$_6$ solvent recorded at 400 MHz showed (Figure 4.3) the formation of a single reaction product that was also supported by the high yield of (**2a**) obtained after sublimation, which excluded the simultaneous presence of other possible species such as fully substituted Sn atoms or oxidative addition product. As a result of deprotonation, the resonance of the (4-H) proton at $\delta =$ 6.56 becomes a doublet by vicinal coupling to (H-3). The associated dd (doublet of doublets) satellite signal showed the coupling between these protons and the ^{119}Sn-nuclei ($^3J_{^1H-^{119}Sn} =$ 25 Hz). The signal splitting of the methylene proton resonances in (**2a**) from the saturated
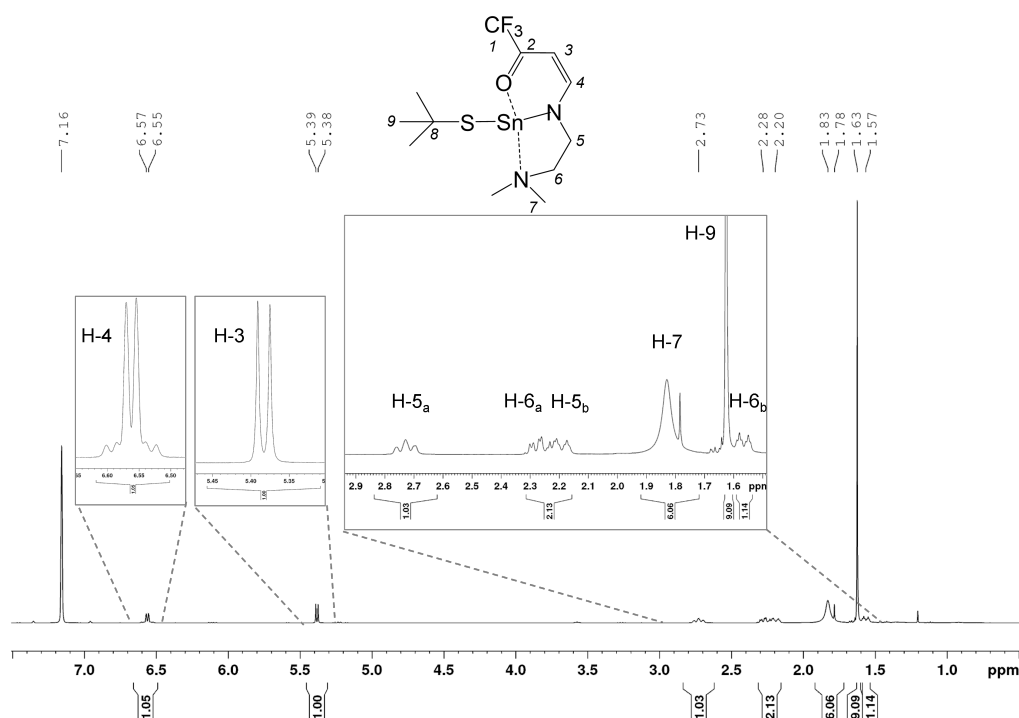
Figure 4.3: ^{1}H-NMR spectrum of (**2a**) in C$_6$D$_6$ recorded at 400 MHz.

region (C-5) and (C-6) of the ligand molecule leads to four distinct chemical shifts δ^1H. This is interpreted as a result of these protons being part of a more or less rigid N−C$_5$−C$_6$−N(CH$_3$)$_2$ framework, which formed a 5-membered ring by the coordination of the nitrogen atoms to the

Sn^{II} central atom (Figure 4.3). Although clearly under the influence of second-order effects, and probably also by dynamic broadening, the not so fully-resolved multiplet of the (H-5_a) and (H-5_b) methylene protons (centered at $\delta = 2.73$ and $\delta = 2.30$, respectively) indicated a typical spin-system, that would arise from the relation between axial (endo) and equatorial (exo) protons of a ring structure. The resonance(s) of the methyl protons from the -N(CH$_3$)$_2$ group at $\delta = 1.83$ displayed an increased linewidth ($\Delta_{1/2} = 25\,\text{Hz}$), as compared to the free protonated ligand (Figure A.7), pointing towards solution dynamics occurring at rates far below than that of free rotation. The sharp signal at $\delta = 1.78$ is attributed to the dynamics of the $-\text{N(CH}_3)_2$ moiety, since both signal integrals add up to six protons. However, in the case of broad signals, this is not a very reliable argument, and its origin may not be conclusively explained within this study. Upon cooling the solution of (**2a**) in toluene-d$_8$, the resonance at $\delta = 1.83$ (H-7) underwent further broadening and flattened out at T $= 268\,\text{K}$; thus the coalescence temperature was noted as T$_c = 278\,\text{K}$. Below this temperature, separate signals for the exchanging conformers are expected to emerge (further cooling was intended but due to instruments conditions of the VT-unit the full capabilities of the spectrometers could not be fully exploited). In the observed temperature range, no significant shift or change in linewidth was observed (Figures A.9 and A.10).

In summary, were the proton resonances from the unsaturated carbon moiety not affected by a dynamic process, and coupling was observed between (H-4) and the central ^{119}Sn nuclei. The methylene protons at the saturated (C-5) and (C-6) carbon atoms are chemically and magnetically not equivalent, and are part of a conformational equilibrium. By (variable temperature) VT-NMR, the coalescence temperature T$_c = 278\,\text{K}$ was determined, for the protons of the $-\text{N(CH}_3)_2$ group, which shows fluxional behavior in solution.

(2a)-i   **(2a)-ii**
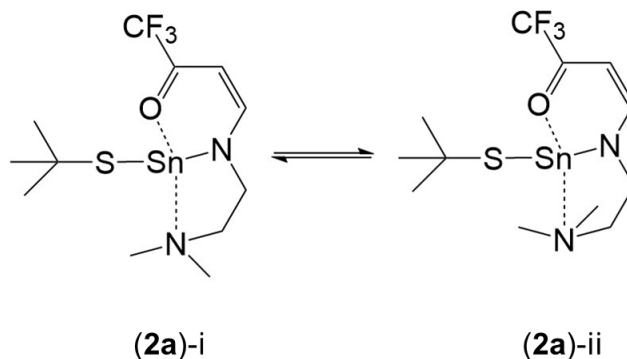
Figure 4.4: Proposed solution dynamics between two conformational isomers.

The ^{119}Sn{^{1}H}-NMR spectrum at room temperature displayed a single broad resonance at $\delta = -157$ (Figure A.11). The value lies well within the chemical shift region (roughly from $+150$ to $-400\,\text{ppm}$) identified with dimers of Sn^{II} present in a threefold coordination by sulfur, oxygen, and nitrogen donor atoms in varying element combinations.[157] Since these compounds become four coordinated in the dimer, there is a high resemblance to the bonding situation in (**2a**). In the above-mentioned chemical shift range, an identical set of donor atoms with identical coordinating geometry around the Sn^{II} central atom may be found separated by more than a hundred ppm, which shows the nature of the ligand to be also highly influential.[157] The chemical shift of Sn(SBu^t)$_2$ is reported at $\delta = 77$ (CH$_2$Cl$_2$) and 63 (THF),[158] which could not be observed, probably due to the fast solution dynamics observed in the reported

signal's linewidth of $\Delta_{1/2} = 1\,\text{kHz}$. The broad linewidth of the $\delta^{119}\text{Sn}$ resonance ($\Delta_{1/2} = 300\,\text{Hz}$) in compound (**2a**) indicated a dynamic exchange present at room temperature (Figure 4.4), supporting the observations made by the $^1\text{H-NMR}$ investigations. Upon cooling the solution down to $\text{T} = 268\,\text{K}$, the chemical shift was observed at $\delta = -167$ ($\Delta_{1/2} = 200\,\text{Hz}$) with narrower linewidth (as compared to the one obtained at room temperature). This slight dependence of the chemical shift on temperature suggested a conformational equilibrium that does not involve changes in the coordination number or geometry of the ^{119}Sn-nuclei.[159] The observation that introducing a nucleophilic solvent such as THF, the chemical shift $\delta^{119}\text{Sn}$ remained constant, showed a stable and saturated coordination sphere at the central Sn^{II} atom. Additionally, in the absence of a concentration-dependence of the $\delta^{119}\text{Sn}$ chemical shift, self-association processes such as aggregation or dimerization become unlikely.[159–161] Finally, the coupling between the central ^{119}Sn nuclei and (H-6$_{\text{a,b}}$) and (H-5$_{\text{a,b}}$) methylene protons is shown by a $^{119}\text{Sn},^1\text{H-HMBC}$ experiment (Figure A.8).

To summarize the results from the NMR experiments, it was shown that the structure of (**2a**) observed in the solid state is maintained in solution and suggest the presence of dynamic conformational equilibrium in the temperature range between $\text{T} = 298\text{–}268\,\text{K}$ as displayed in (Figure 4.4). If (**2a**) is kept in solution for a prolonged duration, gradual formation of the oxidized product $\text{Sn}(\text{SBu}^t)_4$ along with disulfide is observed. However, if stored under inert conditions, (**2a**) remained stable without any detectable signs of degradation for several months.

4.2.4 Mass Spectrometry of (2a)

The fragmentation behavior of (**2a**) was analyzed by mass spectrometry. For simplicity, the O^N^N-donor ligand moiety in compound (**2a**) is abbreviated as L ($L=$ tfb-dmeda$^-$) and, therefore, (**2a**) and its fragment notation as molecular peak are written as (L)-Sn-(SBu^t) and $[L\text{-Sn}-\text{SC}_4\text{H}_9]^+ = [\text{M}]^+$, respectively. Mass spectrometric analysis showed that the molecule exists as a monomer in the gas phase, as identified by its molecular peak $[\text{M}]^+$ (m/z 418) (Figure 4.5a). The signal of highest relative intensity belongs to the cationic

m/z 418
molecular peak
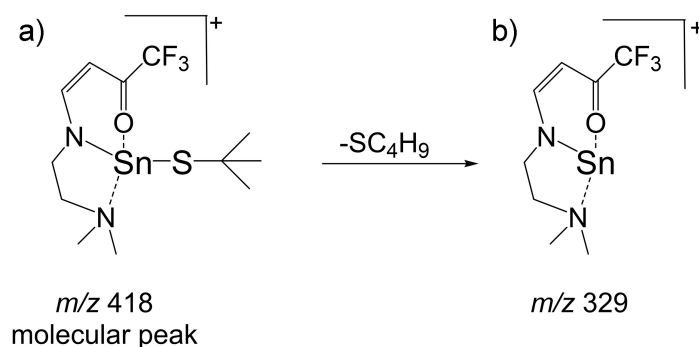
m/z 329

Figure 4.5: Scheme of the gas phase fragmentation of $[L\text{-Sn}-\text{SC}_4\text{H}_9]^+$ (m/z 418) a) into $[L-\text{Sn}]^+$ (m/z 329) species b) under EI-MS conditions.

'tin-ligand' species $[L\text{-Sn}]^+$ (m/z 329, $[\text{M}-\text{SC}_4\text{H}_9]^+$ (Figure 4.5b) as a result of the loss of the alkylthiolate radical fragment. The only signals that account for further fragmentation of $[L-\text{Sn}]^+$ are found with the smallest ion fragments (m/z 28 and 58), which are typical organic carbon-hetero atom(s) fragments in the different element combinations of C,H,N,O).

In other words, the ligand L in $[L-Sn]^+$ leaves the Sn^{II} central atom in one piece prior to its own fragmentation. There is no fragment ion with a tin atom bound to oxygen or nitrogen, unlike the complex $[Re(tfb\text{-}dmeda)(CO)_3]$, where partial decomposition of the $tfb\text{-}dmeda$ ligand while being bonded to the metal center has been observed by mass spectrometry.[142] An initial fragmentation step of $[M]^+$ that cleaves the bond between the ligand L and a complete $Sn-SC_4H_9$ unit generates either one of the two fragments $[L]^+$ (m/z 209) and $[Sn-SC_4H_9]^+$ (m/z 209) that are, by coincidence, identical in their m/z values. The signal detected at m/z 209 is most likely $[Sn-SC_4H_9]^+$, as explained further in the following text. The remaining signals could conclusively be assigned to tin alkylthiolate species (Scheme 5) which showed a high resemblance to the fragment ions previously reported for $Sn(SBu^t)_4$[59] and to $Sn(SBu^t)_2$. For the latter compound, no literature data was available, therefore, it was analyzed for comparison purposes in this work. All three compounds share at least partially a common decomposition pathway.

$$[Sn(SC_4H_9)_4]^{+\cdot} \xrightarrow{-SC_4H_9^\cdot} [Sn(SC_4H_9)_3]^+ \xrightarrow{-C_4H_8} [Sn(SH)(SC_4H_9)_2]^+ \xrightarrow{-C_4H_8} [Sn(SH)_2(SC_4H_9)]^+ \xrightarrow{-C_4H_8} [Sn(SH)_3]^+$$

m/z 476 $\quad$ m/z 387 $\quad$ m/z 331 $\quad$ m/z 275 $\quad$ m/z 219

$$\xrightarrow{-HSC_4H_9\ -C_4H_8} [Sn(S)(SC_4H_9)]^+$$

m/z 241

$$\xrightarrow{-2SC_4H_9^\cdot} [Sn(SC_4H_9)]^+$$

m/z 209
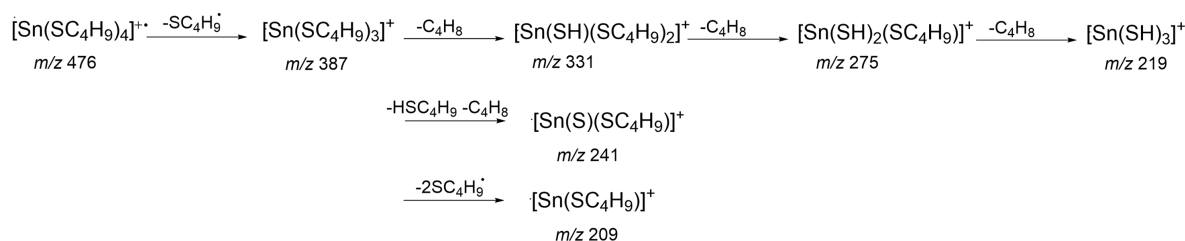
Scheme 5: Fragment ions detected together with (**2a**) by EI-MS, and which are attributed to species occurring also in the EI-MS of $Sn(SBu^t)_4$.

For $Sn(SBu^t)_4$, the consecutive loss of alkyl groups in the decomposition pattern was reported earlier.[59] Which in this context is equivalent to a preference for retaining the 'Sn-S' bond. From (Scheme 5), this became obvious by the sheer number of fragments with a Sn-S bond present in the gas phase. The mass spectrometric analysis showed that the fragmentation pattern of $Sn(SBu^t)_4$ could partially be found also in the fragmentation pattern of $Sn(SBu^t)_2$ (Figure A.13). $Sn(SBu^t)_2$ and $[Sn(SR)_2]$ ($R = $ alkyl) were generally prone to oxidation upon heating. The experimental conditions, namely the sublimation step prior to fragmentation in the mass spectrometer, may explain the observation of Sn^{IV} species in the gas phase. The observation was different for (**2a**), which is sublimable without decomposition or any other undesired side-reaction. This was confirmed by repeated resublimation, where (**2a**) was retrieved quantitatively after each sublimation step, and its identity was confirmed by NMR spectroscopy of the sublimate. To exclude the presence of possible contamination by oxidized species, such as $Sn(SBu^t)_4$, the purity of (**2a**) and $Sn(SBu^t)_2$ was confirmed by ^{1}H- and ^{119}Sn-NMR spectroscopy prior to the measurements. An investigation on the exact mechanisms that proceed under (electron impact) EI conditions in the gas phase was beyond the scope of this work and was not further looked into. $Sn(SPh)_4$ and $Sn(SBu^t)_4$ have been reported to yield Sn_2O_3 films by CVD.[129,152] Given the similarities observed here in the fragments of (**2a**), $Sn(SBu^t)_4$ and $Sn(SBu^t)_2$, the reported tin oxide formation by gas phase deposition may likely not be an inherent property of the molecules, but rather due to experimental conditions such as the usage and nature of solvent during the aerosol-assisted CVD process. However, remains the applicability of $[Sn(SR)_2]$ and $[Sn(SR)_4]$ ($R = $ alkyl, phenyl) for CVD limited since these compounds lack the desired sublimation properties.

4.2.5 Thermogravimetric Analysis of (2a)

Thermogravimetric analysis was performed under continuous $N_2(g)$ flow to further investigate the decomposition behavior of 1 in relation to the temperature (Figure 4.6). Interestingly, the
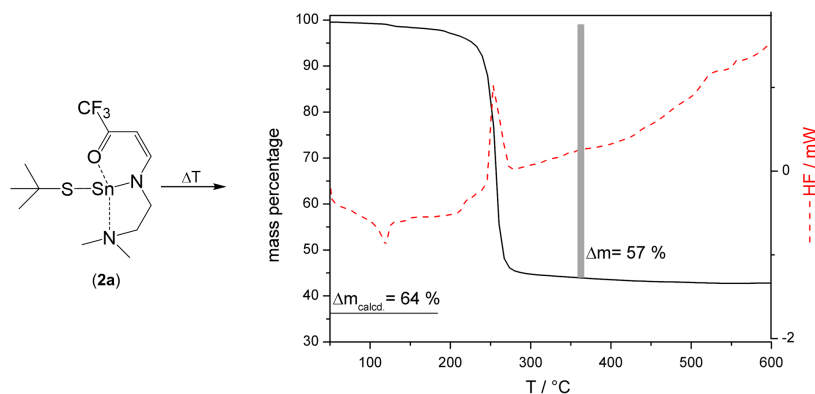
Figure 4.6: TG-DTA plot of the precursor $[Sn(SBu^t)(tfb\text{-}dmeda)]$ (**2a**). The TGA curve is shown as red line, whereas the black line represents the DTA curve.

thermal decomposition of (**2a**) occurred in one well-defined single step, as indicated by a steep mass loss in the TGA curve in the narrow temperature range between 250 °C to 275 °C. No significant mass difference or thermodynamic event was registered beyond 300 °C that indicated the formation of a solid of definite composition. The experimental mass loss determined by TG-DTA is $\Delta m_{exp.} = 57\,\%$, which is below the theoretical value $\Delta m_{th.} = 64\,\%$, assuming the formation of SnS as the final product. One-step decomposition of (**2a**) at remarkably low temperatures underlines its potential as a promising molecular precursor in CVD experiments.

4.2.6 CVD Experiments
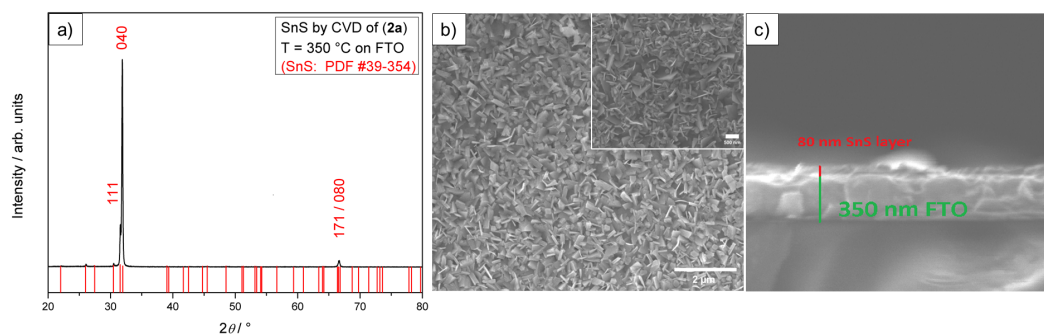
Figure 4.7: a) GI-XRD (recorded in grazing incidence mode) pattern of SnS deposited on FTO substrate at 350 °C. b) SEM top view of SnS on FTO. c) SEM cross-section of SnS on FTO (SnS layer around 80 nm).

The CVD experiments were conducted in a quartz glass tube fitted with an inductively heated graphite holder, where the substrates were mounted on. The precursor temperature for (**2a**) was maintained between 90 °C to 130 °C and substrate temperatures chosen in this study were 300 °C to 450 °C that resulted in crystalline deposits of homogeneous SnS films.

At precursor temperature of 130 °C and substrates maintained at 350 °C, the FTO substrate was uniformly covered by a black layer within 30 min of the processing time. The deposit
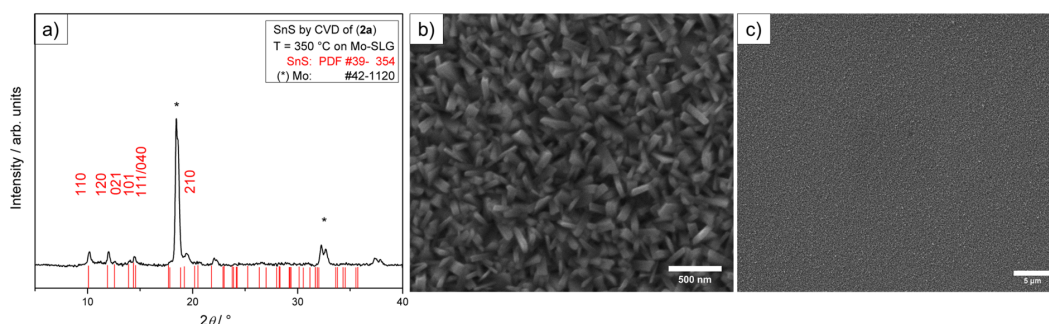
Figure 4.8: XRD pattern a) of SnS deposited at 350 °C, and SEM top view at different magnifications b)+c) of SnS deposited on Mo-SLG at 350 °C.

was identified by XRD analysis to be SnS (Figure 4.7a) that exhibited diffraction peaks corresponding to (040) plane, along with a minor peak due to the (111)-plane. This showed the preferred orientation of grains in SnS films, namely along (040)-planes, parallel to the substrate surface. The SEM images (Figure 4.7b,c) showed the uniform coverage of the substrate surface by flake-like nanostructures. From the cross-sectional SEM (Figure 4.7d), the film thickness was measured to be ~ 80 nm. The (040) surface in SnS is the lowest energy surface[3] and, therefore, favored by kinetically limited growth conditions, such as lower temperatures and sufficiently long diffusion lengths. These low energy surfaces are bonded by van der Waals forces, and an orientation parallel to the substrate surface is favored by corresponding substrates, as previously reported.[162] On transition metals like molybdenum, covalent edge bonding is favored, resulting in (040) planes perpendicular and (101) surface parallel to the substrate surface, which results in the formation of plates growing out of the substrate plane.[163] The strong adhesion of the deposited SnS on FTO is possibly due to a
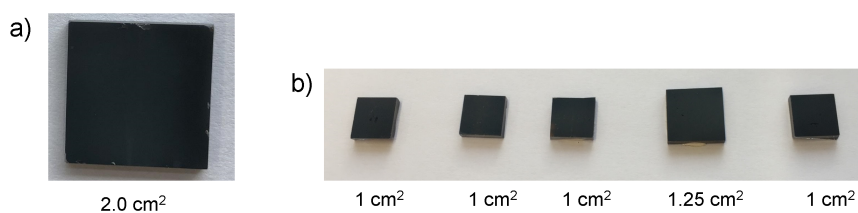
Figure 4.9: Molybdenium on top of soda-lime glass (Mo-SLG) substrates fully covered by SnS after a typical CVD experiment with (**2a**) a) Largest substrate area size of 2 cm² with full coverage by SnS. b) Alternately, multiple smaller substrates covered by SnS after one CVD process.

different bonding situation than the aforementioned Van der Waals interaction, for instance, the formation of a mixed tin oxide-chalcogenide $SnO_{1-x}S_x$ phase at the interface between the substrate and the film. The mechanism that leads to the oriented growth on FTO is not yet fully understood and is subject to further investigations.

In view of the application of SnS in photovoltaic devices and suitable band alignment, the CVD process was investigated on molybdenum substrates. Herein, molybdenum layers of a uniform thickness that were sputtered on soda-lime glass (Mo-SLG) were used. Under
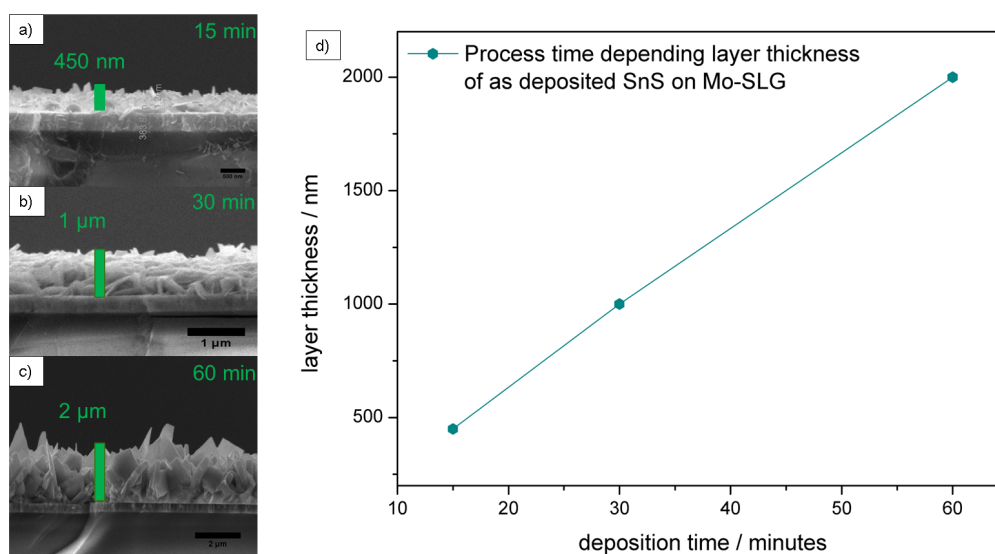
Figure 4.10: Cross-sectional view on the SnS layer thickness obtained after a) 15 min, b) 30 min, c) 60 min, and d) plot of time-depending layer thickness of as-deposited SnS films.

similar deposition conditions as described for the SnS deposition onto FTO (350 °C), successful deposition of the crystalline SnS was observed onto Mo-SLG substrates, as confirmed by XRD measurements (Figure 4.8a). The SEM investigation of as-deposited films showed full coverage of the substrate (Figure 4.8b+c). Also on the macroscopic scale full coverage of the substrates by the SnS deposit was observed, which is shown in (Figure 4.9). Hereby the substrate area size of $2\,\text{cm}^2$ was determined to be the maximum which could evenly be covered by the SnS deposit, within the limiting conditions of the CVD reactor. Alternatively several smaller sized substrates were possible to be uniformly covered by SnS, which is shown in (Figure 4.9b). The film thickness was controlled by the process time (Figure 4.10a–c). By varying deposition times (15 min, 30 min, and 60 min), a linear relationship between the growth rate and deposition time was established (Figure 4.10d). The thicknesses were measured as 440 nm, $1\,\mu$m and $2\,\mu$m, thus, in the given process conditions the layers grew around 33 nm per minute, which is in good agreement with the film growth reported in the literature before.[162] The different SnS films, thicknesses were measured using SEM cross-sectional analyses (Figure 4.10a–c). The low dimensional platelets of SnS were found to be vertically oriented to the substrate surface, as clearly seen in (Figure 4.10c). This morphological attribute offers a huge number of active sites of the layered SnS phase that consequently increases the catalytic behavior of as-deposit material potentially interesting for the application in photovoltaic systems.[164] To analyze the films further by high-resolution transmission electron microscopy (HR-TEM) and selected area electron diffraction (SAED), parts of the film deposited on molybdenum substrate for 15 min at 350 °C were scratched off the substrate surface. The HR-TEM image shows clear lattice fringes, therefore, further confirms the high crystallinity of the material (Figure 4.11). The diffraction spots in the SAED pattern are indexed consistently with the *d*-spacings of orthorhombic SnS (COD # 9008785). The indexed planes correspond to the $[0{-}12]$ zone axis presented as a ring diffraction pattern.
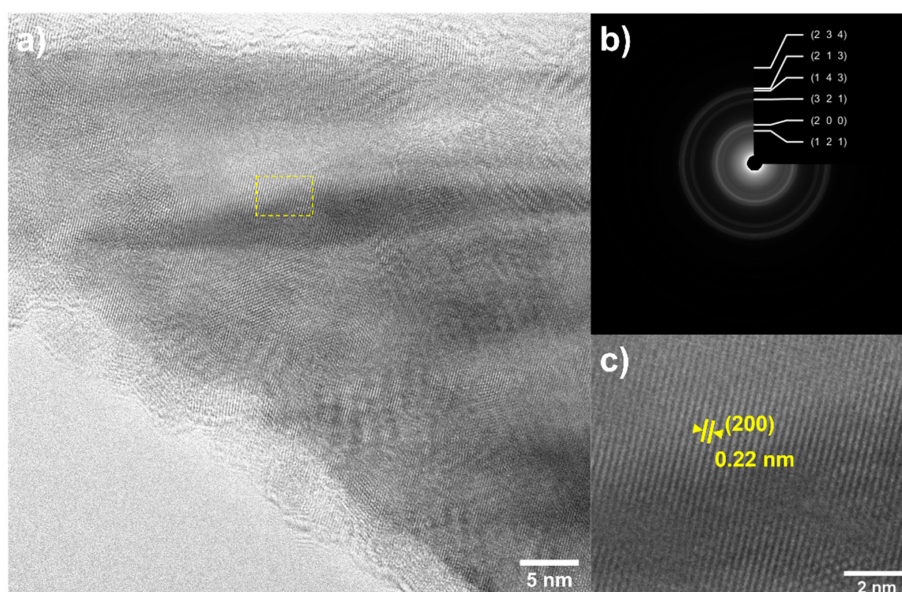
Figure 4.11: (a) TEM image of SnS scratched off from the films deposited on molybdenium substrate at 350 °C for 15 min, (b) ring diffraction pattern (upper inset), and (c) HR-TEM image showing the (200) planes of the orthorhombic SnS (lower inset).

4.3 Conclusion

A new heteroleptic precursor [Sn(SBu^t)(*tfb-dmeda*)] (**2a**) was reported, which was characterized thoroughly in solution and the solid state by multinuclear NMR and single crystal X-ray diffraction and studied for thermal and fragmentation behaviors by thermogravimetric and mass spectrometry, respectively. As compared to corresponding homoleptic Sn^{IV} alkylthiolates, which could not be successfully applied in the CVD process, the heteroleptic configuration of (**2a**) and the resulting increase in the Sn-S bond strength ensures a predictable decomposition pattern for it. So while the tertiary butylthiolate ligand decomposes in a neat and clean manner due to the presence of an inherent decomposition mechanism,[165] the monoanionic tridentate chelate ligand departs in a clean manner without changing the electronic structure of the Sn^{II} center or contaminating the growing SnS film, for example, through probable incorporation of heteroatoms (N, O). This, along with the low precursor temperature, enables deposition of high-quality SnS thin films by CVD under mild conditions. While the use of FTO as substrate generated a preferred orientation of the deposited SnS films along the (040) plane, the films deposited on Mo-coated soda-lime substrate showed no such preference. In both cases, the deposited films were well-crystalline, dense, and of uniform thickness. This work showing the 'launch vehicle' role of the auxiliary ligand underlines the potential of design and subtle choice of ligands and coligands in synthesizing efficient molecular precursors for chemical vapor deposition.

5 Investigations on Lead Alkylthiolates

Manuscript in progress.

This chapter was prepared as manuscript which was to this date not submitted to any journal and summarizes the synthesis, CVD application and structural characterization of Pb^{II} alkylthiolates in solution, the solid state and gas phase, in terms of their fragmentation patterns.
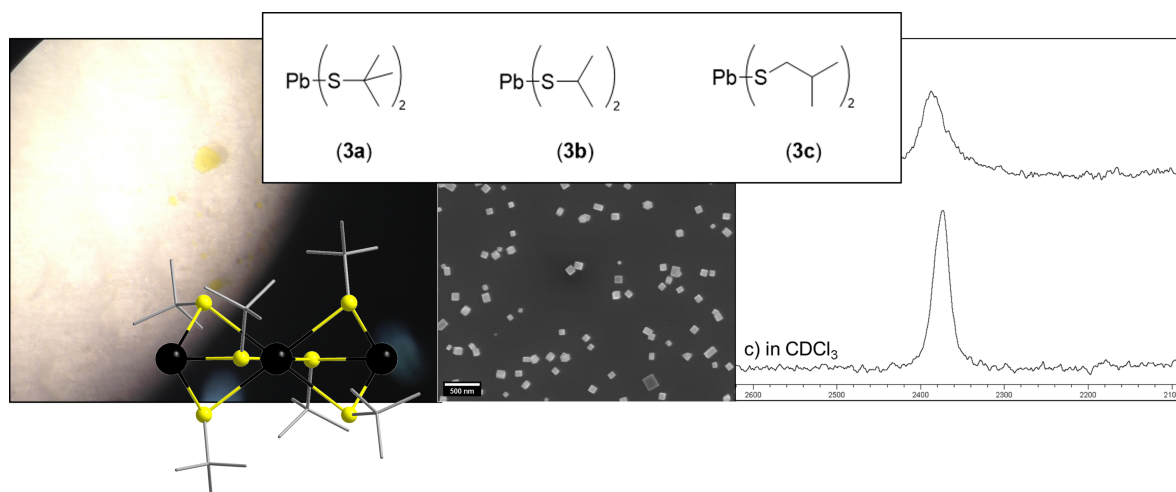
Figure 5.1: Graphical abstract of this chapter, including schematic drawings of the investigated molecular Pb^{II} alkylthiolates and corresponding results. The microscope image on the left-hand side shows the single-crystals of (**3a**) prior to X-Ray diffraction measurement.

5.1 Introduction

PbS crystallizes in the rock-salt structure,[26] and is a direct band gap semiconductor, which has as a wide range of applications, such as photovoltaics,[166–170] sensors,[171,172] thermoelectric material,[173,174] photodetectors,[175–177] solar concentrators[178] and transistors.[179] Worth mentioning is also the well-known and distinctive quantum confinement effects of nanocrystalline or quantum-dot sized PbS.[180] Pb^{II} alkylthiolates have a long historical background and date back over one century.[56,181–184] The first report of $Pb(SBu^t)_2$ (**3a**) dates back to 1932,[181] whereas $Pb(SPr^i)_2$ (**3b**) and $Pb(SBu^i)_2$ (**3c**) were first reported in 1929.[183] The general synthesis route for $Pb(SR)_2$ (R = alkyl, aryl) compounds involves the reaction of $Pb(OAc)_2$ with the corresponding thiol in aqueous alcohol solutions, and $Pb(SR)_2$ (R = alkyl,aryl) compounds were in general reported as non or low soluble in common organic solvents and to be non-volatile.[185–188] Increased solubility in common solvents was reported for $Pb(S\text{-}2,6\text{-}(Me)_2C_6H_3)_2$.[187,189] The decomposition of the Pb^{II} alkylthiolates $Pb(SBu^t)_2$ and $Pb(SBu^i)_2$ to PbS were analyzed in detail by solid-state thermolysis and refluxing in decalin for 3 days.[79] Further investigations on Pb^{II} alkylthiolates were not reported.

Single-Source Precursor for PbS by CVD

Reports on PbS by CVD include mainly dithiocarbamate complexes $Pb(S_2CNR_2)$ (R = alkyl) and dichalcogenoimidodiphosphinato complexes $Pb[(SPPr^i_2)_2N]_2$ which have been deposited by remote (plasma-enhanced) PE-CVD,[190] (aerosol-assisted) AA-CVD[191,192] and low-pressure CVD.[193] These are generally stable metal complexes[194] and in return require relatively high precursor (120 °C–250 °C) and substrate temperatures (300 °C–500 °C).[16,195] There is no report on the application of Pb^{II} alkylthiolates as single-source precursor for CVD.

5.2 Results and Discussion

5.2.1 Synthesis of the Molecules (3a)–(3c)

The Pb^{II} alkylthiolates were synthesized by protolysis of $Pb[N(SiMe_3)_2]_2$[143,196] in THF and obtained in quantitative yield as outlined in (Scheme 6).

The compounds (**3a**)–(**3c**) were stored and handled under N_2(g) to avoid any contamination,

$$Pb[N(SiMe_3)_2]_2 \quad + \quad 2\,HSR \quad \xrightarrow[-\ 2\ HN(SiMe_3)_2]{0\ °C,\ 0.5\ h,\ THF} \quad Pb(SR)_2$$

$$R = \text{-}Bu^t\,(\textbf{3a}),\ \text{-}Pr^i\,(\textbf{3b}),$$
$$\text{-}Bu^i\,(\textbf{3c}).$$
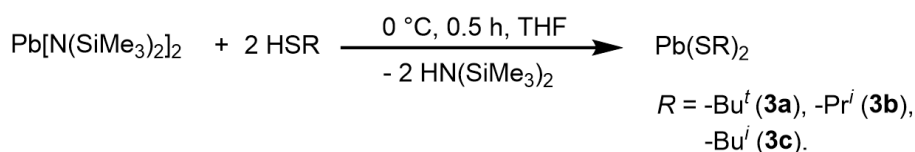
Scheme 6: Synthesis of the molecules (**3a**)–(**3c**)

although no sensitivity towards ambient laboratory atmosphere and light was observed over several weeks, in contrast to previous reports were (**3c**) was reported to decompose within 1–2 weeks when exposed to ambient daylight.[79] Only in (**3b**) after several weeks a minor color change from yellow to black was observed when excessively exposed to daylight for prolonged time (several months). When (**3b**) was in solution the formation of minor amounts of a black precipitate was noted within few hours, whereas (**3a**) and (**3c**) precipitated from solution without decomposition after several days to weeks. Compounds (**3a**)-(**3c**) were fairly

soluble in common deuterated solvents such as $CDCl_3$ and to a lesser extent also in C_6D_6, in contrast to previous reports where (**3a**) was reported to be only soluble in chlorinated hydrocarbons.[79] Interesting to note is that compounds (**3a**)-(**3c**) were more readily solvated when freshly synthesized according to (Scheme 6), compared to the same batch remeasured in benzene-d_6 or $CDCl_3$ after several weeks. This observation is possibly related to the formation of Pb^{II} oxygen thiolate cluster compounds.[187] The enhanced photostability of (**3b**) and (**3c**), together with the solubility change over time shows the advantage of the synthesis route outlined in (Scheme 6) by avoiding ionic impurities and the absence of a Pb-O bond in the starting molecules, as in the formation of Pb^{II} oxygen thiolate cluster the Pb-O bond was assumed to be already present before exposure to oxygen.[187]

For (**3a**) and (**3c**) only ^{1}H-NMR chemical shifts in $CDCl_3$ were available in the literature.[79] Within this work additionally their ^{207}Pb- and ^{13}C-NMR chemical shifts are reported, and for (**3b**) the ^{1}H- and ^{13}C-NMR chemical shifts. The reaction course in (Scheme 6) was monitored by ^{1}H-NMR and partially by ^{207}Pb-NMR spectroscopy. The chemical shift of $Pb[N(SiMe_3)_2]_2$ was detected readily at $\delta^{207}Pb = 4908$, which is in accordance with the reported value $\delta^{207}Pb = 4918$.[197] Whereas the attempted measurement of the chemical shifts $\delta^{207}Pb$ of the Pb^{II} alkylthiolates (**3a**)–(**3c**) proved to be unexpectedly difficult. This was most probably due to solution dynamics in form of rapid site exchange the ^{207}Pb-nuclei were undergoing, as evaluated later in text. The chemical shift of (**3a**) was detected in $CDCl_3$ as
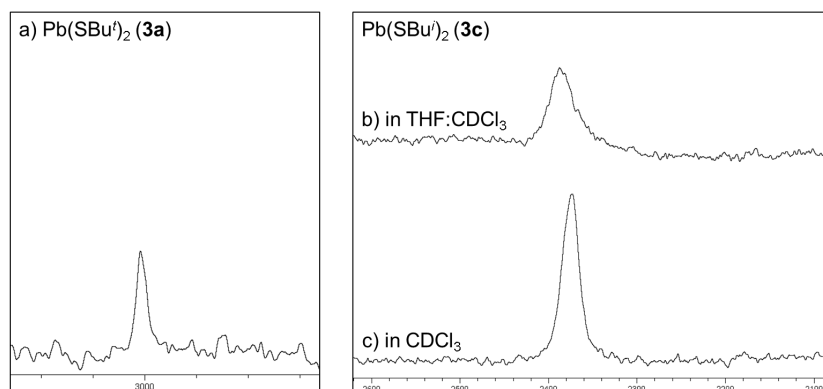
Figure 5.2: a) ^{207}Pb-NMR spectra at 125.9 MHz of $Pb(SBu^t)_2$ (**3a**) in $CDCl_3$. The spectrum was processed at line broadening of lb = 150 MHz. b+c) ^{207}Pb-NMR spectra at 62.9 MHz of $Pb(SBu^i)_2$ (**3b**) b) in $CDCl_3$:THF 1:10 (v:v): $\delta^{207}Pb = 2372$ ($\Delta_{1/2} = 1400$ Hz) and c) in $CDCl_3$: $\delta^{207}Pb = 2387$ ($\Delta_{1/2} = 2700$ Hz). All spectra summarized in this figure were processed at line broadening of lb = 150 MHz.

weak signal at $\delta^{207}Pb = 3002$ (Figure 5.2a) on an AV 600 MHz spectrometer equipped with a BBO probe head, within the measurement parameters of (number of scans) $ns = 8000$ and (spectral window) of $sw = 500$. For (**3c**) the chemical shift was readily detected in $CDCl_3$ at $\delta^{207}Pb = 2387$ on an AV 300 MHz spectrometer under routine operational parameter which were $ns = 1028$ and $sw = 1000$. Interestingly when (**3c**) was dissolved in THF and added $CDCl_3$ in the volume ratio of 10:1 (v:v) the chemical shift $\delta^{207}Pb$ was observed at $\delta^{207}Pb = 2372$ (Figure 5.2). This negligible difference of $\Delta\delta^{207}Pb = 15$ implies that in solution the THF molecules are not coordinating to the Pb^{II} central atom in $Pb(SBu^i)_2$. The $\delta^{207}Pb$ measured from (**3a**) and (**3c**) in $CDCl_3$ are located close to the reported ^{207}Pb-NMR chemical shift region for the 'PbS$_3$' coordination environment $\delta^{207}Pb = 2519 - 2999$, which has been determined from $[Pb(SR)_3]^-$ (R = Me, Et, Ph, C_6H_{11}) anions in MeOH solution

and as δ^{207}Pb = 2868 for [Pb(SPh)$_3$]$^-$ in CHCl$_3$, as well as for various Pb^{II} complexes with N-acetylcysteine, glutathione and peptide complexes which comprise the 'PbS$_3$' coordination environment.[186,198–204] In the plumbylene Pb(SAr(Pr^i)$_4$)$_2$, is Pb^{II} two-coordinate and the chemical shift was determined as δ^{207}Pb = 4283 in C$_6$D$_6$.[150] The chemical shift δ^{207}Pb = 3002 of (**3a**) is located at the downfield border and the chemical shift δ^{207}Pb = 2387 of (**3c**) further high-field from the above mentioned 'PbS$_3$' chemical shift region. The significant chemical shift difference $\Delta(\delta^{207}$Pb$) \sim 700$ between (**3a**) and (**3c**) is not likely to arise from the constitution of the alkyl group in the ligand moiety of the molecules. The highfield shift observed for (**3c**) may point towards either an increased coordination number on the ^{207}Pb-nuclei in form of the 'PbS$_4$' coordination environment or to an increased nuclearity of the solution species within the 'PbS$_3$' coordination environment. The trimeric structural motif [Pb$_3(\mu$-SBu^t)$_6$] of (**3a**) in the solid-state determined in this work is isostructural to [Pb$_3(\mu$-OBu^t)$_6$],[205–207] which was reported to be dimeric as [Pb$(\mu$-OBu^t)$_2$]$_2$ in the gas phase and in benzene solution[208] and was also investigated by ^{207}Pb-NMR studies in solution. In previous reports the chemical shift of [Pb$_3(\mu$-OBu^t)$_6$] was reported as δ^{207}Pb = 1191,[208] which was later identified as the population averaged shift of two sites under rapid exchange in solution.[209] In toluene-d$_8$ solution two distinctive chemical shifts were resolved for the different coordination sites in the trimer [Pb$_3(\mu$-OBu^t)$_6$] and reported as δ^{207}Pb = 2044 for the terminal 'PbO$_3$' coordinated ^{207}Pb nuclei and δ^{207}Pb = -417 for the 'PbO$_6$' coordinated ^{207}Pb nuclei in the center, and one addition signal at δ^{207}Pb = 1770 was suggested to arise from a dimer [Pb$(\mu$-OBu^t)$_2$]$_2$.[209] The chemical shift of (**3a**) is possibly also the result of an averaged signal between two terminal 'PbS$_3$' coordination sites and the 'PbS$_6$' coordination of the bridging ^{207}Pb nuclei due to inter-site exchange in solution, which would also explain the pronounced difficulty to obtain a signal from (**3a**) and is subject to further investigation by (variable temperature) VT-NMR.

For Pb(SPr^i)$_2$ (**3b**) no chemical shift δ^{207}Pb in solutions of C$_6$D$_6$, CDCl$_3$, CD$_3$CN and CDCl$_2$ was detected. Difficulties in obtaining a δ^{207}Pb signal were also reported from [Pb$(\mu$-OPr^i)$_2$]$_n$ which was investigated by VT-NMR in the temperature range between $-80\,°$C to 80$\,°$C.[210]

5.2.2 The crystal structure of (3a): [Pb$_3(\mu$-SBu^t)$_6$]

Crystals of (**3a**) suitable for single crystal X-Ray diffraction were obtained from THF solvent. The space group was determined as $P\bar{1}$ (2) with $Z = 3$ molecules of the trimer [Pb$_3(\mu$-SBu^t)$_6$] in the unit cell.

Each tert-butylthiolato (SBu^t)$^-$ ligand molecule is coordinating one terminal and one central Pb(n)-atom in μ-bridging mode (Figure 5.3). The two terminal Pb(n) $(n = 1, 3)$ atoms in one trimeric unit are coordinated by three (SBu^t)$^-$ ligand molecules in trigonal-pyramidal geometry, the Pb(1)-S(n) and Pb(3)-S(n) bond lengths range between (Pb-S: 262.8(4) pm–266.0(4) pm) and the bond angles S(n)-Pb(1)-S(n) and S(n)-Pb(3)-S(n) range between (S-Pb-S: 86.62(13)$°$-89.38(13)$°$). The central Pb(2)-atom of the trimeric unit is octahedrally coordinated by six sulfur atoms, whereby the bond lengths Pb(2)-S(n) range between (Pb-S: 295.5(5) pm–305.8(5) pm). All Pb-S bond lengths lie within the sum of Van der Waals-radii (Σ_{VdW}(Pb,S): 382 pm),[84] and those involving the terminal Pb(1) and Pb(3) atoms are close to the sum of covalent radii (Σ_{cov}(Pb-S): 257 pm).[144] The bond angle S(n)-Pb(2)-S(n) between the apical positions are observed to be slightly distorted (S-Pb-S: 172.47(10)$°$–80.00(11)$°$), whereas two sets of different equatorial bond angles between the sulfur atoms at the vertices and central Pb(2) atom show an increased degree of distortion from the ideal octahedral geometry, which are (73.75(11)–75.47(11)$°$) and (104.80(11)$°$–107.51(10)$°$). In (Table 5.1) selected bond lengths
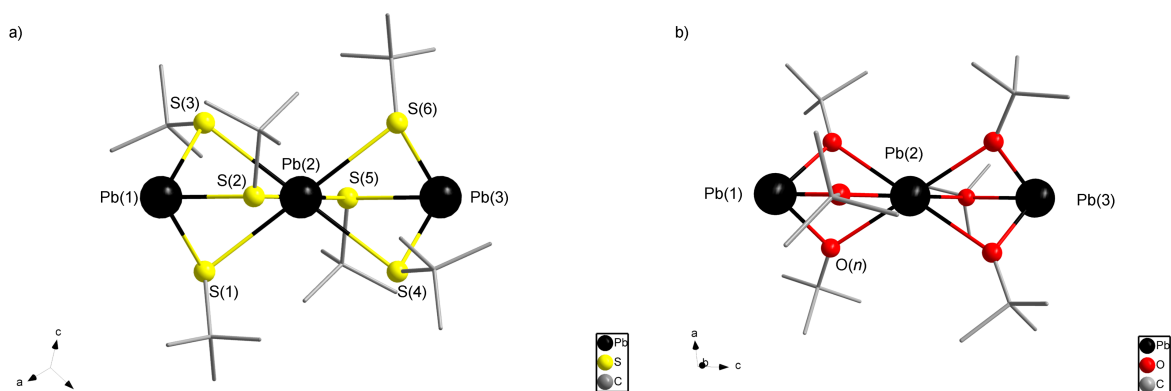
Figure 5.3: a) Trimeric unit $[Pb_3(\mu\text{-}SBu^t)_6]$ of (**3a**) in the solid-state. b) For comparison is the previously reported alkoxy-derivative $[Pb_3(\mu\text{-}OBu^t)_6]^{[205-207]}$ shown, which was generated from the cif-file reported in the reference.[206] The hydrogen atoms are omitted for clarity.

Table 5.1: Selected bond lengths $[Pb_3(\mu\text{-}SBu^t)_6]$ (**3a**)

Pb(n)-S(n)	bond length / pm	Pb(n)-S(n)	bond length / pm
Pb(1)–S(1)	264.1(4)	Pb(2)–S(1)	299.4(4)
Pb(1)–S(2)	264.2(4)	Pb(2)–S(2)	305.8(4)
Pb(1)–S(3)	262.9(4)	Pb(2)–S(3)	296.6(4)
Pb(3)–S(4)	265.9(4)	Pb(2)–S(4)	295.3(4)
Pb(3)–S(5)	264.8(4)	Pb(2)–S(5)	302.5(4)
Pb(3)–S(6)	263.6(4)	Pb(2)–S(6)	305.4(4)

are presented from the crystal structure of (**3a**) and the extended crystallographic tables are presented in the appendix (Table C.19). In the linear trimeric arrangement of the Pb(n) atoms ($n = 1 - 3$), the octahedral coordination geometry around the central Pb(2)-atom indicates the absence of a stereochemical active lone pair, in contrast to the terminal Pb(1)- and Pb(3)-atoms. The trimeric motif of (**3a**) is isostructural with the *tert*-butoxy derivative $[Pb_3(\mu\text{-}OBu^t)_6]^{[205-207]}$ (Figure 5.3), whereby the terminal Pb-O bonds (Pb-O: 217(1) pm) were described as covalent and the Pb-O bonds between the central Pb^{II} atom and oxygen (Pb-O: 255(1) pm) to be of dative nature.[206] Interesting to note, that in the trimeric structure $[Pb_3\{S\text{-}2,6\text{-}(Pr^i)_2C_6H_3\}_6]$ the terminal Pb^{II} atoms are three-coordinate in trigonal-pyramidal and the central Pb^{II} atom four-coordinate in tetrahedral coordination geometry and the Pb-S bond lengths range between (Pb-S: 255.4(4) pm–289.6(3) pm).[146]

5.2.3 The crystal structure of (3c): $[Pb_5(\mu\text{-}SBu^i)_4(SBu^i)_6]$

Compound (**3c**) was recrystallized from n-pentane and the space group was determined as Cc (9) with $Z = 4$ formula units of the pentamer $[Pb_5(\mu\text{-}SBu^i)_4(SBu^i)_6]$ (Figure 5.4) in the unit cell. The Pb(n) (n=1–5) atoms are at the apex of a trigonal pyramid and coordinated by three different sulfur atoms at the corners of the basal plane. On each Pb(n) atom two of the three $(SBu^i)^-$ ligand molecules are coordinating in μ_2-bridging mode, which display slightly longer Pb-S bond lengths (Pb-S: 270.7(8) pm–310.8(7) pm) than in non-bridging mode (Pb-S: 262.1(7) pm–267.8(8) pm). Selected Pb-S bond lengths are tabulated in (Table 5.2) and for better visualization the asymmetric unit of the coordination polymer is shown in (Figure
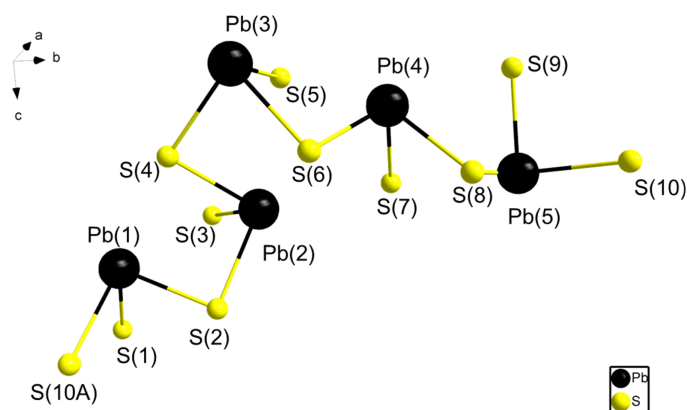
Figure 5.4: Pentameric $[Pb_5(\mu\text{-}SBu^i)_4(SBu^i)_6]$ unit of the crystal structure of (**3c**). The asymmetric unit is complemented by one additional sulfur atom S(10A) to show consistently the coordination environment on all Pb(n) atoms ($n = 1 - 5$). The carbon and hydrogen atoms are omitted for clarity.

5.4) without the carbon and hydrogen atoms of the $(SBu^i)^-$ ligand moiety and complemented by one additional sulfur atom S(10A). Extended crystallographic information and tables are presented in the appendix (Table C.19). The bond lengths found in (**3a**) and (**3c**) are

Table 5.2: Selected bond lengths $[Pb_5(\mu\text{-}SBu^i)_4(SBu^i)_6]$ (**3c**)

Pb(n)-S(n)	bond length / pm	Pb(n)-S(n)	bond length / pm
Pb(1)-S(1)	267.8(8)	Pb(4)-S(7)	262.1(8)
Pb(1)-S(2)	285.0(8)	Pb(4)-S(8)	281.4(8)
Pb(2)-S(3)	262.5(9)	Pb(4)-S(5)	310.8(7)
Pb(2)-S(2)	270.7(8)	Pb(5)-S(9)	264.8(8)
Pb(2)-S(4)	278.2(7)	Pb(5)-S(8)	272.0(7)
Pb(3)-S(5)	262.1(7)	Pb(5)-S(10)	281.5(7)
Pb(3)-S(6)	279.7(7)		
Pb(3)-S(4)	282.7(8)		

comparable to reported Pb^{II} arylthiolate compounds, which is evaluated in the following text. For example, in the two-coordinate plumbylene $Pb[S\text{-}2,6\text{-}(2,6\text{-}(Pr^i)_2C_6H_3)C_6H_3]_2$ the Pb-S bond lengths were reported as (Pb-S: 256.56(9) pm).[150] In three-coordinate anionic complexes $[Pb(SOCPh)_3]^-$ and also $[Pb(SPh)_3]^-$ the Pb^{II} central atom is trigonal-pyramidal coordinate and the Pb-S bond lengths are (Pb-S: 270.3(3) pm–276.3(2) pm)[211] and (Pb-S: 261.9(1) pm–264.7(1) pm) respectively.[198] In the ethanedithiolate complex Pb(edt) two short Pb-S bond lengths (Pb-S: 266.0(3) pm) and (Pb-S: 266.5(3) pm) and four additional longer bonds to bridging ethandithiolate sulfur atoms (Pb-S: 305.6(3) pm–358.4(3) pm) were reported and the Pb^{II} metal to be in either distorted octahedral or pentagonal bipyramidal coordination, depending on the interpretation of the stereochemical activity of the Pb^{II} lone pair.[151] In the oligomeric $[Pb_{10}\{S\text{-}2,6\text{-}(Me)_2C_6H_3\}_{20}]$ the Pb-S bonds were reported in the range (Pb-S: 255.8(5) pm–317.5(4) pm) with differently coordinated Pb^{II} in distorted tetrahedral and octahedral coordination, whereas within one oligomeric unit two Pb^{II} atoms were not distinguishable to be either four- or five-coordinate.[187] With less bulkier ligands polymeric structures were reported as in the two polymorphs α-Pb(SPh)$_2$ and β-Pb(SPh)$_2$ with three covalent Pb-S bonds in the range (Pb-S: 255.6(5) pm–286.1(2) pm) and one longer

distance (Pb-S: 344.4(1) pm) and (Pb-S: 347.4(4) pm) respectively.[188,212] As for the Pb^{II} coordination with oxygen donor atoms[213] it appears that the Pb^{II} coordination chemistry with sulfur donor atoms defies a certain assignment of a coordination number and geometry. In contrast to some above mentioned Pb^{II} arylthiolate compounds, it was reported that the Pb-S coordination chemistry with only sulfur donor atoms is dominated by the preference of the Pb^{II} central atom for either the trigonal-pyramidal three-coordinate 'PbS_3' in solution or the higher-coordinate 'PbS_n' ($n \geq 5$) coordination environment in the solid state.[214] The preference for 'PbS_3' together with the tendency "*to avoid four-coordinate 'PbS_4' coordination geometry*"[214] in solution was associated with the toxicity of Pb^{II} by bonding to cysteine rich sites and preventing proper protein folding.[214]

5.2.4 The crystal structure of the lead(II) oxygen thiolate cluster $[Pb_{12}O_6(SPr^i)_{12} \cdot C_6H_6]$ (3d) and $[Pb_{12}O_6(SBu^i)_{12}] \cdot 6(NC_5H_5)$ (3e)

For (**3b**) it was not possible to obtain crystals in suitable quality for single-crystal X-Ray diffraction, that would consist of purely $Pb(SPr^i)_2$. The oxygen analogous of (**3b**) was described as an infinite coordination polymer in the solid state $[Pb(\mu\text{-}OPr^i)_2]_n$ although the crystal quality was not sufficient to report data on bond length and angles.[206] During the numerous crystallization attempts for (**3b**) the Pb^{II} oxygen thiolate cluster $[Pb_{12}O_6(SPr^i)_{12} \cdot (C_6H_6)]$ (**3d**) was obtained, by recrystallizing (**3b**) from benzene. Compound (**3d**) crystallizes in
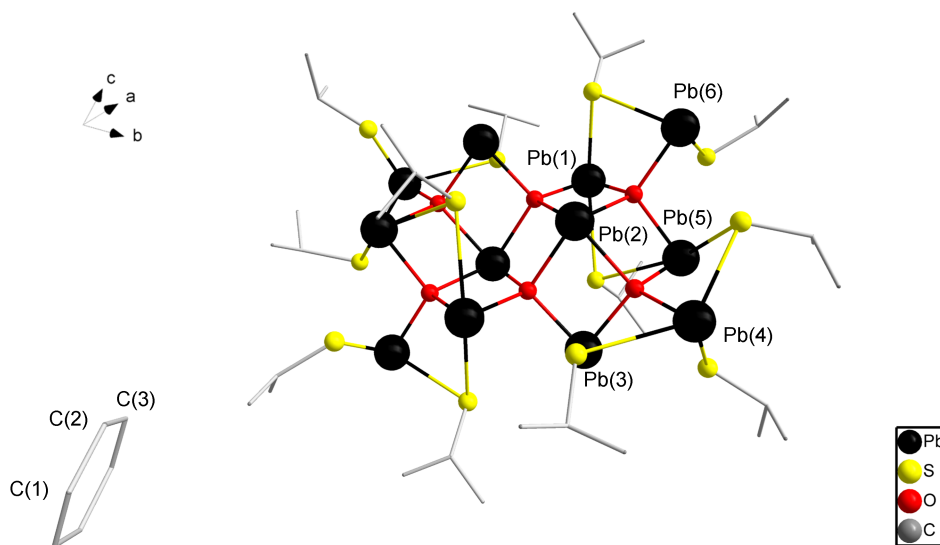
Figure 5.5: Crystal structure of $[Pb_{12}O_6(SPr^i)_{12} \cdot C_6H_6]$ (**3d**). Only the Pb(n) ($n = 1 - 6$) atoms in the $[Pb_{12}O_6(SPr^i)_{12}]$-moiety and the C(n) ($n = 1 - 3$) atoms of the C_6H_6 benzene molecule are numbered, which altogether comprise the asymmetric unit. The hydrogen atoms are omitted for clarity.

the space group $P\bar{1}$ (2) with $Z = 1$ ($Z' = 0.5$) formula units in the unit cell (Figure 5.5). The asymmetric unit comprises half of the formula unit $[Pb_{12}O_6(SPr^i)_{12} \cdot C_6H_6]$, as there is a center of symmetry in the center of the benzene molecule and in the center of the $[Pb_{12}O_6(SPr^i)_{12}]$ moiety, of which the coordination at the Pb^{II} atoms is described by the formula $[Pb_{12}(\mu_4\text{-}O)_6(\mu_2\text{-}SPr^i)_6(SPr^i)_6]$. The Pb-S distances in (**3d**) are in the range of weak bonds (Pb-S: 280.8(3) pm–3.121(2) pm), and one distance Pb(6)-S(6) is significantly shorter

(Pb-S: 261.6(2) pm) yet also exceeds the sum of covalent radii (Σ_{cov}(Pb-S): 257 pm).[144] The oxygen atoms O(n) ($n = 1 - 3$ and symmetry equivalents) lie in one plane, whereas the Pb(4) atom is four-coordinate by the quadratic arrangement of four oxygen atoms in one plane while its symmetry equivalent is located on the alternate side of the plane. The remaining five Pb(n) atoms of the asymmetric unit are three- to four-coordinate simultaneously to oxygen and sulfur of the (SPr^i)$^-$ ligand molecules. The Pb-O bond lengths (Pb-O: 221.9(4) pm–242.3(4) pm) average to d(Pb-O)$_{av}$ = 229.8(4) pm, and the structural motif of the central 'PbO$_4$' units is also present in red PbO (Pb-O: 230.9 pm).[215] There are no intermolecular contacts between the protons of the benzene molecule and the protons in the (SPr^i)$^-$ alkyl moiety. Also no weak coordination is present between the Pb^{II} atoms and the benzene molecule in (**3d**), as reported for Pb$_2$Li$_2$[OCH(CF$_3$)$_2$]$_6 \cdot$ (C$_6$H$_6$)[216] and Pb$_5$O(SR$_f$)$_8 \cdot 2$ (C$_7$H$_8$)[217] with (R$_f$ = -2, 4, 6-(CF$_3$)$_3$C$_6$H$_2$. The nearest distance between Pb(n) and the center of the C$_6$H$_6$ benzene molecule in the crystal structure of (**3d**) was measured as 552.8 pm, which is by its value beyond any interaction. The Pb(n)-Pb(n) ($n = 1 - 6$) interatomic distances (Pb-Pb: 360.48(5) pm–368.31(4) pm) lie within the sum of their Van der Waals-radii Σ_{VdW}(Pb,Pb): 404 pm).[84]

The structural motif of (**3d**) is also present in [Pb$_{12}$O$_6$(SBu^t)$_{12}$]$\cdot 6$ (NC$_5$H$_5$) (**3e**) which crystallizes in the space group $P\bar{1}$ (2) with $Z = 1$ ($Z' = 0.5$) formula units in the unit cell (Figure 5.6). Extended tables with crystallographic information is presented in (Table C.20). The asymmetric unit contains half of the [Pb$_{12}$O$_6$(SBu^t)$_{12}$] moiety, which is completed by
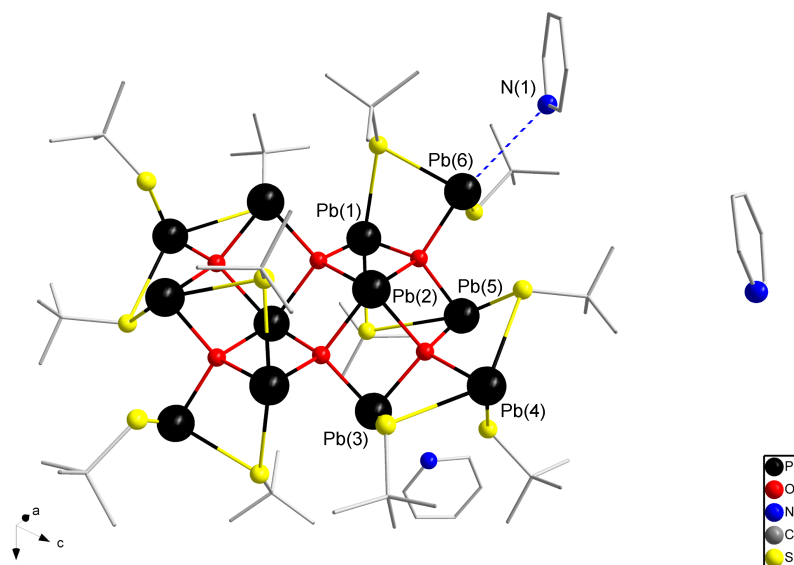
Figure 5.6: Crystal structure of [Pb$_{12}$O$_6$(SBu^t)$_{12}$]$\cdot 6$ (NC$_5$H$_5$) (**3e**). Only the Pb(n) ($n = 1 - 6$) atoms in the asymmetric unit are numbered, whereas the numbering of N(1) in one pyridine molecule is intended to highlight the interaction Pb(6)-N(1), as described in the main text. The hydrogen atoms and the three additional pyridine molecules present in the unit cell are omitted for clarity.

a center of symmetry. The coordination of the Pb^{II} atoms is described in the notation [Pb$_{12}$(μ_4-O)$_6$(μ_2-SBu^t)$_6$(SBu^t)$_6$]. In contrast to (**3d**) there are intermolecular hydrogen H$\cdots$H contacts present in (**3e**) between the pyridine C-H and CH$_3$ protons of the (SBu^t)$^-$ *tert*-butyl moiety, as well as between two pyridine molecules in the form of N$\cdots$H-C. Additionally

one weak Pb$\cdots$N interaction (Pb-N: 334.5 pm) is present between the N(1) nitrogen atom of one pyridine molecule and the Pb(6) central atom, which is below the sum of van der Waals-radii of the elements Σ_{VdW}(Pb,N): 357 pm).[84] The Pb-S bond lengths range between (Pb-S: 272.8(6) pm–309.9(6) pm), whereas one Pb(6)-S(2) bond is shorter (Pb-S: 262.1(6) pm). The Pb-O bond lengths range between (Pb-O: 222.1(15) pm–242.1(13) pm) and average to d(Pb-O)$_{av}$ = 230.3(14) pm. The Pb(n)-Pb(n) ($n = 1 - 6$) interatomic distances (Pb-Pb: 362.70(13) pm–368.18(13) pm) in (**3e**) are also below the sum of the elements Van der Waals-radii Σ_{VdW}(Pb,Pb): 404 pm).[84]

Comparable mixed Pb^{II} oxygen thiolate cluster with the same central 'PbO$_4$' unit flanked by terminal thiolate ligands were reported from [Pb$_{14}$O$_6${S-2, 6-(Me)$_2$C$_6$H$_3$}$_{16}$] with Pb-S bond lengths ranging from (Pb-S: 262.7(6) pm–315.0(6) pm) and Pb-O bond lengths in the range of (Pb-O: 221.5(10) pm–232.0(10) pm)[187] and also from the polymeric [Pb$_{14}$O$_6$ (SPr^i)$_{16}$]$_n$, obtained by refluxing [Pb(SPr^i)$_2$]$_n$ in DMF, where [Pb$_{14}$O$_6$(SPr^i)$_{18}$]$^{2-}$ units bridged by (SPr^i)$^-$ ligands form a layer, with average Pb-S and Pb-O bond lengths reported as d(Pb-S)$_{av.}$ = 281.5(2) pm and d(Pb-O)$_{av.}$ = 227.7(3) pm respectively.[218] Interestingly does the cationic cluster [Pb$_{13}$O$_8$(SPr^i)$_6$]$^{4+}$, as present in [Pb$_{13}$O$_8$(SPr^i)$_6$](NO$_3$)$_4$ not comprise the 'PbO$_4$' unit, instead was described as spherical cage structure with the central Pb^{II} atom in octahedral coordination by six oxygen atoms.[218] The Pb-S bond lengths in the pentanuclear Pb^{II} oxygen thiolate cluster [Pb$_5$O{S-2, 4, 6-(CF$_3$)$_3$C$_6$H$_2$}$_8$] $\cdot$ 2 (C$_7$H$_8$) were reported to range between (Pb-S: 285.4(3) pm–318.0(3) pm). In the planar central 'Pb$_3$O' unit the Pb-O bond lengths (Pb-O: 220.5 pm) were reported to be in resemblance to those present in the tetragonal rutile structure of PbO$_2$.[217] The presence of a planar central 'Pb$_3$O' unit was also reported from the octanuclear [Pb$_8$O$_2${S-2, 4-(Me)$_2$C$_6$H$_3$}$_{12}$].[187]

For comparison, in the THF solvent adduct [Pb{S-2, 4, 6-(CF$_3$)$_3$C$_6$H$_2$}$_2 \cdot$ THF] two {SR$_f$}$^-$ is Pb^{II} coordinated by one THF and one ligand molecule (Pb-S: 263.9(1) pm), whereby the Pb-O bond length (Pb-O: 249.5(10) pm)[219] is elongated compared to those in the 'PbO$_4$' units of (**3e**) and (**3d**). The formation of (**3e**) and (**3d**) is likely to be the result of oxygen intrusion while allowed for crystallization in a flask sealed with silicon grease and possibly also the presence of oxygen in the solvent used for crystallization. It is also worth mentioning that compounds (**3d**) and (**3e**) were not a serendipitous singular observation, instead have been encountered at several crystallization attempts of the corresponding Pb^{II} alkylthiolates.

5.2.5 Thermogravimetric Analysis of (3a)-(3c)

The (thermogravimetric) TG decomposition profile is presented together with the (differential thermo analysis) DTA curve in one plot for each in molecular compound. For comparative purpose (**3a**) and (**3b**) are shown in (Figure 5.7) and (**3c**) in (Figure 5.8). All compounds show a well-defined decomposition profile to yield PbS, as previously reported for (**3a**) and (**3c**).[79]

The decomposition of (**3a**) reaches a first plateau between the temperatures 300 °C to 350 °C which corresponds to a mass loss Δm = 38 %, which is identical to the calculated value Δm$_{calcd.}$ assuming full conversion to PbS, and is in accordance to previous report on the decomposition of (**3a**).[79] The second and final plateau that begins at the temperature 430 °C corresponds to a final mass loss value of Δm = 42 %, which is attributed to partial oxidation at elevated temperatures. As compound (**3a**) and (**3c**) are identical in the elemental constitution as Pb(SC$_4$H$_9$)$_2$, the just mentioned calculated mass loss values hold also for the following discussion. The steep mass loss step of the TG curve of (**3c**) (Figure 5.8) enters at the
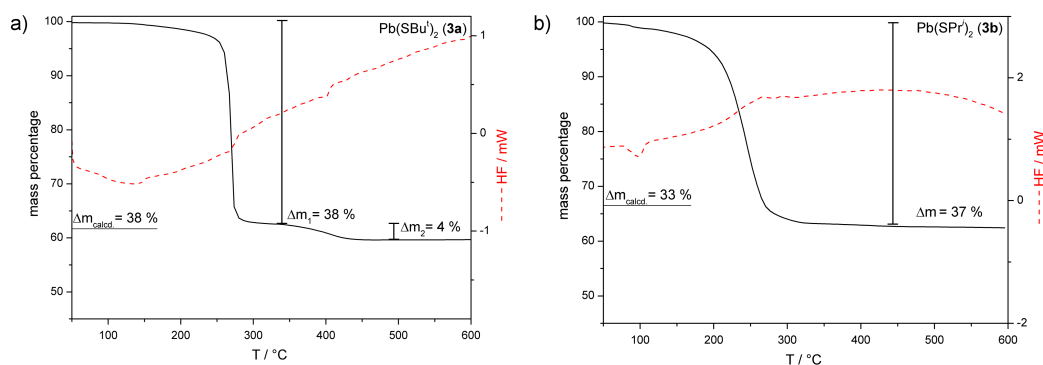
Figure 5.7: TG-DTA of a) Pb(SBu^t)$_2$ (**3a**) and b) Pb(SPr^i)$_2$ (**3b**). The solid line corresponds to the TG curve which indicates the mass loss Δm as function of temperature. The dashed line corresponds to the measured heat flow (HF). The inset horizontal lines on the mass loss axis indicate the calculated value for a quantitative decomposition to PbS.

temperature of 280 °C a continuous shallow decline and reaches a constant value around 450 °C and the mass loss value of Δm = 41 %. Here the formation of PbS in the temperature windows between 280 °C to 450 °C is less well-defined than observed for (**3a**). The endothermic event at 100 °C flags the melting of (**3c**), whereas the exothermic event located at 260 °C accompanies the decomposition step. For compound (**3b**) the endothermic event around the temperature
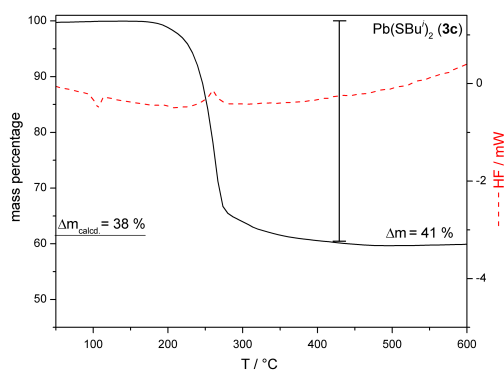
Figure 5.8: TG-DTA of Pb(SBu^i)$_2$ (**3b**). The solid line corresponds to the TG curve which indicates the mass loss as function of the temperature. The dashed line corresponds to the measured heat flow (HF). The inset horizontal line on the mass loss percentage axis indicate the mass loss value calculated for a quantitative decomposition to PbS.

= 90 − 100 °C is accompanied by a continuous mass loss and attributed to sublimation of the molecules. Assuming full conversion to PbS, the mass loss was calculated as Δm$_{\text{calcd.}}$ = 33 %, which is exceeded by the experimental mass loss Δm = 37 % read at the temperature of 340 °C. The slight difference arises from sublimation prior to the decomposition step.

5.2.6 Mass Spectrometry of (3b) and (3c).

The EI-MS gas phase fragmentation pattern was successfully determined for (**3b**) and (**3c**), whereas from (**3a**) no detectable gas phase species were present in two separate attempts to obtain a fragmentation pattern. The gas phase species are reported by their values and sum formula as: [fragment ion] (rel. Int. in %, m/z).
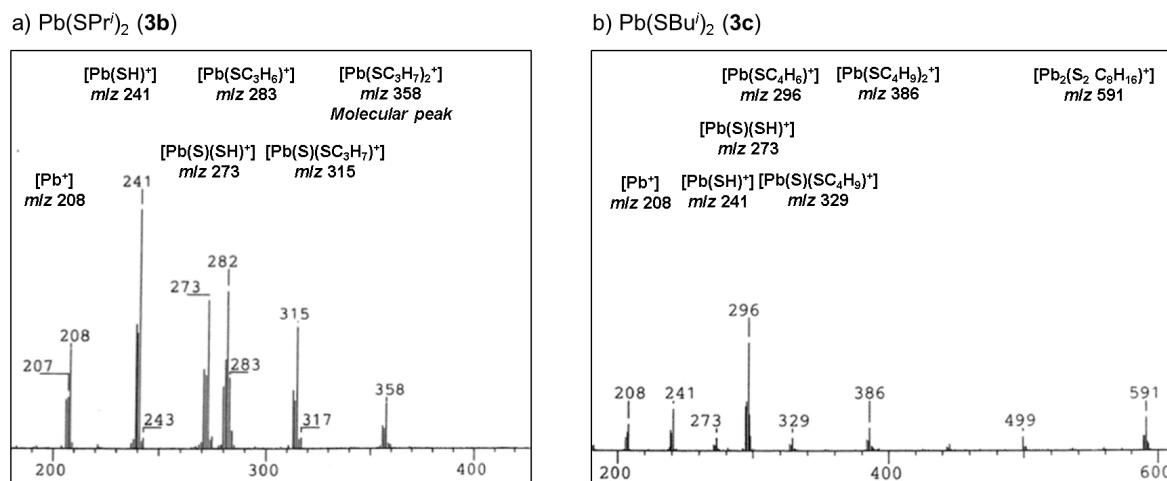
Figure 5.9: EI-MS (20 eV) fragmentation patterns in the range ($m/z > 200$) of possible Pb-isotope including fragment ions, showing of a) Pb(SPr^i)$_2$ (**3b**) and b) Pb(SBu^i)$_2$ (**3c**) within the range $m/z < 600$ of detected signals. The full pattern of (**3b**) is presented in (Figure A.15) and of (**3c**) for ($m/z < 600$) in (Figure A.14).

The fragmentation of the mononuclear species [Pb(SC$_4$H$_9$)$_n$]$^+$ and [Pb(SC$_3$H$_7$)$_n$]$^+$ ($n = 1, 2$) can be summarized for (**3b**) and (**3c**) to be dominated by the loss of alkyl fragments, following the cleavage of the sulfur-carbon bond in the (PbS$-$C$_n$H$_{2n+1}$)-moiety of a given fragment ion (Figure 5.9 and 5.10a). The fragment ions are listed in detail in the experimental part. For Pb(SPr^i)$_2$ (**3b**) the molecular peak was detected as [Pb(SC$_3$H$_7$)$_2$]$^+$ (10, m/z 358). For (**3c**) the molecular ion peak was not assigned since it was not possible to decide between [Pb(SC$_4$H$_9$)$_2$]$^+$ (m/z 386) to be a fragment of [Pb$_2$(SC$_4$H$_9$)$_3$]$^+$ (m/z 683) or to sublimate simultaneously as individual species. The EI-MS gas phase fragmentation pattern of (**3c**) showed in the range $m/z = 310$–780 (Figure 5.10a) the presence of the following dinuclear species (in order of decreasing m/z value) [Pb$_2$(SC$_4$H$_9$)$_3$]$^+$ (20, m/z 683), [Pb$_2$(S$_2$C$_8$H$_{15}$)$_2$]$^+$ (100, m/z 591), [Pb$_2$(S$_2$C$_4$H$_7$)$_2$]$^+$ (8, m/z 535). Hereby it is possible that these are follow-up fragments of the assumed dimer [Pb$_2$(SC$_4$H$_9$)$_4$]$^+$ which was not detected, and not further pursued since its calculated value (m/z 772) would be located at the far edge of the spectrometer operative conditions, which did not enable to extend the search for higher values than $m/z > 780$.

The peaks at (30, m/z 499) and (9, m/z 559) were not possible to assign to a plausible species in the context of the pattern of (**3c**) and were treated as impurities of unknown origin. Nevertheless was the existence of a dinuclear Pb^{II} alkylthiolate species in the gas phase unambiguously assigned by the fragment ions and isotopic pattern (Figure 5.10)). There were no reports on the gas phase fragmentation of compounds (**3a**)–(**3c**) in the literature, and only one report dealing with the mass spectrometric analysis of the volatile by-products from the thermolysis of (**3a**) and (**3c**), whereby it was found that 90 % of the gaseous decomposition products from (**3a**) to be the dialkyl disulfide R$_2$S$_2$ ($R = -$C$_4$H$_9$) and (**3c**) produced mainly
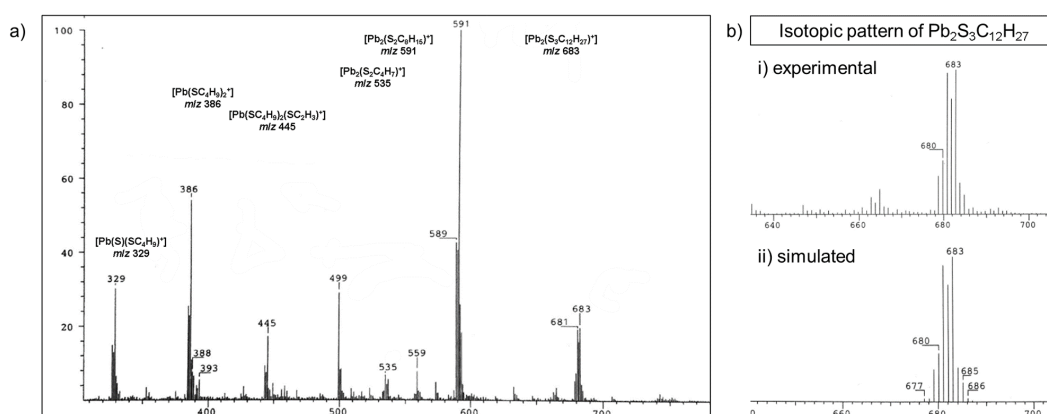
Figure 5.10: a) EI-MS (20 eV) fragmentation pattern of $Pb(SBu^i)_2$ (**3c**) within the range $m/z = 300$ to 780 of detected signals, recorded at enlarged resolution. b) experimental and simulated isotopic pattern for the dinuclear gas phase species observed in the fragmentation pattern of $Pb(SBu^i)_2$ (**3c**).

the thioether RSR (70 %) and in lower amounts R_2S_2 (30 %).[79]

5.2.7 $Pb(SPr^i)_2$ (3b) as single-source precursor for PbS by CVD on Si at 350 °C

Only with $Pb(SPr^i)_2$ (**3b**) it was possible to obtain a deposition by CVD. Attempts to apply (**3a**) and (**3c**) for CVD were not successful. (**3b**) was observed to melt into an orange-brown waxy solid between T $= 90 - 120$ °C under low-pressure conditions.
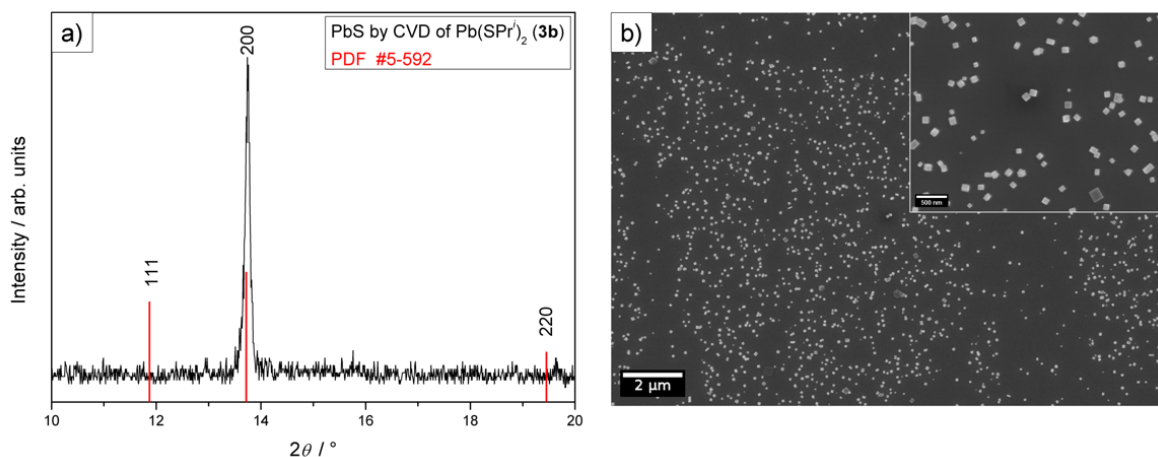
Figure 5.11: a) XRD pattern of PbS obtained by CVD of $Pb(SPr^i)_2$ (**3b**) on Si at 350 °C. The reference pattern for PbS (PDF # 5-592) is shown as inset in red color. b) SEM top-view image and inset at enlarged magnifications of PbS by CVD of $Pb(SPr^i)_2$ (**3b**) on Si at 350 °C.

From the powder diffraction pattern PbS was identified (Figure 5.11a) by the peak at $2\theta = 13.7°$ which corresponds to the (200) plane, which is listed as the highest intensity peak ($I_{rel.} = 100$) in the reference file for PbS (ICSD # 5-592). The 2nd and 3rd intensive peaks are given in the reference as $2\theta = 11.87°$ ($I_{rel.} = 84$) and $2\theta = 19.45°$ ($I_{rel.} = 57$), which correspond to the (111) and (220) respectively. These and further peaks from the reference pattern for bulk PbS are not present in the diffraction pattern of PbS obtained by CVD

of (**3b**). This is indicative of oriented growth on the substrate. The SEM images shown in (Figure 5.11) reveal the presence of nanosized cubes with a diameter of around 100 nm. The fact that diffraction was observed solely from the (200) indexed plane is therefore in accordance with the SEM images as the (h00) planes represent the outer surface of the cube morphology. An increased intensity of the diffraction peak from the (200) plane, while all peaks from the reference pattern were present, was reported from CVD with $Pb(S_2CN_nBu_2)$ which was deposited on Si at a temperature of 500 °C and similarly for PbS synthesized by spin-coating with $Pb(S_2CNEt_2)$.[193,220]

5.3 Conclusion

The crystal structures of Pb^{II} alkylthiolates (**3a**) and (**3c**), and of two Pb^{II} oxygen alkylthiolates cluster (**3d**) and (**3e**) was presented. Additionally (**3b**) was revealed to be monomeric in the gas phase and (**3c**) to exist as monomeric and dinuclear species in the gas phase. The erroneous statements in the literature about solubility and volatility of Pb^{II} alkylthiolates was disproven, opening the wy to explore these long-known and underestimated precursor molecules under a new light for the synthesis of PbS.

Part II

Multinuclear NMR Studies on Lead Halide Perovskites Solute-Solvent System.

6 Multinuclear ^{207}Pb- , ^{133}Cs- and ^{1}H-NMR Investigations on the PbI$_2$, MAI and CsI Solute-Solvent System in DMSO and DMF.

Manuscript in progress.

This chapter was prepared as manuscript, which was not submitted to any journal and summarizes the results from the multinuclear NMR investigations, as one main pillar and an essential part throughout the experimental work en route this thesis.
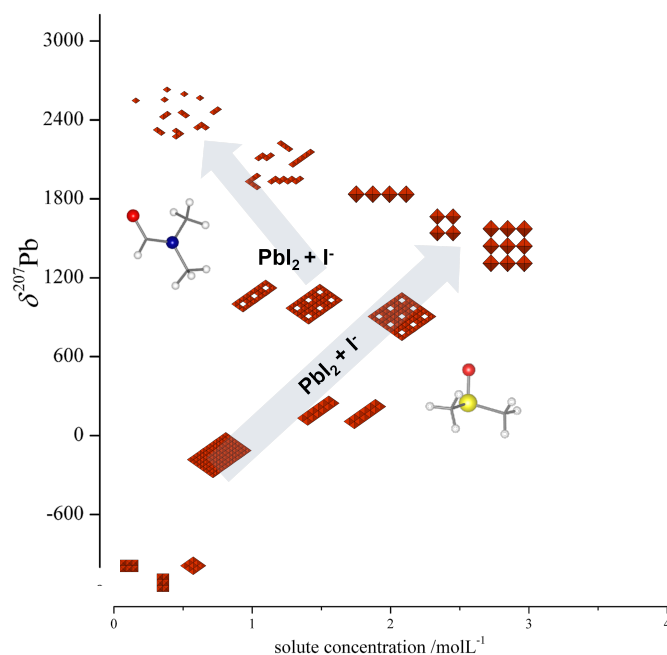
Figure 6.1: Graphical abstract summarizing the experimentally observed chemical shift ranges from PbI$_2$ and PbI$_2$+nMAI in DMSO and DMF and related solution dynamics involving frameworks of condensed (PbI$_6$)$_n^{z-}$–octahedra. Introducing iodide into a solution of PbI$_2$ as PbI$_2$+nMAI resulted in DMSO finally in the formation of the 'perovskite-type' of condensed all corner-sharing (PbI$_{6/2}$)$_n^-$ octahedra, and in DMF in fragmentation of the present species into their smaller building units.

6.1 Introduction

For studies on perovskite precursor solutions, ^{207}Pb-nuclear magnetic resonance spectroscopy (NMR) acts as a valuable technique, since it can provide information on the solution chemistry in the high concentration range, filling the gap between the non-practical diluted solutions typically used for optical studies in the (mM–μM) concentration range[34,35,221,222] and the highly concentrated perovskite inks required for solar-cell fabrication. The NMR studies on the dynamic behavior of Pb^{II} are scarce and limited to solution equilibria of Pb(NO$_3$)$_2$ (aq) in D$_2$O[223,224] together with NMR data on few molecular complexes such as Pb(OAc)$_2$, Pb(O$_2$CC$_6$F$_5$)$_2$ and Pb(S$_2$P(OR)$_2$)$_2$ in different organic solvents.[225] Complexation studies have been reported from Pb^{II} triflate[226] and calixarene complexes in solution.[227] Pb^{II} halogenide PbX$_2$ related ^{207}Pb-NMR studies include so far (X$^-$ = Cl$^-$, Br$^-$) in ionic liquids and also in DMSO and DMF solution.[228,229] Recently ^{207}Pb-NMR studies that involve PbI$_2$ and MAI in DMF, DMSO and mixtures thereof were reported that either did not take into account the equilibrium nature of solution dynamics[230] or were focused on a single solvent property.[231] In literature reported investigations related with the solution chemistry of PbI$_2$+I$^-$ there´s a general desire to point out a single solvent parameter accompanied by DFT based calculations,[34–36,231–233] which obviously fall short to accomplish the envisaged task due to lack in capabilities when polynuclear (Pb$_n$I$_m$)$^{z-}$ species are involved.[36] The following text shows that established methods such as NMR titration[234–240] in combination with the donor-acceptor concept[241,242] still stand the test of time to investigate the fundamental solution chemistry of the PbI$_2$+I$^-$ system in solution.

^{207}Pb is a spin $I = 1/2$ nucleus with a natural abundance of 22.6 % and receptivity 11.9 times higher than the ^{13}C-nuclei. The chemical shifts for the ^{207}Pb isotope cover a range of around ~ 17000 ppm from -6000 to $+11000$, thus even small variations in the structural and electronic environment are readily observable as significant changes in the chemical shift of the lead ions in solution.[40,243,244] Typically, the regions of observed chemical shifts can be associated with oxidation state, coordination number or different geometries around the lead atom. Within a class of compounds an increase in the coordination number denotes higher magnetic shielding of the lead nucleus. Moreover, magnetic shielding increases with the stronger donor attached to or interacting with the ^{207}Pb nuclei e.g., donor ligands in the order S < N < O.[200,204]

Throughout the ^{207}Pb-NMR investigations a strong concentration and temperature dependence of the chemical shifts δ^{207}Pb was observed. In the variable temperature NMR experiments (VT-NMR) the initially observed shifts at room temperature were fully recovered again. The concentration and temperature dependence in chemical shifts is typically observed for nuclei involved in dynamic exchange in solution.[237,245,246] The observed resonances δ^{207}Pb are considered, if not stated otherwise, to be under fast-exchange conditions according to $\delta_{obs} = \Sigma \alpha_n \delta_n$ (1). That is, as the population averaged shift of the individual resonances δ_n that are part of the dynamic exchange.[237] The solution system was investigated by step-wise varying external accessible parameter such as concentration, the ratio of starting materials and the temperature. The response of the solution system was recorded by means of multinuclear NMR spectroscopy following the resonances from the ^{207}Pb, ^{133}Cs and ^{1}H nuclei. (The ^{13}C nuclei was of low diagnostic value and is not presented.) The advantage that NMR spectroscopy offers is that the analytical response upon applying a macroscopically disturbance to the system in equilibrium, is obtained directly from the local electronic environment of the nuclei which are part of the dynamics. First the boundaries of the solution dynamics were determined

by increasing the concentration of only one precursor until saturation by invariance of the chemical shift δ^{207}Pb was observed. Varying the concentration of two precursors in constant ratio by a dilution experiment, was intended to determine the lower concentration limiting conditions.

6.2 Results and Discussion

6.2.1 NMR Titration of PbI$_2$ with MAI and CsI in DMSO solvent
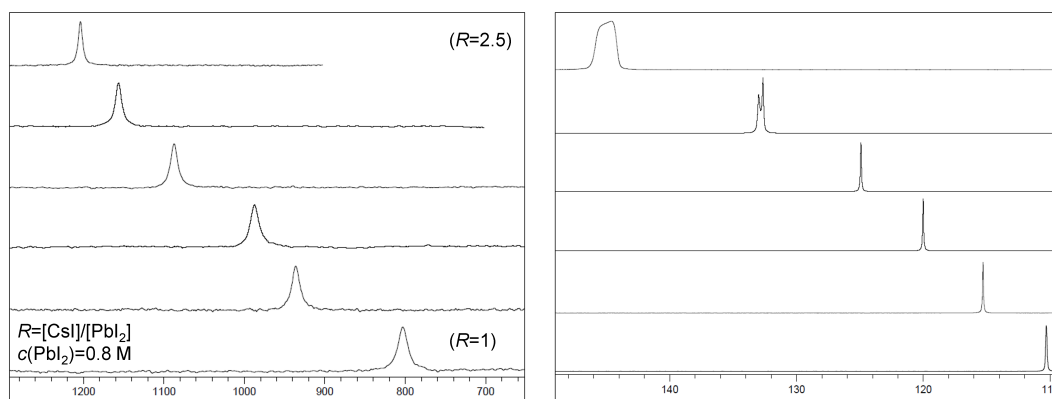
Figure 6.2: Stacked plots of the ^{207}Pb- (left) and ^{133}Cs-NMR (right) spectra recorded in the [CsI]/[PbI$_2$] titration experiment at $c(\text{PbI}_2) = 0.8$ M in DMSO. The bottom spectra correspond to the equimolar precursor ratio ($R = 1$) and the spectrum designated as ($R = 2.5$) to the final constant value δ^{207}Pb$_{\text{final}}$.

(Details on the notation of solution compositions is presented in 6.5.1.) At first the relation between δ^{207}Pb and different precursor ratios $R = [A\text{I}]/[\text{PbI}_2]$ ($A^+ = \text{Cs}^+$, CH_3NH_3^+) was investigated, with one inorganic (cesium iodide, CsI) and one organic (methylammonium iodide, CH$_3$NH$_3$I) iodide source, starting from neat PbI$_2$ solution in DMSO. The concentration of $c(\text{PbI}_2)$ was held constant throughout one titration experiment.
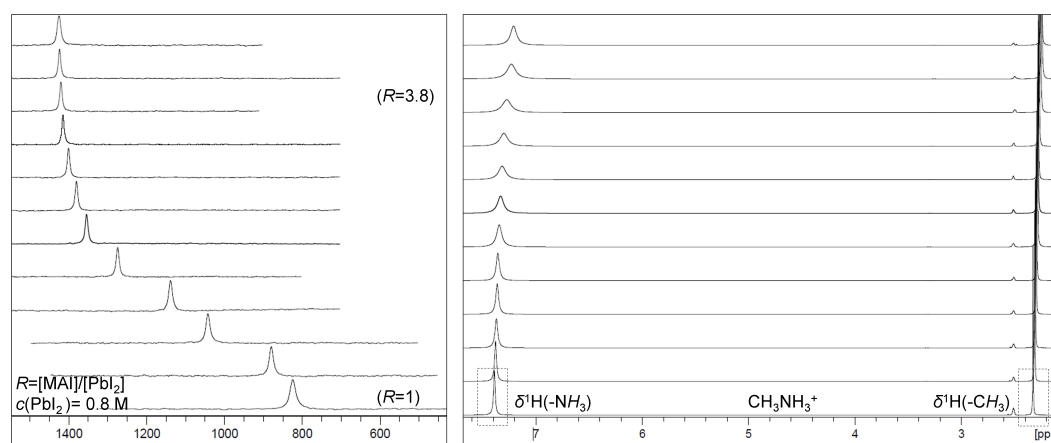
Figure 6.3: Stacked plots of the ^{207}Pb (left) and ^{1}H NMR (right) spectra recorded in the [MAI]/[PbI$_2$] titration experiments at $c(\text{PbI}_2) = 0.8$ M in DMSO. The bottom spectra corresponds to the equimolar precursor ratio ($R = 1$) and the spectrum designated as ($R = 3.8$) to δ^{207}Pb$_{\text{final}}$.

For both cations the titrations were performed at $c(\text{PbI}_2) = 0.2\,\text{M}$, $0.4\,\text{M}$, and $0.8\,\text{M}$ in solution. At each step when R was increased the ^{207}Pb-NMR and depending on the counter-ion ^{133}Cs- or ^{1}H-NMR spectra were recorded. This procedure was repeated until no further change in δ^{207}Pb was observed. The chemical shift remaining constant upon further increasing the iodide concentration as $R = [AI]/[\text{PbI}_2]$ is denoted as δ^{207}Pb$_{\text{final}}$, and the corresponding concentration as $c(AI)_{\text{final}}$. The results from the $[\text{CsI}]/[\text{PbI}_2]$ and $[\text{MAI}]/[\text{PbI}_2]$ titration experiments in DMSO are summarized in (Table 6.1) and (Figure 6.4). The corresponding
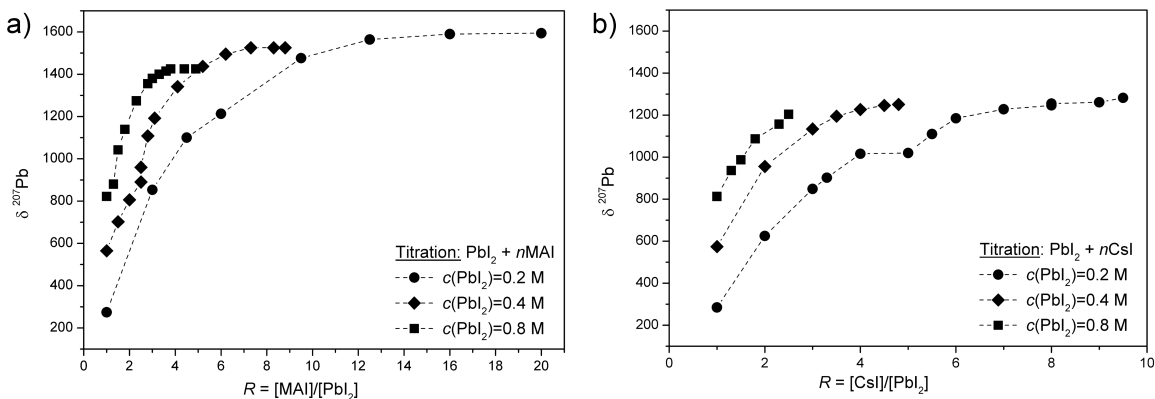
Figure 6.4: δ^{207}Pb as function of a) the precursor ratio $R = [\text{MAI}]/[\text{PbI}_2]$ b) $R = [\text{CsI}]/[\text{PbI}_2]$ The data points are connected by a dashed line for visualization purposes.

plots show the chemical shift δ^{207}Pb as function of the precursor ratio ($R \geq 1$). As R was increased, the resonances of the ^{207}Pb nuclei became further deshielded until a cation-specific value δ^{207}Pb$_{\text{final}}$ was reached. Only beyond an equimolar ratio of precursors ($R > 1$) (Figure 6.4) the cation influence became apparent, as distinct chemical shifts δ^{207}Pb were obtained from solutions containing CsI and MAI, this trend continued until the titration end-points were reached. In the presence of MA$^+$ as counter-ion these values are obtained with $c(\text{PbI}_2) = 0.8\,\text{M}$, $0.4\,\text{M}$, and $0.2\,\text{M}$ as δ^{207}Pb$_{\text{final}} = 1425$, 1525 and 1594 respectively, while with the inorganic counter-ion Cs$^+$ these values were δ^{207}Pb$_{\text{final}} = 1204$, 1251 and 1282 for the concentrations $c(\text{PbI}_2) = 0.8\,\text{M}$, $0.4\,\text{M}$, and $0.2\,\text{M}$. These values are together with the corresponding solution parameter presented for $c(\text{PbI}_2) = 0.4\,\text{M}$ and $0.8\,\text{M}$ in solution in (Table 6.1). The corresponding titration data tables for all concentrations $c(\text{PbI}_2)$ are presented in (Tables B.7 to B.13) and stacked plots of NMR spectra for $c(\text{PbI}_2) = 0.2\,\text{M}$ for $[\text{MAI}]/[\text{PbI}_2]$ in (Figure B.2) and for $[\text{CsI}]/[\text{PbI}_2]$ in (Figure 6.8). The stacked plots of NMR spectra for the titration of $c(\text{PbI}_2) = 0.4\,\text{M}$ as $[\text{CsI}]/[\text{PbI}_2]$ in (Figure B.3) and as $[\text{MAI}]/[\text{PbI}_2]$ in (Figure 6.12+ B.1).

6.2.2 The Link Between ^{207}Pb-NMR in Solution and Solid State

From solid state NMR spectroscopy ssNMR, it is the isotropic chemical shift $\delta_{\text{iso}}(^{207}\text{Pb})$ that can be compared to solution NMR chemical shift values (always denoted as δ^{207}Pb). Not only in ^{207}Pb-NMR spectroscopy is this an established and well-documented procedure, which is capable of providing reliable information on the structural environment of the ^{207}Pb nuclei.[40,186,243,244,247,248] The vast chemical shift range ($\sim 17000\,\text{ppm}$) in ^{207}Pb-NMR spectroscopy is the consequence of the high sensitivity of the ^{207}Pb nuclei towards small changes in the structural environment. Thus, such drastic changes as in the coordination

Table 6.1: Selection of solution parameter from the ^{207}Pb-NMR titration experiments in DMSO, for the concentrations $c(\text{PbI}_2) = 0.4\,\text{M}$ and $0.8\,\text{M}$. For each cation the first and last titration points are presented and the corresponding solution parameter. $\delta^{207}\text{Pb}_{\text{final}}$ denotes the final chemical shift value and R denotes the precursor ratio $[AI]/[\text{PbI}_2]$ ($A^+ = \text{MA}^+$, Cs^+).

	$c(\textbf{PbI}_2) = \textbf{0.4\,M}$				$c(\textbf{PbI}_2) = \textbf{0.8\,M}$		
R	$c(\text{MAI})\ /\ \text{molL}^{-1}$	$\delta^{207}\text{Pb}$	$\Delta_{1/2}\ /\ \text{Hz}$	R	$c(\text{MAI})\ /\ \text{molL}^{-1}$	$\delta^{207}\text{Pb}$	$\Delta_{1/2}\ /\ \text{Hz}$
	0	-28	1100		0	114	1300
	0.4	565	1000	1.0	0.8	822	900
	2.9	1525	500	3.8	3.1	1425	400
R	$c(\text{CsI})\ /\ \text{molL}^{-1}$	$\delta^{207}\text{Pb}$	$\Delta_{1/2}\ /\ \text{Hz}$	R	$c(\text{CsI}\ /\ \text{molL}^{-1}$	$\delta^{207}\text{Pb}$	$\Delta_{1/2}\ /\ \text{Hz}$
1.0	0.4	574	1000	1.0	0.8	813	900
4.8	1.9	1251	400	2.4	1.9	1204	500

number or geometry can result in chemical shift differences $\Delta\delta^{207}\text{Pb}$ of several hundreds to more than thousand, in numbers of ppm. Therefore minimizing the complications that would arise from the fact that in ssNMR multiple referencing methods are applied, where within one method differences in measurement temperature may be present additionally.[249] Nevertheless, for a meaningful comparison and interpretation, it is necessary to have reasonable boundaries within these chemical shifts are correlated and also plausible experimental conditions and trends these values were extracted from.
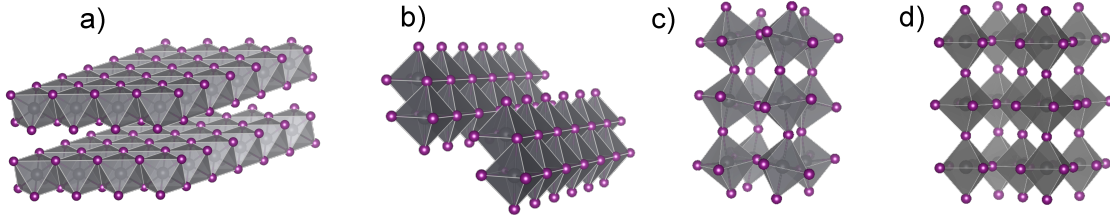
Figure 6.5: Parts of the crystal structures of a) PbI_2[126,250] b) δ-CsPbI$_3$[251] c) γ-CsPbI$_3$[252] d) MAPbI$_3$[253] without the cations, to visualize the 2D network of $(\text{PbI}_{6/3})$ and 3D network of $(\text{PbI}_{6/2})^-$-octahedra in the solid-state.

Comparing the chemical shifts $\delta^{207}\text{Pb}_{\text{final}}$ measured at the titration endpoints, to the isotropic chemical shifts $\delta_{\text{iso}}(^{207}\text{Pb})$ from solid-state NMR (ssNMR) revealed a close relationship to the corresponding parent perovskite compounds (Table 6.2). Namely $\delta^{207}\text{Pb}_{\text{final}}$ from the MAI titration, falls in one region with $\delta_{\text{iso}}(^{207}\text{Pb}) = 1423 - 1482$[254–257] of MAPbI$_3$, as does $\delta^{207}\text{Pb}_{\text{final}}$ from the CsI titration with $\delta_{\text{CS}}(^{207}\text{Pb}) = 1265$[252,258] of γ-CsPbI$_3$ (Tables 6.1 and 6.2). An additional feature was observed at lower concentration in the titration $c(\text{PbI}_2) = 0.2\,\text{M}+n\text{CsI}$, which is shown in (Figure 6.8). Here the titration endpoint was recorded at $\delta^{207}\text{Pb}_{\text{final}} = 1282$ ($R = 9.5$), and the correlation to $\delta_{\text{CS}}(^{207}\text{Pb})$ of γ-CsPbI$_3$ is displayed earlier ($R = 8$) by the separated chemical shifts $\delta^{207}\text{Pb} = 1246 + 1255$ and by its effect on the time-scale in form of signal splitting, which is mirrored by the resonances of $\delta^{133}\text{Cs} = 127 + 124$. The same phenomenon is observed at $\delta^{207}\text{Pb} = 1020(\pm50)$ and $\delta^{133}\text{Cs} = 103 + 109$ when ($R = 5$) and associated with $\delta_{\text{iso}}(^{207}\text{Pb}) = 1065(10)$ of δ-CsPbI$_3$.[258]

Table 6.2: Reported isotropic shifts $\delta_{\text{iso}}(^{207}\text{Pb})$ of PbI$_2$, MAI and CsI related
compounds.$^{a)}$

	$\delta_{\text{iso}}(^{207}\text{Pb})$	$\delta_{\text{iso}}(^{133}\text{Cs})$
PbI$_2$	$-31.1(10)^{[261]}$, $-29.1^{[262]}$, $-25^{[263]}$	
δ-CsPbI$_3$	$1065(15)^{[258]}$, $1160^{[264]}$	$240^{[265]}$, $247.0^{[258]}$
γ-CsPbI$_3$	$1265(20)^{[258]\,b)}$	$166.9^{[258]}$
MAPbI$_3$	$1423^{[257]}$, $1430^{[254]}$, $1448^{[255]}$, $1482(10)^{[256]}$	
GA$_2$PbI$_4$	$1515^{[260]}$	

$^{a)}$ For details on referencing see (Table 6.6)
$^{b)}$ Reported as peak maximum δ_{CS}.

The correlation between the values $\delta^{207}\text{Pb}_{\text{final}}$ and $\delta_{\text{iso}}(^{207}\text{Pb})$ for MAPbI$_3$ and CsPbI$_3$ supports a similar chemical environment for the ^{207}Pb nuclei in both solution and the solid state (Figure 6.5c+d). The structure of δ-CsPbI$_3$ in the solid state (Figure 6.5b) is a dinuclear coordination polymer of condensed $(\text{PbI}_{3/3}\text{I}_{2/2}\text{I}_{1/1})^-$-octahedra, whereby each octahedra has four common edges with its neighboring unit$^{[251]}$ and can be described in equivalent notation as $(\text{Pb}_2\text{I}_6)_n^{2-}$ (see section 6.5.4). These coordination environment are present in solution in form of assemblies of colloidal size and are stabilized by the interaction to the cations, which is discussed together with ^{1}H and ^{133}Cs-NMR later in text. The chemical shifts $\delta^{207}\text{Pb}$ from PbI$_2$+CsI solutions were noticed to be extra-ordinary stable, that if so, did not change by more than 1–2 ppm over at least three months. A deeper understanding of the solute-solvent interactions and the underlying forces may prove valuable to find new strategies in stabilizing the desired γ-CsPbI$_3$ phase in the solid-state over prolonged time. Further compounds listed in (Table 6.2) were regarded as important for the discussion here, that is PbI$_2$(s.) and GA$_2$PbI$_4$(s.). In the solid state PbI$_2$ consists of layers of neutral $(\text{PbI}_{6/3})$-octahedra, each sharing six edges to adjacent octahedra, thereby forming layers of indefinite size (Figure 6.5a). PbI$_2$(s.) displays the most shielded resonances $\delta_{\text{iso}}(^{207}\text{Pb})$ (Table 6.2) and was described as the most dense structure in the Pb-I system.$^{[259]}$ The compound GA$_2$PbI$_4$ is an example for a 2D network of corner-sharing $(\text{PbI}_{4/2}\text{I}_{2/1})_2{}^-$-octahedra that form corrugated layers in the solid state.$^{[260]}$ Sorting the reported $\delta_{\text{iso}}(^{207}\text{Pb})$ by increasing value, empirically the following trends are observed (i) the ^{207}Pb nuclei are most deshielded in a network of corner-sharing octahedra, compared to edge- or face-sharing octahedral connectivity. (PbI$_2$(s.) $\rightarrow$ MAPbI$_3$; δ-CsPbI$_3$ $\rightarrow$ γ-CsPbI$_3$) (ii) Within a type of connectivity, reduced dimensionality of the structure is experienced as deshielding by the ^{207}Pb nuclei. (PbI$_2$(s.) $\rightarrow$ δ-CsPbI$_3$; MAPbI$_3$ $\rightarrow$ GA$_2$PbI$_4$) The latter point describes the shielding of a nuclei in a larger assembly, as it is generally the case in NMR spectroscopy and is mentioned here to differentiate between the types of octahedra connection. The vast difference of $\Delta\delta_{\text{iso}}(^{207}\text{Pb}) \sim 1500$ between PbI$_2$ and MAPbI$_3$ shows the paramount influence of octahedral connectivity on the isotropic shift $\delta_{\text{iso}}(^{207}\text{Pb})$, since there is no change in the coordination number (c.n. $= 6$) or in the octahedral coordination geometry in these compounds.

Dissolving the perovskite compounds in the amounts as given by the sum formulae of the solid-state compounds as $c(\text{'MAPbI}_3\text{'}) = 0.8\,\text{M}$ and $c(\text{'CsPbI}_3\text{'}) = 0.8\,\text{M}$ the chemical shifts in solution were recorded upfield by $\Delta\delta^{207}\text{Pb} \sim 700$ and $\Delta\delta^{207}\text{Pb} \sim 400$ in the same order, compared to the isotropic shifts $\delta_{\text{iso}}(^{207}\text{Pb})$ observed from their solid-state structures. These were attained in solution by increasing the concentration of the iodide source up to $c_{\text{final}}(\text{MAI}) = 3.0\,\text{M}$ and $c_{\text{final}}(\text{CsI}) = 1.9\,\text{M}$, that is the 4- and 2.5-fold excess relative to

$c(\text{PbI}_2)$. This shows the stoichiometric relation of the solid-state is translated into solution as an equilibrium partitioning, which depends on the concentrations $c(\text{PbI}_2)$, $c(A\text{I})$ and their ratio $R = [A\text{I}]/[\text{PbI}_2]$, ($A^+ = \text{Cs}^+$, $\text{CH}_3\text{NH}_3{}^+$).

6.2.3 The solution conditions of $\delta^{207}\text{Pb}_{\text{final}}$

Depending on $c(\text{PbI}_2)$ the titration endpoints were reached at different $\delta^{207}\text{Pb}_{\text{final}}$, while the final concentrations $c_{\text{final}}(\text{MAI})$ and $c_{\text{final}}(\text{CsI})$ for each cation, remained constant in value (Table 6.1) and (extended data tables B.7–B.12). Important to note that MAI was readily dissolved in excess of $c_{\text{final}}(\text{MAI}) = 3.0\,\text{M}$, which underlines the significance of $\delta^{207}\text{Pb}_{\text{final}}$ and $c_{\text{final}}(\text{MAI})$ as a landmark solution condition. Spectroscopic evidence, for this being a point of saturation was provided by the linewidth trend $\Delta_{1/2}(^{207}\text{Pb})$ in the DMSO titrations, that revealed exchange broadening to account for $\Delta\Delta_{1/2}(^{207}\text{Pb}) \sim 800 - 600\,\text{Hz}$, as difference between the begin and the end of the titration (Table 6.1) and (Tables B.7–B.12). The effect of exchange broadening is proportional to $(\Delta\nu^2)$ ($\Delta\nu$ = chemical shift difference $\delta_i - \delta_j$ in units of Hz) which can be substantial in case of large chemical shift difference $\Delta\delta = \delta_i - \delta_j$ between two sites $A_i \rightleftharpoons A_j$ exchanging at intermediate to fast rates.[266] As the given equilibrium was consecutively shifted towards saturation by iodide addition, the population of one species grew smaller, thereby minimizing the effect of dynamic exchange between sites separated by a large chemical shift difference. This is expressed in the linewidth trends towards lower values by all titration experiments in DMSO. Comparable values as result of exchange broadening were reported from NMR spectroscopic investigations of the ^{205}Tl isotope in thallium halide solutions[235,267] the element neighboring to lead in the periodic table has a comparable wide chemical shift range and linewidths in the same order of magnitude as observed here for the ^{207}Pb nuclei.[268,269] A more detailed discussion on the linewidths $\Delta_{1/2}(^{207}\text{Pb})$ is given in (Section 6.5.3).

The precursor CsI was not dissolved beyond the final concentration of $c_{\text{final}}(\text{CsI}) = 1.9\,\text{M}$. Considering the lower solubilities of CsI and CsI+PbI$_2$ ($R = 1$) in DMSO, the larger value of $c_{\text{final}}(\text{CsI})$ can be regarded as an extension of its limited solubility range, rather than a limiting factor. This follows the fact that all features of the MAI titration such as, the correspondence to $\delta_{\text{iso}}(^{207}\text{Pb})$, minimizing of exchange broadening, the cation features in ^1H and $^{133}\text{Cs-NMR}$, and the inter-dependency of solution parameters at $\delta^{207}\text{Pb}_{\text{final}}$ are displayed in the same manner. The $c(\text{PbI}_2)$ concentration dependence of $\delta^{207}\text{Pb}_{\text{final}}$ is partially the result of fast saturation at higher concentrations $c(\text{PbI}_2)$ before the solution final shift of the system was reached.[270,271] Lowering the concentration $c(\text{PbI}_2)$, the system is relieved from this early saturation effect. This is best illustrated by the [CsI]/[PbI$_2$] titrations, approaching the nearby $\delta^{207}\text{Pb}_{\text{final}}$ going from $c(\text{PbI}_2) = 0.8\,\text{M}$ to $0.4\,\text{M}\,(0.2\,\text{M})$ and the corresponding values $\delta^{207}\text{Pb}_{\text{final}} = 1204$ to $1251\,(1282)$. The same trend is displayed in the MAI titrations (Table 6.1). It can be estimated for CsI+PbI$_2$ the value be within $\delta^{207}\text{Pb}_{\text{final,solution}} \sim 1200 - 1350$ and for MAI+PbI$_2$ these values to lie within $\delta^{207}\text{Pb}_{\text{final,solution}} \sim 1590 - 1650$, which is the solvent influence and of the smaller structure compared to the solid-state. Since there are different individual shifts for the different dimensionality of the structures which are equilibrating between different sized oligomers, these limiting shifts were considered of limited significance. It can be estimated these values are nearby, following the $\frac{1}{2}c(\text{PbI}_2) \rightarrow 2R$ trend in (Table 6.1), that is going from $c(\text{PbI}_2) = 0.4\,\text{M}$ to $c(\text{PbI}_2) = 0.2\,\text{M}\,(0.1\,\text{M}, 0.5\,\text{M})$ increases the precursor ratio as $R = [\text{MAI}]/[\text{PbI}_2] \sim 16(\sim 32, \sim 64)$ to reach saturation. Additionally, dynamic exchange between colloidal assemblies of different size is suggested to be present

in solution. Based on $c(\text{PbI}_2)_{\text{DMSO}}$, that is influential on $\delta^{207}\text{Pb}_{\text{final}}$, to contain partially an equilibrium between n-meric species itself, whereas an ionic equilibrium is regarded as unlikely to have such an impact at this stage. And by the VT-NMR experiments carried out at $\delta^{207}\text{Pb}_{\text{final}}$, that was observed further deshielded at elevated temperatures and fully recovered at room temperature (Section 6.5.2), which may point towards an exchange process between aggregates of different size, favoring higher aggregated species at lower temperatures. The chosen concentrations $c(\text{PbI}_2)$ for the titration experiments are therefore the right balance to investigate the solution chemistry in the practical high concentration regime and to minimize the effects by oversaturation, that allows the extrapolation of the results to higher and lower concentrated solutions.

6.2.4 ^{1}H and ^{133}Cs-NMR Spectroscopy

Having identified the solution conditions that enable the formation of a 3D perovskite network in solution (Table 6.1), the role of the cations by multinuclear NMR spectroscopy were investigated. In the following the trends in the ^{1}H and ^{133}Cs-NMR spectra related to the MA$^+$ and Cs$^+$ cation interaction with the $(\text{Pb}_m\text{I}_n)^{z-}$ solution species are presented. From both the ^{1}H and ^{133}Cs-nuclei two parallel running trends were observed, one is the variation in the chemical shifts $\Delta\delta$, that shows the change in the structural environment, and one in the linewidths $\Delta_{1/2}$ of the resonances, as an effect on the dynamic time-scale. Both are related to the observations in ^{207}Pb-NMR spectroscopy at the titration endpoints.

^{1}H-NMR Spectroscopy

Hydrogen bonding (HB) in solution occurs between the $-\text{NH}_3^+$ protons in MA$^+$ and the carbonyl oxygen atoms of the DMF and DMSO solvent molecules.[272] In solutions of solely MAI in DMSO, that is the solvent with stronger HB ability, the proton exchange dynamics are slowed down so far, that the corresponding $(-\text{NH}_3^+)$ resonance is clearly observable in the ^{1}H-NMR spectra. In contrast to solutions of DMF, here the ammonium proton $(-\text{NH}_3^+)$ resonance is subject to huge line broadening due to rapid exchange by HB. The trends δ^1H and $\Delta(^1\text{H})$ is displayed by the protons of the ammonium moiety $(-\text{NH}_3^+)$ in the MA$^+$ cation is explained in the following text.
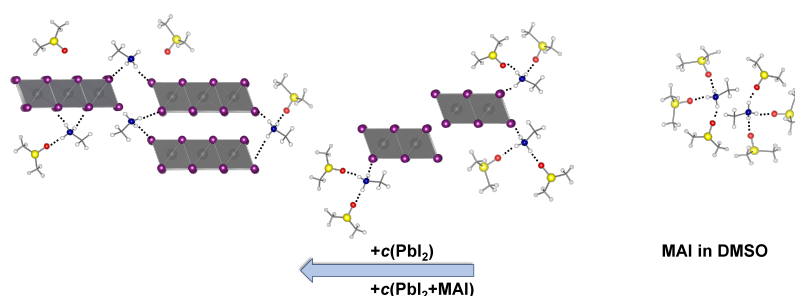
Figure 6.6: Scheme to illustrate the shielding observed by δ^1H of the $(-\text{NH}_3^+)$ moiety in MA$^+$ in the presence of PbI$_2$ and PbI$_2$+I$^-$ by reorientation of the ammonium moiety $(-\text{NH}_3^+)$ between the oxygen atom in DMSO and given $(\text{Pb}_m\text{I}_n)^{z-}$ species in solution.

Increasing the concentration $c(\text{MAI})$ in the presence of PbI$_2$ (Figure 6.3+6.3) and (Tables B.7 to B.9) resulted in a continuous upfield shift of δ^1H$(-\text{NH}_3^+)$. These values range between $\Delta\delta^1$H $= 0.14\text{-}0.28$ and reach up to $\Delta\delta^1$H $= 0.59$ in the $c(\text{PbI}_2) = 0.4\,\text{M}$ titration in DMF. It is

a characteristic feature of protons involved in HB to experience further reduced electron density at higher concentrations.[272] The opposite chemical shift trend was recorded for these protons in the presence of PbI_2 consistently in all titration and dilution experiments. Important to note is this being neither related to self-aggregation of MAI molecules nor to an interaction between the 'free' iodide ions in solutions and MA^+ since there was no significant difference in δ^1H between $c(MAI) = 0.4\,M$ and $2.0\,M$ of solely MAI in DMSO-d_6. The constant value in this case arises from the fact the hydrogen-bonding system MAI-DMSO being beyond the saturation point.
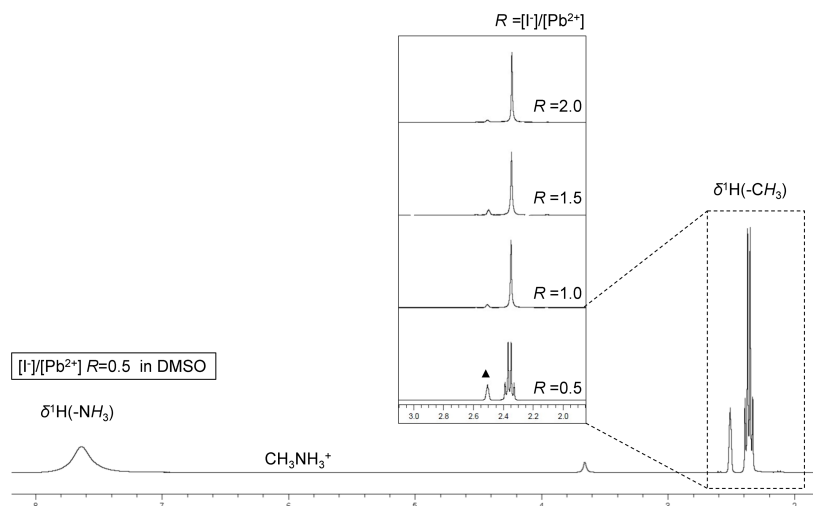
Figure 6.7: a) ^{1}H-NMR spectra of $Pb(NO_3)_2$+0.5MAI in DMSO showing the quartet formation of the $-CH_3$ moiety of MA^+, that is a singulet in all other solution compositions. The triangle (▲) marks the residual protons signal from DMSO-d_6. The methyl ($-CH_3$) proton resonances for four further MAI addition steps is presented as inset in the spectrum. The corresponding NMR plot with DMF as solvent is shown in (Figure B.4).

The higher electron density at the ammonium protons ($-NH_3^+$) in the presence of $(Pb_mI_n)^{z-}$, shows before all, the diminishing hydrogen-bonding interaction between MAI and the donor solvent molecules DMF and DMSO. The conclusion that arises from here, is that by introducing PbI_2 (in form of any $(Pb_mI_n)^{z-}$ species) into the solution, a fully or partially reorientation of the ammonium moiety ($-NH_3^+$) away from the solvent oxygen atoms takes place. This is illustrated in (Figure 6.6). A possible explanation of this observation, on a speculative basis, are emerging non-covalent interactions between these protons and iodide atoms bound to lead $(Pb-I_n^-\cdots H_3N^+)$ or is of electrostatic nature because of stronger interaction between the negatively charged $(Pb_mI_n)^{z-}$ ($n > 2$) solution species $(Pb-I_n^-\cdots {}^+NH_3)$ and the ammonium moiety. In the solid-state structure of $MAPbI_3$, beyond charge balancing the ammonium moiety interacts by hydrogen-bonding with the iodide atoms in the octahedral $((PbI_{6/2})^-)$-network.[273] Parallel to $\delta^1H(-NH_3^+)$ the corresponding linewidths $\Delta_{1/2}(^1H)$ increase towards a maximum, to then decrease again afterwards. As difference between the maximum point and begin of titration, these are $\Delta\Delta_{1/2}(^1H) = 20 - 40\,Hz$ in DMSO and significantly larger $\Delta\Delta_{1/2}(^1H) = 120 - 130\,Hz$ in DMF (Tables B.7–B.9 and B.13–B.14). The maximum in linewidths $\Delta_{1/2}(^1H)_{max}$ was reached either close before or at the final concentration $c_{final}(MAI)$ that corresponds to $\delta^{207}Pb_{final}$. The drop in value occurred in any case after passing this point of concentration. This can be observed in (Figure 6.6), that shows the ^{1}H-NMR spectra
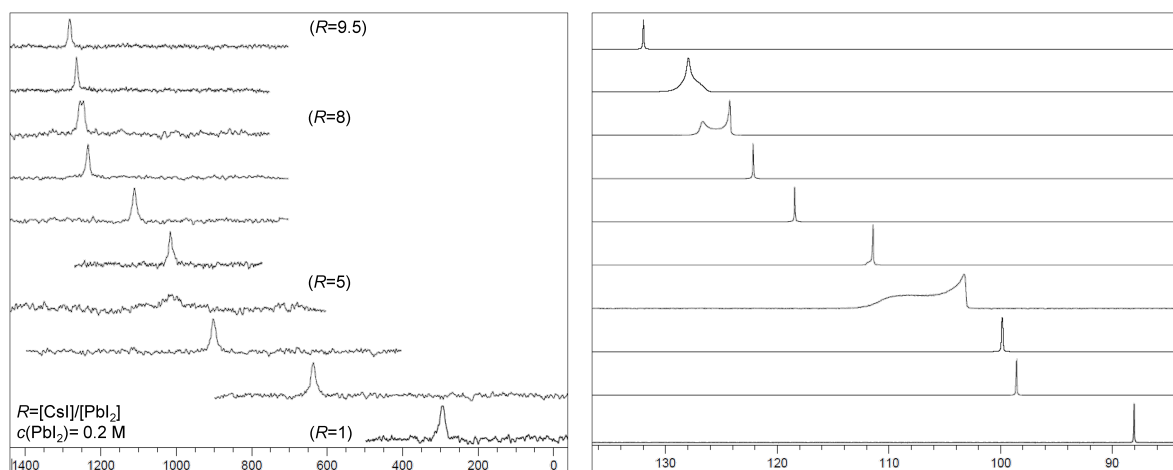
Figure 6.8: plots of the ^{207}207Pb (left) and ^{133}Cs NMR (right) spectra recorded in the [CsI]/[PbI$_2$] titration experiment at $c(\text{PbI}_2) = 0.2$ M in DMSO. In the δ^{207}Pb signal at ($R = 5$) the silhouette of a triplet of multiplets may be anticipated, but efforts to increase the resolution were not successful and the signal became too broadened within 1–2 days. The error induced to the signal position by the intermediate- to slow-exchange was estimated to be around $\Delta\delta^{207}$Pb±50.

recorded from the $c(\text{PbI}_2) = 0.8$ M$+n$MAI titration experiment. The broadening in linewidths $\Delta_{1/2}(^1\text{H})$ shows the hydrogen-bonding exchange dynamics these protons are involved in to slow down. In the titration experiment of Pb(NO$_3$)$_2$+nMAI (Figure 6.7) at the initial addition step ($R = 0.5$), the resonance of the methyl group ($-\text{CH}_3$) was observed as quartet, by coupling to the neighboring ammonium ($-\text{NH}_3{}^+$) protons, that were maximum in value $\Delta_{1/2}(^1\text{H})$ at this point. This type of coupling to protons undergoing HB related rapid exchange is generally not observed, due to different timescales of HB and the coupling interaction. Similar observations were reported earlier with the MAI/$\alpha-$CD (cyclodextrin) system, where a gradual change from singlet to a quartet was observed with higher ratios ($R > 1{:}4$) of MAI/$\alpha-$CD, and the slower dynamics were associated with stronger complexation of MAI by the cyclodextrin cavity.[274] Considering the existence of a maximum in the trends, complexation appears unlikely in this case.

^{133}Cs-NMR Spectroscopy

The effect on the dynamic time-scale is displayed in a different form in the ^{133}Cs-NMR spectra (Figure 6.8 and B.3). Here, it is not a continuous trend in the linewidths, but the onset of intermediate to slow-exchange typically observed for coalescence. The signal splitting and related broadening do not separate and when the limiting spectra was reached fast-exchange conditions were reestablished. The correlation between $\delta_{\text{iso}}(^{207}\text{Pb})$ and $\Delta_{1/2}(^{133}\text{Cs})$ was clearly observed in all titration experiments and became more pronounced at lower concentration $c(\text{PbI}_2)$, the reason for this is unclear at this stage.

The undeniable proof that the ^{207}Pb and ^{133}Cs nuclei are involved in the same dynamic process was provided by the simultaneous signal splitting in the ^{207}Pb and ^{133}Cs resonance at ($R = 8$), as shown in (Figure 6.8). As the concentration $c(\text{CsI})$ was increased as [CsI]/[PbI$_2$] and by dilution at ($R = 1$) the chemical shift δ^{133}Cs was observed further downfield in both solvents, whereas δ^{133}Cs was observed deshielded by $\Delta\delta^{133}$Cs $= 60 - 80$ downfield in DMSO compared to DMF. The solvent and concentration dependence in δ^{133}Cs was reported earlier and interpreted in terms of *solvent-separated* ions and *contact-ion pair* formation.[275] The

mainly influential solvent parameters were identified as the dielectric constant ε and donor number (DN), in varying contributions.[238,239,275] The deshielded resonances δ^{133}Cs in DMSO are interpreted in this context as result of stronger complexation of the Cs$^+$ cation and the solvents ability to fully dissociate CsI and stabilize the Cs$^+$ and I$^-$ ions separated from each other. The more shielded δ^{133}Cs values in DMF are related to the solvents incapability to fully dissociate CsI, therefore the observed shielding reflects the presence of $(\mathrm{Cs}^+\cdots\mathrm{I}^-)$ ion-pair formation in DMF, as increased electron density is imposed on the ^{133}Cs nuclei by the iodide. The chemical shifts at infinite dilution as the state of highest solvation were reported (referenced to Cs$^+$ in DMF as δ^{133}Cs $= 0.5$ and δ^{133}Cs $= -68$ in DMSO.[275] The possible shielding on δ^{133}Cs that would arise by the interaction between Cs$^+$ and iodide bound $(\mathrm{Pb}_m\mathrm{I}_n)^{z-}$ was not detected or possible to be separated by the interaction between Cs$^+$ and DMSO. The solid-state ^{133}Cs-NMR shift of γ-CsPbI$_3$ is reported as $\delta(^{133}$Cs$) = 166.9$[258] and is approached by the solution shifts in the DMSO titrations at δ^{133}Cs $= 146$ and 136 (132) for the titrations in concentrations of $c(\mathrm{PbI}_2) = 0.8\,\mathrm{M}$ and $0.4\,\mathrm{M}$ $(0.2\,\mathrm{M})$ respectively. This observation is difficult to explain in terms of the above-described solvent separated ion-pair concept since there is no solvent influence on solid-state shift $\delta(^{133}$Cs$) = 166.9$ in γ-CsPbI$_3$. And this value was clearly approached by the solution δ^{133}Cs values in three different titration experiments (Tables B.10–B.12). For this no explanation can be provided at this stage. It appears there are yet unknown factors that influence δ^{133}Cs , as was mentioned in the context of the puzzling shielded value of $\delta(^{133}$Cs$) = 247.0$ observed in δ-CsPbI$_3$.[258] There is, to the best of the author's knowledge, no comparable study reported in the literature that involves the ^{207}Pb nuclei in a combined multinuclear approach. From ^{1}H-NMR titrations performed mainly in the context of supramolecular chemistry, linewidth phenomena were observed in various forms and defy a single explanation, thus its origin, if possible, has to be evaluated for each investigated system.[276] This situation is rather more intricate for ^{207}Pb-NMR (Section 6.5.3). No explanation on the origin of the time-scale phenomena is available at this point, which was also beyond the scope of this work. It should be pointed out here that only those linewidth phenomena were considered of diagnostic value, when simultaneously observed by two different nuclei, correlated in a plausible manner to ssNMR or related to landmark solution conditions.The trend in $\Delta_{1/2}(^1$H$)$ completed latest when the limiting spectra was reached for MAI+PbI$_2$. The linewidth phenomenon was observed in a more distinctive character for CsI+PbI$_2$, and the occurrence of $\Delta_{1/2}(^{133}$Cs$)$ was associated with the corresponding ssNMR shifts, displaying a transition event. In both cation resonances the linewidths $\Delta_{1/2}(^1$H$)$ and $\Delta_{1/2}(^{133}$Cs$)$ show the exchange dynamics these nuclei are involved in to slow down, at the same solution conditions when the chemical shift in solution δ^{207}Pb was closely related to $\delta_{\mathrm{iso}}(^{207}Pb)$ of the parent solid-state compounds. The effect on the time-scale is interpreted as an indicator for a transition between different structural environments, that is between the cation interaction to solvent molecules and colloidal $(\mathrm{Pb}_m\mathrm{I}_n)^{z-}$ species.

6.2.5 ^{207}Pb-NMR Dilution experiments with PbI$_2$, MAI and CsI at constant precursor ratio in DMSO solvent

Variation of the cation A$^+$ in PbI$_2$+*A*I (A$^+$ = Cs$^+$, MA$^+$, GA$^+$) at constant precursor ratio (*R* = 1)

The solution parameters that constitute the boundary to the emerging influence of the cation were subject to a more detailed investigation. For this, the measurements were extended to different cation combinations (MAI, CsI and GAI = guanidinium iodide) and dilution

series of $c(\mathrm{PbI_2}+AI)$ (A^+ = Cs$^+$, MA$^+$) ($R = 1$) and $c(\mathrm{PbI_2})$ in DMSO and in DMF. The values for concentrations different than $c(\mathrm{PbI_2}+AI) = 0.8\,\mathrm{M}$ are plotted in (Figure 6.10) and tabulated in (Tables B.6–B.5). Independently of whether an organic or inorganic cation or a mixture of both was applied, there was no significant cation effect on δ^{207}Pb observed from solutions of the precursor combination $1\,\mathrm{PbI_2} + 1\,AI$ ($R = 1$) below the total concentration $c(\mathrm{PbI_2}+AI) \leq 1.0\,\mathrm{M}$. For example, in a $c(\mathrm{PbI_2}+AI) = 0.8\,\mathrm{M}$ solution composition the chemical shift δ^{207}Pb is indifferent of the cation in the iodide source, while in the same composition at higher concentration $c(\mathrm{PbI_2}+AI) = 1.2\,\mathrm{M}$ the applied cation A^+ can be identified by the chemical shift δ^{207}Pb to be Cs$^+$ or MA$^+$.

Table 6.3: Chemical shifts δ^{207}Pb of different cations as iodide source in the precursor ratio ($R = 1$)

	DMF		DMSO	
	δ^{207}Pb	$\Delta_{1/2}$ / Hz	δ^{207}Pb	$\Delta_{1/2}$ / Hz
$c(\mathrm{CsI+PbI_2}) = 0.8\,\mathrm{M}$	$^{a)}$		813	900
$c(\mathrm{MAI+PbI_2}) = 0.8\,\mathrm{M}$	1832	600	822	900
$c(\mathrm{GAI+PbI_2}) = 0.8\,\mathrm{M}$	1820	500	821	900
$c(\mathrm{Cs_{0.5}MA_{0.5}I+PbI_2}) = 0.8\,\mathrm{M}$	1837	2500 $^{b)}$	821	900

$^{a)}$ Above solubility limit in DMF
$^{b)}$ The reason for the large linewidth value was not resolved

Finally, the cation independence of the ($R = 1$) solution composition was shown by a capillary NMR-experiment, that was prepared by immersing a glass capillary that was filled with a solution of $c(\mathrm{GAI+PbI_2}) = 0.8\,\mathrm{M}$ into a standard 5mm-NMR tube that was pre-filled with a solution of $c(\mathrm{MAI+PbI_2}) = 0.8\,\mathrm{M}$, and the same procedure was repeated vice versa. The spectra in (Figure 6.9) were measured at a (Bruker) AV 400 spectrometer.
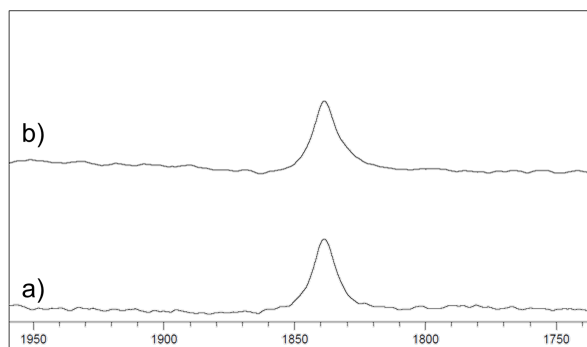
Figure 6.9: ^{207}Pb-NMR spectra of the capillary experiments: a) $c(\mathrm{GAI+PbI_2}) = 0.8\,\mathrm{M}$ in the glass capillary, that is immersed in a $c(\mathrm{MAI+PbI_2}) = 0.8\,\mathrm{M}$ solution in a standard 5-mm NMR-tube. b) vice versa.

The electronic structure of the ^{207}Pb nuclei, that gives rise to a certain shift δ^{207}Pb will be the result of the ligand arrangement in the first coordination sphere. The cation has certainly a fundamental part in the formation of this structures, already from the dissolution process to any stage in solution, also shown by ^{1}H and ^{133}Cs spectroscopy in this manuscript. The charge balancing and hydrogen-bonding, will naturally influence the electronic structure of the ^{207}Pb nuclei such as slight changes in the 'Pb-I' bond polarization or structural distortion of octahedra

around the Pb^{II} central atom. The magnitude of this effect in numbers of ppm can be estimated to be between $\Delta\delta^{207}Pb = \pm 5$ up to ± 20, when comparing the same solution composition, in the presence of different cations, as in (Table 6.1). This is also the error range that was determined for solutions of the same overall cation and composition prepared in DMF, whereas that in DMSO would be given by a lower value $\Delta\delta^{207}Pb = \pm 15$. The effect of protonated vs. deuterated solvent was detected by measuring $c(PbI_2+MAI) = 0.8\,M$ ($R = 1$) in a single solvent mixture of DMF-d$_7$:DMF and DMSO-d$_6$:DMSO 1:3 (v:v, deuterated:non-deuterated volume ratio) for both solvents to range between $\Delta\delta^{207}Pb = \pm(10\text{ to }30)$. These altogether provide an orientational value for the influence from the 2$^{\text{nd}}$ coordination or solvation sphere for the same structure. Since this influence is exerted not *in*, but *on* the first coordination sphere of the ^{207}Pb nuclei, in terms of the above mentioned octahedral distortion and bond polarization, the discussion is limited on the direct coordination by iodide atoms.

6.2.6 ^{207}Pb-NMR Dilution Experiments with PbI$_2$ and MAI in DMSO
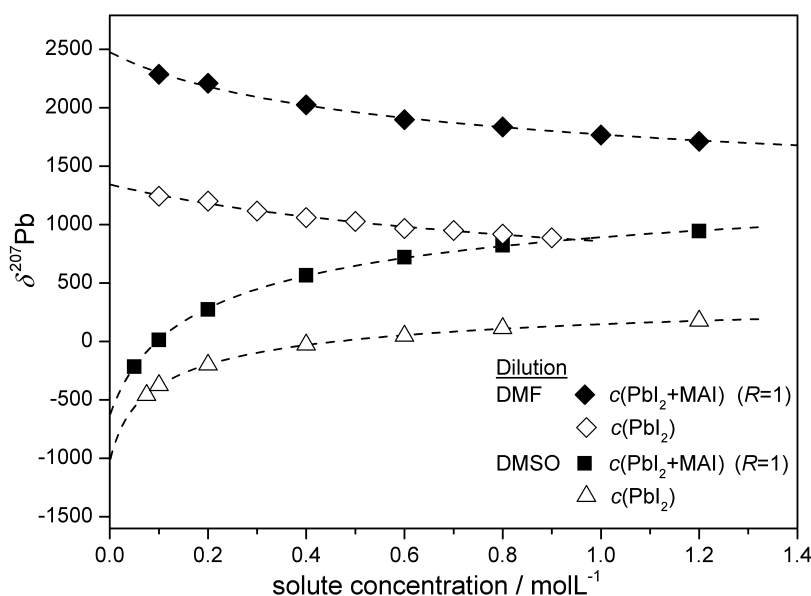
Figure 6.10: Dilution experiments : $\delta^{207}Pb$ as function of the concentration $c(PbI_2)$ and $c(PbI_2+MAI)$ ($R = 1$) in solutions of DMSO and DMF. The dashed lines are from the fit procedure according to a monomer-dimer equilibrium $2\,A_n \rightleftharpoons (A_2)_n$ (2) and were cut-off beyond experimental accessible concentrations. whereas A stands for any assembly or building unit of a *n*-meric species that may form in the PbI$_2$+I$^-$ system in DMSO or DMF. This was chosen based on the assumption this is the best approximation for the observed solution dynamics.

Generally, for DMSO solutions, increasing the amount of precursor in any form results in deshielding of the ^{207}Pb nuclei (Figure 6.10). Whereas in DMF, this was true for raising the iodide concentration $c(MAI)$ in form of the ratio [MAI]/[PbI$_2$] (Figure 6.14), while increasing the concentration of the solutes $c(PbI_2)_{DMF}$ and $c(PbI_2+MAI)_{DMF}$ (Figure 6.10) was experienced as shielding by the ^{207}Pb nuclei. The latter dilution experiment is discussed together with the titration experiments in DMF separately later in text. The reason for this is that $c(PbI_2)_{DMF}$ crosses $c(PbI_2+MAI)_{DMSO}$ towards experimental high concentrations (Figure 6.12) around the concentration $c(MAI) = 1.0 \pm 0.1\,M$ and chemical shift $\delta^{207}Pb = 880$,

suggesting a structural relation in these systems. A common structural origin can be inferred at the low concentration limits of the solutes in DMSO that is estimated between the values of δ^{207}Pb $= -600$ to -1000.

c(PbI$_2$) and c(PbI$_2$+MAI) ($R = 1$) and in DMSO The general NMR spectroscopic context is briefly described for the dilution experiments in DMSO, and c(PbI$_2$)$_{\text{DMSO}}$ in relation to available literature reports on ^{207}Pb-NMR. For dissolving PbI$_2$ and PbI$_2$+MAI ($R = 1$) at different concentrations in the solvents DMSO and DMF (Figure 6.10), a simplified notation is introduced for the sake of a qualitative discussion on different types of octahedral connectivity in the context of an equilibrium and general concepts of NMR spectroscopy. Assuming the representative equilibria :

$$\text{PbI}^+ + \text{I}^- \rightleftharpoons \text{PbI}_2 \qquad\qquad \text{(eq.1)}$$
$$\text{PbI}_2 + \text{I}^- \rightleftharpoons \text{PbI}_3{}^- \qquad\qquad \text{(eq.2)}$$

PbI$_2$ stands for neutral condensed (PbI$_{6/3}$)$_n$ octahedra of finite size (i.e., of reduced size and nuclearity than in the solid-state structure), PbI$^+$ can be any n-meric or polynuclear structure (Pb$_n$I$_{m-1}$)$^{z+}$ ($z \geq +1$) that may form by formally removing one iodide atom from the PbI$_2$ structure, and PbI$_3{}^-$ can be any n-meric or polynuclear (Pb$_n$I$_m$)$^{z-}$ or (PbI$_3$)$_n^-$ related structure that may form in a PbI$_2$+I$^-$ system, if not stated otherwise.

The curves in DMSO have the common feature to be relatively flat at higher concentrations compared to the steep decline at lower concentrations ($c_{\text{solute}} < 0.2\,\text{M}$). This type of curve suggests the presence of more than two species, such as monomeric units that undergo (auto-)ionization at lower concentrations and self-associate at higher concentrations to form dimeric or n-meric species.[270,277–279] Associating the observed deshielding at higher concentration in DMSO with dimerization (or any n-merization) or by an increase in the coordination number on the metal atom, may be excluded, at least for homoleptic coordination by iodide, as this would inevitably result in shielding. The complexation (=increasing the c.n. of the central metal atom by +1, and the charge of the complex by -1) in its generalized form (eq.2) cannot account for the experimentally observed deshielding in δ^{207}Pb as function of increasing concentration c(MAI), since 'PbI$_3{}^-$' has when compared to 'PbI$_2$' one additional iodide atom plus the negative charge, which in two ways results in shielding. The downfield shift at higher concentrations was previously interpreted in terms of ^{207}Pb-NMR as dissociation Pb(OAc)$_2 \rightleftharpoons$ PbOAc$^+$ + OAc$^-$ (eq.3) in aqueous solution.[225] Following the approach in (eq.3) and assuming an auto-ionization in the form PbI$_2 \rightleftharpoons$ PbI$^+$ + I$^-$ (eq.1), higher concentrations will drive the equilibrium towards the neutral species on the left-side, which explains the observed deshielding of δ^{207}Pb in the same direction. The shielding effect of the positive charge follows from the highfield shift of Pb$^{\text{II}}$ at δ^{207}Pb(Pb^{2+}) $= -2961$ (D$_2$O) and -2575 (DMSO).[225,229,280,281] In view of this large difference $\Delta\delta^{207}$Pb $\sim 1500 - 2500$, the following ionization step PbI$^+ \rightleftharpoons$ Pb^{2+} + I$^-$ (eq.4) is unlikely to be present in significant portions.

The results from the c(PbI$_2$+MAI)$_{\text{DMSO}}$ dilution experiments are, due to overlap of chemical shift regions discussed in the following text together with the titration experiments in DMSO.

6.2.7 The relation between the ^{207}Pb-NMR Titration and Dilution Experiments in DMSO

The plots in (Figure 6.11) show the initially presented titration experiments in DMSO, δ^{207}Pb as function of the added precursor concentration c(MAI) and c(CsI). In (Figure 6.11) the MAI titrations are summarized and in (Figure 6.11) the CsI and MAI titrations at c(PbI$_2$) = 0.4 M. The dilution experiments in DMSO shown in (Figure 6.11) were identically replotted as inset.
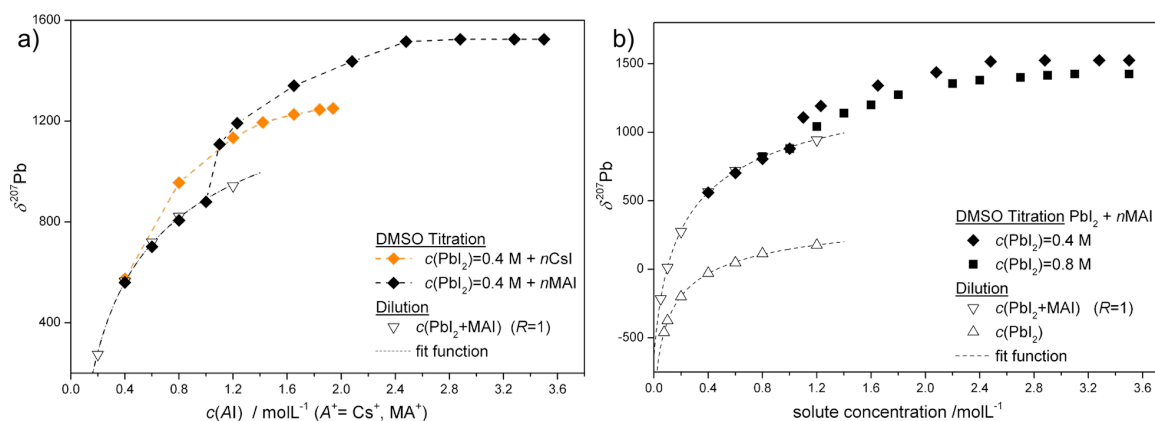
Figure 6.11: a) δ^{207}Pb as function of added iodide concentration, comparison of the c(PbI$_2$) = 0.4 M titration experiments with MAI and CsI. b) δ^{207}Pb as function of added iodide concentration c(MAI). The dilution experiment insets show δ^{207}Pb as function of c(PbI$_2$) and as function of c(PbI$_2$+MAI) ($R = 1$). The fit functions apply only to the dilution experiments.

Following the titrations PbI$_2$+nMAI by concentration of added precursor up to the concentration c(MAI) $\leq$ 1.0 M, the same δ^{207}Pb dependence was observed as varying the concentration c(PbI$_2$+MAI)$_{DMSO}$. That is, for example in c(PbI$_2$) = 0.4 M+nMAI titration within the ratios ($1 \leq R \leq 2.5$). The results in previous sections showed cation was interchangeable for ($R = 1$) up to c(PbI$_2$+AI) = 1.0 M without noticeable effect on δ^{207}Pb. Thus, a cation influence by MA$^+$ is exerted earliest at c(MAI) $\geq$ 1.0 M, and below this value the iodide concentration c(I$^-$) is the dominant factor. Comparing the c(PbI$_2$) = 0.4 M titrations of MAI and CsI as representative example in (Figure 6.11), the solution that contains the Cs$^+$ cation is obviously not part of this interrelation. The common δ^{207}Pb dependence is observed at different experimental concentrations. The chemical shift δ^{207}Pb = 822 corresponds to the titration point c(PbI$_2$) = 0.4 M, c(MAI) = 0.8 M and the dilution is here at c(PbI$_2$) = 0.8 M, c(MAI) = 0.8 M. This means at half concentration c(PbI$_2$) the 2-fold ratio [MAI]/[PbI$_2$] results in the same chemical shift. This $\frac{1}{2}c$(PbI$_2$) $\rightarrow 2R$ relation was also observed at the titration endpoints (Table 6.1), yet at different values of δ^{207}Pb$_{final}$. The experimental procedures satisfy therefore the same iodide consuming equilibria within c(MAI) $\leq$ 1.0 M. When c(MAI) = 1.0 M was reached, the titration curves entered a different δ^{207}Pb dependence, that finally ends at the chemical shift region observed for 3D networks of (PbI$_{6/2}$)$_n^-$-octahedra. The dilution experiment continued up to c(PbI$_2$+MAI)$_{DMSO}$ = 1.3 M, which is most likely the result of supersaturation above c(PbI$_2$) $\geq$ 1.0 M, since varying the concentration of solutions in the precursor ratio ($R = 1$) is equivalent with the titration points ($R = 1$) at different concentrations c(PbI$_2$).

At the concentration c(MAI) = 1.0 ± 0.1 M that corresponds to δ^{207}Pb = 880, several events culminate, which is shown in (Figure 6.12) as the magnified and edited section of (Figure
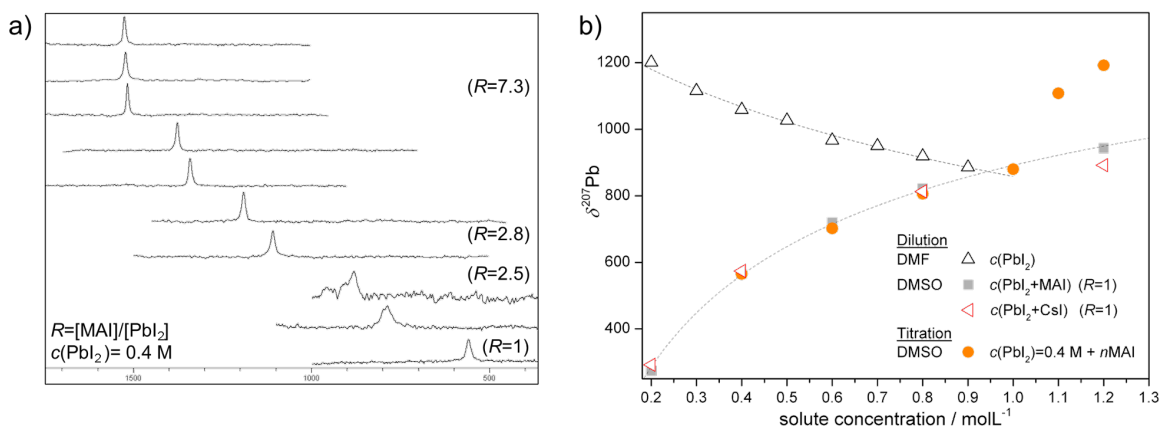
Figure 6.12: a) Stacked plots of ^{207}Pb-NMR spectra of the [MAI]/[PbI$_2$] titration at $c(\text{PbI}_2) = 0.4$ M. b)Magnified and edited section of (Figure 6.11) to visualize the events at $c(\text{MAI}) = 1.0 \pm 0.1$ M.

6.10). (1.) At its solubility limit $c(\text{PbI}_2)_{\text{DMF}}$ crosses the curve of $c(\text{PbI}_2+\text{MAI})_{\text{DMSO}}$. (2.) The cation influence of MA$^+$ emerges from this value on. (3.) The cation independence of δ^{207}Pb for precursor combinations in the ratio ($R = 1$) stops to be valid around this concentration. Worth mentioning here is also, that in the $c(\text{PbI}_2) = 0.2$ M$+n$CsI titration experiment the correlation with $\delta_{\text{iso}}(^{207}\text{Pb})$ from (δ-CsPbI$_3$) at δ^{207}Pb $= 1020$ was at the concentration $c(\text{CsI}) = 1.0$ M. In the $c(\text{PbI}_2) = 0.4$ M$+n$MAI titration experiment a similar broadening in the $\Delta_{1/2}(^{207}\text{Pb})$ linewidth was observed around $c(\text{MAI}) = 1$ M and δ^{207}Pb $= 880$ (Figure 6.12a). It is not clear whether these second transitions are present when $c(\text{PbI}_2) > 0.2$ M or related to lower concentrated solutions. It is also likely, this were obscured by fast saturation at higher concentration. Nevertheless, if a ssNMR shift was to be predicted within the chemical shift range δ^{207}Pb $\sim 880 - 1200$ for a structure related with PbI$_2$+MAI in DMSO, one candidate would be (MA)$_2$(DMSO)$_2$Pb$_3$I$_8$[282–284] Following its structure description as "trinuclear strips of (PbI$_2$)$_n$ coordinated by I$^-$"[283] expressed in the formula (MA$^+$)$_2$[(PbI$_3{}^-$)$_2$PbI$_2 \cdot$ DMSO$_2$][283] this compound would fit the picture in between $\delta_{\text{iso}}(^{207}\text{Pb}) = -29$ from (PbI$_2$)(s.) and $\delta_{\text{iso}}(^{207}\text{Pb}) = 1423 - 1482$[254–257] from MAPbI$_3$. In this context $\delta_{\text{iso}}(^{207}\text{Pb}) = 1065$ from δ-CsPbI$_3$ shall be mentioned, which comprises by the formula PbI$_3^-$ a double-chain of edge-sharing condensed PbI$_6$-octahedra.[251] The same structural motif in terms of PbI$_6$-octahedra condensation is present in the compounds (CH$_3$NH$_3$)PbI$_3 \cdot$ DMF and (MA)$_2$(DMF)$_2$Pb$_2$I$_6$[285,286] which are actually identical (see section 6.5.4). Thus describe (PbI$_3$)$_n^-$ and (Pb$_2$I$_6$)$_n^{2-}$ equivalently the structural motif of a 'double-chain' of two edge-sharing condensed PbI$_6$-octahedra.

Independent of the above mentioned suggestion, the edge- or face-sharing octahedral (see 6.5.5) connectivity in lower dimensional structures, comparable to the non-perovskite phase δ-CsPbI$_3$, can be located within the chemical shift region δ^{207}Pb $\sim 12500 - 800$ as an orientation value. Taking into account that $c(\text{PbI}_2)_{\text{DMSO}}$ covers, before the steep decline around $c(\text{PbI}_2)_{\text{DMSO}} = 0.2$ M, the chemical shifts range δ^{207}Pb $= -200$ to 177 in vicinity to $\delta_{\text{iso}}(^{207}\text{Pb}) = -29$ of (PbI$_2$)(s.) (Table 6.2 and Section 6.5.5) the correspondence between the ssNMR $\delta_{\text{iso}}(^{207}\text{Pb})$ and experimental titration procedure PbI$_2$+MAI$\rightarrow$MAPbI$_3$ and PbI$_2$+CsI$\rightarrow$CsPbI$_3$ is apparent, in terms of a parallel chemical shift trend in solution. This begins with dissolving PbI$_2$(s.) in DMSO and follows the ^{207}Pb-NMR titration until the endpoints δ^{207}Pb$_{\text{final}}$. Expressing the octahedral connectivity in the Niggli-notation, the sum
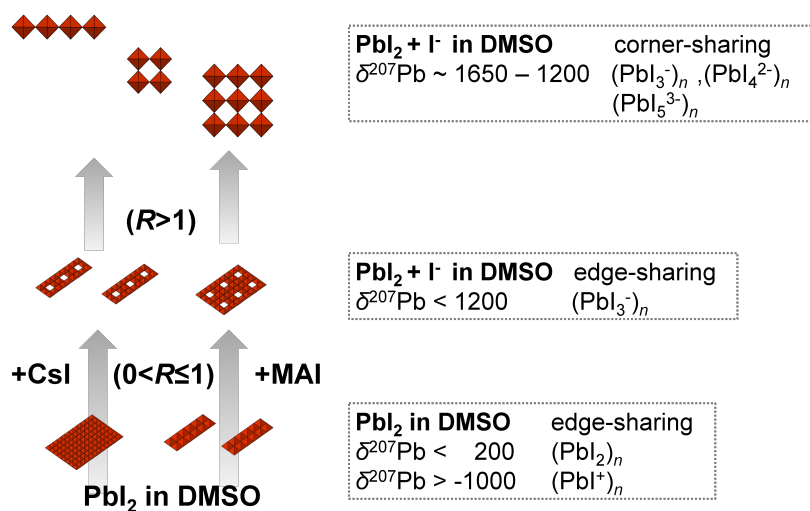
Figure 6.13: Visual summary of the suggested chemical shift regions for the different type of octahedral connectivity for the PbI_2+CsI and PbI_2+MAI systems in DMSO as solvent.

formulae are obtained for PbI_2(s.) from $PbI_{6/3=2}$ and for $MAPbI_3$ from $PbI_{6/2=3}$ which illustrates the formulation $PbI_2+(MA^+I^-) \rightarrow MAPbI_3$ without changes in the coordination number on the central Pb^{II} atom. More importantly, is hereby the iodide I^- consumption of PbI_2 in DMSO could be linked with the deshielding trend of $\delta^{207}Pb$, as expression of the transition from edge- to corner-sharing condensed PbI_6-octahedra (i.e., by reducing the degree of octahedra condensation in the solution species), which is in full accordance with the previously trend deduced from reported ssNMR shifts $\delta_{iso}(^{207}Pb)$ in (Section 6.2.2)

By these experimental observations (Figure 6.4+6.11) and (Figure 6.13) the uptake of iodide by PbI_2 in DMSO solution may be associated with the formation of a polynuclear n-meric species formally as $(PbI_3)_n^-$ that comprises the ^{207}Pb nuclei in a deshielded structural environment, compared to its predecessor structure, while the coordination number $(c.n.(Pb^{II}) = 6)$ and octahedral geometry remains unchanged around the Pb^{II} central atom. In $c(PbI_2)_{DMSO}$, within the experimental concentration range $c(PbI_2)_{DMSO} = 0.2\,M–1.2\,M$, the dominant species is assumed to be closely related to the coordination environment present in PbI_2(s.), as solvated $(PbI_2)_n$ layers of definite size.

And below $c(PbI_2)_{DMSO} < 0.2\,M$ a cationic $(PbI)_n^+$ species is suggested to emerge (see section 6.2.12). This is summarized in the scheme (Figure 6.13), showing the suggested chemical shift regions for a given type of octahedra condensation. The model equilibrium $PbI_2 + I^- \rightleftharpoons PbI_3^-$ (eq.2) describes therefore the evolution of solution NMR chemical shifts $\delta^{207}Pb$ in the titration experiments by analogy to isotropic chemical shifts from ssNMR $\delta_{iso}(^{207}Pb)$ and therefore to structural transition PbI_2(s.) $\rightarrow MAPbI_3$ and PbI_2(s.) $\rightarrow \delta$-$CsPbI_3 \rightarrow \gamma$-$CsPbI_3$ of comparable solvated PbI_6-octahedral frameworks in combination with an iodide consuming equilibrium processes.

6.2.8 ^{207}Pb-NMR Dilution Experiments with PbI_2 in DMF

The experimentally determined solubility limit of $c_L(PbI_2) = 1.0\,M$ in DMF matches literature reported values[36] and can be extrapolated from $\delta^{207}Pb = 886$ at $c(PbI_2) = 0.9\,M$ to $\delta^{207}Pb$

$= 880 \pm 10$ (Figure 6.10), which is noticeable close to chemical shift of $c(\mathrm{MAI}) = 1.0\,\mathrm{M}$. This flags the point where two equilibrium dynamics are related by saturation of at least parts of the constituents in the $c(\mathrm{PbI_2+MAI})_{\mathrm{DMSO}}$ and $c(\mathrm{PbI_2})_{\mathrm{DMF}}$ system. The coincidence of these events at the solubility limit $c_{\mathrm{L}}(\mathrm{PbI_2})_{\mathrm{DMF}}$ justifies the formulation of the solubility product $c_{\mathrm{L}}(\mathrm{PbI_2}) = c(\mathrm{A}_i)_n * \mathrm{A}_j)_n$ (eq.5), since there must be at least two solution species A_i and A_j in the equilibrium concentrations $[\mathrm{A}_i]$ and $[\mathrm{A}_j]$ which fulfill either of these conditions:

$$c\left(\mathrm{PbI_2} + \mathrm{I}^-\right) = 1.0\,\mathrm{M} = c_{\mathrm{L}}(\mathrm{PbI_2}) \tag{eq.6a}$$

$$c\left((\mathrm{PbI_2})_2\right) = 1.0\,\mathrm{M} = c_{\mathrm{L}}(\mathrm{PbI_2}) \tag{eq.6b}$$

Considering here the representative model equilibria $\mathrm{PbI}^+ + \mathrm{I}^- \rightleftharpoons \mathrm{PbI_2}$ (eq.1) and $\mathrm{PbI_2} + \mathrm{I}^- \rightleftharpoons \mathrm{PbI_3}^-$ (eq.2): The condition (eq.6a) demands from $c(\mathrm{PbI_2})_{\mathrm{DMF}}$ the presence of a negative ion to meet the charge balance (-1), such as $\mathrm{PbI_3}^-$. And (eq.6b) demands two neutral species in the solution dynamics for $c(\mathrm{PbI_2+I}^-)$ in DMSO at this point, which cannot be fully ruled out.

Nevertheless, does (eq.6a) gain a certain likelihood by the fact the chemical shift $\delta^{207}\mathrm{Pb}$ $= 1243 - 886$ span by $c(\mathrm{PbI_2})_{\mathrm{DMF}}$ is centered around the isotropic ssNMR shift of δ-$\mathrm{CsPbI_3}$ (Table 6.2). The chemical shift domain of $c(\mathrm{PbI_2})_{\mathrm{DMF}}$ is not only deshielded from $c(\mathrm{PbI_2})_{\mathrm{DMSO}}$ but the gap in between is consistently covered by the $\mathrm{PbI_2}+n\mathrm{MAI}$ titration and $c(\mathrm{PbI_2+MAI})$ dilution experiment in DMSO, these are both the expression of iodide addition $\mathrm{PbI_2+I}^-$. Therefore, it may be suggested that at least partially there is an anionic component present in $c(\mathrm{PbI_2})_{\mathrm{DMF}}$. This requires $\mathrm{PbI_2}$ to disproportionate in DMF and DMSO solution according to :

$$2\,\mathrm{PbI_2} \rightleftharpoons \mathrm{PbI}^+ + \mathrm{PbI_3}^- \tag{eq.7}$$

The equilibrium formulation of (eq.7) is actually also the sum of (eq.1)+(eq.2), of which both are as equilibria fundamental in order to understand the solution chemistry of the $\mathrm{PbI_2+I}^-$ system in DMF and DMSO. It is worth mentioning, that (eq.7) is not a purely theoretical hypothesis, since the existence of (eq.1) was cross-referenced by NMR and potentiometric measurements[225,280,281] and (eq.2) is basically the formulation of the experimental NMR titration procedure, which corresponded by evolution of chemical shifts $\delta^{207}\mathrm{Pb}$ in solution and solid-state NMR according to $\mathrm{PbI_2(s.)} \to \mathrm{MAPbI_3}$ and $\mathrm{PbI_2(s.)} \to \mathrm{CsPbI_3}$ in previous sections. Dissolving $\mathrm{PbI_2(s.)}$ at different concentration in either DMSO or DMF, the resulting curves in (Figure 6.10) are the expression of the same dynamic equilibrium (eq.7), which is present *simultaneously in both* solvents, shifted in favor of different species depending on the solvent properties. This may also be anticipated by the almost symmetrical curvature in (Figure 6.10). By including the influence of solvent properties, the trends in $\delta^{207}\mathrm{Pb}$ can be expressed in terms of shifting the position of the equilibria (eq.1) and (eq.2) in favor of one side. The chemical shift ranges span by the experimental concentrations can be assigned to the dominant presence of either one species in (eq.1)+(eq.2). This is for $c(\mathrm{PbI_2})_{\mathrm{DMF}}$ the range between $\delta^{207}\mathrm{Pb} = 1243 - 886$, and $(\mathrm{PbI_3})_n^- \gg (\mathrm{PbI_2})_n$. Within the full chemical shift range from $\delta^{207}\mathrm{Pb} = -1000$ to 177 span by $c(\mathrm{PbI_2})$ in DMSO, the differentiation between experimentally higher (towards the solubility limit c_{L}) and lower concentrations is made $c(\mathrm{PbI_2})_{\mathrm{DMSO}} \to c_{\mathrm{L}}(\mathrm{PbI_2})_{\mathrm{DMSO}}$: $(\mathrm{PbI_2})_n \gg (\mathrm{PbI})_n^+$ and accordingly towards lower concentrations $c(\mathrm{PbI_2})_{\mathrm{DMSO}} \to 0$: $(\mathrm{PbI})_n^+ \gg (\mathrm{PbI_2})_n$.

The presence of neutral $(\mathrm{PbI_2})_n$ and cationic $(\mathrm{PbI})_n^+$ species in DMSO can be regarded the effect of higher coordination and cation solvation strength by DMSO compared to DMF, as

expressed in the higher donor number (DN), whereas the higher acceptor number (AN) of DMSO indicates the more efficient and stable solvation of (iodide) anions (Table 6.5). DMF's reduced ability in solvating iodide, is offset in solution as incorporation of iodide in the species formed by PbI_2+I^-, as result of equilibrium shifting towards $(PbI_3)_n^-$, which would represent therefore edge-sharing PbI_6-octahedral structures of reduced size and dimensionality compared to $(PbI_2)_n$ related structures in DMSO. By this the difference in the titration curve performed in DMSO with CsI can be understood as the stronger electrostatic interaction between Cs^+ and $(PbI_3)_n^-$, than exerted by MA^+.

The disproportionation of PbI_2 in DMSO and DMF is in combination with the solvents donor (DN) and acceptor (AN) properties capable to rationalize the observed $\delta^{207}Pb$ downfield trends in DMSO and DMF as changes in type of octahedral connectivity and dimensionality of the corresponding species, as being finally the result of the solvents iodide solvation capability at higher concentrations.

6.2.9 ^{207}Pb-NMR Titration and Dilution of PbI_2 with MAI in DMF

The dilution experiment $c(PbI_2+MAI)_{DMF}$ covers the chemical shift range $\delta^{207}Pb = 2286 - 1712$, within experimental concentrations $c(PbI_2+MAI) = 0.1\,M - 1.2\,M$. As for the concentration series $c(PbI_2)_{DMF}$ this is interpreted as aggregation of smaller units with increasing concentration. Extending to $c(PbI_2+MAI)_{DMF} = 2.0\,M$ the chemical shift was observed $\delta^{207}Pb = 1593$, as short-time stable solution therefore only the concentration range up to $c = 1.2\,M$ was considered.
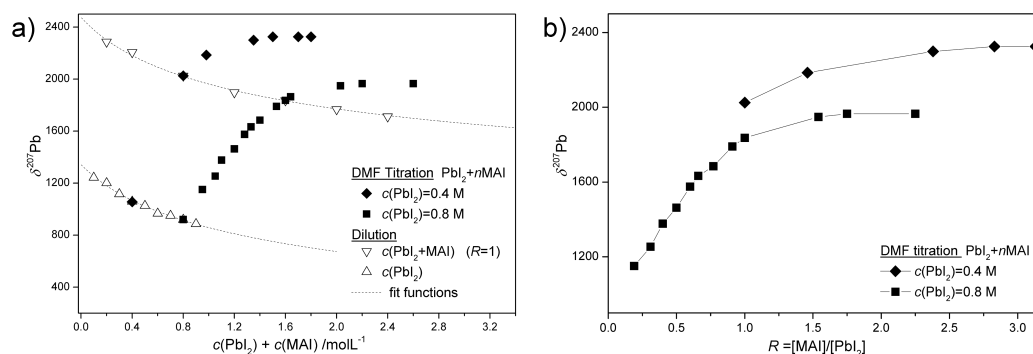
Figure 6.14: a) Summary of chemical shift $\delta^{207}Pb$ vs. solute concentration and composition for the PbI_2+MAI system in DMF. The experimental input concentrations were added up in value as $c(PbI_2)+c(MAI)$, to enable comparison to the dilution experiment of $c(PbI_2)$. b) $\delta^{207}Pb$ as function of precursor ratio $R=[MAI]/[PbI_2]$ in DMF, at constant concentrations $c(PbI_2) = 0.4\,M$ and $c(PbI_2) = 0.8\,M$.

The same experimental procedure as described for the MAI titrations was attempted in DMF as solvent, introducing a comparable small excess of CsI, to a solution of $c(PbI_2) = 0.4\,M$ up to ($R = 1.5$) no signal was observed in the chemical shift range $\delta^{207}Pb = 4800$ to 700, The fate of the $\delta^{207}Pb$ resonance was not resolved, which possibly has disappeared from the NMR-timescale due to different exchange dynamics. The final points of the titration in DMF were indicated same as in DMSO, by an invariant chemical shift $\delta^{207}Pb_{final}$ when a constant value $c_{final}(MAI)$ was reached, that was below the solubility limit of MAI in DMF. Here a comparable lower value of $c_{final}(MAI) = 1.3\,M$ (averaged from $1.2\,M$ and $1.4\,M$), thus

Table 6.4: Selection of solution parameter from the ^{207}Pb-NMR titration experiments in DMF. For each concentrations $c(\text{PbI}_2) = 0.4\,\text{M}$ and $0.8\,\text{M}$, in addition to $(R = 0)$ and the last titration point, the data for $(R = 1)$ and the corresponding solution parameter is presented. $\delta^{207}\text{Pb}_{\text{final}}$ denotes the final chemical shift value and R denotes the precursor ratio $[AI]/[\text{PbI}_2]$ ($A^+ = \text{MA}^+$, Cs^+).

	$c(\textbf{PbI}_2) = \textbf{0.4\,M}$				$c(\textbf{PbI}_2) = \textbf{0.8\,M}$		
R	$c(\text{MAI})\ /\ \text{molL}^{-1}$	$\delta^{207}\text{Pb}$	$\Delta_{1/2}\ /\ \text{Hz}$	R	$c(\text{MAI})\ /\ \text{molL}^{-1}$	$\delta^{207}\text{Pb}$	$\Delta_{1/2}\ /\ \text{Hz}$
	0	1054	800		0	919	800
1.0	0.4	2025	550	1.0	0.8	1836	500
3.0	1.2	2325	1800	1.8	1.4	1965	3300

saturation at lower values of R was noticed (Table 6.4).

The plot in (Figure 6.14) shows $\delta^{207}\text{Pb}$ as function of $R = [\text{MAI}]/[\text{PbI}_2]$ at constant concentrations $c(\text{PbI}_2) = 0.4\,\text{M}$ between $(1 \leq R < 3)$ and $c(\text{PbI}_2) = 0.8\,\text{M}$ between $(0.2 \leq R < 2.5)$. The latter was chosen for a more detailed investigation of the range $(R < 1)$, which encloses the chemical shift region identified as the perovskite type coordination environment of corner-sharing octahedra from the DMSO titrations. This is presented in (Figure 6.14) and shows that this region was surpassed without any noticeable event. Following the evolution of
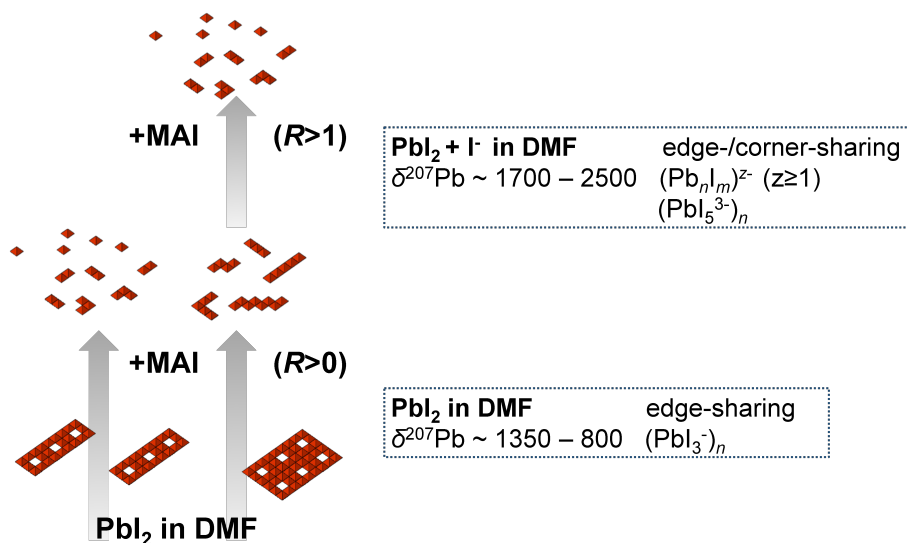
Figure 6.15: Scheme illustrating the relation between chemical shift regions, observed with PbI$_2$ and PbI$_2$+MAI in DMF, and associated solution species in terms of type of octahedral condensation. Whereby the experimentally attained $\delta^{207}\text{Pb}$ ranges noted on the left-hand side have to be considered as exchange averaged values between two or more sites, displaying by $\delta^{207}\text{Pb}$ value only an excerpt of a wider range of solution dynamics.

linewidths and precursor ratio R (Table 6.4) at the final points, the low concentration limit of $c(\text{PbI}_2+\text{MAI})_{\text{DMF}}$ $(R = 1)$, estimated between $\delta^{207}\text{Pb} \sim 2500 - 3000$, is anticipated as the limiting shift value also for the titration in DMF. The chemical shift values from the PbI$_2$ titration with MAI in DMF (Table B.13) could therefore not be assigned to the surpassed chemical shift region for 3D and 2D corner-sharing octahedra, since these are the population averaged shifts between the dynamic processes present within $c(\text{PbI}_2)_{\text{DMF}}$ and the suggested

limiting shift value between δ^{207}Pb $\sim 2500 - 3000$. Hereby it is likely that further limiting shift values arising from several interfering equilibria have to be considered additionally, which were not possible to be further specified. The fact that increasing the precursor concentration c(MAI) in [MAI]/[PbI$_2$] is displayed as deshielding, is interpreted such as that introducing iodide ($R > 0$) in solutions of PbI$_2$ dissolved in DMF results in the fragmentation of larger building blocks into smaller units, and is illustrated in (Figure 6.15). Whereas the shielding trend observed in the c(PbI$_2$+MAI)$_{\text{DMF}}$ dilution curve (Figure 6.10 and 6.14a), which is a cross-section of the titrations at ($R = 1$) for all possible concentrations c(PbI$_2$)$_{\text{DMF}}$, represents the aggregation of smaller units to larger building blocks with increasing precursor concentration at equal ratio. The charge on the generalized polynuclear (Pb$_m$I$_n$)$^{z-}$ species, being the result of fragmentation, is assumed to be generally increased ($z \geq 1$) when compared to the species related with the chemical shift regions c(PbI$_2$)$_{\text{DMF}}$ and covered by DMSO as solvent (Figure 6.19). This can be inferred by extrapolating the deshielding trend from 3D and 2D to 1D (PbI$_5$)$_n^{3-}$ single corner-sharing type of octahedra condensation (3D (PbI$_3$)$_n^- \rightarrow$ 2D (PbI$_4$)$_n^{2-} \rightarrow$ 1D (PbI$_5$)$_n^{3-}$), which visualizes within the same type of octahedral connectivity, the parallel running trend of increased charge with the lower dimensional structure at further deshielded chemical shift values. From here, it follows that (PbI$_5$)$_n^{3-}$ and related structures can be located around chemical shift values δ^{207}Pb $\geq 1650 - 1700$. The identical trend ((PbI$_2$)$_n \rightarrow$ (PbI$_3$)$_n^-$) was present with edge-sharing octahedra going from PbI$_2$(s.) to δ-CsPbI$_3$ in terms of isotropic chemical shifts, of which the latter was associated with the chemical shift region span by c(PbI$_2$)$_{\text{DMF}}$, which is between δ^{207}Pb $\sim 800 - 1350$. The value δ^{207}Pb ~ 1700 also appears as a natural barrier that is approached by the dilution of c(PbI$_2$+MAI)$_{\text{DMF}}$ ($R = 1$) and not attained by any ratio [MAI]/[PbI$_2$] for a given concentration c(PbI$_2$)$_{\text{DMF}}$ as obvious from (Figure 6.14a) and (Table 6.4). Therefore, the addition of iodide to PbI$_2$ dissolved in DMF can be understood as shifting the present solution species from edge-sharing (PbI$_3$)$_n^-$ structures towards corner-sharing (PbI$_5$)$_n^{3-}$ and further to smaller units of both types, ultimately down to single PbI$_6^{4-}$-octahedra, which are likely to be located at chemical shifts between δ^{207}Pb $>\sim 1700$ and δ^{207}Pb $<\sim 3000$. Hereby, all kind of equilibria between units of different size, composition and connectivity, including also the face-sharing type, have to be considered for a detailed discussion. In comparison to DMSO, a reduced tendency for larger or higher dimensional (3D and 2D) structures which can be formed by the PbI$_2$+MAI system became apparent in DMF. The dominant presence of these fragmented and lower dimensional structures is considered as the result of iodide incorporation by increasing the amount of peripheric iodide atoms bound to lead, and is the consequence of the lower acceptor number (AN) of DMF (Table 6.5) thus reduced strength in anion stabilization. In this picture fits also the large number of reported crystal structures obtained from DMF,[287–293] with nearly as much different structural motifs in terms of the octahedral connectivity, whereas only few were reported from DMSO (see also section 6.5.4). A fragmentation upon adding extra-stoichiometric amounts of iodide was reported earlier by solution Raman studies with γ-GBL.[294] In view of the similar solvent parameter (Table 6.5), it was attempted to determine the chemical shift of a c(PbI$_2$+MAI) $= 0.8$ M solution in γ-GBL, whereby unfortunately no signal was detected between δ^{207}Pb $= 0 - 3400$. The measurement was performed on a 400 MHz by a capillary experiment, with DMSO-d$_6$ as lock solvent.

6.2.10 ^{207}Pb-NMR Investigations on the Role of DMSO and DMF Solvent Coordination

NMR spectroscopy is capable of providing quantitative and qualitative information on the strength of a particular donor solvent, following the chemical shift of the NMR active nuclei, which is coordinated by the donor solvent molecules.[40,243,244,268,295–299] The stronger coordination strength by the solvent higher in donor number (DN), imposes larger electron density on the metal nuclei, which is displayed as high-field shift of the signal.
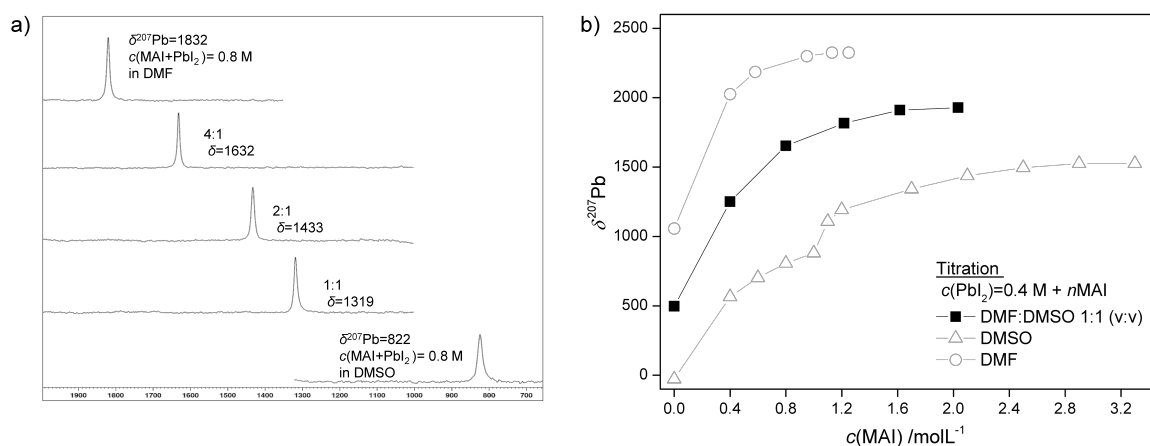
Figure 6.16: Titration experiment δ^{207}Pb as function of c(MAI) starting with c(PbI$_2$) = 0.4 M in a 1:1 (v:v) mixture of DMSO:DMF, for comparison the titration curves in the corresponding pure solvents are shown.

The influence of a coordinative interaction by DMF and DMSO on the chemical shift δ^{207}Pb was investigated by a typical NMR experiment. For this purpose, δ^{207}Pb was recorded in the PbI$_2$+MAI system at constant concentration c(PbI$_2$) = 0.8 M and ratio ($R = 1$) varying the bulk volume ratio (v:v) of the binary solvent system DMF:DMSO (Figure 6.16a). Next the solvent influence at different iodide concentrations was investigated by varying the precursor ratio $R = $ [MAI]/[PbI$_2$] in constant ratio DMF:DMSO 1:1 (v:v) of solvents and concentration c(PbI$_2$) = 0.4 M (Figure 6.16b). Here the lower concentration c(PbI$_2$) was chosen to ensure a wider range of R for comparison. Throughout all experiments a single resonance was observed, in linewidths $\Delta_{1/2}(^{207}$Pb) comparable to those in the pure solvents. Changing the experimental procedure did not affect the chemical shift in each composition e.g., dissolving in DMSO and diluting with DMF (and vice versa) or avoiding the dilution step, by applying a previously stirred mixture in the corresponding DMF:DMSO ratio for the solution preparation. Throughout all experiments a linear relation between the bulk solvent ratio (v:v) and chemical shift distance $\Delta\delta^{207}$Pb$_{\mathrm{DMF:DMSO}}$ (in numbers of ppm), referenced to δ^{207}Pb values in the pure solvents, was observed. As shown in (Figure 6.16) the measured shift δ^{207}Pb$_{\mathrm{DMF:DMSO}} = 1319$ from equal volume ratio (v:v) DMF:DMSO 1:1 represents the mean between shifts in the pure solvents (c(MAI+PbI$_2$) = 0.8 M: δ^{207}Pb$_{\mathrm{DMF}} = 1832$, δ^{207}Pb$_{\mathrm{DMSO}} = 822$). The same linear relation is present independently of the iodide concentration and [MAI]/[PbI$_2$] precursor ratio. As from the start of the titration experiment (c(MAI) = 0) δ^{207}Pb = 497 up to the final shift value δ^{207}Pb$_{\mathrm{final}} = 1928$ at (c(MAI) = 2.0 M, $R = 5$), the mean of $\Delta\delta^{207}$Pb$_{\mathrm{DMF:DMSO}}$ for a given ratio R is observed. This linearity was found, by multiple random picks throughout the titration or dilution experiments, to persist at any precursor ratio R and concentration (0.4 M

$\leq c(\text{PbI}_2) \leq 1.2\,\text{M})$.

The experimental result of this section can be summarized such as the chemical shift difference $\Delta\delta^{207}\text{Pb}$ displays on the ppm scale the bulk volume ratio (v:v) of the solvents DMF:DMSO, referenced to the calculated distances $\Delta\delta^{207}\text{Pb}_{\text{DMF:DMSO}}$ between $\delta^{207}\text{Pb}$ in the pure solvents.

The Role of the Donor Number (DN)

In view of the here experimentally observed large $\delta^{207}\text{Pb}$ chemical shift differences in pure DMSO and DMF, this linear relationship was unexpected. If it is the stronger coordinating strength of DMSO, that generates these large highfield shifts compared to those in DMF, the mixtures of these were expected to display pronounced tendency to remain close to the $\delta^{207}\text{Pb}$ values in DMSO.

This linear relation of equal contributions is the result of either two solvents with equal DN, exhibiting the same donor strength or the absence of any direct coordination between the donor solvent molecules and the ^{207}Pb nuclei. Per definition the donor number concept is a scale for the variation of the donor strength in solvents[241,300,301] that excludes an equal contribution from donors with different DN. And since the frequencies measured by NMR spectroscopy are the analytic response to changes in the ^{207}Pb nuclei's electronic structure, the absence of any significant Pb-O oxygen coordination or bonding interaction at higher solute concentrations ($c_{\text{solute}} \geq 0.4\,\text{M}$) must be concluded. This leaves one with a homoleptic ligand sphere of iodide atoms surrounding the Pb^{II} central atom. The exchange rates of solvents coordinated to a metal are generally slow, enabling the resolution of bound and bulk solvent signals in the ^{1}H- and ^{13}C-NMR spectra.[302,303] No signs of solvent coordination were detected in these either. In the presence of colloids or any polynuclear structure solvent coordination located at the outer surface or terminal atoms will have negligible impact regarding the total atom number in the structure. The difference in coordination strength (ΔDN) between DMSO and DMF and its implications on the structural chemistry in dilute solution (e.g.,UV-Vis[34,35,221,304] spectroscopy) and the solid state is beyond doubt. On the other hand, it is also this very interaction, that would contrast the easiness of DMF vs. DMSO exchange in case of a Pb-O coordination.

The effect the choice of solvent has on the solution species manifests itself throughout this work in the large chemical shift differences and trends in $\Delta\delta^{207}\text{Pb}$. The interpretation of these solely in terms of their DN appears convenient at first sight yet does not withstand the experimental results presented in this and previous sections. Solutions of comparable concentration range ($c(\text{PbI}_2) < 0.4\,\text{M}$) and $c(\text{MAI+PbI}_2) \sim 1\,\text{M}$) in DMF significant Pb-O bonding was reported by (EXAFS) XANES.[305] Here the different time-scale and sensitivity of experimental methods may be considered, and as mentioned earlier by means of NMR spectroscopy the average of structures that are under dynamic exchange is measured, that is including site exchange within a given structure, since NMR can't resolve all these individual species. The concentration dependent agglomeration in a mixture of solvents has recently been reported by combined ^{207}Pb-NMR spectroscopy and SAXS measurements.[230] Regarding the above observed linear relationship from DMF:DMSO mixtures, the so far dominant presence of structures involving PbI$_6$-octahedra without direct solvent coordination to the Pb^{II} central atom and following the results of this and previous sections, strongly suggests taking the acceptor properties of the solvents and the role of anion solvation more into consideration. This finally provides a conclusive explanation of the solvent mixture experiments, in continuation of the model equilibrium (eq.1) and (eq.2), as shown in the next section.

6.2.11 The Relation Between DMF and DMSO Solvent Mixtures and Solution Composition

In pure DMSO the titration endpoint $\delta^{207}\text{Pb}_{\text{final}} = 1425$, associated with the perovskite type of 3D corner-sharing $(\text{PbI}_{6/2})^-$-octahedra, was reached by the solution conditions $c(\text{PbI}_2)$ = 0.8 M and $c(\text{MAI}) = 3.0\,\text{M}$ ($R = 4$) (Table 6.1). Here the chemical shift is noted as $\delta^{207}\text{Pb}$ = 1431 at equimolar solution conditions $c(\text{PbI}_2) = 0.8\,\text{M}$ and $c(\text{MAI}) = 0.8\,\text{M}$ ($R = 1$) by applying the solvent mixture DMF:DMSO 2:1, which is a difference by the factor 4.

The structure in terms of octahedral connection in solution was described in the previous section as the interrelation between $c(\text{PbI}_2)$ and $R = [\text{MAI}]/[\text{PbI}_2]$ within the main frame $c_{\text{final}}(\text{MAI})$, and analogous for CsI as iodide source. The value of $c_{\text{final}}(\text{MAI})$ is considered to reflect qualitatively the efficiency in the stabilizing interaction between the iodide in solution and the solvent. Considering the model equilibrium $\text{PbI}_2 + \text{I}^- \rightleftharpoons \text{PbI}_3^-$ (eq.2) efficient iodide solvation will favor the left side, by 'removing' I^- from the equilibrium. Therefore, in DMSO increased amounts of iodide is required to shift the balance in (eq.2) to the right. When applying a mixture of DMSO:DMF, again the parameter $c(\text{PbI}_2)$ and R regulate the structure formation according to (eq.2) within the 'environmental' solution conditions provided by the solvents in terms of their acceptor and dielectric properties. The DMF solvent contributes by lowering the 'anion stabilization capacity' in the total volume DMF+DMSO, compared to the same volume of purely DMSO. Thereby shifting the equilibrium to the right-side at lower values of R. In case of the example at the beginning of this section PbI_3^- would represent corner-sharing $(\text{PbI}_{6/2})^-$-octahedra. The additive property in the bulk solvent features points hereby more towards on the influence by a macroscopic constant, that is the relative permittivity ε. This can be summarized that solvent mixtures DMF:DMSO provide a shortcut to structures in solution that otherwise required larger amount of precursor and these in higher values of R to form.
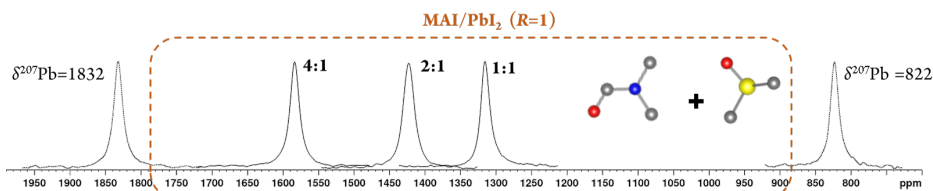
Figure 6.17: Stacked plot of ^{207}Pb-NMR spectra of $c(\text{PbI}_2+\text{MAI}) = 0.8\,\text{M}$ in different solvent ratios DMSO:DMF (v:v).

The spectra plot showed in (Figure 6.17) is intended to visualize the results of this section, which may provide a rational on the efficacy of solvent mixtures that are applied for the solar cell fabrications.[306,307] These binary solvent mixtures DMF:DMSO provide an elegant mean to move any ratio of precursors, for example PbI_2+MAI ($R = 1$) to chemical shifts, thus to structures of the solution species that resembles the structural environment of the final material MAPbI$_3$.

By adjusting the (v:v) volume ratio of the binary solvent mixture the precursor ratio can be placed at any desired chemical shift value between that of the pure solvents. This may provide helpful not only for the fabrication of perovskite inks. In connection with crystallization studies of the solid material, ^{207}Pb-NMR provides the tool to analyze the solution before solid

formation and the solution composition thereafter, that is the equilibrium position at any stage of crystallization.

6.2.12 ^{207}Pb-NMR Titration of Pb(NO$_3$)$_2$ with MAI in DMF and DMSO

The chemical shift in $c(\text{Pb(NO}_3)_2) = 0.8\,\text{M}$ prior to addition of any iodide were measured as $\delta^{207}\text{Pb} = -2610$ in DMSO and $\delta^{207}\text{Pb} = -2799$ in DMF (Figure 6.18), whereas both signals shared the same linewidths of $\Delta_{1/2}(^{207}\text{Pb}) = 32\,\text{Hz}$. These are comparable to the chemical shift range Pb(NO$_3$)$_2$ in aqueous solution whereby $\delta^{207}\text{Pb} = -2851$ to -2961 covers a large part of low and high concentrations.[225] The more shielded value in DMF can be explained as was done for CsI, here the larger electron density is probably imposed by the nitrate anion NO$_3^-$ compared to the neutral oxygen donor atom in the solvent. When MAI was introduced into
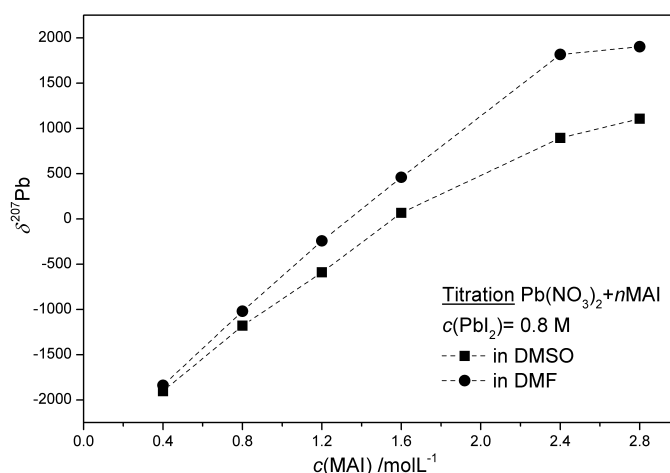
Figure 6.18: Pb(NO$_3$)$_2$+nMAI titration, δ^{207}Pb as function of c(MAI).

the solution at $(R = 0.5)$ the linewidths jumped to $\Delta_{1/2}(^{207}\text{Pb}) = 2000 - 4000\,\text{MHz}$, and at precursor ratios [MAI]/[Pb(NO$_3$)$_2$] as low as $(R = 2-3)$ the chemical shift range of condensed PbI$_6$-octahedra was reached (Figure 6.18) and (Tables B.15, B.16). The enormous linewidths imply an exchange between species largely separated in chemical shifts, and the low R values provide a hint on the preference to form polynuclear octahedral $(\text{Pb}_n\text{I}_m)^{z-}$ structures rather than to react by ligand substitution in a single molecule of the type $[\text{PbI}_{6-n}(\text{solvent})_n]^{(4-n)-}$. This was only investigated in higher concentrated solutions $c(\text{PbI}_2) = 0.8\,\text{M}$ and if the Pb-I system is not doomed to form polynuclear species at any concentration, a possible threshold value favoring the formation molecular complexes may be located around the operational range of UV-Vis spectroscopy ($c \sim$mM–μM).

Comment on the Lower Concentration Regime in DMF and DMSO   The steep change in curvature at lower concentrations (Figure 6.10) in DMSO, which is not present in that form for DMF, implies a more pronounced influence of the DMSO solvent's donor-acceptor properties. That will probably be displayed as iodide substitution by solvent molecules in the Pb-I solution species that is present towards lower concentrations. In case of DMF this can be explained as continuation of the solvents incapability to interfere with the Pb-I species by direct coordination to the Pb$^{\text{II}}$ central atom. The downfield shift in DMF is therefore associated

with decreasing nuclearity or size of a given assembly $(\mathrm{Pb}_n\mathrm{I}_m)^{z-}$, including the possibility of decreasing coordination number to c.n.$(\mathrm{Pb^{II}}) = 5$ or 4. It was not possible to narrow down the chemical shift range for any of these assumed species at low solute concentrations in DMF and DMSO. Nevertheless was shown in this work, that solvent coordinated species of the form $[\mathrm{PbI}_{6-n}(\text{solvent})_n]^{(4-n)-}$ are *not* present at least in significant portions in the high concentration regime of the solutes $c_{\text{solute}} \geq 0.4\,\mathrm{M}$.

6.3 The Solute-Solvent System Lead Iodide in DMSO and DMF

The plot in (Figure 6.19) show δ^{207}Pb as function of $c(\mathrm{PbI}_2)$ and $c(\mathrm{PbI}_2+\mathrm{MAI})$ at $(R = 1)$ in DMSO and DMF and is the summary of the PbI$_2$+MAI solution chemistry in both solvents. The chemical shifts span over $\Delta\delta^{207}$Pb $\sim 3500\,\mathrm{ppm}$, that is from the low concentration limit of $c(\mathrm{PbI}_2+\mathrm{MAI})_{\mathrm{DMF}}$ at δ^{207}Pb $= 2500$ to that of $c(\mathrm{PbI}_2)_{\mathrm{DMSO}}$ at δ^{207}Pb $= -1000$. This range provides the frame in terms of δ^{207}Pb for the Pb-I systems solution chemistry in DMSO and DMF, as it also includes the chemical shifts δ^{207}Pb at any attainable ratio $[\mathrm{I}^-]/[\mathrm{PbI}_2]$.
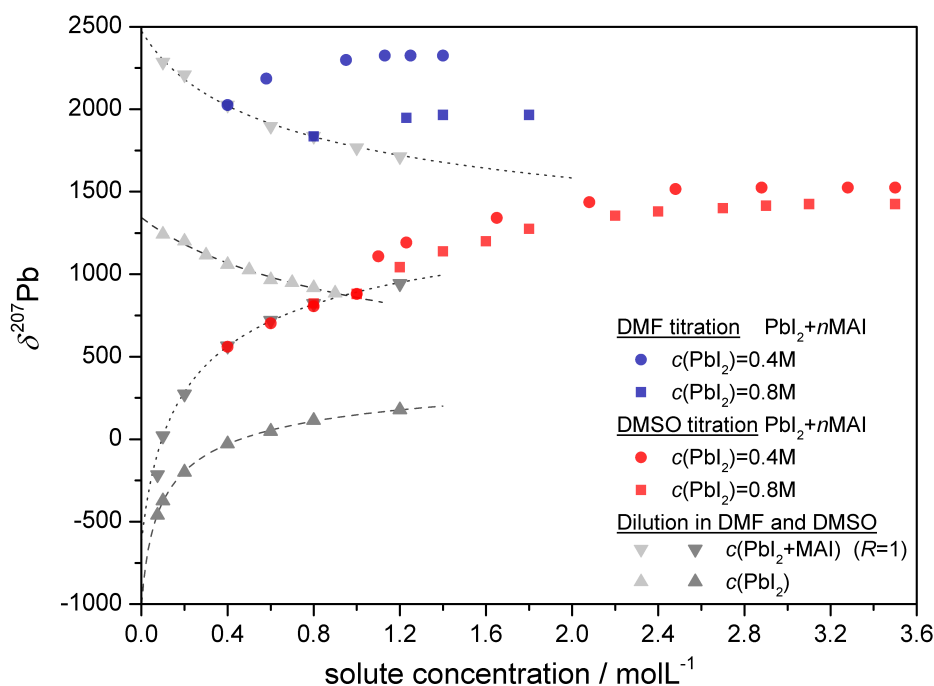
Figure 6.19: Overview of the PbI$_2$+MAI solution system in DMSO and DMF, δ^{207}Pb as function $c(\mathrm{PbI}_2)$ and $c(\mathrm{PbI}_2+\mathrm{MAI})$ in the dilution experiments, and as function of $c(\mathrm{MAI})$ in the titrations.

In DMSO more shielded values of δ^{207}Pb are observed compared to DMF, that is obviously the effect of solvent but not the effect of preference for one solvent, in terms of a stronger interaction between the given $(\mathrm{Pb}_m\mathrm{I}_n)^{z-}$ solution species and DMSO, for example. This follows the results from the previous sections and can be extended to any concentration in (Figure 6.10) these plots may be used as sort of 'phase diagram' for the relation between the solvent ratio DMF:DMSO and δ^{207}Pb, at least for concentrations $c \geq 0.4\,\mathrm{M}$ which were in the focus of this work. That is when drawing a straight line from any point of the $c(\mathrm{PbI}_2+\mathrm{MAI})$ or $c(\mathrm{PbI}_2)$ curve in DMSO to that of DMF, any point on this line as ratio of the distance

between the two points, will give the chemical shift δ^{207}Pb of the solute in the corresponding solvent ratio. For example, δ^{207}Pb for any solute concentration in a 1:1 (v:v) DMF:DMSO mixture can be read at half distance between two points.

Moreover, visualizes (Figure 6.19) several of the key findings in this study, beginning with the fundamental different results from the PbI$_2$+MAI titrations in the two solvents. In DMSO a classic endpoint titration was observed, whereas in DMF a fragmentation to smaller building units was present already when ($R > 0$), following a general tendency in DMF for smaller and lower dimensional structures, when compared to DMSO. Symbolic for this is the chemical shift region for 3D and 2D corner-sharing octahedra δ^{207}Pb $\sim 1350 - 1650$, which was not attained by any concentration or increased precursor ratio in DMF as solvent. In DMSO was the range δ^{207}Pb $\sim 1350 - 1650$ reached only when increasing the ratio of precursor ($R > 1$). When ($0 \leq R \leq 1$) only the chemical shift values for edge- (likely also face-)sharing octahedral connectivity were enclosed in DMSO as solvent within the experimental range of chemical shifts δ^{207}Pb ~ -1000 to $+1000$. Worth mentioning that ($R = 1$) is not a clear-cut value, and rather distinguishes emerging dominance regions for either species. The remarkably smaller value of $c_{\text{final}}(\text{MAI}) = 1.3\,\text{M}$ in DMF compared to $c_{\text{final}}(\text{MAI}) = 3.0\,\text{M}$ in DMSO, can be read directly from (Figure 6.19), and showed that generally higher iodide concentrations were required to reach saturation in DMSO. This was traced back to the solvents' acceptor and dielectric properties.

Table 6.5: Comparison of solvent parameter for solvents relevant to this work[241,242,300,308–310]

Solvent	DN (donor number)	AN (acceptor number)	ε (dielectric constant)
DMSO	29.8	19.3	48.9
DMF	26.6	16.0	38.5
γ-GBL	18	17.3	39
H$_2$O	33	54.8	78.5
Pyridine	33.1	14.2	12.3
Acetonitrile	14.1	18.9	36
ethylenediamin	55	20.9	16

The donor-acceptor concept is a powerful empirically derived method when applied as it was meant to in terms of the given solute-solvent system and its interactions.[241,242,301,311] DMSO and DMF have pronounced donor properties but are not efficient acceptor solvents (Table 6.5), and the solvent's ability to stabilize anions by solvation has naturally a significant impact on the solution chemistry.[242,312,313] The interaction between DMF and DMSO and the large and polarizable iodide ion is the result of dispersion. The measure for the solvation of the iodide ion is given by the Gibbs energies of transfer from water to DMF as $\Delta\text{G}_t^0 = 20.4\,\text{kJmol}^{-1}$ and for DMSO $\Delta\text{G}_t^0 = 10.4\,\text{kJmol}^{-1}$, that shows the more efficient solvation strength for this ion by DMSO.[313–315] This is also the case regarding the AN and the dielectric constant ε of the two solvents (Table 6.5). The relative permittivity or dielectric constant is a measure for the solvent's dissociation strength of ionic compounds and is certainly influential but solely not capable to describe the PbI$_2$+I$^-$ system. Its effect is generally displayed in the interplay with the other two parameter, usually the AN, and became apparent in the δ^{133}Cs chemical shift trends, as well as in the solvent mixture experiments. The DN is a measure for the donor-acceptor interaction between a Lewis acid and base, therefore its effect will be displayed in the interaction between oxygen donor solvents such as DMSO and DMF and

the 'naked' Pb^{II} cation and can be studied best in solutions of Pb(ClO$_4$)[244] at chemical shift values shielded by $\Delta\delta^{207}$Pb > 2500 compared to the δ^{207}Pb range that encloses the solution chemistry of the PbI$_2$+I$^-$ system established in this work. It was shown by the chemical shift δ^{207}Pb that for Pb(NO$_3$)$_2$ in DMF and DMSO solution additional interactions must be considered (Section 6.2.12). If PbI$^+$ was included as Lewis acidic species, the range can be roughly estimated δ^{207}Pb(PbI$^+$) < -200. A more detailed discussion together with the solvent influence at lower concentrations was given in (Section 6.2.12). To provide a basic example, upon diluting a c(PbI$_2$) $= 0.8$ M solution in DMSO with ethylenediamine (*en*), which has a DN $= 55$, decoloring was observed and a highfield shift from δ^{207}Pb $= 117$ to δ^{207}Pb $= -460$. This was the only solvent of those listed in (Table 6.5) that would induce a high-field shift and additionally result in a clear solution without precipitate formation. The chelating effect of *en* will certainly have its contribution, nevertheless here the description of the solute-solvent (PbI$_2$+*en*) interaction by a single solvent property (DN) is sufficient, due to its comparable extra-ordinary high DN $= 55$ (Table 6.5). It has been only recently mentioned to take into account the solvents acceptor properties in the Pb-I system.[232] There are numerous examples of theoretical and experimental efforts to rationalize the solution chemistry of the Pb-I system by a single metric.[34–36,231]

It can already be seen in the crystal structures of the PbI$_2$ solvent adducts PbI$_2 \cdot$DMF[316] and PbI$_2 \cdot 2$DMSO[317] that the donor strength of the solvents is not sufficient to displace all iodide atoms in the coordination sphere of the Pb^{II} central atom. Whereas the increased efficiency of DMSO in coordination and solvation, compared to DMF, can be observed by the lattice degradation that proceeds up to a single octahedral strain in DMSO, whereas a dinuclear strain is present with DMF. Which can be considered a picture for the trade-off between the solvent's donor and acceptor properties.

6.4 Conclusion

The capabilities of ^{207}Pb-NMR spectroscopy as measurement technique in high concentration regime of perovskite precursor solutions was proven, which were difficult to access so far, by mapping the solution chemistry of the PbI$_2$+MAI and PbI$_2$+CsI system in two solvents DMSO and DMF within an affordable amount of time and effort. Thereby revealed the landmark solution conditions that are associated with structural transitions between different types of octahedral connectivity, with the PbI$_6$-moiety as building unit. The link between the lead halide perovskite related ssNMR shifts and the solution chemistry of the PbI$_2$+I$^-$ system was established. It is believed this can be the start to a powerful synergy between NMR spectroscopy and the solution processing and optimization process of device fabrication. Worth mentioning is hereby the recently presented benchtop low permanent-field magnet that provides a lab-scale spectrometer operating at lower frequency, that was applied in ^{1}H- and ^{207}Pb-NMR spectroscopic measurements.[318]

6.5 Additional Information and Details on the Multinuclear NMR Investigations

6.5.1 Comment on the Notation of Experimental Solution Compositions

The notation $c(\text{PbI}_2+\text{MAI}) = 0.8\,\text{M}$ describes a solution according to the experimental procedure $\text{PbI}_2+\text{MAI} \rightarrow$ 'MAPbI$_3$' that contains the starting materials in the concentrations $c(\text{PbI}_2) = 0.8\,\text{M}$ and $c(\text{MAI}) = 0.8\,\text{M}$, therefore $c(\text{'MAPbI}_3\text{'}) = c(\text{PbI}_2+\text{MAI}) = 0.8\,\text{M}$. The intention hereby was to avoid the notation 'MAPbI3' when describing the solution constituents. And for the titrations $c(\text{PbI}_2) = 0.4\,\text{M}+n\text{MAI}$, n is the equivalent of the $c(\text{PbI}_2)$ concentration, which was held constant throughout one experiment and R is in any case the precursor ratio [MAI]/[PbI$_2$]. For example, the titration point ($R = 1.5$) for $c(\text{PbI}_2) = 0.4\,\text{M}+n\text{MAI}$, describes a solution that contains $c(\text{PbI}_2) = 0.4\,\text{M}$ and $c(\text{MAI}) = 0.6\,\text{M}$. $c(\text{PbI}_2)_{\text{DMF}}$ describes the full range of experimental concentrations PbI$_2$(s.) dissolved in DMF. $c(\text{PbI}_2+\text{MAI})_{\text{DMF}}$ describes the experimental concentration range of 1 PbI$_2$ + 1 MAI in constant ratio ($R = 1$), which was analogously handled for DMSO. For practical reasons, to the large part individual solutions were prepared, by dissolving the corresponding amount of precursor for a given concentration. It was experimentally verified on several occasions to measure the same chemical shifts by solvent dilution of a given larger concentration. Therefore, it is adhered to the description as *dilution*, designating the nature of the experiment that is changing the concentration by keeping the ratio constant, as it is common practice in the literature. The data points from the dilution experiments were treated under fast-exchange conditions between two sites according to $\delta_{obs} = \Sigma\alpha_n\delta_n$ (For details see 6.5.6)).

6.5.2 Variable Temperature (VT) ^{207}Pb NMR Experiments

Variable Temperature (VT)-NMR experiments were performed at different concentrations $c(\text{PbI}_2)$ and $c(\text{PbI}_2+\text{MAI})$ and cation combinations. Also, on two [MAI]/[PbI$_2$] titration experiments, one was at $\delta^{207}\text{Pb}_{\text{final}}$ for $c(\text{PbI}_2) = 0.4\,\text{M}+n\text{MAI}$ in DMF, as the most deshielded value of all titrations. The second was $c(\text{PbI}_2) = 0.8\,\text{M}+n\text{MAI}$ in DMSO where the VT-NMR experiments were extended to the titration points at ($R = 1$), ($R = 1.5$) and ($R = 3.8$). Three different spectra were recorded in the temperature range between 298 K–328 K separated by 10 K steps. As general trend upon lowering and raising the solution temperature large broadening in $\Delta_{1/2}$ was observed (Tables B.2 and B.3). Regarding the temperature dependency of δ^{207}Pb, no specific effect on the magnitude of deshielding was observed from different solvents and precursor compositions. The accuracy of chemical shifts obtained by varying the temperature will depend on the amount of contribution from time-scale phenomena on the linewidths. These were not possible to be separated from contributions by different effects within the investigated temperature ranges. As large deviations are absent throughout the observed relation of $\Delta\delta = 7 - 9\,\text{ppm/K}$, for all systems a common origin of the temperature effect on δ^{207}Pb is assumed, being related mainly to dynamics between oligomeric species. It has been reported that elevated temperatures favor an increasing number of iodide bound to lead, based on UV-Vis and DFT methods,[221] this appears to be difficult to transferred to the higher concentration regime regarding the constant coordination number of 6 for the ^{207}Pb nuclei in the PbI$_6$-octahedra. The VT-unit was only available at a Bruker Avance 400 spectrometer operating at 400 MHz. The measurements at room temperature suffered already by the undesired effects of higher frequency on ^{207}Pb-nuclei and only limited information was

obtained by this otherwise useful approach. The effect of VT can largely be summarized as broadening at elevated and lower temperatures. For example, the T$_2$(^{207}Pb) scalar relaxation of the second kind is expected to decrease the linewidths at lower temperatures. Whereas the CSA mechanism has the effect of further broadening on the linewidths upon cooling. Increasing the temperature is expected to reduce the broadening caused by slow-tumbling. Depending on the coalescence temperature, exchange phenomena will display narrower linewidths at elevated temperatures.[243,244] Their individual contributions could not be resolved.

6.5.3 The $\Delta_{1/2}$(^{207}Pb) Linewidths

The linewidths of δ^{207}Pb resonances in the investigated Pb-I solution system span approximately a range from 400 Hz to 4000 Hz. Experimental parameter such as magnetic field homogeneity was minimized also by inspection of the shape and linewidths in the ^{1}H-NMR spectra, that were recorded in all cases. In ^{207}Pb-NMR spectroscopy several factors must be considered that may contribute to the observed linewidths, which can be difficult to separate.[243,244] These can be intrinsic spectroscopic properties as result of spin-dynamics and by interaction with nuclei in direct vicinity or solution dynamics, arising from the interplay between the timescale of the measurements in NMR and the exchange rate of the dynamic process in solution.[244,248] For ^{207}Pb nuclei in an anisotropic environment of reduced symmetry, that is lower than cubic symmetry, relaxation by CSA (chemical shift anisotropy) mechanism can cause severe line broadening as result of shorter relaxation. This effect is likely to be one of the main contributions already at a spectrometer frequency of B$_0$ = 300 MHz, since its effect is related to the spectrometer's magnetic field strength B$_0$ and increases in its effect by $\sim B_0^2$. When measuring at B$_0$ = 400 MHz the linewidths $\Delta_{1/2}$(^{207}Pb) were observed to be larger by one third to double the value compared to B$_0$ = 300 MHz. This originates mainly from the exchange broadening that is slowed down at higher spectrometer frequency, in combination with substantial contributions by CSA. The fast *quadrupolar relaxation* of the ^{127}I nuclei in vicinity will affect the ^{207}Pb nuclei by scalar relaxation of the second kind resulting in broadened lines. This relaxation mechanism, commonly too fast to be seen by ^{1}H- and ^{13}C nuclei, has a certain probability to be largely present in the broader linewidths $\Delta_{1/2}$(^{207}Pb). *Exchange broadening* was identified to account for $\Delta(\Delta_{1/2}) \sim 500 - 600$ Hz in the DMSO titrations (see main text and Tables B.7 to B.12). The remaining size of the linewidths, by magnitude $\Delta_{1/2}$(^{207}Pb) = 400–600 Hz, are comparable to those reported for Zintl ions Pb$_{12}^{2-}$ and cluster ions (Pb$_{10}$)$^{2-}$ which was attributed to *slow-tumbling*.[319] That is broadening of linewidths is related to molecular motion and the size of the oligomeric species. Exchange broadening is suspected to be the main reason for the enormous linewidths $\Delta_{1/2}$(^{207}Pb)= 1000 − 4000 MHz in the Pb(NO$_3$)$_2$ titration with MAI in DMSO and DMF (Tables B.15 and B.16).

6.5.4 Coordination Chemistry of Pb^{II} in DMSO and DMF and Lead Iodide Related Perovskite Compounds in the Solid-State

The coordination numbers adopted by lead in the oxidation state (+II) span from c.n. = 2 to 10, with a preference for the coordination numbers 4 and 6, which are observed within a variety of coordination environments.[29] A general classification is done between holo- and hemidirected complexes,[320] describing an even or unevenly distribution of electrons and ligands around the central lead atom. Whereas hemidirected is generally associated with a lower symmetry of

ligand arrangement and can be identified by their single-crystal structures as a void in the coordination sphere. At lower coordination numbers (c.n. $= 2$–5) Pb^{II} is found in hemidirected and for coordination numbers (c.n. $= 9$–10) in holodirected geometry, and in either one of them for coordination numbers in between. As different elements and types of ligands were observed to prefer certain geometries, these concepts become important when discussing possible structures e.g., when analyzing the structures in the CSD Livny et al.[320] pointed out that at least one lead-halogen bond Pb-X (X = Cl, Br, I) containing molecular complexes are almost exclusively found with c.n. $= 6$–8, and only in hemidirected coordination if there´s also a hard oxygen donor ligand present. From LAXS and EXAFS measurements in solution the Pb^{II}-ion was found to be six-coordinate in DMF and DMSO as $[Pb(DMF)_6]^{2+}$ and $[Pb(DMSO)_6]^{2+}$ with suggested hemidirected coordination, whereas for the DMSO complex this could not be determined unambiguously.[321] For the Pb^{II}-DMSO interaction coordination numbers between c.n. $= 6$–8 in holodirected geometry were reported in the solid state.[322] A direct Pb^{II}-DMF interaction was reported as the six-coordinate hemidirected $[Pb(DMF)_6]^{2+}$ unit, which was characterized together with a anionic network $[Pb_5I_{14}]^{4-}$ of face-sharing $[PbI_6]^{4-}$-octahedra in $[(Pr_3{}^n)_2(CH_2)_3][\{Pb(DMF)_6\}Pb_5I_{14}]\cdot DMF$.[289] Simultaneous coordination by DMF and iodide at the Pb^{II} central atom was reported from $[(Pr_3{}^n)_2(CH_2)_3][Pb_6I_{14}]\cdot 4\,DMF$, whereby edge-sharing octahedra of $[PbI_6]^{4-}$ and $[PbI_5(DMF)]^{3-}$ form one-dimensional coordination polymers.[289]

Lead(II) iodide solvent adducts $PbI_2\cdot DMF^{[316]}$ and $PbI_2\cdot 2\,DMSO^{[317]}$ form linear coordination polymers in the solid-state. The oxygen donor molecule occupy in $PbI_2\cdot DMF$ the peripheral axial positions in a 'double-chain' of two condensed PbI_6-octahedra sharing edges, and in $PbI_2\cdot 2\,DMSO$ both axial positions in the 'single-chain' of (*trans-*)edge-sharing condensed PbI_6-octahedra. The structural motif in $PbI_2\cdot DMSO$ is identical with $PbI_2\cdot DMF$,[283] the only difference is that the DMSO molecules occupy the coordination sites of DMF.

In the following summary the notation and structure descriptions are reported as in the corresponding reference, whereby it shall be mentioned that in the related literature varying notations and structure descriptions are often encountered for the same compound. One notable example is provided by the compounds $(CH_3NH_3)PbI_3\cdot DMF$ and $(MA)_2(DMF)_2Pb_2I_6$,[285,286] which are identical by structural motif, asymmetric unit and space group, with minor deviations in the unit cell metrics probably due to different measurement temperature. It can be summarized that in all below mentioned structures there is no bond between the central Pb^{II} atom and any oxygen donor molecule, as all structures are made up of octahedral PbI_6-units. Structures including the organic cation MA^+ and solvent molecules such as $(CH_3NH_3)PbI_3\cdot DMF$ and $(CH_3NH_3PbI_3)\cdot H_2O^{[285,323]}$ consist of double-chains of edge-sharing octahedra, whereby three PbI_6-units share one common corner. These are surrounded by $(CH_3NH_3)^+$ cations, which are strongly H-bonded to the oxygen atom of the DMF molecules. The observed metastability in terms of loss of the H_2O is deduced back to the weaker H-bond between H_2O and MA^+ in comparison with DMF attributed to the longer distance d(N-O) between nitrogen of MA^+ and the oxygen atom. The crystalline compound $(CH_3NH_3)PbI_3\cdot DMF$ was reported to have a 30 % higher solubility in DMSO, compared to a 1:1 mixture of MAI + PbI_2 that was explained by the exchange of DMF for DMSO.[306] The incorporation of more water and organic cations MA^+ into the lattice as observed in $(CH_3NH_3)_4PbI_6\cdot 2\,H_2O^{[323]}$ resulted in the formation of isolated $[PbI_6]^{4-}$ octahedra. In addition to the strong hydrogen bonding between MA^+ and H_2O, weaker interactions of the type N-H$\cdots$I and O-H$\cdots$I

between iodide and hydrogen were reported. The ribbon-like chains of edge-sharing PbI$_6$-octahedra, which were formulated as $\{(Pb_3I_8)_n\}^{2n-}$ and described as "I$^-$-terminated fragments of PbI$_2$(s.)"[284] were crystallized from the corresponding solvents as (MA)$_2$(*solvent*)$_2$Pb$_3$I$_8$ (solvent = DMSO,[282–284] DMF[286] and γ-GBL.[294]) The $\{(Pb_2I_6)_n\}^{2n-}$ double-chains of edge-sharing PbI$_6$-octahedra in (MA)$_2$(DMF)$_2$Pb$_2$I$_6$[286] and the cluster ion in [Pb$_8$I$_{44}$]$^{8-}$ (MA)$_8$(GBL)$_x$Pb$_8$I$_{44}$[294] also represent sections from the layers as present in PbI$_2$(s.). In (MA)$_3$(DMF)PbI$_5$[286] and (MA)$_3$(DMSO)PbI$_5$[284] a linear coordination polymer of trans single-corner sharing PbI$_6$-octahedra is present.

6.5.5 Solid State NMR (ssNMR) Spectroscopy of Lead Iodide Related Perovskite Compounds

The relation between coordination environment and chemical shift is not straightforward in ^{207}Pb-NMR spec-spectroscopy. For example earlier reports investigating the trend in chemical shifts PbX$_2$ (X = F, Cl, Br, I) came to the result that beyond the first coordination sphere a larger picture of the structure has to be taken into account for the explanation of the observed chemical shifts in the solid-state.[249,324] In another approach the isotropic shifts were calculated for different [PbI$_6$]$^{4-}$-cluster of PbI$_2$ polymorphs with reported crystal structures.[325] The results indicate a relation between larger average bond length d(Pb-I) and more deshielded resonance of calculated values $\delta_{iso}(^{207}\text{Pb})$, which span a range from $\delta_{iso}(^{207}\text{Pb}) = 780.3$ to 62.4.

Table 6.6: Reported isotropic shifts $\delta_{iso}(^{207}\text{Pb})$ of PbI$_2$, MAI and CsI related compounds.

	$\delta_{iso}(^{207}\text{Pb})$	$\delta_{iso}(^{133}\text{Cs})$
PbI$_2$	$-31.1(10)^{[261]\,a)}$, $-29.1^{[262]\,b)}$, $-25^{[263]\,c)}$	
MAPbI$_3$	$1423^{[257]\,d)}$, $1430^{[254]\,e)}$, $1448^{[255]f)}$, $1482(10)^{[256]\,g)}$	
GA$_2$PbI$_4$	$1515^{[260]\;h)}$	
δ-CsPbI$_3$	$1065(15)^{[258]\,i)}$, $1160^{[264]j)}$	$240^{[265]\,k)}$, $247.0^{[258]\,l)}$
γ-CsPbI$_3$	$1265(20)^{[258]\,m)}$	$166.9^{[258]\,l)}$

$^{a)}$ $\delta_{iso}=-15.1$ with spinning. Ref. to Pb(CH$_3$)$_4$, by secondary standard Pb(NO$_3$)$_2$.
$^{b)}$ Ref. to Pb(CH$_3$)$_4$, by secondary standard Pb(NO$_3$)$_2$ $\delta_{iso} = -2961$.
$^{c)}$ Ref. to Pb(CH$_3$)$_4$, with c(Pb(NO$_3$)$_2$ (aq)) = 0.5 M (δ_{iso} =−2941).
$^{d)}$ Ref. to Pb(NO$_3$)$_2$, $\delta = -3490$, 22 °C as an external standard.
$^{e)}$ Ref. to Pb(NO$_3$)$_2$, without further info.MAS (14 T): 1470, −404, −600.
$^{f)}$ Ref. to a citation[326] Pb(CH$_3$)$_4$, benzene-d$_6$.
$^{g)}$ Measured at T = 335 K, ref. to Pb(CH$_3$)$_4$, $\delta_{iso} = 0$ by stationary Pb(NO$_3$)$_2$ set to $\delta_{iso} = -3491.6$ at T = 294 K.
$^{h)}$ Ref. to Pb(CH$_3$)$_4$.
$^{i)}$ Ref. to Pb(CH$_3$)$_4$, with solid MAPbCl$_3$ at T = 293 K $\delta = -647.5$.
$^{j)}$ MAS at 20 kHz, r.t., ref. to Pb(CH$_3$)$_4$.
$^{k)}$ Ref. to 1 M CsCl(aq.) with solid CsI δ^{133}Cs = 271.05.
$^{l)}$ Reported as peak maximum δ_{CS}, without further info on ^{133}Cs referencing.
$^{m)}$ Reported as peak maximum δ_{CS}.

The solid-state chemical shift of γ-CsPbI$_3$ $\delta_{CS}(^{207}\text{Pb}) = 1265$, was reported as peak maxima due to large linewidths.[258] In view of the final values $\delta^{207}\text{Pb}_{final} = 1201$ and 1251 were uniquely reached with CsI, and the relation to solution parameter evaluated in the text, it is regarded as reasonable to include the reported peak maxima $\delta_{CS}(^{207}\text{Pb})$ as reference for a qualitative discussion of chemical shift ranges. The effects of in Pb-I bond polarization or distortion in bond angles of the octahedral ligand arrangement around the Pb^{II} central atom,

can be estimated by comparing the solid-state structures to reported $\delta_{\mathrm{iso}}(^{207}\mathrm{Pb})$ chemical shifts, e.g.,MAPbI$_3$[253] $\delta_{\mathrm{iso}}(^{207}\mathrm{Pb}) = 1423 - 1482$[254–257]) to γ-CsPbI$_3$ with $\delta_{\mathrm{iso}}(^{207}\mathrm{Pb}) = 1265$ on one side, on the other side to GA$_2$PbI$_4$ $\delta_{\mathrm{iso}}(^{207}\mathrm{Pb}) = 1515$,[260] that is octahedral tilting within a 3D network and reducing its dimensionality to a 2D network of corner-sharing (PbI$_6$)-octahedra. This is not separable from the cation influence, and in solution the effects by solvation must be considered additionally.

6.5.6 Fit Procedure for the Dilution Experiments

The data from the dilution experiments was treated under fast-exchange conditions between two sites according to $2\,\mathrm{A}_n \rightleftharpoons (\mathrm{A}_2)_n$ (eq.S1) Regarding the fact that the chemical shift $\delta^{207}\mathrm{Pb}$ of the Pb-I solution system in DMF and DMSO is temperature and concentration dependent throughout in solution and given the presence of polynuclear species, these fits are limited to a general discussion about the nature of the observed concentration dependence in the chemical shifts $\delta^{207}\mathrm{Pb}$. The generalized model described by (eq.S1), was applied without further specification of any kind on the species A_n as this was thought to be the appropriate frame, for a general discussion in the background of a constant coordination number of c.n. $= 6$ and octahedral ligand arrangement around the Pb$^{\mathrm{II}}$ central atom. Under fast-exchange conditions the observed chemical shift δ_{obs} is the weighted (x_n) average of individual resonances (δ_n) of all species in the given equilibria: $\delta_{obs} = \Sigma\alpha_n\delta_n$ (eq.S2) The observed resonance is therefore the population weighted average of all exchanging species. (α_n= the dissociation fraction of the n-th species with limiting shift value δ_n, δ_{obs} = observed chemical shift), which in case of a generalized monomer and dimer equilibrium is simplified to $\delta_{obs} = \alpha_m\delta_m + \alpha_d\delta_d$ (eq.S3). Whereby x_n can be expressed as either the mole fraction χ_n of reactants, or as the dissociation fraction α_n of the solutes.[237,278,327,328] Since the fast-exchange approach requires the investigated system to be under fast-exchange conditions throughout the whole titration and dilution range, the influence of intermediate-exchange on the signal positions was not possible to quantify and was estimated to be not too severe. In this context, however one main issue was that any point in the investigated Pb-I system to be part of an equilibrium itself, thus concentration and temperature dependent. The parameters determined as result of the fitting procedures δ_i and K can be used as an orientation value, and allows at least the assessment of, i.e., weak or strong association. The fit function for the single equilibrium were implemented in the non-linear curve fitting tool of the OriginPro 8.6 software. The fit procedure included simultaneous determination of three parameters (K$_i$, δ_m, δ_d) by the least-square refinement method minimizing the sum of squares as $\Sigma(\delta_{obs} - \delta_{fit})^2$ between experimental and calculated chemical shifts $\delta^{207}\mathrm{Pb}$.

The monomer-dimer equilibrium based on dimerization of two not further specified monomeric units A_n in their equilibrium concentrations $[\mathrm{A}_n]$ and $[(\mathrm{A}_2)_n]$, and $[\mathrm{A}]_0$ as the experimental total concentration, the relevant equations are:

$$2\,\mathrm{A}_n \rightleftharpoons (\mathrm{A}_2)_n \qquad\qquad (\mathrm{eq.S1})$$

$$\mathrm{K}_D = [(\mathrm{A}_2)_n]/[\mathrm{A}_n]^2 \qquad\qquad (\mathrm{eq.S1a})$$

$$[\mathrm{A}]_0 = [\mathrm{A}_n] + 2[(\mathrm{A}_2)_n] \qquad\qquad (\mathrm{eq.S1b})$$

and the observed chemical shift δ_{obs} in terms of the dissociation fraction $\alpha = [A]/[A]_0$:

$$\delta_{\mathrm{obs}} = \alpha_m\delta_m + \alpha_d\delta_d \qquad\qquad (\mathrm{eq.S3})$$

Table 6.7: Extracted parameter from the fit procedure.

	K$_D$	$\delta_m{}^{a)}$	$\delta_d{}^{a)}$
DMF			
c(MAI+PbI$_2$) ($R=1$)	$0.7 \pm 21\,\%$	2476 ± 37	850 ± 97
c(PbI$_2$)	$0.3 \pm 40\,\%$	1343 ± 26	-227 ± 321
DMSO			
c(MAI+PbI$_2$) ($R=1$)$^{b)}$	$4.8 \pm 11\,\%$	-1028 ± 85	1622 ± 16
c(PbI$_2$)	$6.0 \pm 16\,\%$	-1029 ± 60	538 ± 17

$^{a)}$ Error margin for chemical shifts are given in absolute values
$^{b)}$ Only data points $0.2\,\mathrm{M} \leq c(\mathrm{MAI+PbI_2}) \leq 1.2\,\mathrm{M}$ were included
in the fit procedure

With δ_m = the chemical shift of the monomer in solution, and δ_d = the chemical shift of the dimer at full saturation in solution, the resulting fir function that relates the observed chemical shift (δ_obs), the experimental ($[A]_0$) and equilibrium concentrations($[A_n]$,$[(A_2)_n]$) is obtained as:

$$\delta_\mathrm{obs}=\delta_m + (\delta_m\text{-}\delta_d)\left(\frac{1 + 4K_D[A]_0 - (1 + 4K_D[A]_0)^2}{4K_D[A]_0}\right) \tag{eq.S4}$$

7 Summary

PART I   In the first part the synthesis of main-group chalcogenide materials Bi_2S_3, SnS and PbS via CVD in preferred oriented growth by applying the single-source precursor molecules $Bi(SBu^t)_3$ (**1a**), $[Sn(SBu^t)(tfb\text{-}dmeda)]$ (**2a**) and $Pb(SPr^i)_2$ (**3b**) was described. The precursor molecules contained the pre-formed element-sulfur bond (Bi-S, Sn-S and Pb-S) as building blocks for the later material in combination with alkyl moieties of low-molecular weight likely to result in highly volatile fragments, thereby minimizing possible contamination of the later material. Whereas, elemental bismuth was obtained by CVD of $Bi(SPr^i)_3$ (**1b**). Prior to the synthesis of Bi^{III}, Sn^{II} and Pb^{II} thiolates the synthesis procedures of the corresponding silylamido complexes were optimized in order to remove the lithium containing species, this contamination issue was previously not noticed and addressed.

Bi_2S_3 was deposited from $Bi(SBu^t)_3$ (**1a**) on FTO, and in preferred oriented growth on the substrates: Si, SiO_2/Si and glass, as inferred from detailed analysis of the XRD patterns. These 2D Bi_2S_3 platelets were of uniform size and morphology as observed by the SEM images. The crystalline nature of Bi_2S_3 obtained on Si at 250 °C was shown by HR-TEM measurements. The photoresponse properties of Bi_2S_3 on Si at 300 °C demonstrated the application potential. The solid-state structure of (**1a**) was elucidated by single-crystal X-Ray crystallography, as the first reported of a Bi^{III} alkylthiolate. The synthesis, characterization and application for CVD of $Bi(SPr^i)_3$ (**1b**) as well as bismuth mesocrystal formation and morphology was previously not reported by any different method. The formation of Bi_2S_3 and Bi as single phase by (**1a**) and (**1b**) respectively was confirmed by TG-DTA, XRD and XPS, and additionally was Bi_2S_3 obtained by CVD of (**1a**) analyzed by HR-TEM, EDX and 2D-SEM-Raman. The origin of the fundamentally different decomposition results was traced back to different 'S-C' bond strengths present in the molecules (**1a**) and (**1b**) by DFT calculations. This was in accordance to the experimental EI-MS fragmentation patterns showing the preferential cleavage of the 'S-C' bond in (**1a**) and 'Bi-S' bond in (**1b**). The molecules (**1a**) and (**1b**) were further characterized by ^{13}C- and ^{1}H-NMR spectroscopy and elemental analysis (CHS).

$[Sn(SBu^t)(tfb\text{-}dmeda)]$ (**2a**) was reported the first time, and was introduced as single-source precursor for the reason homoleptic Sn^{II} alkylthiolates $Sn(SR)_2$ ($R = -Pr^i$, $-Bu^i$ and $-Bu^t$) could not be successfully applied as CVD precursors. The heteroleptic compound (**2a**) was shown by EI-MS to fragment into a tin-alkylthiolate species $[Sn-(SR)_n{}^+]$ ($n = 1-4$), departing from the organic auxiliary $(tfb\text{-}dmeda)^-$ ligand moiety, and was described to act as 'launch-vehicle' bringing the tin-alkylthiolate moiety into the gas phase. The thermal decomposition profile of (**2a**) was established by TG-DTA analysis. SnS was deposited by CVD of $[Sn(SBu^t)(tfb\text{-}dmeda)]$ (**2a**) in preferred oriented growth on FTO (250 °C). A linear relationship between layer thickness and deposition time in the CVD of SnS was established on Mo-SLG substrate, which was selected in view of possible future application for reasons of suitable band alignment between SnS and Mo. The structures of (**2a**), $[Sn(SPr^i)_2]_n$ (**2b**) and $[Sn(SBu^i)_2]_n$ (**2c**) were elucidated by single-crystal X-Ray crystallography and elemental analysis (CHS). (**2a**) was shown to remain monomeric in solution as in the solid state. The

investigation on (**2a**) by variable temperature ^{119}Sn$\{^1$H$\}$- and ^{1}H-NMR revealed the fluxional dynamics involving the $(-\text{NMe}_2)$-moiety of the organic framework in (**2a**). The solution structure of (**2a**) was investigated by 1D ^{119}Sn$\{^1$H$\}$-, ^{19}F-, ^{13}C-APT-, and ^{1}H-NMR, 2D ^{119}Sn, ^{1}H-HMBC, ^{13}C, ^{1}H-HMQC and -HMBC experiments at room temperature.

PbS was deposited by CVD of Pb(SPr^i)$_2$ (**3b**), as first report of a Pb^{II} alkylthiolate single-source precursor for CVD, on Si (325 °C) in preferred oriented growth as nanometer sized cubes in uniform morphology and size. This was inferred from the SEM top-view images in correspondence with the powder XRD pattern. The thermal decomposition profile of Pb(SBu^t)$_2$ (**3a**), Pb(SPr^i)$_2$ (**3b**) and Pb(SBu^i)$_2$ (**3c**), each forming phase pure PbS, was established by TG-DTA analysis. The EI-MS analysis revealed (**3b**) to exist as monomeric and (**3c**) as mono- and dimeric species in the gas phase. As the first reported structural characterization of Pb^{II} alkylthiolates, single-crystal X-Ray crystallography revealed (**3a**) to be trimeric [Pb$_3(\mu$-SBu$^t)_6$] in the solid-state and the linear coordination polymer present in (**3c**) to consist of pentameric [Pb$_5(\mu$-SBu$^i)_4$(SBu$^i)_6$]-units. The δ^{207}Pb chemical shifts of (**3a**) and (**3c**) were determined first time in this work, and showed (**3c**) is three-coordinate also in solution, and pointed for (**3a**) towards a trimeric [Pb$_3(\mu$-SBu$^t)_6$] solution structure undergoing rapid inter-site exchange between the different Pb^{II} coordination sites. Further analysis of (**3a**) and (**3c**) included ^{13}C- and ^{1}H-NMR spectroscopy, elemental analysis (CHS) and EI-MS only in case of (**3c**). (**3b**) was characterized by ^{13}C and ^{1}H-NMR spectroscopy, EI-MS and elemental analysis (CHS). Additionally, were the structures of Pb^{II} oxygen thiolate cluster [Pb$_{12}$O$_6$(SPr$^i)_{12} \cdot$ C$_6$H$_6$] (**3d**) and [Pb$_{12}$O$_6$(SBu$^t)_{12}$] $\cdot$ 6 (NC$_5$H$_5$) (**3e**) elucidated by single-crystal X-Ray crystallography.

PART II The second part described the investigations on the PbI$_2$+MAI and PbI$_2$+CsI solution species in DMSO and DMF by means of multinuclear NMR, which was accomplished by performing and interpreting ^{207}Pb-,^{133}Cs and ^{1}H-NMR titration and dilution experiments. The investigations were mainly focused on higher solute concentrations $c_{\text{solute}} \geq 0.4$ M. It was shown that the stoichiometric relation in the solid state compounds' sum formula e.g., CsPbI$_3$ and MAPbI$_3$ is translated into DMSO and DMF solution as concentration and precursor ratio ($R = [AI]/[\text{PbI}_2]$) dependent equilibrium partitioning between condensed PbI$_6$-octahedra (e.g., edge- vs. corner-sharing) of different size and varying degrees of condensation (e.g., 3D all corner-sharing (PbI$_3)_n^-$ vs. 1D single corner-sharing (PbI$_5)_n^{3-}$). The coordination number of the Pb^{II} central atom remained constant (c.n. $= 6$) within octahedral geometry for any solute concentration ($c_{\text{solute}} \geq 0.4$ M) and precursor ratio R.

The disproportionation of PbI$_2$ in DMSO and DMF according to $2\,$PbI$_2 \rightleftharpoons$ PbI$^+$ + PbI$_3^-$ (eq.7) was derived and rationalized in combination with the solvents donor (DN) and acceptor (AN) properties, the c(PbI$_2$) concentration dependent δ^{207}Pb trends and corresponding chemical shift ranges in both solvents DMSO and DMF. When PbI$_2$ was dissolved in DMF, the δ^{207}Pb values indicated the dominant presence of anionic solution species, related to the constitution (PbI$_3)_n^-$. The δ^{207}Pb chemical shift range and its trend, observed from dissolving PbI$_2$ in DMSO, indicated at higher solute concentrations neutral species (PbI$_2)_n$ and towards lower concentrations cationic species (PbI)$_n^+$. This was interpreted such as the DMF solvent's reduced iodide solvating strength, when compared to DMSO, was offset in solution by forming (PbI$_3)_n^-$. Whereas the higher donor strength of DMSO was considered influential in stabilizing the cationic (PbI)$_n^+$ species, which was assumed to be present by extrapolating the δ^{207}Pb trend towards very low concentrations.

The δ^{133}Cs trends were consistent with $(\text{Cs}^+\cdots\text{I}^-)$ *contact-ion pair* formation in DMF and the presence of *solvent-separated* Cs^+ and I^- in DMSO. Thus, were the primary solute-solvent interaction not of coordinative nature between Cs^+ and the donor solvent molecules, instead governed by the interplay between the solvent's dielectric and acceptor properties.

Increasing the iodide concentration as $c(A\text{I})$ in the ratio $[A\text{I}]/[\text{PbI}_2]$ $(A^+ = \text{CH}_3\text{NH}_3{}^+, \text{Cs}^+)$ was displayed by a downfield trend in both solvents DMSO and DMF and was associated with changes in the type of octahedral condensation from edge- towards corner-sharing PbI_6-octahedra. For PbI_2 dissolved in DMF the addition of iodide $(R > 0)$ combined this transition with the fragmentation into smaller units. The chemical shift regions associated with the perovskite type of 3D corner-sharing octahedra as present in the solid state (e.g., γ-CsPbI$_3$ and MAPbI$_3$) was only reached in DMSO and when the iodide source was introduced in $(R > 1)$ excess to PbI_2.

Increasing the solute concentrations of PbI_2 or $\text{PbI}_2 + A\text{I}$ in constant ratio $(R = 1)$ was displayed by a δ^{207}Pb downfield trend in DMSO, and associated with increasing the amount of terminal iodide vs. bridging iodide atoms, dominantly within the realm of edge-sharing condensed PbI_6-octahedra. Whereas the same experimental procedure was displayed by a δ^{207}Pb highfield trend in DMF, and associated with the aggregation of smaller units to a larger assembly. The neighboring, yet largely non-overlapping chemical shift regions attained by the solutes in the two solvents, showed in DMSO a tendency for the presence of higher dimensional structures (e.g., 3D and 2D corner-sharing PbI_6-octahedra), when compared to DMF (e.g., 1D corner-sharing PbI_6-octahedra).

The link between solution and solid-state NMR was established by relating the chemical shifts $\delta_{\text{CS}}(^{207}\text{Pb})$ and $\delta_{\text{iso}}(^{207}\text{Pb})$ of the parent compounds γ-CsPbI$_3$ and MAPbI$_3$ respectively to (i) the titration endpoints in DMSO and (ii) by an effect displayed on NMR time-scale:

(i) These were identified as such by an invariant chemical shift $\delta^{207}\text{Pb}_{\text{final}}$, combined with the final concentrations $c_{\text{final}}(\text{MAI}) = 3.0\,\text{M}$, $c_{\text{final}}(\text{CsI}) = 1.9\,\text{M}$, the $\frac{1}{2}c(\text{PbI}_2) \to 2R$ relation $(R = [A\text{I}]/[\text{PbI}_2])$ within c_{final} and the exchange broadening trend in the linewidths $\Delta_{1/2}(^{207}\text{Pb})$. The MAI titration in DMSO showed continuously increasing linewidths $\Delta_{1/2}(^{1}\text{H})$ and highfield trend δ^{1}H, in relation to $\delta^{207}\text{Pb}_{\text{final}}$.

(ii) This was displayed as onset of a transition from fast- towards slow- and intermediate-exchange as emerging signal splitting simultaneously in the resonances δ^{133}Cs and δ^{207}Pb in close relation to reported values $\delta_{\text{iso}}(^{207}\text{Pb})$ of δ-CsPbI$_3$ and $\delta_{\text{CS}}(^{207}\text{Pb})$ of γ-CsPbI$_3$.

8 Outlook

8.1 Further Application Potential of the Molecular Precursor

Implementation of the CVD results For Bi_2S_3, SnS and PbS obtained by CVD further investigation on various substrates and deposition parameter in view of the application potential by implementation in a photovoltaic device architecture e.g., by deposition of Bi_2S_3 on TiO_2, CdS, MoO_3, can be the next step. The subsequent or simultaneous deposition of PbS and Bi_2S_3 would already provide a viable p-n hetero-junction in this sense. The Bi_2S_3 platelets are interesting to investigate in terms of their high surface area for e.g., catalytic oxygen evolution reaction (OER) and photoelectrochemical conversion (PEC). The potential of Pb^{II} alkylthiolates (**3a**)-(**3c**) as single-source precursor for the synthesis of PbS nanoparticles and quantum dots by microwave-assisted decomposition may be further explored. The microwave-assisted approach may provide an alternative to hot-injection methods, since preliminary results confirmed the possibility to hereby synthesize PbS within few minutes.

The Synthesis of Bi_2Te_3 The microwave-assisted decomposition of $Bi(SPr^i)_3$ (**1b**) and $Te(SPr^i)_2$ in (*N*-Methyl-2-pyrrolidone) NMP according to reaction (8.1) resulted in the formation single crystalline Bi_2Te_3, which is interesting as topological insulator and also a efficient thermoelectric material.

$$2\,Bi(SPr^i)_3 + 3\,Te(SPr^i)_2 \xrightarrow[-5SC_3H_7]{100\ W,\ 5\ min,\ NMP} Bi_2Te_3 \tag{8.1}$$
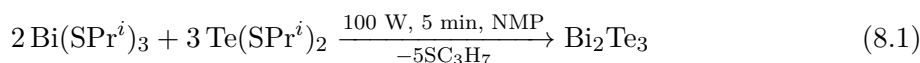
The XRD pattern, HR-TEM image and SAED pattern of as obtained Bi_2Te_3 is presented
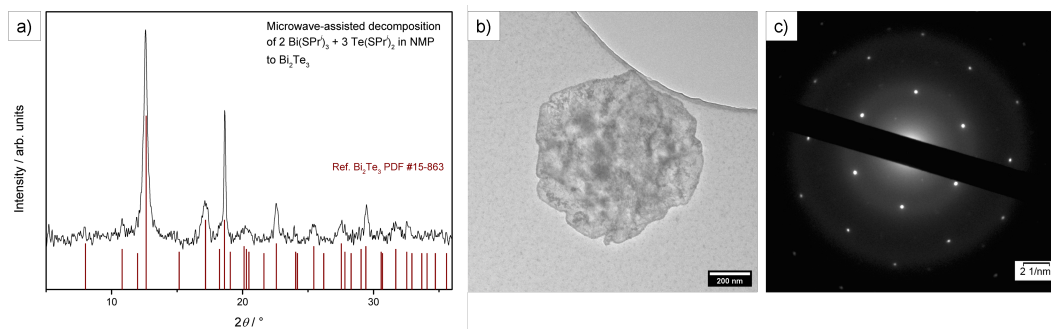
Figure 8.1: a) XRD pattern of Bi_2Te_3 obtained by the reaction of 2 $Bi(SPr^i)_3$ + 3 $Te(SPr^i)_2$ in NMP. Referenced to Bi_2Te_3 PDF #15-863 b) TEM image of Bi_2Te_3 and c) the corresponding SAED pattern.

in (Figure 8.1). This route maybe extended to Bi_2Se_3 and related $Bi_2Te_{3-x}S_x$, $Bi_2Se_{3-x}S_x$ solid solutions. Interesting to note that the microwave-assisted decomposition of $Bi(SPr^i)_3$ (**1b**) resulted in the formation of elemental bismuth whereas $Bi(SBu^t)_3$ (**1a**) yielded Bi_2S_3, in contrast to bismuth formation by both molecules (**1a**) and (**1b**) when exposed to daylight.

The analogous decomposition of $Te(SPr^i)_2$ in NMP yielded elemental tellurium. The suggested reaction path (8.1) was also connected to the idea the $(SPr^i)^-$ ligand moiety would possibly bind onto the surface of nanoparticles to limit the growth and for stabilization. Yet, at this stage was the fate of the $(SPr^i)^-$ ligand molecules not further pursued analytically.

8.2 Investigations on the Molecular Chemistry

Heteroleptic silylamido-thiolato complexes   The molecular chemistry of the lead and bismuth silylamido complexes $Pb[N(SiMe_3)_2]_2$ and $Bi[N(SiMe_3)_2]_3$ were investigated in ligand exchange reactions with sub-stoichiometric equivalents of $tert-$butylthiol $n\,HSBu^t$. When isolated and characterized, one of the goals was to introduce Se- or Te-donor atoms containing ligand moieties at the corresponding central atom. First results of ^{1}H-NMR spectroscopy showed strong indications for partial substitution of $\{N(SiMe_3)_2\}^-$ for $(SBu^t)^-$ when $Pb[N(SiMe_3)_2]_2$ was investigated (Figure 8.2a). Whereas attempting the same ligand exchange reaction with $Bi[N(SiMe_3)_2]_3$ there were no signs of partial substitution ($n = 1, 2$) present in the ^{1}-H NMR spectra as shown in (Figure 8.2b), by which full substitution by $(SBu^t)^-$ in the Bi^{III} coordination sphere in ratio of the applied ligand equivalent may be assumed. This was supported by weighing the reaction product and comparing with the calculated yields. There were also no hints on a $Bi\{N(SiMe_3)_2\}_{3-n}(SBu^t)_n$ solution species from VT-NMR experiments ($-30\,°C$) of the reaction scheme in (8.3), which is not shown here. For the proposed reaction course in (8.2) further support was obtained from the chemical shift $\delta^{207}Pb = 2808$. The final interpretation of this $\delta^{207}Pb$ value and determination of substitution degree is connected with the question whether (**3a**) retains the trimeric structure $[Pb_3(\mu\text{-}SBu^t)_6]$ of the solid-state in solution, and requires further studies.

$$1\,Pb[N(SiMe_3)_2]_2 + 1\,HSR \xrightarrow[-1\,HN(SiMe_3)_2]{\text{diethyl ether, } -28\,°C} [Pb\{N(SiMe_3)_2\}_x(SBu^t)_y] \tag{8.2}$$

$$1\,Bi[N(SiMe_3)_2]_3 + n\,HSBu^t \xrightarrow[-3n\,HN(SiMe_3)_2]{\text{THF, } -28 \text{ to } 25\,°C} (1-\tfrac{n}{3})\,Bi[N(SiMe_3)_2]_3 + \tfrac{n}{3}\,Bi(SBu^t)_3 \tag{8.3}$$
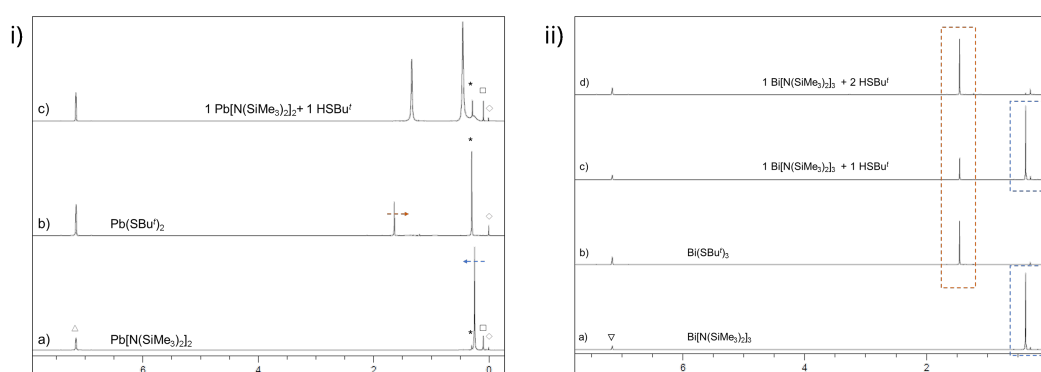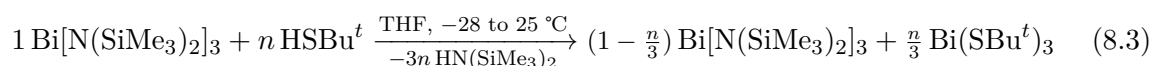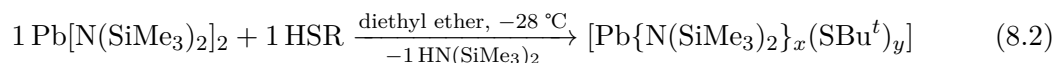
Figure 8.2: Stacked plot comparing the ^{1}H-NMR spectra of the starting molecules recorded in C_6D_6 according to the proposed reaction course i) in (8.2) ii) in (8.3)

Following the results from (Chapter 3) and the calculated difference in bond polarities and strengths, this approach may be extended to varying the alkylthiolates to investigate the possibility of synthesizing $Bi\{N(SiMe_3)_2\}_{3-n}(SR)_n$ with $R = -Pr^i$ and $-Bu^i$.

Heterobimetallic thiolato complexes   The synthesis of heterobimetallic thiolato complexes of (earth-)alkali metals with bismuth was investigated by the reaction of $\text{Bi}(\text{SBu}^t)_3$ with alkali metal thiolates $A(\text{SBu}^t)$ ($A^+ = \text{Li}^+$, Na^+, K^+) (8.4) and (earth-)alkali metals (Li, Na, K, Mg) (8.5). These were especially interesting for the color change from yellow to reddish-orange ($A^+ = \text{Li}^+$, Na^+, K^+) or (Li, Na, Mg) and to red-violet when ($A^+ = \text{K}^+$) or K (Figure 8.3).

$$\text{Bi}(\text{SBu}^t)_3 + A(\text{SBu}^t) \xrightarrow{\text{solvent, } -28 \text{ to } 50\,°\text{C}} \qquad (8.4)$$
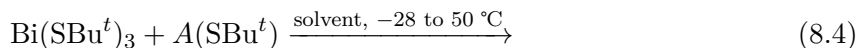
The reason for the observed color remains elusive at this stage, as well as whether and to which degree there´s a 'similarity', when reacting $\text{Bi}(\text{SBu}^t)_3$ (**1a**) with their ions according to (8.4) or with the neat metals according to (8.5):

$$\text{Bi}(\text{SBu}^t)_3 + M \xrightarrow{\text{solvent, } -28\,°\text{C to r.t.}} \qquad (8.5)$$
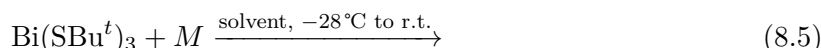
whereas $M = $ Li, Na, K, Mg. It may be worth mentioning that, apart from the herein described examples, virtually all metal-alkylthiolates presented in this work, as well as various combinations of these in all kind of solvents had the same indistinguishable yellow solution color. Preliminary results from UV-Vis spectroscopy of the reaction mixtures in (Figure 8.3) displayed broad absorption bands shifted to higher wavelengths than observed for the starting molecules. The focus was mainly on investigating the reaction $\text{Bi}(\text{SBu}^t)_3$ (**1a**) with $\text{K}(\text{SBu}^t)$ or K, not only for the distinguished and mesmerizing red-violet solution color, yet also having in mind the only reported heterobimetallic alkoxide of bismuth was obtained from the reaction of $\text{Bi}(\text{OBu}^t)_3$ with $\text{K}(\text{OBu}^t)$. Recalling the structural similarity between $\text{Bi}(\text{OBu}^t)_3$ and $\text{Bi}(\text{SBu}^t)_3$ (**1a**) (Chapter 3), it appears difficult to include $\text{K}(\text{SBu}^t)$ into the discussion, since the structure was not reported and not possible to be determined in this work. In view of the (empirically) remarkable lower solubility of $\text{K}(\text{SBu}^t)$ in common organic solvents, when compared to $\text{K}(\text{OBu}^t)$, a tendency towards a polymeric structure was assumed, which is not further evaluated here.

The reactions according to (8.4) and (8.5) were performed in various solvents e.g., THF, pyridine and benzene and in varying stoichiometric relations.
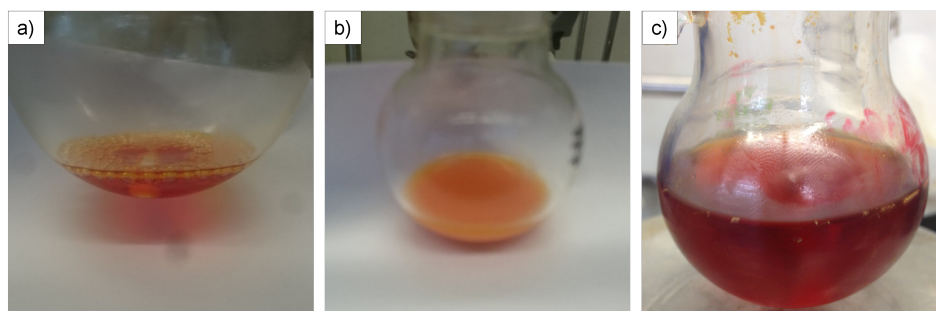
Figure 8.3: Color of the reaction mixtures in THF: a) $\text{Bi}(\text{SBu}^t)_3 + \text{Li}(\text{SBu}^t)$ b) $\text{Bi}(\text{SBu}^t)_3 + \text{Na}(\text{SBu}^t)$ c) $\text{Bi}(\text{SBu}^t)_3 + \text{K}(\text{SBu}^t)$

In these cases ^{1}H-NMR spectroscopy showed noticeable broadened signals at chemical shift values different than those observed from the starting molecules, which were finally of low diagnostic value apart from indicating dynamic exchange. One main focus was put on crystallization of possible reaction products at (freezer) temperatures lower ($< -15\,°\text{C}$), at which the corresponding orange to red color of the reaction mixtures did not change for at least

several weeks to months. At room temperature these turned soon into colorless, accompanied by formation of a black precipitate (Bi↓), which was complete within hours and latest one day. The time span the color remained unchanged, i.e., the time span before a precipitate became visible varied depending on solvent and initial stoichiometry e.g., was the red color of the reaction (8.4) observed to persist in refluxing benzene for several minutes. When reacting $Pb(SBu^t)_2$ according to following reaction scheme:

$$Pb(SBu^t)_2 + K(SBu^t) \xrightarrow{\text{solvent, } -28 \text{ to } 60\text{ °C}} \text{no color change} \tag{8.6}$$
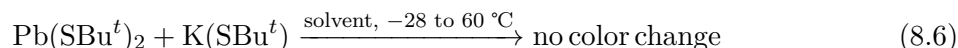
the color of the reaction mixture remained yellow and no changes were indicated in the ^{1}H-NMR spectra.

When attempting to react $Bi(SBu^t)_3 + Pb(SBu^t)$, there were no signs of a reaction comparing the ^{13}C- and ^{1}H-NMR spectra of the individual metal thiolates.

$$Bi[N(SiMe_3)_2]_3 + Pb[N(SiMe_3)_2]_2 \xrightarrow[-5 \, HN(SiMe_3)_2]{5 \, HSR, \, -28\text{ °C}} \tag{8.7}$$
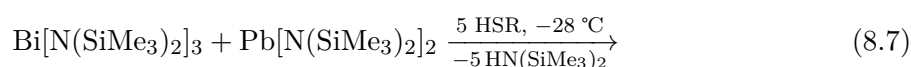
When proceeding the reaction according to reaction (8.7) the ^{1}H-NMR spectrum of the reaction product was different from the starting molecules and possible RSSR dithiol oxidation products. Hereby crystallization attempts were the main focus, which so far require further attention. These investigations on the molecular chemistry may be combined with the quest for single-source precursor for ternary phases (e.g., $KBiS_2$ or even $AgBiS_2$).

8.2.1 Further Investigations by Multinuclear NMR Spectroscopy
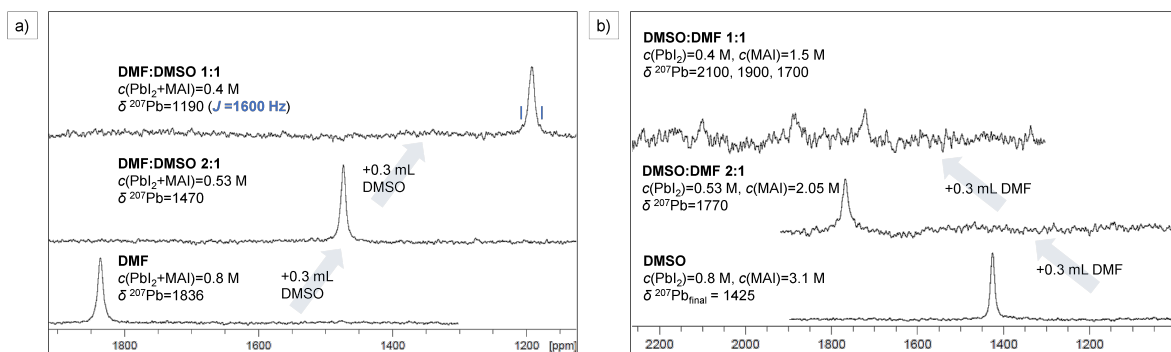
Figure 8.4: Stacked plot of ^{207}Pb-NMR spectra a) step-wise addition of 0.3 mL DMSO to a NMR tube containing $c(\text{PbI}_2+\text{MAI}) = 0.8$ M ($R = 1$) in 0.6 mL DMF b) step-wise addition of 0.3 mL DMF to a NMR tube containing a solution at the $c(\text{PbI}_2)=0.8$ M ($R = 3.8$) MAI titration end-point in 0.6 mL DMSO.

The multinuclear NMR investigations may be extended for a more detailed insight on the solution species. For this e.g., (diffusion-ordered) DOSY–NMR and (exchange spectroscopy) ^{207}Pb–^{207}Pb–EXSY experiments can be considered in the next steps. The exchange dynamics of $CH_3NH_3^+$ can be investigated in more detail by established and readily available ^{13}C–^{1}H-correlation experiments, additionally involving the ^{15}N nuclei. The NMR experiments in binary solvent mixtures of DMSO and DMF were extended including pyridine, (acetonitrile) ACN and γ-GBL, and may provide the basis for more detailed insight on the solute-solvent interactions in combination with further complementary spectroscopic methods such as Raman

spectroscopy or conductivity measurements. One immediate next step could be the search for δ^{207}Pb in γ-GBL, which was performed so far only with the c(PbI$_2$+MA) $= 0.8$ M precursor composition. The solution species present in DMF remained largely unspecified, which could be investigated starting with supersaturation by PbI$_2$+I$^-$ in varying combinations and comparing the evolution of δ^{207}Pb in the supernatant with the composition of the precipitates. At several occasion the fast-exchange conditions showed a tendency to transform into intermediate- to slow-exchange, providing the basis to resolve the solution structures by making ^{207}Pb-^{207}Pb coupling information and isotopomeric signal distributions accessible. This tendency was more often observed when δ^{207}Pb was measured from solutions of (i) sub- and extra-stoichiometric precursors ratios ([CsI]/[PbI$_2$] and [MAI]/[PbI$_2$]) (ii) binary DMF:DMSO solvent mixtures.

The stacked plot in (Figure 8.4a) shows emerging $^{n}J_{^{207}\text{Pb}-^{207}\text{Pb}}$-satellites, which were by value in the typical range for coupling between ^{207}Pb nuclei. Whereas in (Figure 8.4b) the signal from the ^{207}Pb nuclei has clearly reached the slow-exchange regime and was not possible to be resolved further since it disappeared from the NMR time-scale when measuring the same sample the next day. These interesting phenomena can be extended to a more detailed investigations, as there were several more comparable observations of this kind.

9 Experimental Part

9.1 Instrumentation, Software and Data Storage

X-Ray Photoelectron Spectroscopy (XPS) XPS analysis was performed with an ESCA M-Probe from Surface Science Instruments. The samples were irradiated with monochromated Al-K$_\alpha$-rays ($\lambda = 8.33$ Å). Survey scans were recorded with a detector pass energy of 158.9 eV and high-resolution spectra were recorded with a pass energy of 22.9 eV. All spectra were referenced to adventitious carbon (284.8 eV). The spectra were fitted with CasaXPS software (Casa Software Ltd.) using GL(30) line shape for Bi$_2$S$_3$, and DS(0.1,400) line-shape for elemental Bi.

Thermogravimetry Thermogravimetric measurements were performed at a TGA/DSC (Mettler-Toledo GmbH, Gießen, DE) apparatus, samples were characterized in a Al$_2$O$_3$ vial under an atmosphere of dry N$_2$(g) and heating ramp of 10 °C/min to 600 °C.

Elemental analysis were carried out using a HEKAtech CHNS Euro EA 3000 (Wegberg, Germany).

Mass Spectrometry Mass spectrometric analysis was performed on a Finnigan MAT 95 (70 eV) in m/z relative percentage), operating in positive ion mode.

Scanning Electron Microscopy (SEM) and Raman Measurements Scanning electron microscopy (SEM) was performed on NANO SEM 430 (FEI, Hillsboro, USA) and on a Zeiss Sigma 300 (Carl Zeiss Vision GmbH, Aalen, DE). Raman measurements were performed on a RISE-Raman-Microscope (WITec, Ulm, Germany) implemented with a Zeiss Sigma 300.

Transmission Electron Microscopy (TEM) High-resolution transmission electron microscopy (TEM) and selected area electron diffraction (SAED) measurements were carried out on a JEOL JEM-2200FS microscope (Peabody, London, UK).

X-Ray diffraction X-Ray diffraction (XRD) on powder and layers were performed on a STOE Stadi MP diffractometer (STOE and Cie, Darmstadt, Germany) with a linear PSD and Mythen detector.

Single-Crystal X-Ray Diffraction Data collection for X-ray structure elucidation was performed on STOE IPDS 2T/II diffractometer (STOE and Cie, Darmstadt, Germany) using graphite-monochromated Mo-K$_\alpha$ radiation (0.71071 Å).

Additional Software and Programs Data plots were generated by OriginPro 8.6 (OriginLab Corporation, Northhampton, USA). NMR-Spectra were evaluated and plotted with TopSpin 4.0.7. Chemical drawings and illustrations were done by ChemDraw 19.0.1.28 (PerkinElmer Informatics, Waltham, USA). Schemes and figures in Chapter 6 were generated by Vesta 4.6.0.[329] and InkScape 0.9.2.. For editing and merging of figures MS Office 365 PowerPoint was used. For visualization of the crystal structures Diamond 3.2k (Crystal Impact GbR, Bonn, Germany) was used. SEM and TEM images were analyzed and edited with ImageJ (1.5.3q). This thesis was written and edited with TexStudio 4.2.3, Texmaker 5.1.3. and the Texlive 2019 LaTeX distribution implemented in Kubuntu 20.04 and the MikTex 4.7 distribution on a Windows 10 computer.

Availability of primary data The raw and primary data of the here presented results was deposited on the sciebo cloud (The link and details on login were send to the doctoral office and Prof. S. Mathur), additionally are these and herein not included data to be found on the (akm-terminal) server of the RG Mathur. Data recieved in paper form was handed in together with the lab books. The single-crystal X-Ray data is also included, and was deposited also as cif-files in the CSD databse as described en detail further below in this section.

9.2 Nuclear Magnetic Resonance (NMR) Spectroscopy

NMR spectra were recorded on a Bruker Avance II 300 spectrometer (^{1}H 300.1 MHz, ^{7}Li 116.6 MHz, ^{13}C 75.5 MHz, ^{19}F 282.4 MHz, ^{29}Si 59.6 MHz, ^{133}Cs 39.3 MHz, ^{119}Sn 111.95 MHz, ^{207}Pb 62.9 MHz) equipped with a BBO ATM 5 mm probe head, and Avance 400 spectrometer (^{1}H 400.1 MHz, ^{13}C 100.6 MHz, ^{119}Sn 149.2 MHz, ^{207}Pb 83.9 MHz) equipped with a TBI 5 mm probe head. ^{1}H-NMR and ^{13}C-NMR chemical shifts are reported in parts per million relative to external tetramethylsilane (TMS) and were referenced internally to residual (^{1}H) proton impurity and ^{13}C signal of the deuterated lock solvent. ^{119}Sn$\{^1$H$\}$ spectra were calibrated externally to Sn[N(SiMe$_3$)$_2$]$_2$[157,197] in C$_6$D$_6$ (δ^{119}Sn $= 775$) and are reported relative to Sn(CH$_3$)$_4$ in C$_6$D$_6$ (δ^{119}Sn $= 0$). ^{207}Pb chemical shifts were referenced externally to a solution of 1.0 M Pb(NO$_3$)$_2$ in D$_2$O (δ^{207}Pb $= -2986.3$) at T $= 298$ K and are reported relative to Pb(CH$_3$)$_4$ in toluene (δ^{207}Pb $= 0$).[243,330] The ^{133}Cs chemical shifts were referenced to a solution of Cs(NO$_3$) in D$_2$O.

Assignment of ^{13}C-NMR signals was made on the basis of ^{1}H,^{13}C-HMQC, ^{1}H,^{13}C-HMBC, ^{13}C-APT or ^{19}F,^{13}C-HMBC experiments. ^{207}Pb and ^{119}Sn resonances were detected via proton broadband decoupled ^{207}Pb$\{^1$H$\}$ and ^{119}Sn$\{^1$H$\}$ experiments and ^{29}Si resonances via the ^{29}Si$\{^1$H$\}$ DEPT45 pulse program, if not stated otherwise.

Details on ^{207}Pb NMR Measurements

The frequency tuning and matching and magnetic field homogeneity on a Bruker Avance 400 spectrometer was adjusted each time for every sample manually before experiment and monitored during the measurement. A constant pulse width of 12.55 μsec was used during all experiments. Initially the range from $+5000$ to -4000 ppm was scanned to locate all possible resonances. The transmitter frequency offset was moved stepwise over the given range with a spectral width of 900 ppm (75 kHz), collecting 4000–20000 scans. Each measured window was taken care to overlap by 150 ppm with the following one to ensure the detection of resonances possibly located at the edges of the applied spectral windows, where signals generally suffer from low intensity. Once the signal was located, the measurement was repeated, now with the observed resonance as the transmitter frequency offset. Acquisition times between 0.5 s–1.0 s and relaxation delays of 0.5 s–1.5 s were used in the pulse program, enabling collection of several thousand transients in relatively short time. Given the extremely fast relaxation of the ^{207}Pb nuclei in the Pb-I system, readily observed in the short decay of the FID, shorter acquisition times were sufficient while collecting data points. The parameters were chosen to allow for equilibration of solution dynamics related to the excitation process and to obtain a maximum of spectral resolution. Data Processing: The raw FID was multiplied with an exponential window function with a line-broadening parameter (lb) of 200 Hz, if not noted otherwise, before Fourier-transformation to increase the (signal-to-noise) S/N ratio. All spectra were baseline corrected by a polynomial function and a phase correction of 1st and 0th order was applied.

Variable Temperature(VT)-NMR Spectroscopy

Variable temperature NMR was measured on a Bruker Avance 400 spectrometer.

Chapter 5

The cooling rate was adjusted to so that lowering the temperature by $10\,\text{K}$ was reached in $20\,\text{min}$ of time. At each temperature the sample was allowed to equilibrate for $10\,\text{min}$–$15\,\text{min}$, followed by re-calibrating the frequencies by the tune and match procedure and shimming of the magnets. The $^{119}\text{Sn}\{^1\text{H}\}$-NMR spectra were offset to o1p $= -157$, and the spectral widths were narrowed to sw $= 500$. The minimum number of scans for $^{119}\text{Sn}\{^1\text{H}\}$ was ns $= 128$ and the max. ns $= 1000$ (depending on the temperature stability the VT unit of the spectrometers was able to maintain) and in all ^1H-NMR spectra ns $= 32$.

Chapter 6

The sample was first measured at room temperature and cooled down respectively warmed up slowly by $10\,\text{K}$ and allowed to equilibrate for at least 5 minutes at the target temperature to avoid temperature gradients in the sample. After frequency tuning and matching the shim was adjusted to the new temperature, collection of data was begun after pairing the new signal location with the transmitter frequency offset. The number of scans ranging for ^{207}Pb typically between ns $= 200 - 500$ and for ^1H ns $= 32$. This procedure was repeated for each temperature.

9.2.1 DFT Calculation Details

In cooperation with Dr. Eunhwan Jung:
Density functional theory (DFT) calculations for the conformation search to find the lowest structure of $\text{Bi}(\text{SBu}^t)_3$ and $\text{Bi}(\text{SPr}^i)_3$ compounds and the geometry optimization of each compound are carried out at B3LYP/LanL2DZ level of theory. All the optimized geometries are confirmed to be minimum-energy structures with the absence of imaginary frequency. The highest occupied molecular orbital (HOMO) and lowest unoccupied molecular orbital (LUMO) energy levels of each compound are taken from the eigenvalues of the Kohn-Sham equation. The bond dissociation energy of the S-C bond, the formation enthalpies, ΔH_f, for each compound were carried out. In addition, both the zero-point vibrational energy correction and the basis set superposition error (BSSE) energy correction have been considered. The GAUSSIAN 16 suite of program is employed for all the calculations.[102]

9.2.2 Chemical Vapor Deposition (CVD)

The CVD experiments were performed in a horizontal cold-wall reactor system under low-pressure conditions ($p < 10^{-7}\,\text{bar}$). The Si wafer substrates were attached with silver paste (**1b**: at $\text{T}_\text{s} = 250\,°\text{C}$ the Si substrate was attached with Kapton®) on a graphite susceptor that was heated to the pre-set temperature inductively by an outer coil. When the attached flask reached the corresponding temperature (**1a**: $100\,°\text{C}$, **1b**: $90\,°\text{C}$) the precursor molecules were allowed to enter reaction chamber via sublimation. The process time (t $= 15\,\text{min}$–$30\,\text{min}$.) denotes the time span of continuous precursor mass flow, realized by a stop-cock switch between the reaction chamber and the precursor flask. More detailed information can be found in previous publications from the research group.[331–333] The substrates and graphite susceptor were cooled down naturally to room temperature within the reaction chamber. After each process all substrates were uniformly covered by a grayish-black film.

9.2.3 Crystallographic Information

Crystallographic data for the structures reported in this thesis have been deposited with the Cambridge Crystallographic Data Centre (CCDC). These data can be obtained free of charge via `www.ccdc.cam.ac.uk/data_request/cif`. The corresponding numbers are reported below with the details on the structure solution and refinement.

The measurement device type and data collection software was identical for all crystals obtained within this work and was described in the previous instrumentation section. The data were corrected for Lorentz and polarization effects. For unit cell refinement, data collection and integration STOE's X-Area (STOE and Cie, 2002. Darmstadt, Germany) was used. Numerical absorption correction based on crystal-shape optimization was applied for all data by using STOE'sX-Shape and XRED32 (STOE and Cie, 2002. Darmstadt, Germany). The software SHELXL[334,335], SHELXT[336] and ShelXle[337] was used for structure solution and refinement. The CIF files were edited and generated using FinalCif v102.[338]

The crystals were mounted on a glass fiber with the viscous oil-drop method under continuous N_2(g) flow. The hydrogen atoms were refined isotropically on calculated positions using a riding model with their U_{iso} values constrained to 1.5 times the U_{eq} of their pivot atoms for terminal sp^3 carbon atoms and 1.2 times for all other carbon atoms. All non-hydrogen atoms were refined with anisotropic displacement parameters, except for two carbon atoms in (**3d**). Special details on the refinement are given in the text below for the corresponding crystals and can be found in the response form to the checkcif alerts included in the deposited cif-files. Suitable Crystals of Bi(SBu^t)$_3$ (**1a**) for structure determination were obtained by recrystallization from THF. The data were collected from a single crystal at T =170(2) K. The structure was solved using SHELXT[336] and refined by full-matrix least-squares methods against F^2 by SHELXL-2018/3 using ShelXle.[334,337] Twinning was detected in form of a two-component inversion twin and during refinement the following instruction was applied TWIN 0 1 0 1 0 0 0 0 −1. CCDC 2183724 contains the supplementary crystallographic data for (**1a**).

Suitable Crystals of [Sn(SBu^t)(tfb-dmeda)] (**2a**) for structure determination were obtained by sublimation. The data were collected from a single crystal at T = 170(2) K. The structure was solved by direct methods using SHELXS-97[334,335] and refined by full-matrix least-squares methods against F^2 by SHELXL-2018/3 using ShelXle.[334,337] CCDC 2102248 contains the supplementary crystallographic data for (**2a**).

Suitable Crystals of [Sn(SPr^i)$_2$]$_n$ (**2b**) for structure determination were obtained by recrystallization from THF. The data were collected from a single crystal at T = 293(2) K. The structure was solved by direct methods using SHELXS[336] and refined by full-matrix least-squares methods against F^2 by SHELXL-2018/3 using ShelXle.[334,337] Disordered moieties were refined using bond lengths restraints and displacement parameter restraints. CCDC 2192293 contains the supplementary crystallographic data for (**2b**).

Suitable Crystals of [Sn(SBu^i)$_2$]$_n$ (**2c**) for structure determination were obtained by recrystallization from THF. The data were collected from a single crystal at T = 170(2) K. The structure was solved by direct methods using SHELXS[334,335] and refined by full-matrix least-squares methods against F^2 by SHELXL-2018/3 using ShelXle.[334,337] CCDC 2192290 contains the supplementary crystallographic data for (**2c**).

Suitable Crystals of [Pb$_3$(μ-SBu^t)$_6$] (**3a**) for structure determination were obtained by recrystallization from THF. The data were collected from a single crystal at T = 173(2) K. The structure was solved using SHELXS[334,335] and refined by full-matrix least-squares methods against F^2 by SHELXL-2018/3 using ShelXle.[334,337]
The large value of residual electron density, exclusively located nearby the Pb atoms, was due to Fourier truncation errors, which was not possible to avoid as no other crystal of better quality was found. CCDC 2192290 contains the supplementary crystallographic data for (**3a**).

Suitable Crystals of [Pb$_5$(μ-SBu^i)$_4$(SBu^i)$_6$] (**3c**) for structure determination were obtained by recrystallization from n-pentane. The data were collected from a single crystal at T = 170(2) K. The structure was solved using SHELXS[334,335] and refined by full-matrix least-squares methods against F^2 by SHELXL-2018/3 using ShelXle.[334,337] CCDC 2192288 contains the supplementary crystallographic data for (**3c**).

Suitable Crystals of [Pb$_{12}$O$_6$(SPr^i)$_{12}$ $\cdot$ C$_6$H$_6$] (**3d**) for structure determination were obtained by recrystallization from benzene. The data were collected from a single crystal at T = 293(2) K. The structure was solved using SHELXT[336] and refined by full-matrix least-squares methods against F^2 by SHELXL-2018/3 using ShelXle.[334,337] Two carbon atoms were refined with isotropic displacement parameters, because their anisotropic refinement and the attempt to introduce disorder with these would crash the refinement. The hydrogen atoms were refined isotropically on calculated positions using a riding model with their U_{iso} values constrained to 1.5 times the U_{eq} of their pivot atoms for terminal sp^3 carbon atoms and 1.2 times for all other carbon atoms. CCDC 2192291 contains the supplementary crystallographic data for (**3d**).

Suitable Crystals of [Pb$_{12}$O$_6$(SBu^t)$_{12}$] $\cdot$ 6 (NC$_5$H$_5$) (**3e**) for structure determination were obtained by recrystallization from pyridine. The data were collected from a single crystal at T = 150(2) K. The structure was solved using SHELXT[336] and refined by full-matrix least-squares methods against F^2 by SHELXL-2018/3 using ShelXle.[334,337] CCDC 2192292 contains the supplementary crystallographic data for (**3e**).

9.3 Comments on the Synthesis of M[N(SiMe$_3$)$_2$]$_n$ (M = Sn^{II}, Pb^{II} n=2; M = Bi^{III} n=3)

The *bis*(trimethylsilyl)amido [N(SiMe$_3$)$_2$]$^-$ compounds M[N(SiMe$_3$)$_2$]$_n$ (M = Sn^{II}, Pb^{II} n=2; M = Bi^{III} n=3) compounds were applied as initial complexes for the synthesis of the corresponding metal thiolates. Their general properties and applications were investigated extensively and summarized in the literature[339–342] and was not subject of this thesis. In this section the issue of lithium contamination in the final complexes (M = Sn^{II}, Pb^{II} and Bi^{III}) and pecularities that would arise by the choice of the metal halogenid BiCl$_3$ vs. BiBr$_3$ for (M = Bi^{III}) shall be mentioned, as these were encountered and resolved during the experimental work. Sn[N(SiMe$_3$)$_2$]$_2$, Pb[N(SiMe$_3$)$_2$]$_2$[143,196,343] and Bi[N(SiMe$_3$)$_2$]$_3$[344] are monomeric molecular compounds in the solid state, solely in [Li(N{SiMe$_3$}$_2$)]$_n$[345] the silylamido [N(SiMe$_3$)$_2$]$^-$ moiety acts as μ_2-bridging ligand. The bulky ligand moiety N(SiMe$_3$)$^-$ acts as stabilizing environment for the corresponding central atom and provided a suitable starting point for a mild and elegant synthesis route for the synthesis of the metal thiolates. While the

reaction of $Bi[N(SiMe_3)_2]_3$ with bulky arenethiols was reported earlier,[346] Sn^{II} and Pb^{II} thiolates were in general synthesized via salt-metathesis according to the general route $MX_2 + 2\,NaSR \longrightarrow M(SR)_2 + 2\,NaX$ (M = Sn^{II}, Pb^{II}, X = Halogenid). The 'silylamido-route' is therefore often referred to as avoiding ionic impurities. However, it was generally observed that none of the metal complexes were possible to obtain free of Li^I following the reported experimental procedures, or by adjusting parameter within these reported procedures such as reaction time, temperature or by introducing an excess in one of the reaction components from the very start.[143,196,343,344,346–350] The issue of lithium contamination was not addressed in the literature for any of the above-mentioned complexes. Which is most likely due to the non-availability of ^{7}Li-NMR spectroscopy, since routine nuclei such as ^{1}H and ^{13}C did not prove valuable identifying $[Li(N\{SiMe_3\}_2)]_n$ or are basically not capable detecting any, e.g., LiX (X = halogenid) species. Within this work different strategies were developed en route of the experimental work in order to remove any Li^I-bearing species from the final product, which is described in detail in the experimental part and outlined in the following text. While analyzing the purity of the $M[N(SiMe_3)_2]_n$ (M = Sn^{II}, Pb^{II} n=2; M = Bi^{III} n=3) compounds ^{7}Li-NMR proved to be a valuable method confirming the absence of *any* lithium species. The presence or absence was easily detected by ^{7}Li-NMR within few minutes under routine measurement parameters. The inspection of ^{1}H-NMR chemical shifts proved to be unreliable reference for the detection of lithium bearing species already when measuring the proton NMR chemical shift of pure $[Li(N\{SiMe_3\}_2)]_n$. Hereby one to three different signals at varying signal positions where present between $\delta\,^1$H = 0.30 and 0.00, most likely as result of the concentration dependent aggregation degree n and ligand exchange dynamics of $[Li(N\{SiMe_3\}_2)]_n$ in solution. Therefore, the amount of $[Li(N\{SiMe_3\}_2)]_n$ or LiX impurity was not possible to be assessed by ^{1}H-NMR.

Synthesis of Sn[N(SiMe$_3$)$_2$]$_2$ and Pb[N(SiMe$_3$)$_2$]$_2$

For the synthesis of pure $M[N(SiMe_3)_2]_n$ (M = Pb^{II}, Sn^{II} n=2) when according to reported procedures the last purification step, which is distillation under reduced pressure was accomplished, to this an additional amount MCl_2 (M = Pb^{II}, Sn^{II}) between 10–20 mol-% suspended in n-pentane was added and after stirring for 1–2 h and hydrocarbon extraction the distillation was repeated, to yield the desired lithium free pure product.

Synthesis of Bi[N(SiMe$_3$)$_2$]$_3$

Whereas for $Bi[N(SiMe_3)_2]_3$ repeated fractioned sublimation proved to be effective. Introducing an even slight excess of $BiBr_3$ at any given step of the synthesis procedure was observed to be detrimental for the final yield if there was any left. The main reaction product was then an orange oil, yet of unknown composition, which showed multiple resonances in the ^{1}H-, ^{13}C- and ^{29}Si-NMR and was not further pursued. For the same reason, which is minimizing any possible imbalance in the ratio of precursors $Li[N(SiMe_3)_2]$ was pre-synthesized and applied as purified solid for the synthesis of $Bi[N(SiMe_3)_2]_3$.

Unnecessary to mention the importance of having an pure compound, the sheer presence of Li^+ ions can have unexpected implications.[351] Beyond the issue of lithium contamination there were additional peculiarities to keep in mind for the synthesis of $Bi[N(SiMe_3)_2]_3$. It was mentioned that $BiCl_3$ needs to be freshly sublimed prior to the synthesis of $Bi[N(SiMe_3)_2]_3$, otherwise the reaction products would comprise a mixture of unknown composition, as shown by ^{1}H-NMR spectroscopy.[349] Hereby one side product was identified as the cyclic dimer

[Bi(N{SiMe$_3$}$_2$)(μ-NSiMe$_3$)]$_2$ by single-crystal X-Ray analysis.[349] The reason why BiCl$_3$ shows different reactivity was not elucidated so far, and in this context *"the often capricious nature of bismuth chemistry"*[340] was mentioned. Within this work BiBr$_3$ was applied, which was synthesized from the elements and purified by sublimation. The choice for BiBr$_3$ was based on increased solubility in coordinating solvents e.g., THF and diethyl ether, reduced sensitivity towards ambient atmosphere and the higher tendency for sublimation when compared to BiCl$_3$. Except from one report in the literature,[350] BiCl$_3$ is applied for the synthesis of Bi[N(SiMe$_3$)$_2$]$_3$,[344,346–349] which based on purely personal speculation of the author may originate from the more than three-fold higher price for commercial available BiBr$_3$ compared to BiCl$_3$ when searching the product list of common chemical vendors. The above-mentioned puzzling results when applying BiCl$_3$ for the synthesis of Bi[N(SiMe$_3$)$_2$]$_3$ were not observed with BiBr$_3$. Hereby, ^{1}H- and ^{13}C-NMR spectroscopy were applied identifying Bi[N(SiMe$_3$)$_2$]$_3$ by the proton and carbon chemical shifts of the methyl moieties at δ^1H = 0.37 and δ^{13}C = 6.63 in C$_6$D$_6$, in accordance with literature reported values.[344,349] Additionally the ^{29}Si-NMR chemical shift from Bi[N(SiMe$_3$)$_2$]$_3$ is reported the first time within this work as δ^{29}Si = 4.26.

9.4 Experimental Procedures

All experiments were carried out under strict exclusion of moisture and oxygen under an atmosphere of dry $N_2(g)$ using a *Stock* high vacuum apparatus, and exclusion of ambient daylight by using amber glassware and aluminum foil. THF, toluene, diethyl ether, benzene solvents were dried by refluxing over sodium + benzophenone and freshly distilled prior to use and stored over sodium wire. CH_2Cl_2 was dried and distilled from $CaCl_2$. Pyridine was dried and distilled over KOH pellets. The thiols $HSBu^t$, $HSPr^i$ and $HSBu^i$ were used without further purification. Elemental bismuth Bi in powdered form and elemental bromine Br_2 were provided by Dr. Wieland Tyrra and Dr. Corinna Hegemann.
The deuterated solvents DMF-d_7 (DEUTERO Chemicals), DMSO-d_6 (DEUTERO Chemicals) were used as received without further purification.

Table 9.1: Commercially obtained chemicals

Compound	Supplier
(2-methyl-2-propanethiol) $HSBu^t$ (99 %)	Sigma-Aldrich
(2-methyl-1-propanethiol) $HSBu^i$ (99 %)	Sigma-Aldrich
(2-propanethiol) $HSPr^i$ (99 %)	Sigma-Aldrich
(hexamethyldisilazane) $H[N(SiMe_3)_2]$ (98 %)	Carbolution Chemicals
(tin(II) chloride) $SnCl_2$ (99.99 %)	Sigma-Aldrich
(lead(II) chloride) $PbCl_2$ (99.99 %)	Fischer Scientific
(lead(II) iodide) PbI_2 (99.99 %)	TCI Chemicals
(cesium iodide) CsI (99.9 % trace metal basis)	Sigma-Aldrich
(methylammonium iodide) CH_3NH_3I	TCI Chemicals, Solarveni
(guanidinium iodide) $C(NH_2)_3I$	greatcell solar
(lead(II) nitrate) $Pb(NO_3)_2$ (99 %)	Fischer Scientific
(chloroform-d_1) $CDCl_3$	Eurisotop
(benzene-d_6) C_6D_6	Eurisotop
(dimethyl formamide-d_7) DMF-d_7	DEUTERO Chemicals
(dimethyl sulfoxide-d_6) DMSO-d_6	DEUTERO Chemicals
toluene (HPLC grade)	Fischer Scientific
(tetrahydrofuran) THF (techn.)	Fischer Scientific
diethyl ether (techn.)	Fischer Scientific
pyridine (99.5 %)	Fischer Scientific
(dichloromethane) CH_2Cl_2	Fischer Scientific
ethylene diamine (99.5 %)	TCI Chemicals

9.4.1 Synthesis of BiBr₃

$$\text{Bi} + 1.5\,\text{Br}_2 \xrightarrow{\text{CH}_2\text{Cl}_2,\ -28\,°\text{C to r.t.}} \text{BiBr}_3$$
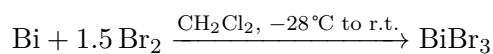
BiBr$_3$ was synthesized from the elements in CH$_2$Cl$_2$ by a modified procedure as reported previously.[352] In a 500 mL three-neck round bottom flask with attached dropping funnel that was closed by a PTFE stopcock, finely ground elemental bismuth (118.62 g, 0.0891 mol) was suspended in 90 mL CH$_2$Cl$_2$ and cooled down by immersing the reaction flask into a mixture of NaCl and crushed ice in 1:3 (v:v) ratio. Prior to cooling elemental bromine Br$_2$ ($\rho = 3.12\,\text{gcm}^{-3}$, 8.2 mL, 0.160 mol) was filled into the dropping funnel from a measuring cylinder. The given temperature of T = $-28\,°$C was maintained for 4 h, while being monitored by a thermometer diving into the outer cooling bath mixture. Then the red-orange suspension was allowed to slowly warm up to room temperature, while stirring was continued for 20 h. After removing all volatile components under reduced pressure, a pale yellow crude powder was obtained, which was further purified by sublimation (T$_{\text{subl.}}$ = 100–115 °C , 10^{-3} mbar) to yield bright shiny yellow crystalline BiBr$_3$ in 95 % yield.

9.4.2 Synthesis of Li[N(SiMe₃)₂]

$$\text{n-BuLi} + \text{H}[\text{N}(\text{SiMe}_3)_2] \xrightarrow[-\text{n-butane}]{\text{n-hexane, 0 °C}} \text{Li}[\text{N}(\text{SiMe}_3)_2]$$
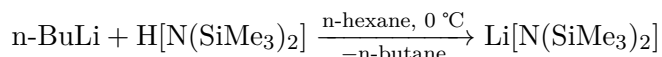
In a 250 mL three-neck round bottom flask with attached dropping funnel H[N(SiMe$_3$)$_2$] ($\rho = 0.774\,\text{gcm}^{-3}$, 36 mL, 144 mmol) was cooled down by an outer crushed ice bath. Then n-BuLi (2.5 M solution in hexane, 68 mL, 144 mmol) was added dropwise ($\sim$1 drop per sec.). When the addition was completed, the cooling dewar was removed and the reaction mixture was stirred vigorously while warming to room temperature (1.5–2 h). After removing all volatile components under reduced pressure, a pale crystalline solid was obtained which was purified by sublimation (T$_{\text{subl.}}$ = 60–80 °C, 10^{-3} mbar, 2 h), to obtain Li[N(SiMe$_3$)$_2$] (22.88 g , 137 mmol) as white crystalline solid in 95 % yield. ^{1}H-NMR (300.1 MHz, C$_6$D$_6$, 25 °C): $\delta = 0.05 - 0.30$ (single to multiple signals in this range). In the ^{7}Li-NMR spectra a single resonance was observed within the range $\delta = 0.80 - 1.40$. The purity of the compound was verified by NMR spectroscopy and sublimation temperature.

9.4.3 Synthesis of Bi[N(SiMe$_3$)$_2$]$_3$

$$\text{BiBr}_3 + 3\,\text{Li}[\text{N}(\text{SiMe}_3)_2] \xrightarrow[-3\,\text{LiBr}]{\text{THF}} \text{Bi}[\text{N}(\text{SiMe}_3)_2]_3$$
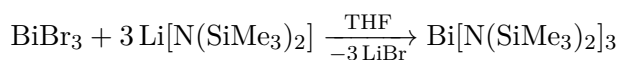
In a 100 mL round bottom flask BiBr$_3$ (20.45 g, 45.58 mmol) was dissolved in 52 mL THF by stirring for 2 h at T$_{\text{oil-bath}}$ = 60 °C. The yellow solution was then cooled down to T = 0 °C and added *slowly* drop-wise to an crushed-ice cooled solution of Li[N(SiMe$_3$)$_2$] (22.88 g, 137 mmol) in THF. When the addition step was complete, the orange-yellow solution was stirred for 4 h while slowly warming to room temperature. After removing the volatile components under reduced pressure an orange-yellow powder was obtained. To this was added 75 mL *n*-pentane and the suspension was stirred vigorously for 1 h, and the *n*-pentane was removed under reduced pressure. Only then the extraction procedure by *n*-pentane was begun. For this to the crude reaction mixture *n*-pentane (20–50 mL) was added, after stirring vigorously for 1–2 min, the solid components in the suspension were allowed to settle down and the supernatant yellow solution was decanted by a cross into a new flask. The extraction procedure was repeated until the supernatant was observed as very pale yellow to colorless solution. The extracted bright yellow solutions should be liberated from *n*-pentane quite soon and not kept until all extraction steps were finished. After removing the *n*-pentane under reduced pressure from the extracted solution a bright yellow powder was obtained, which was purified by sublimation. The outer oil bath temperature was raised slowly within the range T = 60–80 °C until no more Li[N(SiMe$_3$)$_2$] as white solid was observed to sublime. Hereby it is advised to disperse the crude product by a spatula and repeat the sublimation below T = 80 °C. Then the temperature was further raised and between 85–105 °C the sublimation of a yellow crystalline solid was observed. This 2nd fraction of sublimate should be checked by ^{7}Li-NMR to confirm the absence of any lithium bearing species in the final product. Latest when the fractioned sublimation was repeated a 2nd or sometimes 3rd time no ^{7}Li-NMR signal was detected in the final sublimate. Bi[N(SiMe$_3$)$_2$]$_3$ was obtained as yellow crystalline solid in 92 % yield. (Hint: The yield of Bi[N(SiMe$_3$)$_2$]$_3$ depends largely on the eagerness to recycle or discard the second and third fractions of the sublimate and interpretation of 'pale' yellow during the extraction process. It is also strongly advised *not* to further up-scale this reaction.)

Bi[N(SiMe$_3$)$_2$]$_3$: ^{1}H-NMR (300.1 MHz, C$_6$D$_6$, 25 °C): δ = 0.37 (s, $^2J_{^1\text{H}-^{29}\text{Si}}$ = 6 Hz). ^{13}C-APT-NMR (75.7 MHz, C$_6$D$_6$, 25 °C): δ = 6.40 (CH$_3$). ^{29}Si{^{1}H}-DEPT45-NMR (59.6 MHz, C$_6$D$_6$, 25 °C): δ = 4.26 (s, $^1J_{^{29}\text{Si}-^{13}\text{C}}$ = 55 Hz).

9.4.4 Synthesis of the precursors (1a) and (1b)

Both precursor molecules were synthesized via protolysis of $Bi[N(SiMe_3)_2]_3$, which was synthesized by a modified route as described in literature.[350]

$$Bi[N(SiMe_3)_2]_3 + 3\,HSR \xrightarrow[-3\,HN(SiMe_3)_2]{THF,\ 0\,°C} \underset{\textbf{(1a)}\ R = \text{-}Bu^t,\ \textbf{(1b)}\ R = \text{-}Pr^i}{Bi(SR)_3}$$
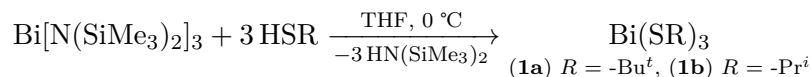
Tris(*tert*-butylthiolato)bismuth(III) $Bi(SBu^t)_3$ (**1a**) and tris(*iso*-propylthiolato)bismuth(III) $Bi(SPr^i)_3$ (**1b**): A solution of $Bi[N(SiMe_3)_2]_3$ (1.00 eq., 1.512 g, 2.191 mmol) in 25 mL THF was added dropwise to an ice-cooled solution of the corresponding thiol (**1a**: $HSBu^t$, $\rho = 0.80\,gcm^{-3}$: 3.00 eq., 0.593 g, 6.573 mmol; **1b** $HSPr^i$, $\rho = 0.82\,gcm^{-3}$: 3.00 eq., 0.501 g, 6.573 mmol) in 10 mL THF, resulting in a bright yellow solution and a yellow precipitate. After the suspension was stirred for 15 min. in the cold, the reaction mixture was allowed to warm up to room temperature before the solvent and volatile by-products were removed under reduced pressure. The yellow powder was further purified by sublimation (**1a**: $Bi(SBu^t)_3$: $T_{subl.}$ = 80–90 °C, 10^{-3} mbar; **1b**: $Bi(SPr^i)_3$: $T_{subl.}$ = 70 °C, 10^{-3} mbar) and obtained in near quantitative yields of 95–98 % as yellow needle-like crystalline solids.

(**1a**) Tris(*tert*-butylthiolato)bismuth $Bi(SBu^t)_3$: ^{1}H-NMR (300.1 MHz, C_6D_6, 25 °C): δ = 1.46 (s).^{13}C-APT-NMR (75.7 MHz, C_6D_6, 25 °C): δ = 36.8 (CH_3), 45.8 (C_q).
EI-MS (70 eV): m/z (%): 476 (22) $[M]^+$, 419 (2) $[Bi(S)(SC_4H_9)_2]^+$, 387 (3) $[Bi(SC_4H_9)_2]^+$, 363 (6) $[Bi(S)(SH)(SC_4H_9)]^+$, 330 (38) $[Bi(S)(SC_4H_9)]^+$, 307 (10) $[Bi(S)(SH)_2]^+$, 298 (8) $[Bi(SC_4H_9)]^+$, 275 (22) $[Bi(SH)_2]^+$, 242 (8) $[Bi(SH)]^+$, 209 (6) $[Bi]^+$. Elemental analysis: calcd.: C 30.25 % H 5.71 % S 20.18 %. Found: C 30.08 %, H 5.71 %,S 20.18 %.
(**1b**) Tris(*iso*-propylthiolato)bismuth $Bi(SPr^i)_3$: ^{1}H-NMR (300.1 MHz, C_6D_6, 25 °C): δ = 1.36 (d, $^3J_{H\text{-}H}$=7 Hz, 6H, CH_3), 4.09 (sept, $^3J_{H\text{-}H}$=7 Hz, 1H, CH).^{13}C-APT-NMR (75.7 MHz, C_6D_6, 25 °C): δ = 29.9 (CH_3), 36.1 (CH).
EI-MS (70 eV): m/z (%): 434 (38) $[M]^+$, 359 (2) $[Bi(SC_3H_7)_2]^+$, 317 (11) $[Bi(SH)(SC_3H_7)]^+$, 284 (14) $[Bi(SC_3H_7)]^+$, 242 (10) $[Bi(SH)]^+$, 209 (6) $[Bi]^+$. Elemental analysis: Calcd.: C 24.90 % H 4.88 % S 22.10 %. Found: C 25.03 %, H 4.93 %, S 22.10 %.

9.4.5 Synthesis of (2a)–(2d)

$$Sn[N(SiMe_3)_2]_2 + 2\,HSR \xrightarrow[-2\,HN(SiMe_3)_2]{toluene,\ 0\,°C} \underset{\textbf{(2b)}\ R = \text{-}Pr^i,\ \textbf{(2c)}\ R = \text{-}Bu^i,\ \textbf{(2d)}\ R = \text{-}Bu^t}{Sn(SR)_2}$$
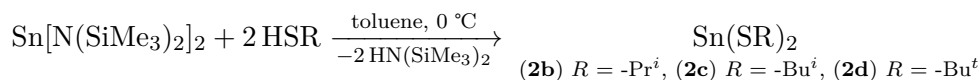
$Sn[N(SiMe_3)_2]_2$ was synthesized as reported earlier.[143,196] $Sn(SBu^t)_2$ (**2d**), $Sn(SPr^i)_2$ (**2b**) and $Sn(SBu^i)_2$ (**2c**) were synthesized via protolysis of the stannylene $Sn[N(SiMe_3)]_2$ in toluene at T = 0 °C under exclusion of ambient light. After removing all volatile components, bright yellow needle-like crystals were obtained and used without further purification.

The ligand *Htfb-dmeda* (3Z)-4-{[2-(dimethylamino)ethyl]amino}-1,1,1-trifluorobut-3-en-2-one, was provided by the working group members and checked by ^{19}F-, ^{13}C- and ^{1}H-NMR prior to use. A detailed synthetic procedure for ligand is described in the reference.[142]

$$Sn(SBu^t)_2 + Htfb\text{-}dmeda \xrightarrow[-1\,HSBu^t]{toluene,\ 0\,°C} \underset{\textbf{(2a)}}{[Sn(SBu^t)(tfb\text{-}dmeda)]}$$
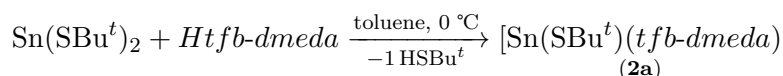
To a solution of *Htfb-dmeda* (1.185 g, 5.640 mmol) in toluene (5 mL) was slowly added a suspension of bis(*tert*-butylthiolato)Sn(II) (1.671 g, 5.624 mmol) in toluene (8 mL) at T = 0 °C by outer cooling with crushed ice. The color of the reaction mixture soon changed into an orange solution. The cooling bath was removed, and the orange solution was stirred for 0.5 h under exclusion of ambient daylight. Removal of all volatile compounds in vacuo left an orange solid, which was further purified by sublimation (90–100 °C, 10^{-3} mbar). After sublimation, (**2a**) was obtained as orange to yellow crystalline solid in 82 % yield.

(**2a**) ^{1}H-NMR (300.1 MHz, C_6D_6, 25 °C) δ = 6.58 (d, $J_{\text{H-H}}$ = 7 Hz, $^2J_{^1\text{H}-^{119}\text{Sn}}$ = 25 Hz, 1H, 4-C) 5.39 (d, $J_{\text{H-H}}$ = 7 Hz, 1H, 3-C), 2.75 (m, 1H, H-5$_a$, 2.23 (m, 1H, H-5$_b$), 2.23 (m, 1H, H-6$_a$), 1.83 (br, 6H, H-7), 1.78 (s, H-7b) 1.62 (s, 9H, H-9), 1.60 (m, 1H, H-6$_b$). ^{13}C{^{1}H}-NMR (75.5 MHz, C_6D_6, 25 °C): 180 (C-2,$^2J_{^{13}\text{C}-^{19}\text{F}}$ = 32 Hz),165.0 (C-4), 134.6 (q, C-1,$^1J_{^{13}\text{C}-^{19}\text{F}}$ = 284 Hz), 91.7 (C-3), 58.1 (C-6), 56.1 (C-5), 44.8 (C-7), 44.1(C-7'), 42.7 (C-8), 38.1 (C-9, $^3J_{^{13}\text{C}-^{119}\text{Sn}}$ = 24 Hz). ^{19}F-NMR (282.4 MHz, C_6D_6, 25 °C) δ = −74.56 (s, $^1J_{^{19}\text{F}-^{13}\text{C}}$ = 284 Hz, $^2J_{^{19}\text{F}-^{13}\text{C}}$ = 32 Hz). ^{119}Sn{^{1}H}-NMR (111.9 MHz, C_6D_6, 25 °C) δ = −157 (s, $\Delta_{1/2}$ = 400 Hz).

^{1}H-NMR (400.1 MHz, C_6D_6, 25 °C) δ = 6.58 (d, $J_{\text{H-H}}$ = 7 Hz, $^3J_{^1\text{H}-^{119}\text{Sn}}$ = 25 Hz, 1H, H-4) 5.39 (d, $J_{\text{H-H}}$ = 7 Hz, 1H, H-3), 2.79-2.67 (m, 1H, H-5$_a$), 2.33-2.23 (m, 1H, H-6$_a$), 2.23-2.15 (m, 1H, H-5$_b$), 1.83 (br, 6H, H-7), 1.78 (s, H-7), 1.63 (s, 9H, H-9), 1.60-1.52 (m, 1H, H-6$_b$). ^{119}Sn{^{1}H}-NMR (149.2 MHz, C_6D_6, 25 °C) δ = −159 (s, $\Delta_{1/2}$ = 300 Hz).

VT-NMR: ^{119}Sn{^{1}H}-NMR (149.2 MHz, C_7D_8) T = 298 K: −159 (s, $\Delta_{1/2}$ = 300 Hz). T = 288 K: −161 (s, $\Delta_{1/2}$ = 300 Hz), T= 278 K: −164 (s, $\Delta_{1/2}$ = 260 Hz), T = 268 K: −167 (s, $\Delta_{1/2}$ = 200 Hz). The proton resonances from the VT NMR experiment are not listed, since in the observed temperature range, the broadening of the (H-7) proton resonances from $-\text{N(Me)}_2$ (δ^1H = 1.83 at r.t.) was the only significant event, as explained in the main text.

(EI, 20 eV) m/z (rel. Int., fragment-ion):

$L-\text{Sn}-\text{SC}_4\text{H}_9$: 418 (10, [M]$^+$); 329 (80, [M$-SC_4H_9$]$^+$); 209 (2, [M$-$SnSC$_4H_9$ or $-$[L]$^+$). $\text{Sn(SC}_4\text{H}_9)_4$: 476 (15, [M]$^+$); 387 (24, [M$-SC_4H_9$]$^+$); 275 (24, [M$-2\,C_4H_8$, -SC$_4H_9$]); 241 (8, [M$-C_4H_8$ $-2\,$SC$_4$H$_9$]; 219 (8, [M$-$SC$_4$H$_9$ $-3\,$C$_4$H$_8$]); 178 [(SC$_4$H$_9)_2$]$^+$.

Elemental Analysis: Calcd. for $C_{12}H_{21}F_3N_2OSSn$: C, 34.55 %; H, 5.09 %; N, 6.72 %; S, 7.6 %. Found: C, 34.63 %; H, 5.09 %; N, 6.97 %; S, 8.23 %.

9.4.6 Synthesis of Pb[N(SiMe$_3$)$_2$]$_2$

The modified synthesized route to lithium-free Pb[N(SiMe$_3$)$_2$]$_2$[143,196] is described below. Hereby Li[N(SiMe$_3$)$_2$] was in-situ generated by reacting *n*-BuLi with H[N(SiMe$_3$)$_2$].

$$\text{PbCl}_2 + 2\,\text{Li[N(SiMe}_3)_2] \xrightarrow[-2\,\text{LiBr}]{\text{THF/diethyl ether, 0 °C}} \text{Pb[N(SiMe}_3)_2]_2$$
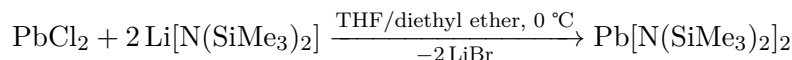
In a 250 mL round-bottom flask PbCl$_2$ (11.76 g, 42.29 mmol) was evacuated for 1 h on the vacuum line to remove surface absorbed water, and suspended afterwards in 20 mL dry THF. In a 100 mL round-bottom flask H[N(SiMe$_3$)$_2$] (22.03 g, 28.46 mL, 84.57 mmol) was cooled down for 0.5 h by a dewar bowl filled with crushed-ice, then n-BuLi (33.83 mL of 2.5 M solution in hexane, 84.57 mmol) was added from a plastic syringe. Whereafter the outer ice-bath was removed, and the suspension was stirred vigorously for 30 min to become a clear solution. Then the n-hexane was removed under reduced pressure until next to the colorless solid only minor amounts of solvent were present. Then the outer ice-cooling was reapplied, and it was begun to add first slowly minor amounts of the PbCl$_2$-THF suspension and later in larger

portions. The yellow suspension was allowed to come to the room temperature and continued stirring overnight. Then all volatile compounds were removed under reduced pressure to yield a bright orange solid. Minor amounts of remaining $PbCl_2$ were flushed with 30 mL n-heptane into the flask with the orange solid and stirred for 2 h. The stirring was stopped and when the solid settled down the orange supernatant was decanted into a newly attached flask to the cross and the volatile compounds were removed under reduced pressure. The extraction procedure was repeated with another 30 mL of n-heptane and afterwards four times with 30 mL n-pentane. Hereby, if kept too long in n-pentane the precipitation of a black solid was observed. The residue of the hydrocarbon extraction procedure was a brown-orange viscous solid, which was evacuated for two days partially by warming with an outer water bath ($T_{water} = 60\,°C$) until the fierce foaming and reboiling was observed no more. This was further purified by distillation under dynamic vacuum at an outer oil-bath temperature between ($T_{oil} = 80$–$90\,°C$), to yield a yellow oil (13.38 g, 59 % yield). In the ^{7}Li-NMR spectrum there was a signal and in the 1H-NMR spectra the resonances of THF were still present, when the distillation product was checked for purity by dissolving in benzene-d_6. (Here it was decided to substitute diethyl ether for THF, which is advised to do so from the very start of the reaction) Then $PbCl_2$ (1.74 g, 6.27 mmol) were suspended in 17 mL diethyl ether and added to the yellow oil, stirred for 1 h allowed to settle down, decanted into a new flask and the volatile compounds removed under reduced pressure. The next day again $PbCl_2$ (1.46 g, 5.25 mmol) were added to the reaction mixture, followed by the two-fold addition of 10 mL n-pentane for the extraction procedure. The extracted orange oil was purified by distillation at an outer oil-bath temperature of ($T_{oil} = 92\,°C$). The distillation product was obtained as a yellow oil (10.56 g, 47 % yield) that was easily converted into a yellow solid by shortly immersing into liquid nitrogen, for better practical handling afterwards. $Pb[N(SiMe_3)_2]_2$: ^{1}H-NMR (300.1 MHz, C_6D_6, 25 °C): $\delta = 0.25$ (s). $^{207}Pb\{^1H\}$-NMR (62.9 MHz, C_6D_6, 25 °C): $\delta = 4906$. ^{13}C-APT-NMR (75.7 MHz, C_6D_6, 25 °C): $\delta = 5.34$. $^{29}Si\{^1H\}$-DEPT45-NMR (59.6 MHz, C_6D_6, 25 °C): $\delta = -4.78$ (s, $^1J_{^{29}Si-^{13}C} = 55$ Hz, $^2J_{^{29}Si-^{207}Pb} = 29$ Hz).

9.4.7 Synthesis of the molecules (3a)–(3c)

The molecules (**3a**)–(**3c**) were synthesized via protolysis of $Pb[N(SiMe_3)_2]_2$, which was synthesized as previously reported and described above.[143,196]

$$Pb[N(SiMe_3)_2]_2 + 2\,HSR \xrightarrow[-2\,HN(SiMe_3)_2]{THF,\ 0\ °C} \underset{(\textbf{3a})\ R = \text{-}Bu^t,\ (\textbf{3b})\ R = \text{-}Pr^i,\ (\textbf{3c})\ R = \text{-}Bu^i}{Pb(SR)_2}$$
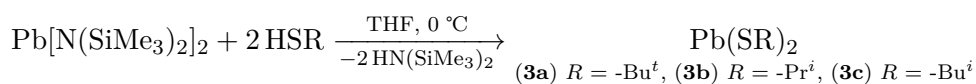
To an ice-cooled solution of $Pb[N(SiMe_3)_2]_2$ (3.318 g, 6.284 mmol) in 18 mL THF was added dropwise the corresponding amount of thiol in slight excess (**3a**: $HSBu^t$, $\rho = 0.80\,gcm^{-3}$: 1.190 g, 13.021 mmol; **3b**: $HSPr^i$, $\rho = 0.82\,gcm^{-3}$: 0.970 g, 12.923 mmol; **3c**: $HSBu^i$, $\rho = 0.83\,gcm^{-3}$: 1.247 g, 13.829 mmol). The bright yellow solution was stirred for 15 min. in the cold and then was allowed to warm up to room temperature and stirred for further 30 min. before the solvent and volatile by-products were removed under reduced pressure. The fine yellow powder of (**3a**)–(**3c**) was obtained in near quantitative yield in each case and was not further purified, also based on the assessment of the ^{1}H- and ^{13}C-NMR spectra. (**3a**) Bis(*tert*-butylthiolato)lead(II) $Pb(SC_4H_9)_2$: ^{1}H-NMR (300.1 MHz, $CDCl_3$, 25 °C): $\delta = 1.53$ (s).^{13}C-APT-NMR (75.7 MHz, $CDCl_3$, 25 °C): $\delta = 38.2$ ($-CH_3$), 46.0 (C_q). ^{207}Pb-NMR (125.9 MHz, $CDCl_3$, 25 °C): $\delta = 3002$ ($\Delta_{1/2} = 560$ Hz).

Elemental analysis: Calcd.: C 24.92 % H 4.71 % S 16.63 %. Found: C 25.06 %, H 4.79 %, S 16.24 %.

(**3b**) Bis(*iso*-propylthiolato)lead(II) $Pb(SC_3H_7)_2$: ^{1}H-NMR (300.1 MHz, CDCl$_3$, 25 °C): $\delta = 1.43$ (d, $^3J_{\text{H-H}} = 7$ Hz, 6H; CH$_3$), 4.12 (sept, $^3J_{\text{H-H}} = 7$ Hz, 1H; CH).^{13}C-APT-NMR (75.7 MHz, CDCl$_3$, 25 °C): $\delta = 30.9$ (CH$_3$), 35.2 (CH).

EI-MS (20 eV): m/z (%): 358 (10) [M]$^+$, 315 (20) [Pb(S)(SC$_3$H$_7$)]$^+$, 282 (26) [Pb(SC$_3$H$_6$)]$^+$, 273 (24) [Pb(S)(SH)]$^+$, 241 (38) [Pb(SH)]$^+$, 208 (18) [Pb]$^+$.

Elemental analysis: Calcd.: C 20.17 % H 3.92 % S 17.92 %. Found: C 20.45 %, H 4.03 %, S 17.50 %.

(**3c**) Bis(*iso*-butylthiolato)lead(II) $Pb(SC_4H_9)_2$: ^{1}H-NMR (300.1 MHz, CDCl$_3$, 25 °C): $\delta = 1.02$ (d, $^3J_{\text{H-H}} = 7$ Hz, 6H; CH$_3$), 1.80 (sept, $^3J_{\text{H-H}} = 7$ Hz, 1H; CH), 3.50 (d, $^3J_{\text{H-H}} = 7$ Hz, 2H; CH$_2$), ^{13}C-APT-NMR (75.7 MHz, CDCl$_3$, 25 °C): $\delta = 22.0$ ($-$CH$_3$), 33.7 (-CH), 38.1 ($-$CH$_2$). ^{207}Pb$\{^1$H$\}$-NMR (62.9 MHz, CDCl$_3$, 25 °C): $\delta = 2387$ ($\Delta_{1/2} = 2700$ Hz).

EI-MS (20 eV) m/z (%): a) measured range $m/z = 300 - 780$: 683 (20) [Pb$_2$(S$_2$C$_{12}$H$_{27}$)]$^+$, 591 (100) [Pb$_2$(S$_2$C$_8$H$_{16}$)]$^+$, 535 (8) [Pb$_2$(S$_2$C$_4$H$_7$)]$^+$, 445 (19) [Pb(SC$_4$H$_9$)$_2$(SC$_2$H$_3$)]$^+$, 386 (55) [Pb(SC$_4$H$_9$)$_2$]$^+$, 329 (35) [Pb(S)(SC$_4$H$_9$)]$^+$. b) measured range $m/z = 300 - 0$: 296 (17) [Pb(SC$_4$H$_8$)]$^+$, 273 (2) [Pb(S)(SH)]$^+$, 241 (4) [Pb(SH)]$^+$, 208 (4) [Pb]$^+$.

Elemental analysis: Calcd.: C 24.92 % H 4.71 % S 16.63 %. Found: C 25.40 %, H 4.96 %, S 16.00 %.

9.4.8 Sample Preparation for the NMR Titration and Dilution Experiments

The samples were partially prepared freshly in a nitrogen filled glovebox from MBraun before measuring. When the contamination by atmospheric moisture and oxygen was observed to be of minor influence the preparation outside the glovebox was preferred. For this either a N$_2$-shower technique or saturation of the NMR-tube and reaction vessels by an Ar (g)-layer was applied. The titration experiments were performed adding the corresponding amount of solid MAI or CsI into the same NMR-tube for one experiment and measured when all solid was dissolved. Towards the end of the titrations a noticeable increase of the sample volume was observed, which was not considered in the volume and concentration calculations. The precursors were dissolved in deuterated solvents in the desired stoichiometry and stirred at room temperature until clear solutions were obtained, towards the end of titrations especially when applying CsI the reaction vessels or NMR tubes were immersed into a ultrasonification or water bath at T = 60 °C to achieve dissolution of the precursor. The solutions were then filled into a glass 5-mm-NMR tube. Exemplary description of the NMR titration experiments: $c(\text{PbI}_2) = 0.8$ M: In a glass vial PbI$_2$ (369.5 mg, 0.8 mmol) was dissolved in 1.0 mL DMSO-d$_6$ (DMF-d$_7$), then 0.6 mL of this solution was transferred into a NMR tube. $c(\text{PbI}_2 + \text{AI}) = 0.8$ M: After measuring the chemical shifts, when the NMR tube was recollected from the spectrometer (AI = CsI : 124.80 mg, 0.48 mmol; AI = MAI: 76.32 mg, 0.48 mmol) was added to the solution in the NMR tube, and the chemical shifts were measured. Then the corresponding amount of CsI (MAI) (Tables B.7 to B.14) was increased by repeating the procedure, while the amount of PbI$_2$ was kept constant. There are few NMR measurements by Feray Ünlü involved in the NMR data, reminiscent of a cooperation that was initially intended.

References

[1] S. Hadke, M. Huang, C. Chen, Y. F. Tay, S. Chen, J. Tang, L. Wong, *Chem. Rev.* **2021**, *122*, 10170–10265.

[2] T. K. S. Wong, S. Zhuk in *Sulfide and Selenide Based Materials for Emerging Applications*, (Eds.: G. Dalapati, T. Shun Wong, S. Kundu, A. Chakraborty, S. Zhuk), Elsevier, **2022**, pp. 195–242.

[3] V. Steinmann, R. Chakraborty, P. H. Rekemeyer, K. Hartman, R. E. Brandt, A. Polizzotti, C. Yang, T. Moriarty, S. Gradečak, R. G. Gordon, T. Buonassisi, *ACS Appl. Mater. Interfaces* **2016**, *8*, 22664–22670.

[4] M.-R. Gao, Y.-F. Xu, J. Jiang, S.-H. Yu, *Chem. Soc. Rev.* **2013**, *42*, 2986.

[5] A. M. Ganose, C. N. Savory, D. O. Scanlon, *Chem. Commun.* **2017**, *53*, 20–44.

[6] K. Ramasamy, M. A. Malik, N. Revaprasadu, P. O'Brien, *Chem. Mater.* **2013**, *25*, 3551–3569.

[7] L. Müchler, H. Zhang, S. Chadov, B. Yan, F. Casper, J. Kübler, S.-C. Zhang, C. Felser, *Angew. Chem., Int. Ed.* **2012**, *51*, 7221–7225.

[8] A. Isaeva, B. Rasche, M. Ruck, *Phys. Status Solidi RRL* **2013**, *7*, 39–49.

[9] S. Kazim, M. K. Nazeeruddin, M. Grätzel, S. Ahmad, *Angew. Chem., Int. Ed.* **2014**, *53*, 2812–2824.

[10] R. E. Brandt, V. Stevanović, D. S. Ginley, T. Buonassisi, *MRS Commun.* **2015**, *5*, 265–275.

[11] J. M. Frost, K. T. Butler, F. Brivio, C. H. Hendon, M. van Schilfgaarde, A. Walsh, *Nano Lett.* **2014**, *14*, 2584–2590.

[12] N. Cates, M. Bernechea, *APL Materials* **2018**, *6*, 084503.

[13] H. T. Shaban, M. M. Nassary, M. S. El-Sadek, *Phys. B (Amsterdam, Neth.)* **2008**, *403*, 1655–1659.

[14] M. A. Tumelero, R. Faccio, A. A. Pasa, *J. Phys. Chem. C* **2016**, *120*, 1390–1399.

[15] M. Ritala, J. Niinisto, S. Krumdieck, P. Chalker, H Aspinall, M. E. Pemble, W. L. Gladfelter, B. Leese, R. A. Fischer, H. Parala, R. Kanjolia, R. D. Dupuis, S. E. Alexandrov, S. J. C. Irvine, R. Palgrave, I. P. Parkin, *Chemical Vapour Deposition, Precursors, Processes and Applications*, (Eds.: A. C. Jones, M. L. Hitchman), The Royal Society of Chemistry, **2009**, pp. 1–582.

[16] M. A. Malik, M. Afzaal, P. O'Brien, *Chem. Rev.* **2010**, *110*, 4417–4446.

[17] S. Schulz, *Coord. Chem. Rev.* **2015**, *297-298*, 49–76.

[18] M. Bochmann, *Chem. Vap. Deposition* **1996**, *2*, 85–96.

[19] A. N. Gleizes, *Chem. Vap. Deposition* **2000**, *6*, 155–173.

[20] V. Kupčík, L. Veselá-Nováková, *TMPM Tschermaks Mineral. und Petrogr. Mitteilungen* **1970**, *14*, 55–59.

[21] A. Kyono, M. Kimata, *Am. Mineral.* **2004**, *89*, 932–940.

[22] E. Makovicky, *Rev. Mineral. Geochem.* **2006**, *61*, 7–125.

[23] R. E. Rundle, D. H. Olson, *Inorg. Chem.* **1964**, *3*, 596–598.

[24] T. Chattopadhyay, J. Pannetier, H. V. Schnering, *J. Phys. Chem. Solids* **1986**, *47*, 879–885.

[25] Y. Noda, K. Masumoto, S. Ohba, Y. Saito, K. Toriumi, Y. Iwata, I. Shibuya, *Acta Crystallogr. Sect. C: Struct. Chem.* **1987**, *43*, 1443–1445.

[26] L. S. Ramsdell, *Am. Mineral.* **1925**, *10*, 281–304.

[27] J. Huheey, E. Keiter, R. Keiter, *Anorganische Chemie: Prinzipien von Struktur und Reaktivität*, 4th ed., (Ed.: R. Steudel), De Gruyter, **2014**.

[28] D. Reinen, M. Atanasov in *Compr. Coord. Chem. II*, (Eds.: J. A. McCleverty, T. J. Meyer), Pergamon, Oxford, **2003**, pp. 661–667.

[29] E. S. Claudio, H. A. Godwin, J. S. Magyar in *Prog. Inorg. Chem. Vol. 51*, (Ed.: K. Karlin), John Wiley & Sons, Ltd., **2002**, Chapter 1, pp. 1–144.

[30] R. S. Drago, *J. Phys. Chem.* **1958**, *62*, 353–357.

[31] M. A. Green, A. Ho-Baillie, H. J. Snaith, *Nat. Photonics* **2014**, *8*, 506–514.

[32] M. Grätzel, *Nat. Mater.* **2014**, *13*, 838–842.

[33] K. Wang, Z. Jin, L. Liang, H. Bian, D. Bai, H. Wang, J. Zhang, Q. Wang, S. Liu, *Nat. Commun.* **2018**, *9*.

[34] E. Radicchi, E. Mosconi, F. Elisei, F. Nunzi, F. De Angelis, *ACS Appl. Energy Mater.* **2019**, *2*, 3400–3409.

[35] J. C. Hamill, J. Schwartz, Y. L. Loo, *ACS Energy Lett.* **2018**, *3*, 92–97.

[36] J. Stevenson, B. Sorenson, V. H. Subramaniam, J. Raiford, P. P. Khlyabich, Y. L. Loo, P. Clancy, *Chem. Mater.* **2017**, *29*, 2435–2444.

[37] B. Wrackmeyer, *Chem. unserer Zeit* **1994**, *28*, 309–320.

[38] B. Wrackmeyer in *eMagRes*, (Eds.: R. Harris, R. Wasylishen), John Wiley & Sons, Ltd, **2007**.

[39] F. G. Riddell in *Encycl. Spectrosc. Spectrom. (3rd Ed.)* (Eds.: J. C. Lindon, G. E. Tranter, D. W. Koppenaal), Academic Press, Oxford, **2017**, pp. 239–246.

[40] B. Wrackmeyer in *Encycl. Magn. Reson.* (Eds.: R. Harris, R. Wasylishen), John Wiley & Sons, Ltd, Chichester, UK, **2011**.

[41] P. Pregosin, H. Rüegger in *Compr. Coord. Chem. II*, (Eds.: J. A. McCleverty, T. J. Meyer), Pergamon, Oxford, **2003**, pp. 1–35.

[42] P. Enghag in *Encyclopedia of the Elements*, (Ed.: P. Enghag), John Wiley & Sons, Ltd, **2004**, Chapter 3, pp. 55–78.

[43] H. A. Godwin, *Curr. Opin. Chem. Biol.* **2001**, *5*, 223–227.

[44] N. Yang, H. Sun in *Biological Chemistry of Arsenic, Antimony and Bismuth*, (Ed.: H. Sun), John Wiley & Sons, Ltd, **2010**, Chapter 3, pp. 53–81.

[45] D. A. Mulford, J. G. Jurcic, *Expert Opin. Biol. Ther.* **2004**, *4*, 95–105.

[46] Y. Kondo, S. Himeno, M. Satoh, A. Naganuma, T. Nishimura, N. Imura, *Cancer Chemoth. Pharm.* **2004**, *53*, 33–38.

[47] N. Yang, H. Sun in *Encyclopedia of Environmental Health*, (Ed.: J. Nriagu), Elsevier, Burlington, **2011**, pp. 414–420.

[48] P. Enghag in *Encyclopedia of the Elements*, (Ed.: P. Enghag), John Wiley & Sons, Ltd, **2004**, Chapter 43, pp. 949–970.

[49] S. F. Hoefler, G. Trimmel, T. Rath, *Monatsh. Chem.* **2017**, *148*, 795–826.

[50] Z. Shi, J. Guo, Y. Chen, Q. Li, Y. Pan, H. Zhang, Y. Xia, W. Huang, *Adv. Mater.* **2017**, *29*, 1605005.

[51] A. D. Ballantyne, J. P. Hallett, D. J. Riley, N. Shah, D. J. Payne, *R. Soc. Open Sci.* **2018**, *5*, 171368.

[52] recyclingtoday.com, News and Information for Recycling Professionals, can be found under https://www.recyclingtoday.com/article/battery-council-international-lead-battery-recycling/, **2022**.

[53] eurobat.org, Association of European Automotive and Industrial Battery Manufacturers, can be found under https://www.eurobat.org/resource/lead-battery-industry-and-value-chain-establish-global-material-stewardship-programme/, **2022**.

[54] M. Claesson, *Bull. Soc. Chim. Fr.* **1876**, *25*, 183–187.

[55] P. Claesson, *Arch. Pharm.* **1878**, *213*, 59–62.

[56] P. Klason, *Ber. Dtsch. Chem. Ges.* **1887**, *20*, 3407–3413.

[57] M. E. Rincón, P. K. Nair, *Semicond. Sci. Technol.* **1997**, *12*, 467–474.

[58] S. Ten Haaf, H. Sträter, R. Brüggemann, G. H. Bauer, C. Felser, G. Jakob, *Thin Solid Films* **2013**, *535*, 394–397.

[59] A. F. Janzen, O. C. Vaidya, C. J. Willis, *J. Inorg. Nucl. Chem.* **1981**, *43*, 1469–1471.

[60] Q. Yang, C. Hu, S. Wang, Y. Xi, K. Zhang, *J. Phys. Chem. C* **2013**, *117*, 5515–5520.

[61] M.-R. R. Gao, S.-H. H. Yu, J. Yuan, W. Zhang, M. Antonietti, *Angew. Chem., Int. Ed.* **2016**, *55*, 12812–12816.

[62] H. H. Yu, J. Wang, T. Wang, H. H. Yu, J. Yang, G. Liu, G. Qiao, Q. Yang, X. Cheng, *CrystEngComm* **2017**, *19*, 727–733.

[63] J. Chao, S. Xing, J. Zhao, C. Qin, D. Duan, Y. Zhao, Q. He, *RSC Adv.* **2016**, *6*, 55676–55681.

[64] D. C. Onwudiwe, O. A. Oyewo, U. Atamtürk, O. Ojelere, S. Mathur, *J. Environ. Chem. Eng.* **2020**, *8*, 103816.

[65] Y. Li, Y. Deng, X. Zhang, G. Ying, Z. Wang, J. Zhang, *Electrochim. Acta* **2021**, *366*, 137406.

[66] K. L. Liu, F. Chen, Y. Liu, D. Li, W. D. Shi, *CrystEngComm* **2017**, *19*, 570–575.

[67] W. Chai, F. Yang, W. Yin, S. You, K. Wang, W. Ye, Y. Rui, B. Tang, *Dalton Trans.* **2019**, *48*, 1906–1914.

[68] S. Wang, W. Li, H. Song, C. Mao, Z. Zhang, H. Peng, G. Li, *Inorg. Chem. Front.* **2019**, *6*, 1275–1281.

[69] W. Luo, F. Li, Q. Li, X. Wang, W. Yang, L. Zhou, L. Mai, *ACS Appl. Mater. Interfaces* **2018**, *10*, 7201–7207.

[70] J. Luo, X. Feng, H. Kan, H. Li, C. Fu, *IEEE Sensors Journal* **2021**, *21*, 1404–1408.

[71] K. Yao, W. W. Gong, Y. F. Hu, X. L. Liang, Q. Chen, L. M. Peng, *J. Phys. Chem. C* **2008**, *112*, 8721–8724.

[72] N. Loudhaief, M. Ben Salem, *Appl. Phys. A Mater. Sci. Process.* **2021**, *127*, 1–11.

[73] A. A. Tahir, M. A. Ehsan, M. Mazhar, K. G. U. Wijayantha, M. Zeller, A. D. Hunter, *Chem. Mater.* **2010**, *22*, 5084–5092.

[74] X. Yu, C. Cao, *Cryst. Growth Des.* **2008**, *8*, 3951–3955.

[75] G. Konstantatos, L. Levina, J. Tang, E. H. Sargent, *Nano Lett.* **2008**, *8*, 4002–4006.

[76] J. Chen, L. M. Wu, L. Chen, *Inorg. Chem.* **2007**, *46*, 586–591.

[77] M. B. Sigman, B. A. Korgel, *Chem. Mater.* **2005**, *17*, 1655–1660.

[78] H. Suzuki, N. Komatsu, T. Ogawa, T. Murafuji, T. Ikegami, Y. Matano, *Organobismuth Chemistry*, Elsevier Science, **2001**, p. 636.

[79] G. Kraeuter, P. Favreau, W. S. J. Rees, *Chem. Mater.* **1994**, *6*, 543–549.

[80] T. Hatanpää, M. Vehkamäki, M. Ritala, M. Leskelä, *Dalton Trans.* **2010**, *39*, 3219.

[81] D. A. Atwood, A. H. Cowley, R. D. Hernandez, R. A. Jones, L. L. Rand, S. G. Bott, J. L. Atwood, *Inorg. Chem.* **1993**, *32*, 2972–2974.

[82] H. Sommer, A. Eichhöfer, D. Fenske, *Z. Anorg. Allg. Chem.* **2008**, *634*, 436–440.

[83] W. Clegg, M. R. Elsegood, L. J. Farrugia, F. J. Lawlor, N. C. Norman, A. J. Scott, *J. Chem. Soc., Dalton Trans.* **1995**, 2129–2135.

[84] M. Mantina, A. C. Chamberlin, R. Valero, C. J. Cramer, D. G. Truhlar, *J. Phys. Chem. A* **2009**, *113*, 5806–5812.

[85] J. Rodriguez-Castro, P. Dale, M. F. Mahon, K. C. Molloy, L. M. Peter, *Chem. Mater.* **2007**, *19*, 3219–3226.

[86] O. C. Monteiro, T. Trindade, J.-H. Park, P. O'Brien, *Chem. Vap. Deposition* **2000**, *6*, 230–232.

[87] W. N. Kun, S. Mlowe, L. D. Nyamen, M. P. Akerman, P. O'Brien, P. T. Ndifon, N. Revaprasadu, *Polyhedron* **2018**, *154*, 173–181.

[88] Y. W. Koh, C. S. Lai, A. Y. Du, E. R. T. Tiekink, K. P. Loh, *Chem. Mater.* **2003**, *15*, 4544–4554.

[89] J. Waters, D. Crouch, J. Raftery, P. O'Brien, *Chem. Mater.* **2004**, *16*, 3289–3298.

[90] O. C. Monteiro, T. Trindade, J.-H. Park, P. O'Brien, *Mater. Lett.* **2004**, *58*, 119–122.

[91] A. Li, N. Sun, Y. Huang, Y. Qin, N. Zhao, J. Gao, M. Li, H. Zhou, L. Qi, *Adv. Funct. Mater.* **2008**, *18*, 1194–1201.

[92]   Y. Zhao, K. T. E. Chua, C. K. Gan, J. Zhang, B. Peng, Z. Peng, Q. Xiong, *Phys. Rev. B: Condens. Matter Mater. Phys.* **2011**, *84*, 205330.

[93]   K. Trentelman, *J. Raman Spectrosc.* **2009**, *40*, 585–589.

[94]   I. Zumeta-Dubé, J. L. Ortiz-Quiñonez, D. Díaz, C. Trallero-Giner, V. F. Ruiz-Ruiz, *J. Phys. Chem. C* **2014**, *118*, 30244–30252.

[95]   C. Powell, X-ray Photoelectron Spectroscopy Database XPS,Version 4.1, NIST Standard Reference Database 20, en, **1989**.

[96]   T. P. Debies, J. W. Rabalais, *Chem. Phys.* **1977**, *20*, 277–283.

[97]   J Grigas, E Talik, V Lazauskas, *Phys. Status Solidi* **2002**, *232*, 220–230.

[98]   J. soo Jung, N. moon Hwang in *Chemical Vapor Deposition*, (Ed.: S. Neralla), Springer Series in Surface Sciences, InTech, Rijeka, **2016**, Chapter 2.

[99]   J. Cheon, J. E. Gozum, G. S. Girolami, *Chem. Mater.* **1997**, *9*, 1847–1853.

[100] A. N. MacInnes, M. B. Power, A. F. Hepp, A. R. Barron, *J. Organomet. Chem.* **1993**, *449*, 95–104.

[101] H. Song, X. Zhan, D. Li, Y. Zhou, B. Yang, K. Zeng, J. Zhong, X. Miao, J. Tang, *Sol. Energy Mater. Sol. Cells* **2016**, *146*, 1–7.

[102] M. J. Frisch, G. W. Trucks, H. B. Schlegel, G. E. Scuseria, M. A. Robb, J. R. Cheeseman, G. Scalmani, V. Barone, G. A. Petersson, H. Nakatsuji, X. Li, M. Caricato, A. V. Marenich, J. Bloino, B. G. Janesko, R. Gomperts, B. Mennucci, H. P. Hratchian, J. V., Gaussian 16, **2016**.

[103] M. Turks, C. J. Exner, C. Hamel, P. Vogel, *Synthesis* **2009**, *2009*, 1065–1074.

[104] S. Wang, B. Y. Cheng, M. Sršen, B. König, *J. Am. Chem. Soc.* **2020**, *142*, 7524–7531.

[105] F. C. Meldrum, H. Cölfen, *Chem. Rev.* **2008**, *108*, 4332–4432.

[106] H. Cölfen, M. Antonietti, *Angew. Chem., Int. Ed.* **2005**, *44*, 5576–5591.

[107] M. Niederberger, H. Cölfen, *Phys. Chem. Chem. Phys.* **2006**, *8*, 3271–3287.

[108] T. Wang, H. Cölfen, M. Antonietti, *J. Am. Chem. Soc.* **2005**, *127*, 3246–3247.

[109] X. Ling, H. Wang, S. Huang, F. Xia, M. S. Dresselhaus, *Proc. Natl. Acad. Sci.* **2015**, *112*, 4523–4530.

[110] X. Huang, H. Woo, P. Wu, H. J. Hong, W. G. Jung, B. J. Kim, J. C. Vanel, J. W. Choi, *Sci. Rep.* **2017**, *7*, 1–9.

[111] N. Koteeswara Reddy, M. Devika, M. Prashantha, K. Ramesh, K. R. Gunasekhar, *EPJ Appl. Phys.* **2012**, *60*, 10102.

[112] J. Ning, K. Men, G. Xiao, L. Wang, Q. Dai, B. Zou, B. Liu, G. Zou, *Nanoscale* **2010**, *2*, 1699–1703.

[113] J. Xia, X. Z. Li, X. Huang, N. Mao, D. D. Zhu, L. Wang, H. Xu, X. M. Meng, *Nanoscale* **2016**, *8*, 2063–2070.

[114] H. Wiedemeier, H. Georg, G. von Schnering, *Z. Kristallogr. - Cryst. Mater.* **1978**, *148*, 295–304.

[115] S. Manzeli, D. Ovchinnikov, D. Pasquier, O. V. Yazyev, A. Kis, *Nat. Rev. Mater.* **2017**, *2*, 1–15.

[116] V. Brune, M. Grosch, R. Weißing, F. Hartl, M. Frank, S. Mishra, S. Mathur, *Dalton Trans.* **2021**, *6*, 16087–16093.

[117] Y. Shan, Y. Li, H. Pang, *Adv. Funct. Mater.* **2020**, *30*, 2001298.

[118] S. F. Wang, W. Wang, W. K. Fong, Y. Yu, C. Surya, *Sci. Rep.* **2017**, *7*, 1–10.

[119] A. S. Sarkar, E. Stratakis, *Adv. Sci.* **2020**, *7*, 2001655.

[120] H. Choi, N. Lee, H. Park, Y. Choi, K. Kim, Y. Choi, J. Kim, S. Song, H. Yuk, H. Jeon, *Appl. Sci.* **2019**, *9*, 4606.

[121] M. Ichimura, K. Takeuchi, Y. Ono, E. Arai, *Thin Solid Films* **2000**, *361*, 98–101.

[122] D. Avellaneda, M. T. S. Nair, P. K. Nair, *J. Electrochem. Soc.* **2008**, *155*, D517.

[123] A. N. Mariano, K. L. Chopra, *Appl. Phys. Lett.* **1967**, *10*, 282–284.

[124] C. Gao, H. Shen, L. Sun, *Appl. Surf. Sci.* **2011**, *257*, 6750–6755.

[125] S. Polivtseva, A. Katerski, E. Kärber, I. Oja Acik, A. Mere, V. Mikli, M. Krunks, *Thin Solid Films* **2017**, *633*, 179–184.

[126] P. Jain, P. Arun, *Thin Solid Films* **2013**, *548*, 241–246.

[127] H. Zhang, Y. Balaji, A. Nalin Mehta, M. Heyns, M. Caymax, I. Radu, W. Vandervorst, A. Delabie, *J. Mater. Chem. C* **2018**, *6*, 6172–6178.

[128] L. S. Price, I. P. Parkin, A. M. Hardy, R. J. Clark, T. G. Hibbert, K. C. Molloy, *Chem. Mater.* **1999**, *11*, 1792–1799.

[129] G. Barone, T. G. Hibbert, M. F. Mahon, K. C. Molloy, I. P. Parkin, L. S. Price, I. Silaghi-Dumitrescu, *J. Chem. Soc., Dalton Trans.* **2001**, 3435–3445.

[130] J. H. Park, S. G. Kang, Y. K. Lee, T. M. Chung, B. K. Park, C. G. Kim, *Inorg. Chem.* **2020**, *59*, 3513–3517.

[131] J. Park, M. Song, W. M. Jung, W. Y. Lee, J. Lee, H. Kim, I. W. Shim, *Bull. Korean Chem. Soc.* **2012**, *33*, 3383–3386.

[132] F. Robinson, P. J. Curran, C. H. De Groot, D. Hardie, A. L. Hector, K. Holloway, R. Huang, D. Newbrook, G. Reid, *Mater. Adv.* **2021**, *2*, 4814–4823.

[133] A. L. Catherall, S. Harris, M. S. Hill, A. L. Johnson, M. F. Mahon, *Cryst. Growth Des.* **2017**, *17*, 5544–5551.

[134] P. Kevin, D. J. Lewis, J. Raftery, M. Azad Malik, P. O'Brien, *J. Cryst. Growth* **2015**, *415*, 93–99.

[135] K. Ramasamy, V. L. Kuznetsov, K. Gopal, M. A. Malik, J. Raftery, P. P. Edwards, P. O'Brien, *Chem. Mater.* **2013**, *25*, 266–276.

[136] B. P. Bade, S. S. Garje, Y. S. Niwate, M. Afzaal, P. O'Brien, *Chem. Vap. Deposition* **2008**, *14*, 292–295.

[137] I. Y. Ahmet, M. Guc, Y. Sánchez, M. Neuschitzer, V. Izquierdo-Roca, E. Saucedo, A. L. Johnson, *RSC Adv.* **2019**, *9*, 14899–14909.

[138] I. Y. Ahmet, M. S. Hill, A. L. Johnson, L. M. Peter, *Chem. Mater.* **2015**, *27*, 7680–7688.

[139] A. T. Kana, T. G. Hibbert, M. F. Mahon, K. C. Molloy, I. P. Parkin, L. S. Price, *Polyhedron* **2001**, *20*, 2989–2995.

[140] T. G. Hibbert, M. F. Mahon, K. C. Molloy, L. S. Price, I. P. Parkin, *J. Mater. Chem.* **2001**, *11*, 469–473.

[141] I. P. Parkin, L. S. Price, T. G. Hibbert, K. C. Molloy, *J. Mater. Chem.* **2001**, *11*, 1486–1490.

[142] M. Frank, L. Jürgensen, J. Leduc, D. Stadler, D. Graf, I. Gessner, F. Zajusch, T. Fischer, M. A. Rose, D. N. Mueller, S. Mathur, *Inorg. Chem.* **2019**, *58*, 10408–10416.

[143] D. H. Harris, M. F. Lappert, *J. Chem. Soc. Chem. Commun.* **1974**, 895–896.

[144] P. Pyykkö, M. Atsumi, *Chem. - Eur. J.* **2009**, *15*, 186–197.

[145] M. Veith, P. Hobein, R. Rösler, *Z. Naturforsch. B: J. Chem. Sci.* **1989**, *44*, 1067–1081.

[146] P. B. Hitchcock, M. F. Lappert, B. J. Samways, E. L. Weinberg, *J. Chem. Soc. Chem. Commun.* **1983**, 1492–1494.

[147] V. N. Khrustalev, I. A. Portnyagin, N. N. Zemlyansky, I. V. Borisova, M. S. Nechaev, Y. A. Ustynyuk, M. Y. Antipin, V. Lunin, *J. Organomet. Chem.* **2005**, *690*, 1172–1177.

[148] N. N. Zemlyanskii, I. V. Borisova, M. G. Kuznetsova, E. N. Khrustalev, M. Y. Antipin, Y. A. Ustynyuk, E. E. Lunin, C. Eaborn, M. S. Hill, J. D. Smith, *Russ. J. Org. Chem.* **2003**, *39*, 491–500.

[149] A. Eichhöfer, J. J. Jiang, H. Sommer, F. Weigend, O. Fuhr, D. Fenske, C. Y. Su, G. Buth, *Eur. J. Inorg. Chem.* **2010**, *2010*, 410–418.

[150] B. D. Rekken, T. M. Brown, J. C. Fettinger, F. Lips, H. M. Tuononen, R. H. Herber, P. P. Power, *J. Am. Chem. Soc.* **2013**, *135*, 10134–10148.

[151] P. A. W. Dean, J. J. Vittal, N. C. Payne, *Can. J. Chem.* **1985**, *63*, 394–400.

[152] G. Barone, T. G. Hibbert, M. F. Mahon, K. C. Molloy, L. S. Price, I. P. Parkin, A. M. Hardy, M. N. Field, *J. Mater. Chem.* **2001**, *11*, 464–468.

[153] M. M. Olmstead, P. P. Power, *Inorg. Chem.* **1984**, *23*, 413–415.

[154] N. N. Zemlyansky, I. V. Borisova, M. G. Kuznetsova, V. N. Khrustalev, Y. A. Ustynyuk, M. S. Nechaev, V. V. Lunin, J. Barrau, G. Rima, *Organometallics* **2003**, *22*, 1675–1681.

[155] C. E. Holloway, M. Melnik, *Main Gr. Met. Chem.* **1998**, *21*, 371–488.

[156] I. Persson, P. D'Angelo, D. Lundberg, *Chem. - Eur. J.* **2016**, *22*, 18583–18592.

[157] L. Wang, C. E. Kefalidis, T. Roisnel, S. Sinbandhit, L. Maron, J. F. Carpentier, Y. Sarazin, *Organometallics* **2015**, *34*, 2139–2150.

[158] W.-W. D. Mont, M. Grenz, *Chem. Ber.* **1985**, *118*, 1045–1049.

[159] N. Pieper, C. Klaus-Mrestani, M. Schürmann, K. Jurkschat, M. Biesemans, I. Verbruggen, J. C. Martins, R. Willem, *Organometallics* **1997**, *16*, 1043–1052.

[160] J. C. Meurice, J. G. Duboudin, M. Ratier, M. Pétraud, R. Willem, M. Biesemans, *Organometallics* **1999**, *18*, 1699–1704.

[161] J. C. Martins, M. Biesemans, R. Willem, *Prog. Nucl. Magn. Reson. Spectrosc.* **2000**, *36*, 271–322.

[162] N. Revathi, S. Bereznev, J. Iljina, M. Safonova, E. Mellikov, O. Volobujeva, *J. Mater. Sci. Mater. Electron.* **2013**, *24*, 4739–4744.

[163] P. Sutter, E. Sutter, *ACS Appl. Nano Mater.* **2018**, *1*, 3026–3034.

[164] H. Lee, W. Yang, J. Tan, J. Park, S. G. Shim, Y. S. Park, J. W. Yun, K. M. Kim, J. Moon, *ACS Appl. Mater. Interfaces* **2020**, *12*, 15155–15166.

[165] S. Gahlot, B. Purohit, E. Jeanneau, S. Mishra, *Chem. - Eur. J.* **2021**, *27*, 10826–10832.

[166] A. K. Rath, M. Bernechea, L. Martinez, G. Konstantatos, *Adv. Mater.* **2011**, *23*, 3712–3717.

[167] A. K. Rath, M. Bernechea, L. Martinez, F. Pelayo Garcia De Arquer, J. Osmond, G. Konstantatos, *Nat. Photonics* **2012**, *6*, 529–534.

[168] T. Blachowicz, A. Ehrmann, *Appl. Sci.* **2020**, *10*, 1743.

[169] S. M. Lee, D. H. Yeon, B. C. Mohanty, Y. S. Cho, *ACS Appl. Mater. Interfaces* **2015**, *7*, 4573–4578.

[170] N. Tripathi, M. Ando, T. Akai, K. Kamada, *ACS Appl. Nano Mater.* **2021**, *4*, 9680–9688.

[171] F. Mitri, A. De Iacovo, M. De Luca, A. Pecora, L. Colace, *Sci. Rep.* **2020**, *10*, 1–9.

[172] F. Mitri, A. De Iacovo, S. De Santis, C. Giansante, G. Sotgiu, L. Colace, *ACS Appl. Electron. Mater.* **2021**, *3*, 3234–3239.

[173] B. Jiang, X. Liu, Q. Wang, J. Cui, B. Jia, Y. Zhu, J. Feng, Y. Qiu, M. Gu, Z. Ge, J. He, *Energy Environ. Sci.* **2020**, *13*, 579–591.

[174] H. Wang, E. Schechtel, Y. Pei, G. J. Snyder, *Adv. Energy Mater.* **2013**, *3*, 488–495.

[175] A. Maier, F. Strauß, P. Kohlschreiber, C. Schedel, K. Braun, M. Scheele, *Nano Lett.* **2022**, *22*, 2809–2816.

[176] C. Dong, S. Liu, N. Barange, J. Lee, T. Pardue, X. Yi, S. Yin, F. So, *ACS Appl. Mater. Interfaces* **2019**, *11*, 44451–44457.

[177] T. Zhang, C. Ling, X. Wang, B. Feng, M. Cao, X. Xue, Q. Xue, J. Zhang, L. Zhu, C. Wang, H. Lu, W. Liu, *Adv. Mater. Technol.* **2022**, 2200250.

[178] Y. Zhou, D. Benetti, Z. Fan, H. Zhao, D. Ma, A. O. Govorov, A. Vomiero, F. Rosei, *Adv. Energy Mater.* **2016**, *6*, 1501913.

[179] J. Schornbaum, Y. Zakharko, M. Held, S. Thiemann, F. Gannott, J. Zaumseil, *Nano Lett.* **2015**, *15*, 1822–1828.

[180] F. W. Wise, *Acc. Chem. Res.* **2000**, *33*, 773–780.

[181] H. Rheinboldt, F. Mott, E. Motzkus, *Journal für praktische Chemie* **1932**, *134*, 257–281.

[182] E. Ott, E. E. Reid, *Ind. Eng. Chem.* **1930**, *22*, 878–881.

[183] P. Borgstrom, L. M. Ellis, E. E. Reid, *J. Am. Chem. Soc.* **1929**, *51*, 3649–3651.

[184] R. Otto, *Ber. Dtsch. Chem. Ges.* **1880**, *13*, 1289–1290.

[185] R. A. Shaw, M. Woods, *J. Chem. Soc. A* **1971**, 1569–1571.

[186] G. G. Briand, A. D. Smith, G. Schatte, A. J. Rossini, R. W. Schurko, M. Allison, V Uni, V Sack, N. Brunswick, C. El, *Inorg. Chem.* **2007**, *46*, 8625–8637.

[187] A. Eichhöfer, *Eur. J. Inorg. Chem.* **2005**, *4*, 1683–1688.

[188] A. D. Rae, D. C. Craig, I. G. Dance, M. L. Scudder, P. A. Dean, M. A. Kmetic, N. C. Payne, J. J. Vittal, *Acta Cryst. B* **1997**, *53*, 457–465.

[189] S. E. Appleton, G. G. Briand, A. Decken, A. S. Smith, *J. Chem. Soc., Dalton Trans.* **2004**, *4*, 3515–3520.

[190] N. I. Fainer, M. L. Kosinova, Y. M. Rumyantsev, E. G. Salman, F. A. Kuznetsov, *Thin Solid Films* **1996**, *280*, 16–19.

[191] M. Afzaal, K. Ellwood, N. L. Pickett, P. O'Brien, J. Raftery, J. Waters, *J. Mater. Chem.* **2004**, *14*, 1310–1315.

[192] N. O. Boadi, P. D. McNaughter, M. Helliwell, M. A. Malik, J. A. Awudza, P. O'Brien, *Inorg. Chim. Acta* **2016**, *453*, 439–442.

[193] T. Trindade, P. O'Brien, *Chem. Vap. Deposition* **1997**, *3*, 75–77.

[194] D. C. Onwudiwe, C. A. Strydom, *Spectrochim. Acta Part A* **2015**, *135*, 1080–1089.

[195] N. O. Boadi, M. A. Malik, P. O'Brien, J. A. Awudza, *Dalton Trans.* **2012**, *41*, 10497–10506.

[196] M. J. Gynane, D. H. Harris, M. F. Lappert, P. P. Power, P. Rivière, M. Rivière-Baudet, *J. Chem. Soc., Dalton Trans.* **1977**, 2004–2009.

[197] B. Wrackmeyer, J. Weidinger, *Z. Naturforsch. B: J. Chem. Sci.* **1997**, *52*, 947–950.

[198] P. A. Dean, J. J. Vittal, N. C. Payne, *Inorg. Chem.* **1984**, *23*, 4232–4236.

[199] J. J. I. Arsenault, P. A. W. Dean, *Can. J. Chem.* **1983**, *61*, 1516–1523.

[200] F. Jalilehvand, N. S. Sisombath, A. C. Schell, G. A. Facey, *Inorg. Chem.* **2015**, *54*, 2160–2170.

[201] K. P. Neupane, V. L. Pecoraro, *J. Inorg. Biochem.* **2011**, *105*, 1030–1034.

[202] K. P. Neupane, V. L. Pecoraro, *Angew. Chem., Int. Ed.* **2010**, *49*, 8177–8180.

[203] N. S. Sisombath, F. Jalilehvand, A. C. Schell, Q. Wu, *Inorg. Chem.* **2014**, *53*, 12459–12468.

[204] N. S. Sisombath, F. Jalilehvand, *Chem. Res. Toxicol.* **2015**, *28*, 2313–2324.

[205] M. Veith, *Chem. Rev.* **1990**, *90*, 3–16.

[206] S. C. Goel, M. Y. Chiang, W. E. Buhro, *Inorg. Chem.* **1990**, *29*, 4640–4646.

[207] M. Veith, J. Hans, L. Stahl, P. May, V. Huch, A. Sebald, *Z. Naturforsch. B: J. Chem. Sci.* **1991**, *46*, 403–424.

[208] R. Papiernik, L. G. Hubert-Pfalzgraf, M. C. Massiani, *Polyhedron* **1991**, *10*, 1657–1662.

[209] D. J. Teff, J. C. Huffman, K. G. Caulton, *J. Am. Chem. Soc.* **1996**, *118*, 4030–4035.

[210] L. Wang, S. Fadlallah, C. Bellini, C. Orione, V. Dorcet, J. F. Carpentier, Y. Sarazin, *Organometallics* **2015**, *34*, 1321–1327.

[211] T. R. Burnett, P. A. Dean, J. J. Vittal, *Can. J. Chem.* **1994**, *72*, 1127–1136.

[212] M. Giffard, N. Mercier, B. Gravoueille, E. Ripaud, J. Luc, B. Sahraoui, *CrystEngComm* **2008**, *10*, 968–971.

[213] J. Harrowfield, *Helv. Chim. Acta* **2005**, *88*, 2430–2432.

[214] J. S. Magyar, T. C. Weng, C. M. Stern, D. F. Dye, B. W. Rous, J. C. Payne, B. M. Bridgewater, A. Mijovilovich, G. Parkin, J. M. Zaleski, J. E. Penner-Hahn, H. A. Godwin, *J. Am. Chem. Soc.* **2005**, *127*, 9495–9505.

[215] J. Leciejewicz, *Acta Crystallogr.* **1961**, *14*, 1304–1304.

[216] D. J. Teff, J. C. Huffman, K. G. Caulton, *Inorg. Chem.* **1997**, *36*, 4372–4380.

[217] F. T. Edelmann, J. K. Buijink, S. A. Brooker, R. Herbst-Irmer, U. Kilimann, F. M. Bohnen, *Inorg. Chem.* **2000**, *39*, 6134–6135.

[218] S. S. Qin, J. L. Liu, F. Hu, A. Q. Jia, C. Xu, Q. F. Zhang, *J. Clust. Sci.* **2020**, *32*, 1593–1599.

[219] D. Labahn, S. Brooker, G. M. Sheldrick, H. W. Roesky, *Z. Anorg. Allg. Chem.* **1992**, *610*, 163–168.

[220] S. A. Saah, N. O. Boadi, D. Adu-Poku, C. Wilkins, *R. Soc. Open Sci.* **2019**, *6*, 190943.

[221] S. Rahimnejad, A. Kovalenko, S. M. Fores, C. Aranda, A. Guerrero, *ChemPhysChem* **2016**, *17*, 2795–2798.

[222] K. G. Stamplecoskie, J. S. Manser, P. V. Kamat, *Energy Environ. Sci.* **2015**, *8*, 208–215.

[223] N. Altounian, A. Glatfelter, S. Bai, C. Dybowski, *J. Phys. Chem. B* **2000**, *104*, 4723–4725.

[224] F. Alkan, T. Small, S. Bai, A. Dominowski, C. Dybowski, *J. Struct. Chem.* **2016**, *57*, 369–375.

[225] P. G. Harrison, M. A. Healy, A. T. Steel, *J. Chem. Soc., Dalton Trans.* **1983**, 1845–1848.

[226] W. Xu, R. F. Evilia, *Inorg. Chim. Acta* **2000**, *308*, 103–106.

[227] D. Bauer, M. Gott, J. Steinbach, C. Mamat, *Spectrochim. Acta - Part A Mol. Biomol. Spectrosc.* **2018**, *199*, 50–56.

[228] F. Coleman, G. Feng, R. W. Murphy, P. Nockemann, K. R. Seddon, M. Swadźba-Kwaśny, *Dalton Trans.* **2013**, *42*, 5025–5035.

[229] T. M. Klapötke, B. Krumm, K. Polbom, C. M. Rienäcker, *Z. Naturforsch. B: J. Chem. Sci.* **2000**, *55*, 377–382.

[230] M. A. Flatken, A. Hoell, R. Wendt, E. Härk, A. Dallmann, A. Prause, J. Pascual, E. Unger, A. Abate, *J. Mater. Chem. A* **2021**, *9*, 13477–13482.

[231] B. A. Sorenson, L. U. Yoon, E. Holmgren, J. J. Choi, P. Clancy, *J. Mater. Chem. A* **2021**, *9*, 3668–3676.

[232] O. Romiluyi, Y. Eatmon, R. Ni, B. P. Rand, P. Clancy, *J. Mater. Chem. A* **2021**, *9*, 13087–13099.

[233] F. Alkan, C. Dybowski, *J. Phys. Chem. A* **2016**, *120*, 161–168.

[234] J. J. Ackerman, T. V. Orr, V. J. Bartuska, G. E. Maciel, *J. Am. Chem. Soc.* **1979**, *101*, 341–347.

[235] J. Glaser, U. Henriksson, *J. Am. Chem. Soc.* **1981**, *103*, 6642–6649.

[236] G. E. Maciel, J. L. Dallas, *J. Am. Chem. Soc.* **1973**, *95*, 3039–3040.

[237] R. S. Macomber, *J. Chem. Educ.* **1992**, *69*, 375.

[238] A. I. Popov, *Pure Appl. Chem.* **1979**, *51*, 101–110.

[239] L. L. Soong, G. E. Leroi, A. I. Popov, *Inorg. Chem.* **1990**, *29*, 1366–1370.

[240] A. G. Vendilo, H. Rönkkömäki, M. Hannu-Kuure, M. Lajunen, Y. Asikkala, A. A. Petrov, V. G. Krasovsky, E. A. Chernikova, P. Oksman, L. H. Lajunen, K. I. Popov, *Russ. J. Coord. Chem. Khimiya* **2008**, *34*, 635–640.

[241] V. Gutmann, *The Donor-Acceptor Approach to Molecular Interactions*, Springer New York, NY, **1978**, p. 295.

[242] U. Mayer, V. Gutmann, W. Gerger, *Monatsh. Chem.* **1975**, *106*, 1235–1257.

[243] B. Wrackmeyer, K. Horchler in *Annu. Rep. NMR Spectrosc.* (Ed.: G. Webb), Annual Reports on NMR Spectroscopy C, Academic Press, **1990**, pp. 249–306.

[244] B. Wrackmeyer in *Annu. Rep. NMR Spectrosc.* Annual Reports on NMR Spectroscopy, Academic Press, **2002**, pp. 1–37.

[245] A. D. Bain, *Prog. Nucl. Magn. Reson. Spectrosc.* **2003**, *43*, 63–103.

[246] I. Bányai, *New J. Chem.* **2018**, *42*, 7569–7581.

[247] J. E. Buston, T. D. Claridge, S. J. Heyes, J. L. Bretherton, M. G. Moloney, M. Stevenson, *Magn. Reson. Chem.* **2001**, *39*, 68–76.

[248] B. Wrackmeyer, K. Horchler, A. Sebald, L. H. Merwin, *Magn. Reson. Chem.* **1990**, *28*, 465–469.

[249] C. Dybowski, G. Neue, *Prog. Nucl. Magn. Reson. Spectrosc.* **2002**, *41*, 153–170.

[250] S. P. Ong, W. D. Richards, A. Jain, G. Hautier, M. Kocher, S. Cholia, D. Gunter, V. L. Chevrier, K. A. Persson, G. Ceder, *Comput. Mater. Sci.* **2013**, *68*, 314–319.

[251] C. C. Stoumpos, C. D. Malliakas, M. G. Kanatzidis, *Inorg. Chem.* **2013**, *52*, 9019–9038.

[252] R. J. Sutton, M. R. Filip, A. A. Haghighirad, N. Sakai, B. Wenger, F. Giustino, H. J. Snaith, *ACS Energy Lett.* **2018**, *3*, 1787–1794.

[253] Y. Yamada, T. Yamada, L. Q. Phuong, N. Maruyama, H. Nishimura, A. Wakamiya, Y. Murata, Y. Kanemitsu, *J. Am. Chem. Soc.* **2015**, *137*, 10456–10459.

[254] C. Roiland, G. Trippé-Allard, K. Jemli, B. Alonso, J. C. Ameline, R. Gautier, T. Bataille, L. Le Pollès, E. Deleporte, J. Even, C. Katan, *Phys. Chem. Chem. Phys.* **2016**, *18*, 27133–27142.

[255] M. P. Hanrahan, L. Men, B. A. Rosales, J. Vela, A. J. Rossini, *Chem. Mater.* **2018**, *30*, 7005–7015.

[256] G. M. Bernard, R. E. Wasylishen, C. I. Ratcliffe, V. Terskikh, Q. Wu, J. M. Buriak, T. Hauger, *J. Phys. Chem. A* **2018**, *122*, 1560–1573.

[257] B. A. Rosales, L. Men, S. D. Cady, M. P. Hanrahan, A. J. Rossini, J. Vela, *Chem. Mater.* **2016**, *28*, 6848–6859.

[258] A. Karmakar, M. S. Dodd, X. Zhang, M. S. Oakley, M. Klobukowski, V. K. Michaelis, *Chem. Commun.* **2019**, *55*, 5079–5082.

[259] L.-M. Wu, L. Chen in *Structures and Properties of Heavy Main-Group Iodometalates*, John Wiley & Sons, Inc., **2009**, pp. 229–266.

[260] M. Szafran, A. Katrusiak, M. Szafrański, A. Katrusiak, *Phys. Rev. B: Condens. Matter Mater. Phys.* **2000**, *61*, 1026–1035.

[261] R. E. Taylor, P. A. Beckmann, S. Bai, C. Dybowski, *J. Phys. Chem. C* **2014**, *118*, 9143–9153.

[262] C. Dybowski, M. L. Smith, M. A. Hepp, E. J. Gaffney, G. Neue, D. L. Perry, *Appl. Spectrosc.* **1998**, *52*, 426–429.

[263] Y. S. Kye, S. Connolly, B. Herreros, G. S. Harbison, *Main Gr. Met. Chem.* **1999**, *22*, 373–383.

[264] M. Aebli, L. Piveteau, O. Nazarenko, B. M. Benin, F. Krieg, R. Verel, M. V. Kovalenko, *Sci. Rep.* **2020**, *10*, 1–9.

[265] D. J. Kubicki, D. Prochowicz, A. Hofstetter, S. M. Zakeeruddin, M. Grätzel, L. Emsley, *J. Am. Chem. Soc.* **2017**, *139*, 14173–14180.

[266] J. K. M. Sanders, *Modern NMR spectroscopy, a guide for chemists*, Oxford University Press, **1993**, p. 314.

[267] J. Glaser, I. Banyai, *J. Am. Chem. Soc.* **1989**, *111*, 3186–3194.

[268] J. F. Hinton in *eMagRes*, (Eds.: R. Harris, R. Wasylishen), John Wiley & Sons, Ltd, **2007**, p. 7952.

[269] J. F. Hinton, *Trends Anal. Chem.* **1982**, *1*, 288–291.

[270] L. Fielding, *Tetrahedron* **2000**, *56*, 6151–6170.

[271] L. Fielding, *Prog. Nucl. Magn. Reson. Spectrosc.* **2007**, *51*, 219–242.

[272] C. Reichardt, T. Welton in *Solvents and Solvent Effects in Organic Chemistry*, John Wiley & Sons, Ltd, **2010**, Chapter 6, pp. 359–424.

[273] M. T. Weller, O. J. Weber, P. F. Henry, A. M. Di Pumpo, T. C. Hansen, *Chem. Commun.* **2015**, *51*, 4180–4183.

[274] S. Masi, F. Aiello, A. Listorti, F. Balzano, D. Altamura, C. Giannini, R. Caliandro, G. Uccello-Barretta, A. Rizzo, S. Colella, *Chem. Sci.* **2018**, *9*, 3200–3208.

[275] W. J. DeWitte, L. Liu, E. Mei, J. L. Dye, A. I. Popov, *J. Solution Chem.* **1977**, *6*, 337–348.

[276] M. P. Williamson, *Prog. Nucl. Magn. Reson. Spectrosc.* **2013**, *73*, 1–16.

[277] R. B. Martin, *Chem. Rev.* **1996**, *96*, 3043–3064.

[278] P. Thordarson, *Chem. Soc. Rev.* **2011**, *40*, 1305–1323.

[279] H. L. Schenck, K. Hui, *J. Chem. Educ.* **2011**, *88*, 1158–1161.

[280] G. H. Nancollas, *J. Chem. Soc.* **1955**, 1458–1462.

[281] H. M. Hershenson, M. E. Smith, D. N. Hume, *J. Am. Chem. Soc.* **1953**, *75*, 507–511.

[282] Y. Rong, Z. Tang, Y. Zhao, X. Zhong, S. Venkatesan, H. Graham, M. Patton, Y. Jing, A. M. M. Guloy, Y. Yao, *Nanoscale* **2015**, *7*, 10595–10599.

[283] Y. Guo, K. Shoyama, W. Sato, Y. Matsuo, K. Inoue, K. Harano, C. Liu, H. Tanaka, E. Nakamura, *J. Am. Chem. Soc.* **2015**, *137*, 15907–15914.

[284] J. Cao, X. Jing, J. Yan, C. Hu, R. Chen, J. Yin, J. Li, N. Zheng, *J. Am. Chem. Soc.* **2016**, *138*, 9919–9926.

[285] F. Hao, C. C. Stoumpos, Z. Liu, R. P. H. Chang, M. G. Kanatzidis, *J. Am. Chem. Soc.* **2014**, *136*, 16411–16419.

[286] A. V. A. Petrov, I. P. Sokolova, N. A. Belich, G. S. Peters, P. V. Dorovatovskii, Y. V. Zubavichus, V. N. Khrustalev, A. V. A. Petrov, M. Grätzel, E. A. Goodilin, A. B. Tarasov, *J. Phys. Chem. C* **2017**, *121*, 20739–20743.

[287] H. Krautscheid, F. Vielsack, *J. Chem. Soc., Dalton Trans.* **1999**, 2731–2735.

[288] H. Krautscheid, F. Vielsack, *Z. Anorg. Allg. Chem.* **1997**, *623*, 259–263.

[289] H. Krautscheid, F. Vielsack, N. Klaassen, *Z. Anorg. Allg. Chem.* **1998**, *624*, 807–812.

[290] H. Krautscheid, F. Vielsack, *Z. Anorg. Allg. Chem.* **2000**, *626*, 3–5.

[291] H. Krautscheid, F. Vielsack, *Angew. Chem., Int. Ed.* **1995**, *34*, 2035–2037.

[292] H. Krautscheid, J.-F. Lekieffre, J. Besinger, *Z. Anorg. Allg. Chem.* **1996**, *622*, 1781–1787.

[293] H. Krautscheid, C. Lode, F. Vielsack, H. Vollmer, *J. Chem. Soc., Dalton Trans.* **2001**, 1099–1104.

[294] S. A. Fateev, A. A. Petrov, V. N. Khrustalev, P. V. Dorovatovskii, Y. V. Zubavichus, E. A. Goodilin, A. B. Tarasov, *Chem. Mater.* **2018**, *30*, 5237–5244.

[295] J. J. Dechter, J. I. Zink, *Chem. Informationsd.* **1975**, *6*, no–no.

[296] J. F. Hinton, R. W. Briggs, *J. Magn. Reson.* **1975**, *19*, 393–397.

[297] R. W. Briggs, J. F. Hinton, *J. Solution Chem.* **1978**, *7*, 1–8.

[298] P. S. Pregosin, *Coord. Chem. Rev.* **1982**, *44*, 247–291.

[299] B. Wrackmeyer in *Annu. Rep. NMR Spectrosc.* (Ed.: G. Webb), Annual Reports on NMR Spectroscopy C, Academic Press, **1999**, pp. 203–264.

[300] V. Gutmann, E. Wychera, *Inorg. Nucl. Chem. Lett.* **1966**, *2*, 257–260.

[301] V. Gutmann, G. Resch, W. Linert, *Coord. Chem. Rev.* **1982**, *43*, 133–164.

[302] G. A. Vidulich, A. Fratiello, *J. Chem. Educ.* **1978**, *55*, 672.

[303] J. C. Boubel, J. J. Delpuech, M. R. Khaddar, A. Peguy, *J. Chem. Soc. Chem. Commun.* **1971**, 1265.

[304] R. J. Stewart, C. Grieco, A. V. Larsen, G. S. Doucette, J. B. Asbury, *J. Phys. Chem. C* **2016**, *120*, 12392–12402.

[305] A. Sharenko, C. Mackeen, L. Jewell, F. Bridges, M. F. Toney, *Chem. Mater.* **2017**, *29*, 1315–1320.

[306] M. Ozaki, A. Shimazaki, M. Jung, Y. Nakaike, N. Maruyama, S. Yakumaru, A. I. Rafieh, T. Sasamori, N. Tokitoh, P. Ekanayake, Y. Murata, R. Murdey, A. Wakamiya, *Angew. Chem., Int. Ed.* **2019**, *58*, 9389–9393.

[307] A. G. Ortoll-Bloch, H. C. Herbol, B. A. Sorenson, M. Poloczek, L. A. Estroff, P. Clancy, *Cryst. Growth Des.* **2020**, *20*, 1162–1171.

[308] V. Gutmann, G. Resch, *Zeitschrift für Chemie* **1979**, *19*, 406–412.

References

[309] F. Cataldo, *Eur. Chem. Bull.* **2015**, *4*, 92–97.

[310] K. Xu, *Chem. Rev.* **2004**, *104*, 4303–4417.

[311] U. Mayer, V. Gutmann, *Monatsh. Chem.* **1970**, *101*, 912–922.

[312] A. G. Sharpe, *J. Chem. Educ.* **1990**, *67*, 309–315.

[313] Y. Marcus, *Ions in Solution and their Solvation*, Wiley, p. 312.

[314] B. G. Cox, W. E. Waghorne, *Chem. Soc. Rev.* **1980**, *9*, 381–411.

[315] M. Johnsson, I. Persson, *Inorg. Chim. Acta* **1987**, *127*, 15–24.

[316] A. Wakamiya, M. Endo, T. Sasamori, N. Tokitoh, Y. Ogomi, S. Hayase, Y. Murata, *Chem. Lett.* **2014**, *43*, 711–713.

[317] H. Miyamae, Y. Numahata, M. Nagata, *Chem. Lett.* **1980**, *9*, 663–664.

[318] G. M. Bernard, V. K. Michaelis, *Magn. Reson. Chem.* **2020**, *58*, 1203–1212.

[319] E. N. Esenturk, J. Fettinger, B. Eichhorn, *J. Am. Chem. Soc.* **2006**, *128*, 9178–9186.

[320] L. Shimoni-Livny, J. P. Glusker, C. W. Bock, *Inorg. Chem.* **1998**, *37*, 1853–1867.

[321] I. Persson, K. Lyczko, D. Lundberg, L. Eriksson, A. Pjaczek, *Inorg. Chem.* **2011**, *50*, 1058–1072.

[322] J. M. Harrowfield, B. W. Skelton, A. H. White, *J. Chem. Soc., Dalton Trans.* **1993**, 2011–2016.

[323] B. R. Vincent, K. N. Robertson, T. S. Cameron, O. Knop, *Can. J. Chem.* **1987**, *65*, 1042–1046.

[324] M. Nizam, M. Allavena, Y. Bouteiller, B. H. Suits, D. White, *J. Magn. Reson.* **1989**, *82*, 441–453.

[325] O. Dmitrenko, S. Bai, C. Dybowski, *Solid State Nucl. Magn. Reson.* **2008**, *34*, 186–190.

[326] R. K. Harris, E. D. Becker, S. M. Cabral De Menezes, P. Granger, R. E. Hoffman, K. W. Zilm, *Pure Appl. Chem.* **2008**, *80*, 59–84.

[327] K. Hirose, *Determination of Binding Constants*, (Ed.: C. Schalley), Wiley-VCH Verlag GmbH & Co. KGaA, **2007**, pp. 17–54.

[328] P. Thordarson in *Supramolecular Chemistry*, (Eds.: P. Gale, J. Steed), John Wiley & Sons, Ltd, **2012**.

[329] K. Momma, F. Izumi, *J. Appl. Crystallogr.* **2011**, *44*, 1272–1276.

[330] E. S. Claudio, M. A. Ter Horst, C. E. Forde, C. L. Stern, M. K. Zart, H. A. Godwin, *Inorg. Chem.* **2000**, *39*, 1391–1397.

[331] J. Schläfer, D. Graf, G. Fornalczyk, A. Mettenbörger, S. Mathur, *Inorg. Chem.* **2016**, *55*, 5422–5429.

[332] R. Müller, F. Hernandez-Ramirez, H. Shen, H. Du, W. Mader, S. Mathur, *Chem. Mater.* **2012**, *24*, 4028–4035.

[333] D. Graf, J. Schläfer, S. Garbe, A. Klein, S. Mathur, *Chem. Mater.* **2017**, *29*, 5877–5885.

[334] G. M. Sheldrick, *Acta Crystallogr. Sect. C: Struct. Chem.* **2015**, *71*, 3–8.

[335] G. M. Sheldrick, *Acta Crystallogr. Sect. A Found. Crystallogr.* **2008**, *64*, 112–122.

[336] G. M. Sheldrick, *Acta Crystallogr. Sect. A: Found. Adv.* **2015**, *71*, 3–8.

[337] C. B. Hübschle, G. M. Sheldrick, B. Dittrich, *J. Appl. Crystallogr.* **2011**, *44*, 1281–1284.

[338] D. Kratzert, FinalCif-v105, Program to edit and finalize CIF files for small molecule crystallography, **2022**.

[339] R. E. Mulvey, S. D. Robertson, *Angew. Chem., Int. Ed.* **2013**, *52*, 11470–11487.

[340] M. P. Coles, *Coord. Chem. Rev.* **2015**, *297-298*, 24–39.

[341] M. He, L. Protesescu, R. Caputo, F. Krumeich, M. V. Kovalenko, *Chem. Mater.* **2015**, *27*, 635–647.

[342] M. Yarema, M. V. Kovalenko, G. Hesser, D. V. Talapin, W. Heiss, *J. Am. Chem. Soc.* **2010**, *132*, 15158–15159.

[343] T. Fjeldberg, H. Hope, M. F. Lappert, P. P. Power, A. J. Thorne, *J. Chem. Soc. Chem. Commun.* **1983**, 639–641.

[344] M. Vehkamäki, T. Hatanpää, M. Ritala, M. Leskelä, *J. Mater. Chem.* **2004**, *14*, 3191–3197.

[345] D. Mootz, A. Zinnius, B. Böttcher, *Angew. Chem., Int. Ed.* **1969**, *8*, 378–379.

[346] M. Bochmann, X. Song, M. B. Hursthouse, A. Karaulov, *J. Chem. Soc., Dalton Trans.* **1995**, 1649–1652.

[347] M. J. S. Gynane, A. Hudson, M. F. Lappert, P. P. Power, H. Goldwhite, *J. Chem. Soc., Dalton Trans.* **1980**, 2428–2433.

[348] C. J. Carmalt, N. A. Compton, R. J. Errington, G. A. Fisher, I. Moenandar, N. C. Norman, K. H. Whitmire in *Inorg. Synth.* John Wiley & Sons, Inc., **2007**, pp. 98–101.

[349] W. J. Evans, D. B. Rego, J. W. Ziller, *Inorg. Chim. Acta* **2007**, *360*, 1349–1353.

[350] W. A. Herrmann, N. W. Huber, R. Anwander, T. Priermeier, *Chem. Ber.* **1993**, *126*, 1127–1130.

[351] E. Hevia, R. E. Mulvey, *Angew. Chem., Int. Ed.* **2011**, *50*, 6448–6450.

[352] H. M. Haendler, F. A. Johnson, D. S. Crocket, *J. Am. Chem. Soc.* **1958**, *80*, 2662–2664.

A Additional Experimental Data for the Chapters 3 to 5

A.1 Appendix to Chapter 3

Figure A.1: EDX spectra of Bi_2S_3 by CVD of (**1a**).
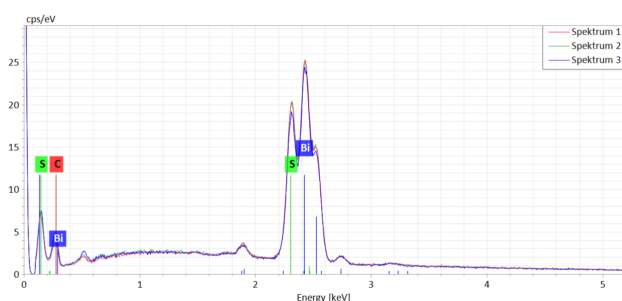
Table A.1: EDX spectra data.

Spectrum	Normalized Mass Concentration in %		
	Carbon	Sulfur	Bismuth
Spectrum 1	0.77	18.43	80.80
Spectrum 2	0.89	18.37	80.74
Spectrum 3	1.18	17.86	80.96
mean	0.94	18.22	80.83
σ	0.21	0.31	0.11
σ_{mean}	0.12	0.18	0.07
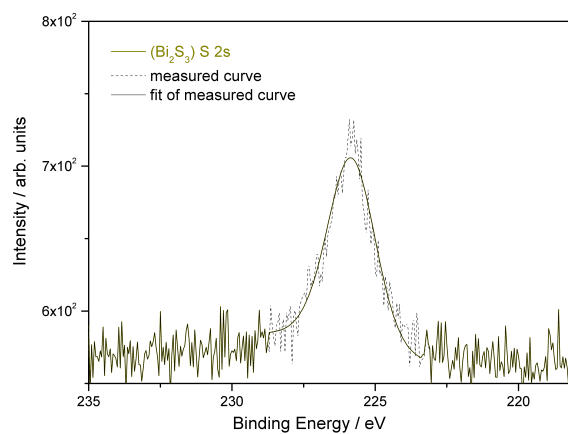
Figure A.2: High resolution XPS of the S 2s core level assigned to Bi_2S_3 from by CVD with (**1a**).
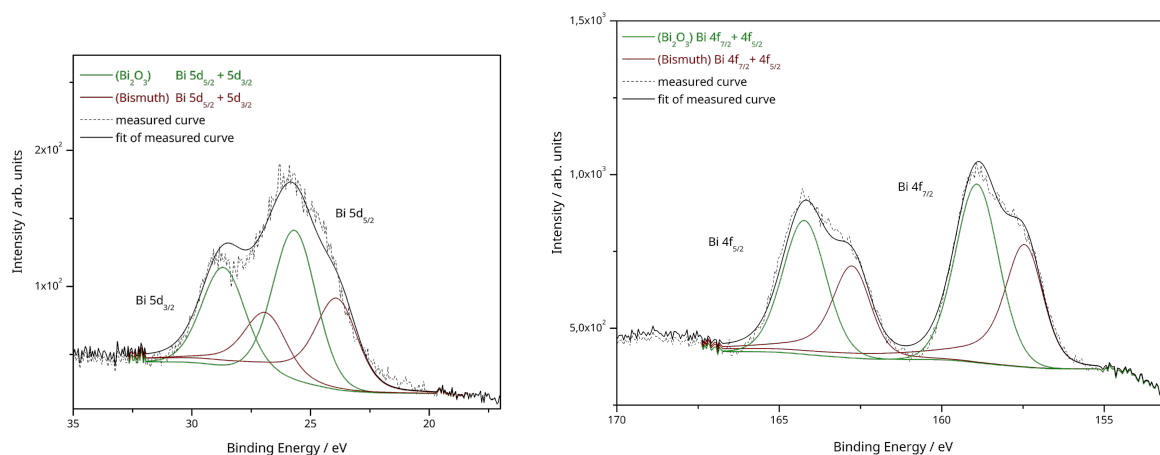
Figure A.3: High resolution XPS of the Bi 5d and 4f spin-orbit doublet assigned to bismuth from CVD with (**1b**). The oxidized surface was fit to the bismuth oxide in the form of Bi_2O_3.
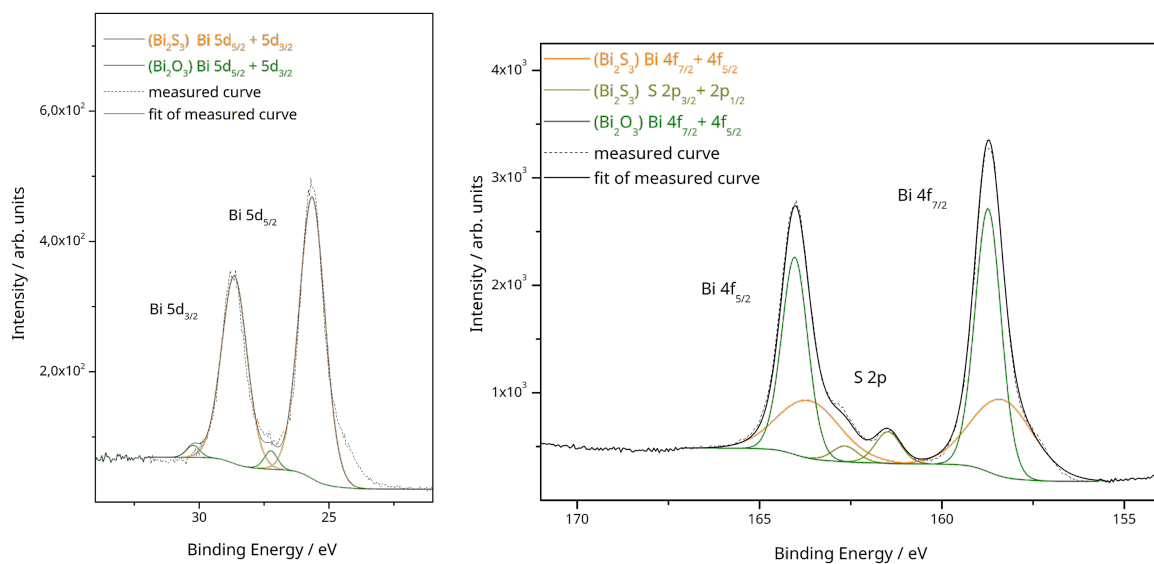
Figure A.4: High resolution XPS of the Bi 5d (*left-hand side*) and Bi 4f and S 2p spin-orbit doublets (*right-hand side*) assigned to Bi_2S_3 from by CVD with (**1a**). The oxidized surface was fit to the bismuth oxide in the form of Bi_2O_3.

Table A.2: XPS data from the layers obtained by CVD at 250 °C with the molecules (**1a**) and (**1b**).[a]

	Bi from (**1b**) BE / eV	Bi_2S_3 from (**1a**) BE / eV
Bi $5d_{5/2}$ (Bi_2S_3)		25.7
$5d_{3/2}$		28.7
Bi $5d_{5/2}$ (Bi)	23.9	
$5d_{3/2}$	26.9	
Bi $5d_{5/2}$ (Bi_2O_3)	26.0	27.2
$5d_{3/2}$	29.0	30.2
Bi $4f_{7/2}$ (Bi_2S_3)		158.3
$4f_{5/2}$		163.6
Bi $4f_{7/2}$ (Bi)	157.4	
$4f_{5/2}$	162.7	
Bi $4f_{7/2}$ (Bi_2O_3)	158.9	158.7
$4f_{5/2}$	164.2	164.0
Bi $4d_{5/2}$	441	442
$4d_{3/2}$	465	466
S $2p_{3/2}$ (Bi_2S_3)		161.5
$2p_{1/2}$		162.7
2s		225.8
O 1s	532	533
Si 2p (SiO_2)	104	104
2p (Si)	99	

[a] The four digit values were obtained from high-resolution spectra, whereas three-digit values from survey scans.
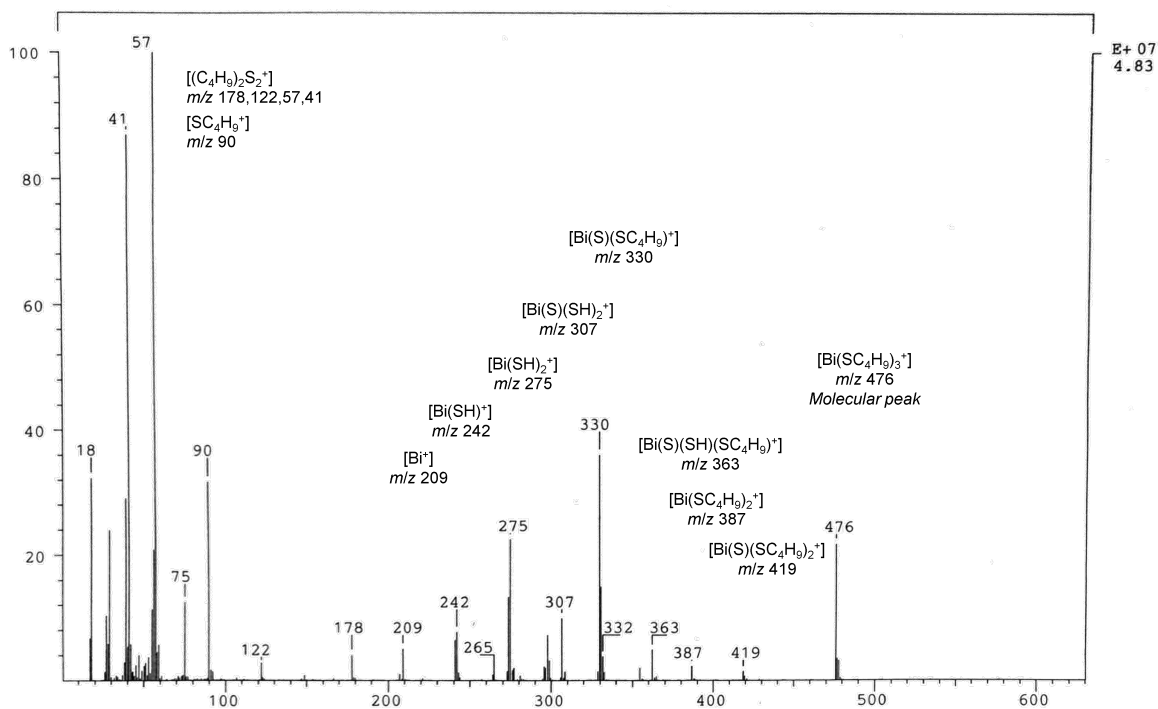
Figure A.5: Full EI-MS fragmentation pattern of Bi(SBu^t)$_3$ (**1a**).
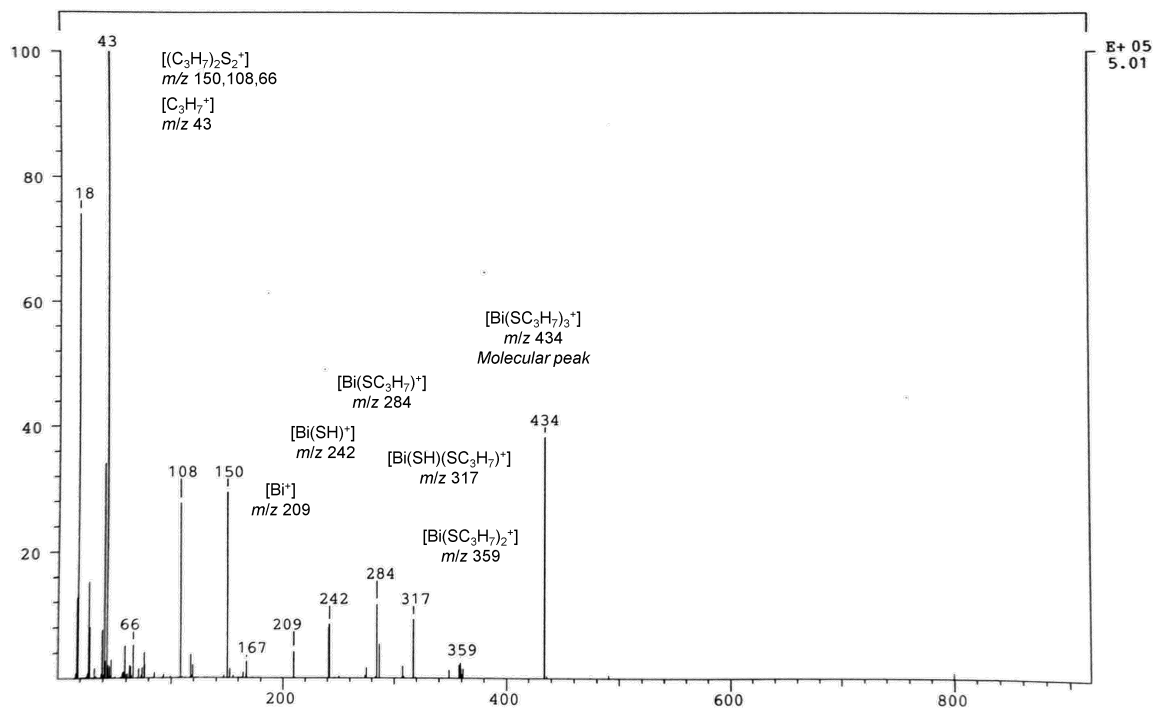
Figure A.6: Full EI-MS fragmentation pattern of Bi(SPr^i)$_3$ (**1b**).

A.2 Appendix to Chapter 4

Table A.3: Selected bond angles of (**2a**).

Atom-Atom-Atom	Bond angles /°	Atom-Atom-Atom	Bond angles /°
N(11)-Sn(1)-S(11)	84.93(7)	O(11)-Sn(1)-S(11)	90.77(6)
N(21)-Sn(2)-S(21)	83.85(7)	O(21)-Sn(2)-S(21)	91.46(6)
N(31)-Sn(3)-S(31)	83.12(6)	O(31)-Sn(3)-S(31)	92.53(6)
N(41)-Sn(4)-S(41)	84.33(7)	O(41)-Sn(4)-S(41)	91.01(6)
N(12)-Sn(1)-S(11)	88.26(7)	O(11)-Sn(1)-N(12)	154.04(8)
N(22)-Sn(2)-S(21)	86.47(7)	O(21)-Sn(2)-N(22)	154.10(9)
N(32)-Sn(3)-S(31)	87.10(6)	O(31)-Sn(3)-N(32)	153.01(8)
N(42)-Sn(4)-S(41)	87.96(6)	O(41)-Sn(4)-N(42)	153.76(9)

Mass spectrometry For $Sn(SBu^t)_4$ the literature reported[59] chemical formulae of the fragment ions is listed below. No rel. intensity and corresponding m/z values were given, the latter was added manually for comparison. $Sn(SBu^t)_4$: $[Sn(SC_4H_9)_4]^+$ ($[M]^+$, m/z 476), $[Sn(S)(SC_4H_9)_3]^+$ (m/z 419), $[Sn(SC_4H_9)_3]^+$ (m/z 387), $[Sn(SH)(SC_4H_9)_2]^+$ (m/z 331), $[Sn(SH)_2(SC_4H_9)]^+$ (m/z 275), $[Sn(SH)_3]^+$ (m/z 219). The fragment ion series (Figure A.12) generated by loss of -C_4H_9 (56 u) is accounting for a large part of the mass spectra observed for (**2a**) (Figure A.13): $[Sn(SC_4H_9)_4]^+$ (m/z 476), $[Sn(SC_4H_9)_3]^+$ (m/z 387), $[Sn(SH)(SC_4H_9)_2]^+$ (m/z 331), $[(Sn(SH)_2(SC_4H_9)]^+$ (m/z 275), $[(Sn(S)(SC_4H_9)]^+$ (m/z 241), $[Sn(SH)_3]^+$ (m/z 219). For $Sn(SBu^t)_2$ the molecular peak calculated as $[Sn(SC_4H_9)_2]^+$ (m/z 298) is absent. Two fragment ions with the corresponding chemical formulae $[(Sn(SC_4H_7)]^+$ (m/z 207) and $[(Sn(SC_8H_{16})]^+$ (m/z 296) point towards the decomposition of a dimer, calculated as $[(Sn(SC_4H_9)_2)_2]^+$ (m/z 596), which requires analysis by an extended detection range in order to draw further conclusions.
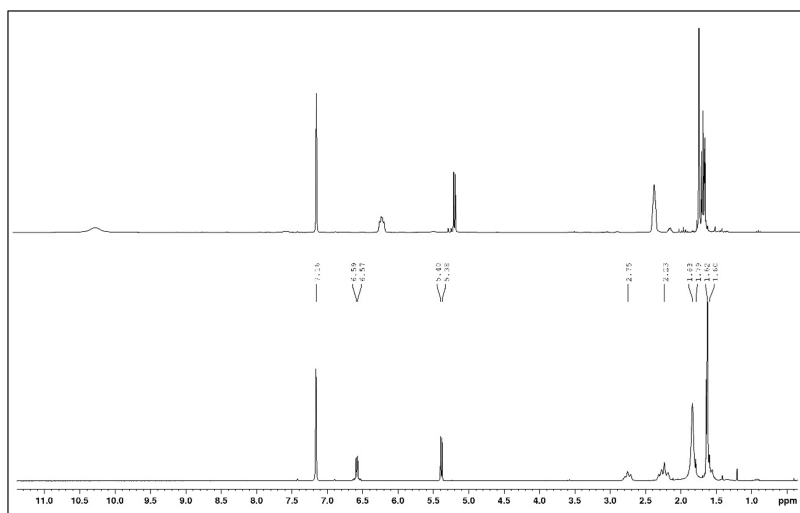
Figure A.7: Comparison of the ^{1}H-NMR spectra of *Htfb-dmeda* and (**2a**) in C_6D_6 recorded at 300 MHz.
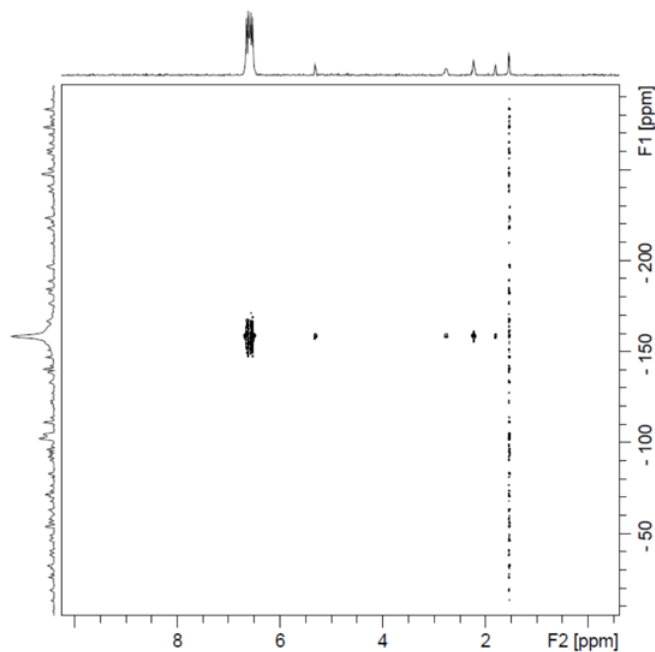
Figure A.8: ^{119}Sn,^{1}H-HMBC spectrum of (**2a**), recorded at 300 MHz.
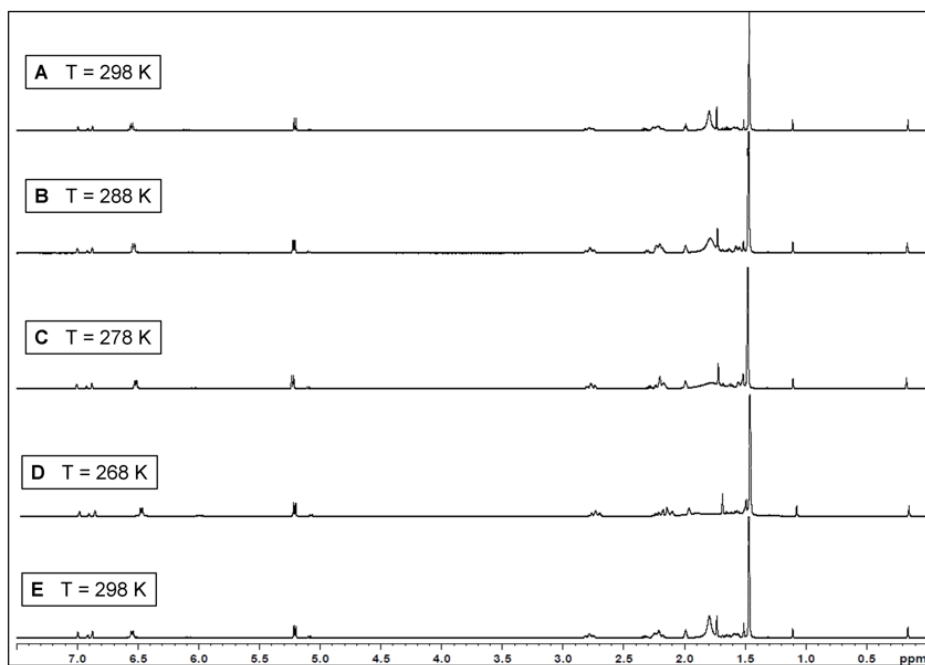
Figure A.9: ^{1}H-NMR variable temperature spectra of (**2a**) in toluene-d$_8$. The bottom spectrum at T = 298 K was recorded after cooling, when the NMR tube was warmed up to room temperature again, showing the full reversibility of the observed equilibria.
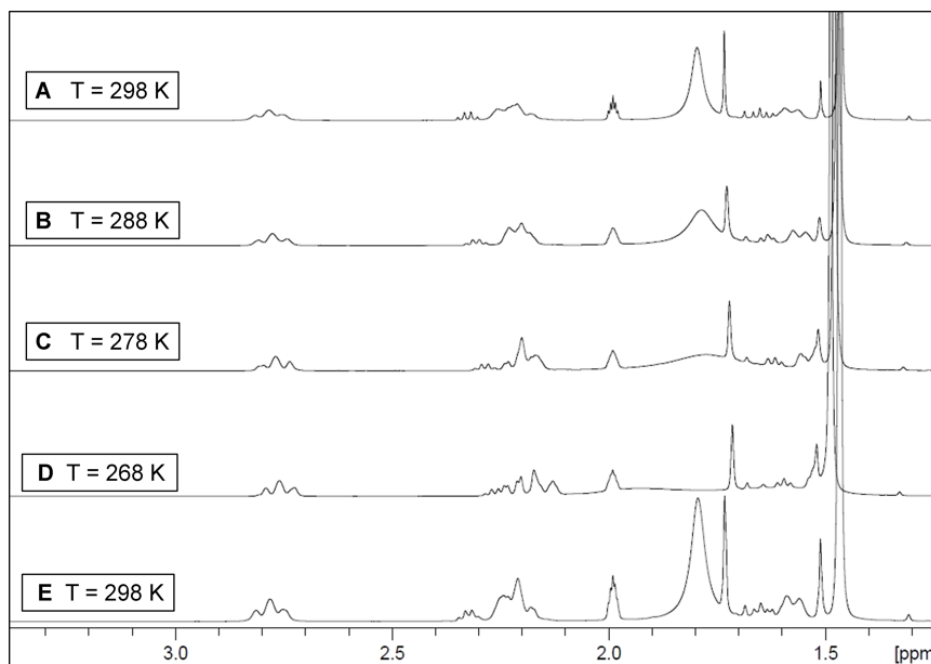
Figure A.10: Enlarged part of the ^{1}H-NMR variable temperature spectra of (**2a**) shown in (Figure A.9) for better visualization.
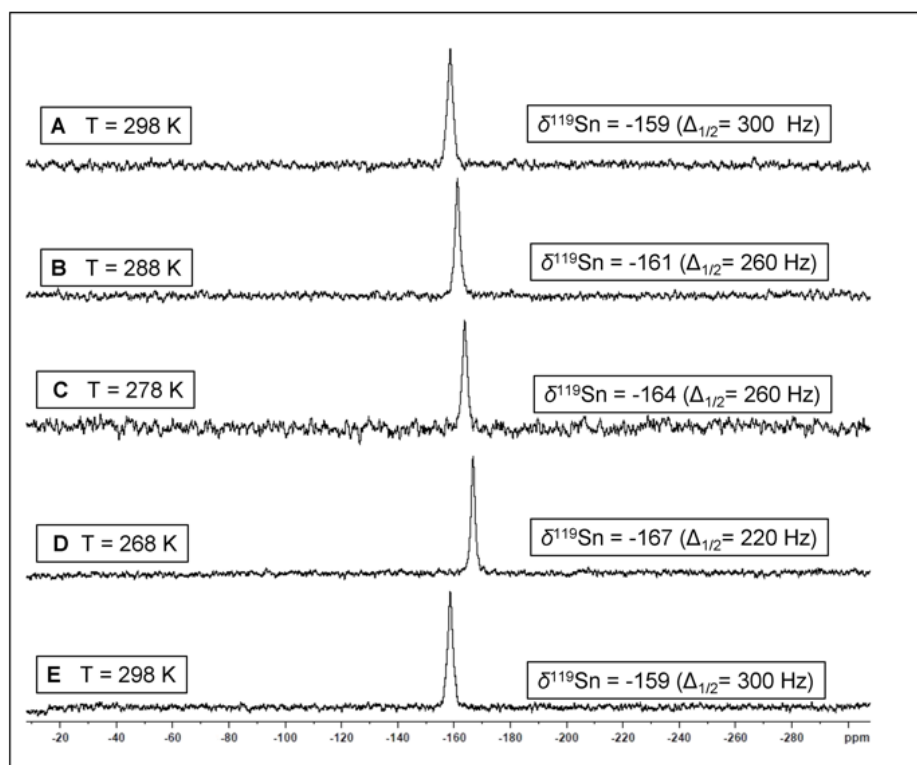
Figure A.11: Variable temperature ^{119}Sn-NMR spectra of (**2a**). The bottom spectrum at T = 298 K was recorded at room temperature, after cooling, showing the initial chemical shift is restituted.
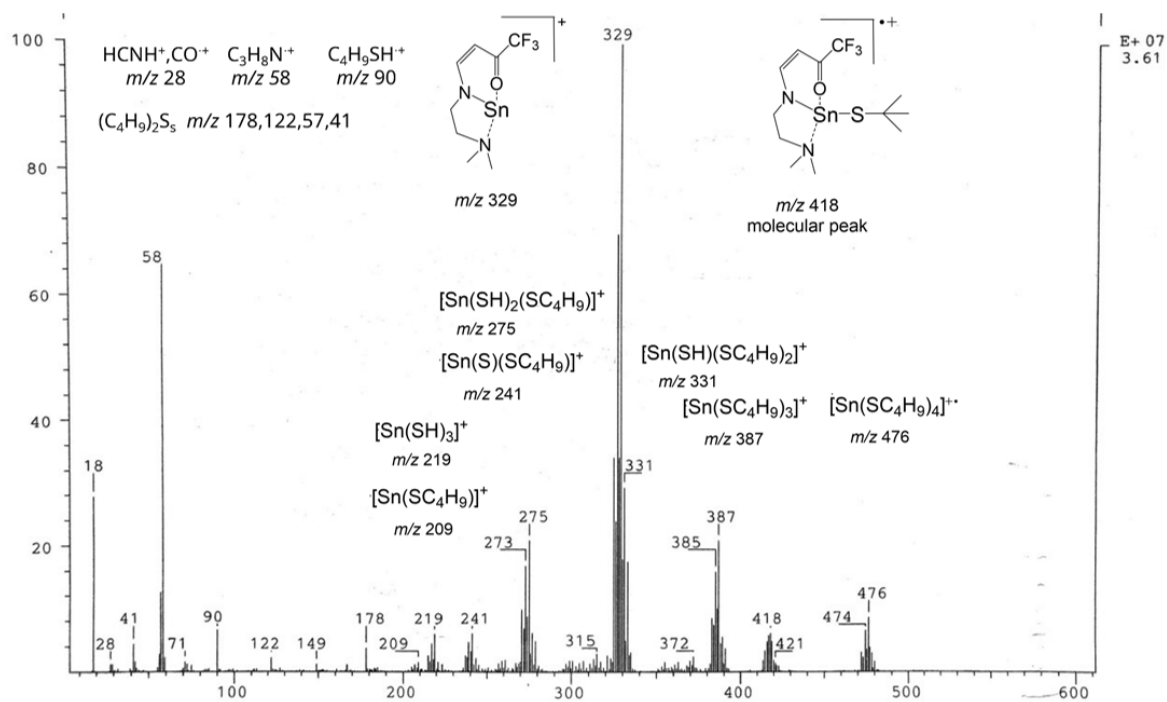
Figure A.12: Experimental EI-MS fragmentation pattern of (**2a**).
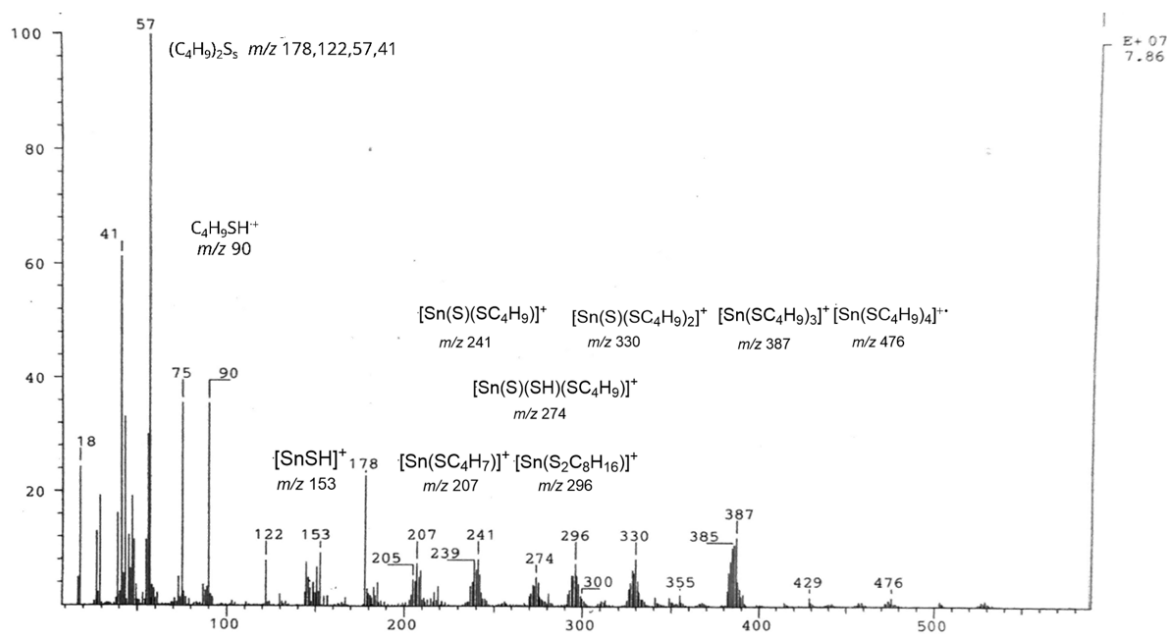
Figure A.13: Experimental EI-MS fragmentation pattern of Sn(SBu^t)$_2$.

A.3 Appendix to Chapter 5
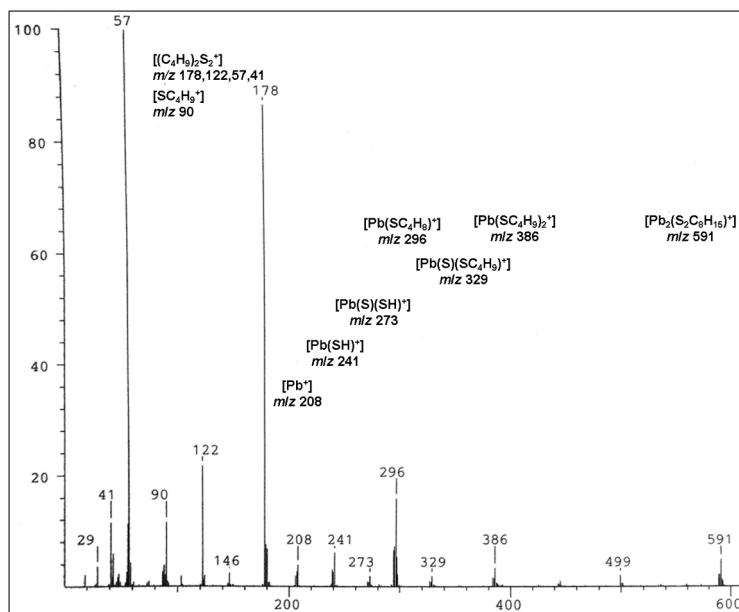
Figure A.14: Experimental EI-MS fragmentation pattern of (**3c**).
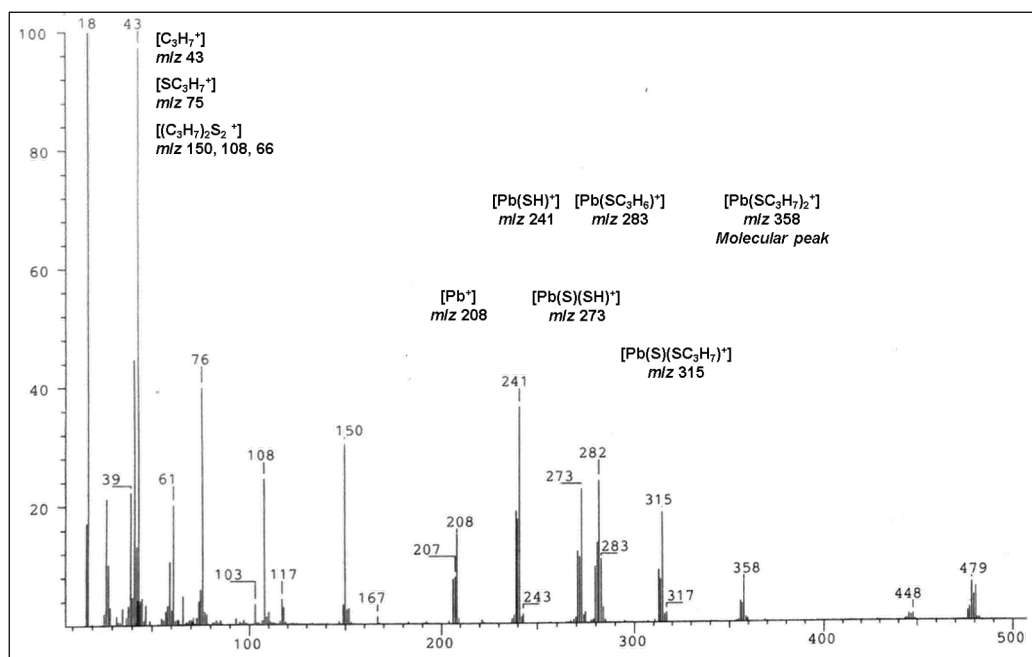
Figure A.15: Experimental EI-MS fragmentation pattern of (**3b**).

B NMR Data Tables

Table B.1: VT-NMR data of PbI_2 and PbI_2+MAI in DMF

T / K	$c(PbI_2) = 0.8\,M$		$c(PbI_2) = 0.8\,M,\ R = 1$		$c(PbI_2) = 0.4\,M,\ R = 2.8$	
	$\delta\,^{207}Pb$	$\Delta_{1/2}$ / Hz	$\delta\,^{207}Pb$	$\Delta_{1/2}$ / Hz	$\delta\,^{207}Pb$	$\Delta_{1/2}$ / Hz
298	900	1300	1832	1300	2325	1800
308	980	1000	1911	850	2405	1400
318	1052	1300	1986	1100	2476	1200
328			2056	1300		
328			2145	1500		

Table B.2: VT-NMR data from various stages of the PbI_2+MAI titration in DMSO.

T / K	$c(PbI_2) = 0.8\,M,\ R = 1$		$c(PbI_2) = 0.8\,M,\ R = 1.5$		$c(PbI_2) = 0.8\,M,\ R = 3.8$	
	$\delta\,^{207}Pb$	$\Delta_{1/2}$ / Hz	$\delta\,^{207}Pb$	$\Delta_{1/2}$ / Hz	$\delta\,^{207}Pb$	$\Delta_{1/2}$ / Hz
298	822	1500	881	1200	1412	600
308	932	1500	988	1300	1500	700
318	1044	1700	1060	2300	1594	700

Table B.3: VT-NMR data of PbI_2 and $c(PbI_2$+MAI$) = 1.2\,M$ in DMSO and DMF (last two columns).

T / K	$c(PbI_2) = 0.2\,M$		$c(PbI_2) = 0.8\,M$		$c(PbI_2) = 1.2\,M,\ R = 1$		$c(PbI_2)_{DMF} = 1.2\,M,\ R = 1$	
	$\delta\,^{207}Pb$	$\Delta_{1/2}$ / Hz	$\delta\,^{207}Pb$	$\Delta_{1/2}$ / Hz	$\delta\,^{207}Pb$	$\Delta_{1/2}$ / Hz	$\delta\,^{207}Pb$	$\Delta_{1/2}$ / Hz
293	-246	2200			905	1700	1678	1000
298	-183	2000	114	1800	943	1400	1712	600
308	-75	1500	208	1600	1030	1400	1780	900
318	8	1300	297	1800	1102	1600		
328	125	1700						

Table B.4: δ^{207}Pb and linewidths ($\Delta_{1/2}$) varying the concentration c(PbI$_2$) in DMF and DMSO.

	c(PbI$_2$) in DMF			c(PbI$_2$) in DMSO	
c / molL^{-1}	δ^{207}Pb	$\Delta_{1/2}$ / Hz	c / molL^{-1}	δ^{207}Pb	$\Delta_{1/2}$ / Hz
0.1	1243	1200	0.075	-460	1200
0.2	1201	850	0.1	-374	1800
0.3	1116	650	0.2	-200	1200
0.4	1059	800	0.4	-28	1100
0.5	1027	750	0.6	48	1200
0.6	967	2200	0.8	114	1300
0.7	950	650	1.2	17	1400
0.8	919	800			
0.9	886	800			

Table B.5: δ^{207}Pb with linewidths ($\Delta_{1/2}$) and δ^1H varying the concentration PbI$_2$+MAI ($R = 1$) in DMF and DMSO.

	c(MAI+PbI$_2$) in DMF			c(MAI+PbI$_2$) in DMSO		
c / molL^{-1}	δ^{207}Pb	$\Delta_{1/2}$ / Hz	δ^1H a)	δ^{207}Pb	$\Delta_{1/2}$ / Hz	δ^1H[a)]
0.05	[b)]			-216	700	7.48, 2.38.
0.1	2286	600	7.98, 2.72.	12	900	7.48, 2.37.
0.2	2209	600	7.96, 2.72.	274	1100	7.47, 2.36.
0.4	2025	550	7.94, 2.72.	565	1000	7.44, 2.35.
0.6	1897	470	7.92, 2.72.	720	930	7.42, 2.33.
0.8	1832	560	7.87, 2.71.	822	900	7.39, 2.32.
1.0	1767	620	7.87, 2.72.			
1.2	1712	600	7.83, 2.72.	943	900	7.34, 2.31.
2.0	1593[c)]	670	7.72, 2.71.			

[a)] All signals from proton NMR were observed as singulets, which is together with the linewidths omitted for clarity.
[b)] No signal could be detected at this concentration.
[c)] At this high concentration the solution was only short-time stable. However sufficiently long to record the NMR spectrum, after precipitation of a yellow solid the signal moved to delta^{207}Pb = 1610 with very broad linewidth in the presence of larger amount of solid in the NMR tube.

Table B.6: δ^{207}Pb and δ^{133}Cs with linewidths ($\Delta_{1/2}$) varying the concentration PbI$_2$+CsI ($R = 1$) in DMSO and DMF.

	c(CsI+PbI$_2$) in DMF				c(CsI+PbI$_2$) in DMSO			
c / molL^{-1}	δ^{207}Pb	$\Delta_{1/2}$ / Hz	δ^{133}Cs	$\Delta_{1/2}$ / Hz	δ^{207}Pb	$\Delta_{1/2}$ / Hz	δ^{133}Cs	$\Delta_{1/2}$ / Hz
0.1	2305	700	17	2				
0.2	2193	600	22	2	292	970	88	2
0.4	2000	2500	31	2	574	950	97	2
0.8					813	930	111	3
1.2					892	900	123	4
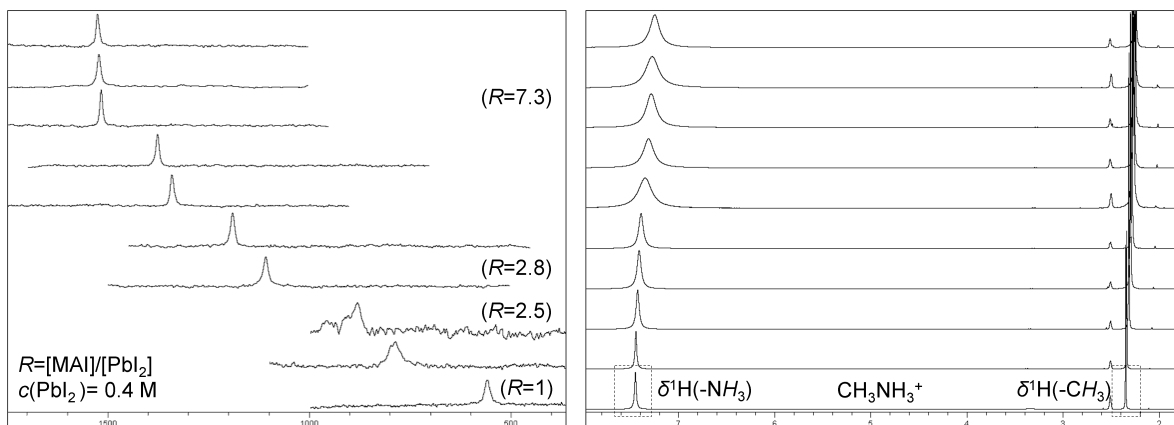
Figure B.1: Stacked plots of the ^{207}Pb (*left-hand side*) and ^{1}H NMR (*right-hand side*) spectra recorded in the [MAI]/[PbI$_2$] titration experiments at c(PbI$_2$) = 0.4 M in DMSO. The bottom spectra correspond to the equimolar precursor ratio ($R = 1$) and the spectrum designated as ($R = 7.3$) is the limiting spectra which corresponds to the final constant value δ^{207}Pb$_{\text{final}}$.
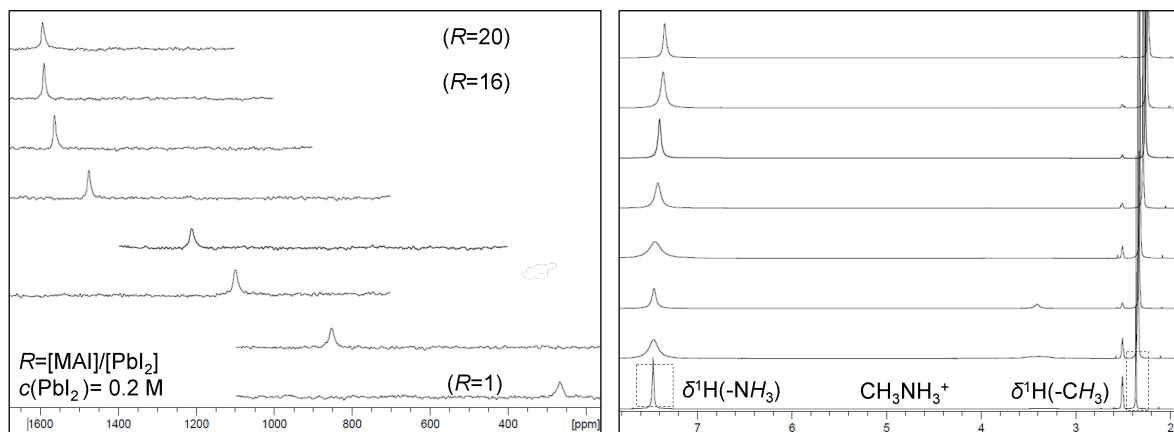
Figure B.2: Stacked plots of the ^{207}Pb (*left-hand side*) and ^{1}H NMR (*right-hand side*) spectra recorded in the [MAI]/[PbI$_2$] titration experiments at c(PbI$_2$) = 0.2 M in DMSO. The bottom spectra correspond to the equimolar precursor ratio ($R = 1$) and the spectrum designated as ($R = 16$) is the limiting spectra which corresponds to the final constant value δ^{207}Pb$_{\text{final}}$.

Table B.7: δ^{207}Pb, δ^1H and linewidths ($\Delta_{1/2}$) of the c(PbI$_2$)=0.8 M titration with MAI in DMSO.

R=[MAI]/[PbI$_2$]	c(MAI) / molL^{-1}	δ^{207}Pb	$\Delta_{1/2}$ / Hz	δ^1H$^{a)}$
	0	114	1300	
1.0	0.8	822	900	7.39 (s, $\Delta_{1/2}$ = 8 Hz), 2.33 (s)
1.3	1.0	880	900	7.38 (s, $\Delta_{1/2}$ = 12 Hz), 2.33 (s)
1.5	1.2	1042	800	7.38 (s, $\Delta_{1/2}$ = 6 Hz), 2.31 (s)
1.8	1.4	1139	700	7.38 (s, $\Delta_{1/2}$ = 6 Hz), 2.31 (s)
2.3	1.8	1274	580	7.36 (s, $\Delta_{1/2}$ = 9 Hz), 2.30 (s)
2.8	2.2	1355	544	7.34 (s, $\Delta_{1/2}$ = 17 Hz), 2.28 (s)
3.0	2.4	1380	509	7.33 (s, $\Delta_{1/2}$ = 21 Hz), 2.27 (s)
3.3	2.7	1400	480	7.32 (s, $\Delta_{1/2}$ = 24 Hz), 2.27 (s)
3.6	2.9	1415	450	7.30 (s, $\Delta_{1/2}$ = 26 Hz), 2.26 (s)
3.8	3.1	1425	460	7.27 (s, $\Delta_{1/2}$ = 30 Hz), 2.25 (s)
4.4	3.5	1425	500	7.23 (s, $\Delta_{1/2}$ = 28 Hz), 2.24 (s)
4.9	3.9	1425	500	7.21 (s, $\Delta_{1/2}$ = 21 Hz), 2.24 (s)

$^{a)}$ The linewidths $\Delta_{1/2}(^1$H) of the ammonium proton ($-$NH$_3{}^+$) resonances are reported, $\Delta_{1/2}(^1$H) of the methyl protons ($-$CH$_3$) range between $\Delta_{1/2}$ = 1–5 Hz and are omitted for clarity.

Table B.8: δ^{207}Pb and δ^1H with linewidths ($\Delta_{1/2}$) of c(PbI$_2$) = 0.4 M titration with MAI in DMSO.

R=[MAI]/[PbI$_2$]	c(MAI) / molL^{-1}	δ^{207}Pb	$\Delta_{1/2}$ / Hz	δ^1H$^{a)}$
	0	-28	1100	
1.0	0.4	565	1000	7.44 (s, $\Delta_{1/2}$ = 5 Hz), 2.32 (s)
1.5	0.6	702	1200	7.44 (s, $\Delta_{1/2}$ = 10 Hz), 2.32 (s)
2.0	0.8	822	1200	7.44 (s, $\Delta_{1/2}$ = 10 Hz), 2.32 (s)
2.5	1.0	890,960	2000,2000	7.44 (s, $\Delta_{1/2}$ = 8 Hz), 2.32 (s)
2.8	1.1	1108	900	7.43 (s, $\Delta_{1/2}$ = 12 Hz), 2.32 (s)
3.1	1.2	1192	800	7.41 (s, $\Delta_{1/2}$ = 11 Hz), 2.31 (s)
4.1	1.7	1341	700	7.41 (s, $\Delta_{1/2}$ = 15 Hz), 2.30 (s)
5.2	2.1	1437	600	7.39 (s, $\Delta_{1/2}$ = 15 Hz), 2.30 (s)
6.2	2.6	1475	500	7.39 (s, $\Delta_{1/2}$ = 17 Hz), 2.28 (s)
7.3	2.9	1525	500	7.31 (s, $\Delta_{1/2}$ = 36 Hz), 2.26 (s)
8.3	3.3	1525	500	7.25 (s, $\Delta_{1/2}$ = 37 Hz), 2.25 (s)
8.8	3.5	1525	540	7.24 (s, $\Delta_{1/2}$ = 36 Hz), 2.24 (m)

$^{a)}$ The linewidths $\Delta_{1/2}(^1$H) of the ammonium proton ($-$NH$_3{}^+$) resonances are reported, $\Delta_{1/2}(^1$H) of the methyl protons ($-$CH$_3$) range between $\Delta_{1/2}$ = 2–3 Hz and are omitted for clarity.

Table B.9: $\delta\,^{207}$Pb and $\delta\,^{1}$H with linewidths ($\Delta_{1/2}$) of $c(\text{PbI}_2) = 0.2\,\text{M}$ titration with MAI in DMSO.

$R=[\text{MAI}]/[\text{PbI}_2]$	$c(\text{MAI})$ / molL^{-1}	$\delta\,^{207}$Pb	$\Delta_{1/2}$ / Hz	$\delta\,^{1}$H $^{a)}$
-	0	-200	1200	
1.0	0.2	274	1100	7.47 (s, $\Delta_{1/2} = 5\,\text{Hz}$), 2.36 (s)
3.0	0.6	853	900	7.46 (s, $\Delta_{1/2} = 34\,\text{Hz}$), 2.34 (s)
4.5	0.9	1100	970	7.46 (s, $\Delta_{1/2} = 15\,\text{Hz}$), 2.32 (s)
6.0	1.2	1213	800	7.46 (s, $\Delta_{1/2} = 9\,\text{Hz}$), 2.33 (s)
9.5	1.9	1476	600	7.45 (s, $\Delta_{1/2} = 43\,\text{Hz}$), 2.32 (s)
12.5	2.5	1564	470	7.41 (s, $\Delta_{1/2} = 20\,\text{Hz}$), 2.31 (s)
16	3.2	1590	460	7.40 (s, $\Delta_{1/2} = 11\,\text{Hz}$), 2.27 (s)
20	4.0	1594	600	7.36 (s, $\Delta_{1/2} = 16\,\text{Hz}$), 2.25 (s)

$^{a)}$ The linewidths $\Delta_{1/2}(^1\text{H})$ of the ammonium proton ($-\text{NH}_3{}^+$) resonances are reported, $\Delta_{1/2}(^1\text{H})$ of the methyl protons ($-\text{CH}_3$) range between $\Delta_{1/2} = 1\text{--}3\,\text{Hz}$ and are omitted for clarity.
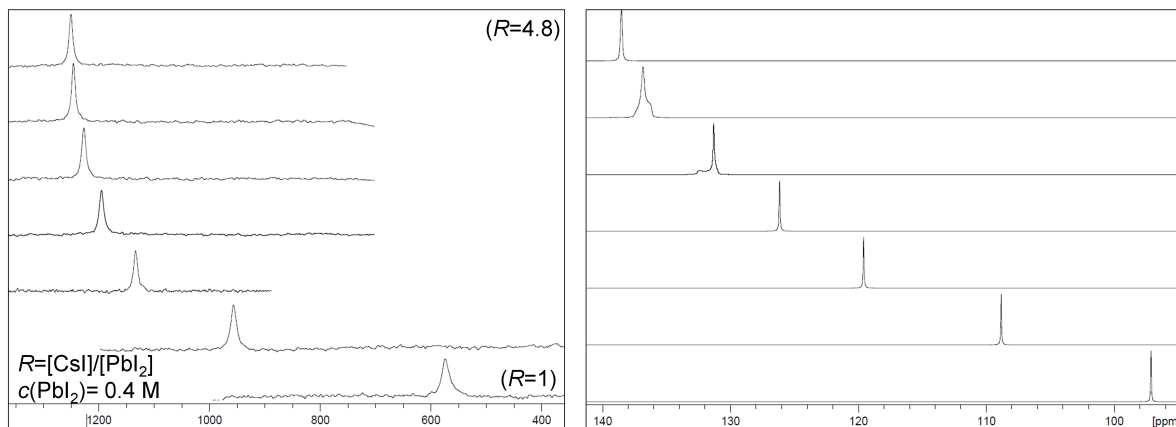
Figure B.3: Stacked plots of the ^{207}Pb (*left-hand side*) and ^{133}Cs-NMR (*right-hand side*) spectra recorded in the [CsI]/[PbI$_2$] titration experiments at $c(\text{PbI}_2) = 0.4\,\text{M}$ in DMSO. The bottom spectra correspond to the equimolar precursor ratio ($R = 1$) and the spectrum designated as ($R = 4.8$) is the limiting spectra which corresponds to the final constant value $\delta\,^{207}\text{Pb}_\text{final}$.

Table B.10: $\delta\,^{207}$Pb and $\delta\,^{133}$Cs with linewidths ($\Delta_{1/2}$) of $c(\text{PbI}_2) = 0.8\,\text{M}$ titration with CsI in DMSO.

$R=[\text{CsI}]/[\text{PbI}_2]$	$c(\text{CsI})$ / molL^{-1}	$\delta\,^{207}$Pb	$\Delta_{1/2}$ / Hz	$\delta\,^{133}$Cs	$\Delta_{1/2}$ / Hz
	0	114	1300		
1.0	0.8	813	900	110	5
1.3	1.0	936	800	115	3
1.5	1.2	987	800	121	3
1.8	1.5	1087	700	125	4
2.3	1.8	1157	600	132,133$^{a)}$	20
2.5	1.9	1204	500	144-146	67

$^{a)}$ The two signals were not fully separated, however visible as two individual resonances, best described as an intermediate state between coalescence and slow exchange.

Table B.11: δ^{207}Pb and δ^{133}Cs with linewidths ($\Delta_{1/2}$) of c(PbI$_2$) = 0.4 M titration with CsI in DMSO.

R=[CsI]/[PbI$_2$]	c(CsI) / molL^{-1}	δ^{207}Pb	$\Delta_{1/2}$ / Hz	δ^{133}Cs	$\Delta_{1/2}$ / Hz
	0	-28	1100		
1.0	0.4	574	1000	97	3
2.0	0.8	956	780	109	3
3.0	1.2	1134	640	120	3
3.5	1.4	1195	610	126	3
4.0	1.6	1227	580	131,132[a]	62
4.5	1.8	1246	500	137	17
4.8	1.9	1251	400	139	7

[a] The two signals were not fully separated, best described as an intermediate state between coalescence and slow exchange.

Table B.12: δ^{207}Pb and δ^{133}Cs with linewidths ($\Delta_{1/2}$) of c(PbI$_2$) = 0.2 M titration with CsI in DMSO.

R=[CsI]/[PbI$_2$]	c(CsI) / molL^{-1}	δ^{207}Pb	$\Delta_{1/2}$ / Hz	δ^{133}Cs	$\Delta_{1/2}$ / Hz
	0	-200	1100		
1.0	0.2	285	960	88	3
2.0	0.4	612	960	94	3
3.0	0.6	849	800	96	7
3.3	0.65	902	800	99	3
4.0	0.8	1016	750	106	2
5.0	0.97	1020	3000	103,109[a]	67
5.5	1.1	1110	750	112	3
6.0	1.2	1185	600	118	3
7.0	1.4	1228	600	122	3
8.0	1.6	1246,1255[a]	1300	124,127[a]	94
9.0	1.8	1261	450	128	3
9.5	1.9	1282	450	134	3

[a] The two signals were not fully separated, best described as an intermediate state between coalescence and slow exchange.

Table B.13: δ^{207}Pb and δ^1H with linewidths ($\Delta_{1/2}$) for c(PbI$_2$) = 0.8 M titration with MAI in DMF.

R=[MAI]/[PbI$_2$]	c(MAI) /molL^{-1}	δ^{207}Pb	$\Delta_{1/2}$ / Hz	δ^1H[a]
0.2	0.2	1151	640	7.90 (s, $\Delta_{1/2}$ = 34 Hz), 2.70 (s)
0.3	0.3	1254	590	7.90 (s, $\Delta_{1/2}$ = 50 Hz), 2.70 (s)
0.4	0.3	1377	570	7.90 (s, $\Delta_{1/2}$ = 51 Hz), 2.70 (s)
0.5	0.4	1463	490	7.90 (s, $\Delta_{1/2}$ = 61 Hz), 2.70 (s)
0.6	0.5	1575	470	7.90 (s, $\Delta_{1/2}$ = 58 Hz), 2.71 (s)
0.7	0.5	1633	440	7.90 (s, $\Delta_{1/2}$ = 57 Hz), 2.71 (s)
0.8	0.6	1684	450	7.90 (s, $\Delta_{1/2}$ = 62 Hz), 2.71 (s)
0.9	0.7	1790	500	7.89 (s, $\Delta_{1/2}$ = 28 Hz), 2.71 (s)
1.0	0.8	1836	500	7.88 (s, $\Delta_{1/2}$ = 74 Hz), 2.71 (s)
1.5	1.2	1948	2600	7.83 (s, $\Delta_{1/2}$ = 150 Hz), 2.69 (s)
1.8	1.4	1965	3000	7.80 (s, $\Delta_{1/2}$ = 72 Hz), 2.69 (s)
2.3	1.8	1965	3300	7.70 (s, $\Delta_{1/2}$ = 54 Hz), 2.64 (s)

[a] The linewidths $\Delta_{1/2}(^1$H) of the ammonium proton ($-$NH$_3{}^+$) resonances are reported, $\Delta_{1/2}(^1$H) of the methyl protons ($-$CH$_3$) range between $\Delta_{1/2}$ = 1–3 Hz and are omitted for clarity.

Table B.14: δ^{207}Pb and δ^1H with linewidths ($\Delta_{1/2}$) for $c(PbI_2) = 0.4$ M titration with MAI in DMF.

R=[MAI]/[PbI$_2$]	c(MAI) / molL^{-1}	δ^{207}Pb	$\Delta_{1/2}$ / Hz	δ^1H[a]
1.0	0.4	2025	550	7.94 (s, $\Delta_{1/2}$ = 12 Hz), 2.72 (s)
1.5	0.6	2185	880	7.80 (s, $\Delta_{1/2}$ = 170 Hz), 2.73 (s)
2.4	1.0	2299	1600	7.50 (s, $\Delta_{1/2}$ = 138 Hz), 2.68 (s)
2.8	1.1	2325	1600	7.49 (s, $\Delta_{1/2}$ = 146 Hz), 2.65 (s)
3.0	1.2	2325	1800	7.25 (s, $\Delta_{1/2}$ = 116 Hz), 2.65 (s)

[a] The linewidths $\Delta_{1/2}(^1$H) of the ammonium proton ($-$NH$_3^+$) resonances are reported, $\Delta_{1/2}(^1$H) of the methyl protons ($-$CH$_3$) range between $\Delta_{1/2}$ = 1–3 Hz and are omitted for clarity.

Table B.15: δ^{207}Pb and δ^1H with linewidths ($\Delta_{1/2}$) of $c(Pb(NO_3)_2) = 0.8$ M titration with MAI in DMSO.

R=[MAI]/[Pb^{II}]	c(MAI) / molL^{-1}	δ^{207}Pb	$\Delta_{1/2}$ / Hz	δ^1H
	0	-2610	32	
0.5	0.4	-1903	2500	7.63 (s, $\Delta_{1/2}$ = 48 Hz), 2.36 (q, $J_{H\text{-}H}$ = 6 Hz)
1.0	0.8	-1180	4100	7.61 (s, $\Delta_{1/2}$ = 34 Hz), 2.35 (s.)
1.5	1.2	-590	4000	7.59 (s, $\Delta_{1/2}$ = 30 Hz), 2.35 (s.)
2.0	1.6	67	4000	7.56 (s, $\Delta_{1/2}$ = 21 Hz), 2.34 (s.)
3.0	2.4	894	1200	7.51 (s, $\Delta_{1/2}$ = 40 Hz), 2.33 (q, $J_{H\text{-}H}$ = 6 Hz)
3.5	2.8	1107	1200	7.49 (s, $\Delta_{1/2}$ = 34 Hz), 2.32 (s.)

Table B.16: δ^{207}Pb and δ^1H with linewidths ($\Delta_{1/2}$) of $c(Pb(NO_3)_2) = 0.8$ M titration with MAI in DMF.

R=[MAI]/[Pb^{II}]	c(MAI) / molL^{-1}	δ^{207}Pb	$\Delta_{1/2}$ / Hz	δ^1H
	0	-2799	32	
0.5	0.4	-1838	1800	8.03 (s, $\Delta_{1/2}$ = 65 Hz), 2.65 (q, $J_{H\text{-}H}$ = 6 Hz)
1.0	0.8	-1020	3000	8.01 (s, $\Delta_{1/2}$ = 28 Hz), 2.62 (s)
1.5	1.2	-243	4000	8.01 (s, $\Delta_{1/2}$ = 24 Hz), 2.65 (s)
2.0	1.6	460	3800	7.99 (s, $\Delta_{1/2}$ = 37 Hz), 2.65 (s)
3.0	2.4	1816	1300	7.96 (s, vb), 2.28 (s)
3.5	2.8	1903	2200	7.92 (s, vb), 2.66 (s)

Table B.17: δ^{207}Pb and δ^1H with linewidths ($\Delta_{1/2}$) of $c(PbI_2) = 0.4$ M titration with MAI in DMF:DMSO 1:1 (v:v) solvent ratio.

R=[MAI]/[PbI$_2$]	c(MAI) / molL^{-1}	δ^{207}Pb	$\Delta_{1/2}$ / Hz	δ^1H
	0.0	484	1000	
1.0	0.4	1250	1000	7.69 (s, $\Delta_{1/2}$ = 65 Hz), 2.54 (s)
2.0	0.8	1653	620	7.69 (s, $\Delta_{1/2}$ = 11 Hz), 2.42 (s)
3.0	1.2	1816	680	7.58 (s, $\Delta_{1/2}$ = 12 Hz), 2.40 (s)
4.0	1.6	1911	500	7.56 (s, $\Delta_{1/2}$ = 21 Hz), 2.37 (s)
5.0	2.0	1928	600	7.48 (s, $\Delta_{1/2}$ = 70 Hz), 2.35 (s)
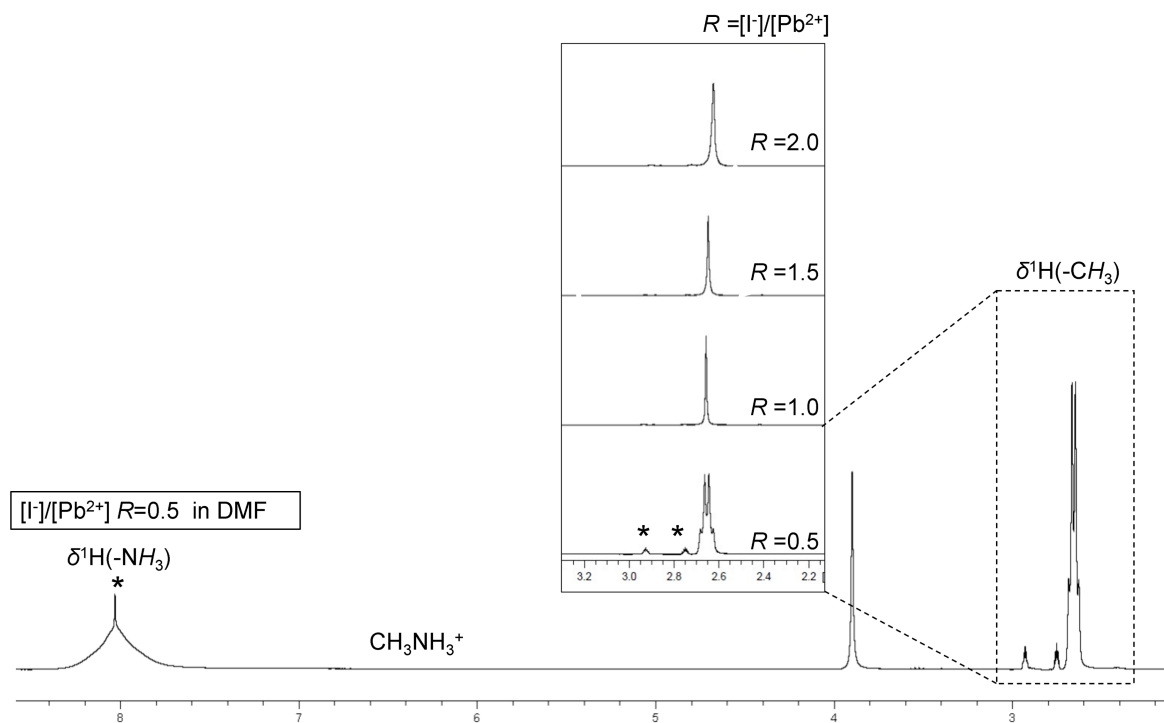
Figure B.4: a) ^{1}H-NMR spectra of $Pb(NO_3)_2+0.5MAI$ in DMF showing the quartet formation of the $-CH_3$ moiety of MA^+, that is a singulet in all other solution compositions. The triangle (▲) marks the residual protons signal from DMSO-d$_6$. The methyl ($-CH_3$) proton resonances for four further MAI addition steps is presented as inset in the spectrum. The corresponding NMR plot with DMSO as solvent is shown in (Figure 6.7).

Table B.18: δ^{207}Pb with linewidths and δ^1H in various ratios of DMF:DMSO by volume (v:v).

Compound	DMF:DMSO (v:v)	δ^{207}Pb	$\Delta_{1/2}$ / Hz	δ^1H
$c(PbI_2) = 0.4\,M$	1:1	509	1000	
$c(PbI_2) = 0.8\,M$	1:1	492	1000	
$c(PbI_2+MAI) = 0.8\,M$	2:1	1422	600	7.54 (s), 2.43 (s)
$c(PbI_2+MAI) = 0.8\,M$	4:1	1632	480	7.61 (s), 2.48 (s)

C Crystallographic Data Tables

Table C.1: Crystallographic information table for Bi(SBu^t)$_3$ (**1a**).

Empirical formula	C$_{12}$H$_{27}$S$_3$Bi
Formula weight	476.9
Temperature / K	170(2)
Crystal system	hexagonal
Space group (number)	$P6_3$ (173)
a / Å	18.140(3)
b / Å	18.140(3)
c / Å	9.4580(19)
α / °	90
β / °	90
γ / °	120
Volume / Å^3	2695.3(9)
Z	6
ρ_{calc} / gcm^{-3}	1.761
μ / mm^{-1}	10.140
$F(000)$	1380
Crystal size / mm^3	$0.5 * 0.5 * 0.2$
Crystal color	yellow
Crystal shape	needle
Radiation	Mo-K$_\alpha$ ($\lambda = 0.71073$ Å)
2θ range / °	4.49 to 53.58 (0.79 Å)
Index ranges	$-22 \leq h \leq 22$
	$-23 \leq k \leq 23$
	$-11 \leq l \leq 11$
Reflections collected	38015
Independent reflections	3779
	$R_{int} = 0.0778$
	$R_{sigma} = 0.0304$
Completeness to	99.9 %
$\theta = 25.242°$	
Data / Restraints / Parameters	3779/1/115
Goodness-of-fit on F^2	1.063
Final R indexes	$R_1 = 0.0432$
$[I \geq 2\sigma(I)]$	$wR_2 = 0.1019$
Final R indexes	$R_1 = 0.0564$
[all data]	$wR_2 = 0.1188$
Largest peak/hole /eÅ^{-3}	$7.86/-2.01$
Flack X parameter	0.264(13)

Table C.2: Atomic coordinates and $U_{eq}/\text{Å}^2$ for Bi(Bu^t)$_3$ (**1a**).

Atom	x	y	z	U_{eq}[a]
Bi(01)	0.666667	0.333333	$-0.07497(7)$	0.0489(4)
S(01)	0.7845(3)	0.3457(4)	0.0842(8)	0.0572(10)
C(11)	0.8867(14)	0.4233(14)	$-0.004(2)$	0.052(4)
C(12)	0.8927(18)	0.3820(18)	$-0.139(2)$	0.060(6)
C(13)	0.8917(16)	0.5072(13)	$-0.022(3)$	0.069(6)
C(14)	0.9536(17)	0.4300(19)	0.106(3)	0.080(7)
Bi(02)	0.666667	0.333333	0.43158(7)	0.0489(4)
S(02)	0.5461(3)	0.3159(4)	0.5902(7)	0.0565(10)
C(21)	0.4472(15)	0.2385(16)	0.498(2)	0.061(6)
C(22)	0.4468(16)	0.1574(15)	0.469(3)	0.063(5)
C(23)	0.3770(17)	0.2208(17)	0.603(3)	0.078(6)
C(24)	0.4393(19)	0.2822(18)	0.367(3)	0.067(6)
Bi(03)	0	0	1.14303(11)	0.0507(4)
S(03)	0.1213(3)	0.0207(4)	0.9855(8)	0.0553(11)
C(31)	0.2166(14)	0.0984(15)	1.078(2)	0.054(5)
C(32)	0.2155(16)	0.1823(15)	1.112(3)	0.059(5)
C(33)	0.228(2)	0.0635(18)	1.217(2)	0.066(7)
C(34)	0.2896(13)	0.117(2)	0.980(3)	0.079(8)

[a] $U_{eq.}$ is defined as $\frac{1}{3}$ of the trace of the orthogonalized U_{ij} tensor.

Table C.3: Bond lengths and bond angles $Bi(Bu^t)_3$ (**1a**)

Atom-Atom$^{a)}$	Bond Length / pm	Atom-Atom-Atom$^{a)}$	Bond Angle /°
Bi(01)-S(01)	2.530(6)	S(01)-Bi(01)-S(01)#1	88.2(2)
Bi(01)-S(01)#1	2.530(6)	S(01)-Bi(01)-S(01)#2	88.2(2)
Bi(01)-S(01)#2	2.530(6)	S(01)#1-Bi(01)-S(01)#2	88.2(2)
S(01)-C(11)	1.87(2)	C(11)-S(01)-Bi(01)	106.1(6)
C(11)-C(13)	1.49(3)	C(13)-C(11)-C(12)	115.3(19)
C(11)-C(12)	1.51(3)	C(13)-C(11)-C(14)	111(2)
C(11)-C(14)	1.55(3)	C(12)-C(11)-C(14)	111(2)
Bi(02)-S(02)#2	2.537(6)	C(13)-C(11)-S(01)	110.5(16)
Bi(02)-S(02)#1	2.537(6)	C(12)-C(11)-S(01)	107.0(16)
Bi(02)-S(02)	2.537(6)	C(14)-C(11)-S(01)	101.8(15)
S(02)-C(21)	1.85(2)	S(02)#2-Bi(02)-S(02)#1	88.6(2)
C(21)-C(22)	1.49(4)	S(02)#2-Bi(02)-S(02)	88.6(2)
C(21)-C(24)	1.51(3)	S(02)#1-Bi(02)-S(02)	88.6(2)
C(21)-C(23)	1.52(3)	C(21)-S(02)-Bi(02)	105.2(8)
Bi(03)-S(03)	2.524(6)	C(22)-C(21)-C(24)	114.4(19)
Bi(03)-S(03)#3	2.524(6)	C(22)-C(21)-C(23)	109(2)
Bi(03)-S(03)#4	2.524(6)	C(24)-C(21)-C(23)	111(2)
S(03)-C(31)	1.82(2)	C(22)-C(21)-S(02)	111.0(17)
C(31)-C(33)	1.51(3)	C(24)-C(21)-S(02)	107.3(18)
C(31)-C(34)	1.51(3)	C(23)-C(21)-S(02)	104.0(15)
C(31)-C(32)	1.56(3)	S(03)-Bi(03)-S(03)#3	88.7(2)
		S(03)-Bi(03)-S(03)#4	88.7(2)
		S(03)#3-Bi(03)-S(03)#4	88.7(2)
		C(31)-S(03)-Bi(03)	104.5(7)
		C(33)-C(31)-C(34)	110(2)
		C(33)-C(31)-C(32)	108(2)
		C(34)-C(31)-C(32)	110(2)
		C(33)-C(31)-S(03)	111.6(17)
		C(34)-C(31)-S(03)	105.2(16)
		C(32)-C(31)-S(03)	112.5(14)

$^{a)}$ Symmetry transformation to generate equivalent atoms: #1: $-x + y + 1$, $-x + 1$, z; #2: $-y + 1$, $x - y$, z; #3: $-x + y$, $-x$, z; #4: $-y$, $x - y$, z.

Table C.4: Anisotropic displacement parameters ($Å^2 * 10^3$)for Bi(SBu^t)$_3$ (**1a**). The anisotropic displacement factor exponent takes the form: $-2\pi^2[h^2a^2 * U^{11} + ... + h^2k^2a^2 * b^2 * U^{12}]$.

	U^{11}	U^{22}	U^{33}	U^{23}	U^{13}	U^{12}
Bi(01)	51(1)	51(1)	45(1)	0	0	26(1)
S(01)	51(3)	61(3)	58(2)	7(3)	−2(3)	27(3)
C(11)	52(11)	54(11)	51(9)	7(8)	−2(8)	28(9)
C(12)	66(15)	68(14)	56(10)	12(9)	14(9)	41(13)
C(13)	67(14)	45(11)	84(14)	4(11)	11(13)	20(10)
C(14)	62(14)	100(20)	71(13)	7(15)	−9(12)	37(14)
Bi(02)	50(1)	50(1)	47(1)	0	0	25(1)
S(02)	52(3)	61(3)	57(2)	−5(3)	3(3)	29(2)
C(21)	53(11)	68(15)	54(10)	−3(10)	−2(8)	24(10)
C(22)	56(11)	53(11)	68(11)	−6(11)	−6(10)	19(9)
C(23)	60(14)	76(16)	87(15)	−5(15)	15(14)	26(12)
C(24)	74(16)	59(14)	71(12)	−13(11)	−24(12)	35(13)
Bi(03)	47(1)	47(1)	58(1)	0	0	24(1)
S(03)	47(2)	66(3)	54(3)	−11(3)	−5(3)	29(2)
C(31)	53(11)	52(12)	60(9)	6(11)	1(9)	30(10)
C(32)	56(12)	56(12)	67(12)	−4(10)	−7(10)	31(10)
C(33)	66(16)	61(14)	78(15)	1(9)	−10(10)	37(13)
C(34)	39(11)	110(20)	77(13)	−13(16)	1(12)	31(12)

Table C.5: Crystallographic information table for [Sn(SBu^t)(*tfb-dmeda*)] (**2a**).

Empirical formula	C$_{12}$H$_{21}$F$_3$N$_2$OSSn
Formula weight	417.08
Temperature / K	170(2)
Crystal system	triclinic
Space group (number)	$P\bar{1}$ (2)
a / Å	11.5557(4)
b / Å	13.9496(5)
c / Å	23.8212(8)
α / °	102.490(3)
β / °	93.094(3)
γ / °	112.236(3)
Volume / Å^3	3430.8(2)
Z	8
ρ_{calc} / gcm^{-3}	1.615
μ / mm^{-1}	1.637
$F(000)$	1664
Crystal size / mm^3	$0.2 * 0.2 * 0.2$
Crystal color	yellow
Crystal shape	prism
Radiation	Mo-K$_\alpha$ ($\lambda = 0.71073$ Å)
2θ range / °	3.53 to 53.51 (0.79 Å)
Index ranges	$-14 \leq h \leq 14$
	$-17 \leq k \leq 17$
	$-30 \leq l \leq 30$
Reflections collected	45844
Independent reflections	14528
	$R_{int} = 0.0607$
	$R_{sigma} = 0.0453$
Completeness to	100.0 %
$\theta = 25.242°$:	
Data / Restraints / Parameters	14528/0/721
Goodness-of-fit on F^2	1.000
Final R indexes	$R_1 = 0.0303$
$[I \geq 2\sigma(I)]$	$wR_2 = 0.0698$
Final R indexes	$R_1 = 0.0441$
[all data]	$wR_2 = 0.0771$
Largest peak/hole /eÅ^{-3}	$1.03/-0.66$

Table C.6: Atomic coordinates and $U_{eq}/\text{Å}^2$ for [Sn(SBu^t)(*tfb-dmeda*)] (**2a**).

Atom	x	y	z	$U_{eq}{}^{a)}$
Sn(1)	0.15793(2)	0.03770(2)	0.90623(2)	0.03175(6)
Sn(3)	0.43175(2)	0.52474(2)	0.60815(2)	0.03219(6)
Sn(4)	0.09727(2)	0.71301(2)	0.87228(2)	0.03224(6)
Sn(2)	0.30707(2)	0.18127(2)	0.60300(2)	0.03754(6)
S(31)	0.41667(7)	0.70015(6)	0.64477(3)	0.03396(16)
S(21)	0.25025(8)	0.00427(6)	0.62577(3)	0.03683(17)
S(41)	0.09209(7)	0.52873(6)	0.84146(4)	0.03755(17)
S(11)	0.20211(8)	0.21318(6)	0.88394(3)	0.03751(17)
O(11)	0.34936(19)	0.04450(18)	0.88479(9)	0.0360(5)
O(41)	−0.0054(2)	0.69303(19)	0.78459(9)	0.0397(5)
O(21)	0.1240(2)	0.18845(18)	0.62631(10)	0.0415(5)
O(31)	0.5152(2)	0.52854(19)	0.69596(10)	0.0411(5)
F(12)	0.5745(2)	0.1057(2)	0.79111(9)	0.0659(7)
F(23)	−0.0931(2)	0.2207(2)	0.65851(14)	0.0770(8)
F(22)	−0.1027(2)	0.1261(2)	0.71921(11)	0.0735(7)
F(21)	−0.1190(2)	0.0582(2)	0.62881(12)	0.0794(8)
N(11)	0.1053(2)	-0.0304(2)	0.80937(11)	0.0332(5)
F(43)	−0.0405(3)	0.5853(3)	0.63492(10)	0.0825(9)
N(21)	0.3643(2)	0.2464(2)	0.69970(12)	0.0369(6)
N(41)	0.2640(2)	0.7575(2)	0.82452(11)	0.0324(5)
F(13)	0.5738(2)	0.2085(2)	0.86987(13)	0.0859(9)
N(31)	0.2518(2)	0.46195(19)	0.64661(11)	0.0335(5)
F(11)	0.5868(2)	0.0628(3)	0.87096(14)	0.0875(9)
N(32)	0.2471(2)	0.4794(2)	0.53003(11)	0.0357(6)
N(42)	0.2952(3)	0.7625(2)	0.94462(11)	0.0379(6)
N(22)	0.5366(3)	0.2080(2)	0.62579(13)	0.0437(7)
N(12)	−0.0766(3)	-0.0078(2)	0.88130(12)	0.0421(6)
F(41)	−0.1692(3)	0.5424(3)	0.69322(14)	0.1310(16)
C(13)	0.3171(3)	0.0232(2)	0.78282(13)	0.0360(7)
C(12)	0.3873(3)	0.0536(2)	0.83572(13)	0.0329(6)
F(33)	0.5244(3)	0.6021(4)	0.84536(11)	0.1241(15)
C(44)	0.2598(3)	0.7376(3)	0.76866(13)	0.0363(7)
C(14)	0.1833(3)	-0.0221(2)	0.77215(13)	0.0377(7)
C(42)	0.0320(3)	0.6718(2)	0.73586(13)	0.0368(7)
C(34)	0.2450(3)	0.4739(3)	0.70192(14)	0.0383(7)
C(26)	0.5588(3)	0.2170(3)	0.68835(16)	0.0433(8)
C(39)	0.5659(3)	0.8078(2)	0.63853(15)	0.0384(7)
C(33)	0.3447(3)	0.5180(3)	0.74870(14)	0.0392(7)
F(42)	−0.1179(4)	0.6906(3)	0.67402(14)	0.1204(15)
C(24)	0.2879(3)	0.2410(3)	0.73758(14)	0.0401(7)
C(32)	0.4679(3)	0.5422(3)	0.74292(14)	0.0385(7)
C(43)	0.1521(3)	0.6912(3)	0.72565(14)	0.0399(7)

$^{a)}$ $U_{eq.}$ is defined as $\frac{1}{3}$ of the trace of the orthogonalized U_{ij} tensor.

Table C.7: *Continuation of previous table* Atomic coordinates and U_{eq}/ Å^2 for [Sn(SBu^t)(*tfb-dmeda*)] (**2a**).

Atom	x	y	z	$U_{eq}{}^{a)}$
F(31)	0.6436(4)	0.5482(4)	0.79839(15)	0.1399(19)
C(45)	0.3902(3)	0.8043(3)	0.85951(14)	0.0390(7)
C(25)	0.4994(3)	0.2877(3)	0.72123(16)	0.0476(8)
C(22)	0.0852(3)	0.1813(2)	0.67527(15)	0.0382(7)
C(35)	0.1326(3)	0.4131(3)	0.60642(15)	0.0412(7)
C(36)	0.1389(3)	0.4737(3)	0.56046(15)	0.0409(7)
C(23)	0.1547(3)	0.2040(3)	0.72774(15)	0.0431(8)
C(11)	0.5299(3)	0.1062(3)	0.84088(14)	0.0419(7)
C(15)	−0.0304(3)	-0.0801(3)	0.78635(15)	0.0453(8)
C(46)	0.3902(3)	0.7512(3)	0.90846(14)	0.0411(7)
C(16)	−0.0980(3)	-0.0166(3)	0.81928(16)	0.0468(8)
C(47)	0.3343(4)	0.8736(3)	0.97931(16)	0.0502(9)
C(37)	0.2728(4)	0.5594(3)	0.49610(15)	0.0484(8)
C(49)	−0.0627(3)	0.4384(3)	0.85494(16)	0.0423(8)
C(311)	0.6789(3)	0.7874(3)	0.65824(18)	0.0518(9)
C(29)	0.1589(4)	-0.0975(3)	0.55846(16)	0.0495(9)
C(41)	−0.0736(3)	0.6219(3)	0.68458(16)	0.0503(9)
C(38)	0.2298(4)	0.3759(3)	0.49128(16)	0.0502(9)
C(19)	0.2779(4)	0.3141(3)	0.95366(17)	0.0539(10)
C(48)	0.2694(4)	0.6904(3)	0.98316(16)	0.0532(9)
F(32)	0.6370(5)	0.6917(3)	0.7989(2)	0.169(2)
C(21)	−0.0575(3)	0.1463(3)	0.67115(18)	0.0510(9)
C(27)	0.5623(4)	0.1181(3)	0.59220(18)	0.0566(10)
C(310)	0.5664(4)	0.8167(3)	0.57596(18)	0.0589(10)
C(312)	0.5674(4)	0.9094(3)	0.6781(2)	0.0590(11)
C(18)	−0.1118(4)	0.0765(4)	0.91448(19)	0.0639(11)
C(31)	0.5662(4)	0.5907(3)	0.79684(17)	0.0535(9)
C(17)	−0.1450(4)	-0.1072(4)	0.8969(2)	0.0687(12)
C(111)	0.3838(5)	0.2949(4)	0.9818(2)	0.0794(16)
C(211)	0.1404(5)	-0.2044(3)	0.5708(3)	0.0850(17)
C(28)	0.6161(4)	0.3063(4)	0.6105(2)	0.0691(13)
C(212)	0.0326(5)	-0.0931(4)	0.5460(3)	0.0874(18)
C(112)	0.3235(6)	0.4205(3)	0.9400(3)	0.0946(19)
C(110)	0.1798(6)	0.3092(5)	0.9952(2)	0.0918(18)
C(410)	−0.0649(5)	0.3285(4)	0.8393(4)	0.120(3)
C(412)	−0.1655(4)	0.4456(6)	0.8205(4)	0.141(3)
C(411)	−0.0717(8)	0.4674(5)	0.9184(3)	0.146(4)
C(210)	0.2318(7)	-0.0823(6)	0.5086(2)	0.166(4)

$^{a)}$ $U_{eq.}$ is defined as $\frac{1}{3}$ of the trace of the orthogonalized U_{ij} tensor.

Table C.8: Bond lengths [Sn(SBu^t)(*tfb-dmeda*)] (**2a**).

Atom-Atom	Bond Length / pm	Atom-Atom	Bond Length / pm
Sn(1)-N(11)	224.9(2)	N(42)-C(48)	146.5(4)
Sn(1)-O(11)	226.9(2)	N(42)-C(46)	146.6(4)
Sn(1)-S(11)	248.61(8)	N(42)-C(47)	147.1(4)
Sn(1)-N(12)	254.2(3)	N(22)-C(26)	146.8(5)
Sn(3)-O(31)	223.7(2)	N(22)-C(28)	146.8(4)
Sn(3)-N(31)	226.0(2)	N(22)-C(27)	147.5(5)
Sn(3)-S(31)	248.89(8)	N(12)-C(17)	145.3(5)
Sn(3)-N(32)	254.1(3)	N(12)-C(16)	145.5(5)
Sn(4)-N(41)	224.2(2)	N(12)-C(18)	147.2(5)
Sn(4)-O(41)	225.4(2)	F(41)-C(41)	129.9(5)
Sn(4)-S(41)	249.27(8)	C(13)-C(12)	135.1(4)
Sn(4)-N(42)	255.7(3)	C(13)-C(14)	141.5(5)
Sn(2)-N(21)	224.6(3)	C(12)-C(11)	151.5(4)
Sn(2)-O(21)	224.8(2)	F(33)-C(31)	127.9(5)
Sn(2)-S(21)	249.25(8)	C(44)-C(43)	140.8(5)
Sn(2)-N(22)	254.5(3)	C(42)-C(43)	135.6(5)
S(31)-C(39)	184.9(3)	C(42)-C(41)	151.5(5)
S(21)-C(29)	184.4(3)	C(34)-C(33)	140.6(5)
S(41)-C(49)	185.0(3)	C(26)-C(25)	151.4(5)
S(11)-C(19)	184.6(4)	C(39)-C(311)	151.0(5)
O(11)-C(12)	128.5(4)	C(39)-C(312)	151.6(5)
O(41)-C(42)	127.5(4)	C(39)-C(310)	152.2(5)
O(21)-C(22)	128.3(4)	C(33)-C(32)	135.5(5)
O(31)-C(32)	128.0(4)	F(42)-C(41)	130.6(5)
F(12)-C(11)	131.8(4)	C(24)-C(23)	141.3(5)
F(23)-C(21)	133.6(5)	C(32)-C(31)	151.1(5)
F(22)-C(21)	132.5(5)	F(31)-C(31)	124.9(5)
F(21)-C(21)	132.6(4)	C(45)-C(46)	151.1(5)
N(11)-C(14)	129.0(4)	C(22)-C(23)	135.5(5)
N(11)-C(15)	147.0(4)	C(22)-C(21)	152.3(5)
F(43)-C(41)	132.0(4)	C(35)-C(36)	151.1(5)
N(21)-C(24)	129.0(4)	C(15)-C(16)	151.7(5)
N(21)-C(25)	146.2(4)	C(49)-C(412)	145.4(6)
N(41)-C(44)	129.4(4)	C(49)-C(410)	148.7(6)
N(41)-C(45)	147.0(4)	C(49)-C(411)	149.8(7)
F(13)-C(11)	132.7(4)	C(29)-C(210)	149.9(7)
N(31)-C(34)	130.2(4)	C(29)-C(212)	150.0(6)
N(31)-C(35)	146.3(4)	C(29)-C(211)	152.1(6)
F(11)-C(11)	132.3(4)	C(19)-C(112)	149.0(6)
N(32)-C(36)	146.4(4)	C(19)-C(111)	150.1(6)
N(32)-C(37)	146.7(4)	C(19)-C(110)	153.6(7)
N(32)-C(38)	147.0(4)	F(32)-C(31)	132.3(6)

Table C.9: Bond angles [Sn(SBu^t)(*tfb-dmeda*)] (**2a**).

Atom-Atom-Atom	Bond Angle /°	Atom-Atom-Atom	Bond Angle /°	Atom-Atom-Atom	Bond Angle /°
N(11)-Sn(1)-O(11)	81.41(8)	C(37)-N(32)-Sn(3)	112.2(2)	N(31)-C(35)-C(36)	110.3(3)
N(11)-Sn(1)-S(11)	84.93(7)	C(38)-N(32)-Sn(3)	105.7(2)	N(32)-C(36)-C(35)	110.6(3)
O(11)-Sn(1)-S(11)	90.77(6)	C(48)-N(42)-C(46)	111.4(3)	C(22)-C(23)-C(24)	124.4(3)
N(11)-Sn(1)-N(12)	72.66(9)	C(48)-N(42)-C(47)	109.7(3)	F(12)-C(11)-F(11)	107.3(3)
O(11)-Sn(1)-N(12)	154.04(8)	C(46)-N(42)-C(47)	111.4(3)	F(12)-C(11)-F(13)	105.4(3)
S(11)-Sn(1)-N(12)	88.26(7)	C(48)-N(42)-Sn(4)	110.4(2)	F(11)-C(11)-F(13)	104.9(3)
O(31)-Sn(3)-N(31)	80.92(9)	C(46)-N(42)-Sn(4)	104.84(18)	F(12)-C(11)-C(12)	115.2(3)
O(31)-Sn(3)-S(31)	92.53(6)	C(47)-N(42)-Sn(4)	109.0(2)	F(11)-C(11)-C(12)	112.2(3)
N(31)-Sn(3)-S(31)	83.12(6)	C(26)-N(22)-C(28)	112.2(3)	F(13)-C(11)-C(12)	111.1(3)
O(31)-Sn(3)-N(32)	153.01(8)	C(26)-N(22)-C(27)	110.4(3)	N(11)-C(15)-C(16)	110.2(3)
N(31)-Sn(3)-N(32)	72.24(9)	C(28)-N(22)-C(27)	108.5(3)	N(42)-C(46)-C(45)	109.7(3)
S(31)-Sn(3)-N(32)	87.10(6)	C(26)-N(22)-Sn(2)	105.78(19)	N(12)-C(16)-C(15)	110.6(3)
N(41)-Sn(4)-O(41)	81.40(9)	C(28)-N(22)-Sn(2)	107.7(2)	C(412)-C(49)-C(410)	111.6(5)
N(41)-Sn(4)-S(41)	84.33(7)	C(27)-N(22)-Sn(2)	112.2(2)	C(412)-C(49)-C(411)	110.4(6)
O(41)-Sn(4)-S(41)	91.01(6)	C(17)-N(12)-C(16)	113.5(3)	C(410)-C(49)-C(411)	108.4(5)
N(41)-Sn(4)-N(42)	72.41(9)	C(17)-N(12)-C(18)	108.9(3)	C(412)-C(49)-S(41)	110.6(3)
O(41)-Sn(4)-N(42)	153.76(9)	C(16)-N(12)-C(18)	110.4(3)	C(410)-C(49)-S(41)	106.4(3)
S(41)-Sn(4)-N(42)	87.96(6)	C(17)-N(12)-Sn(1)	107.2(2)	C(411)-C(49)-S(41)	109.3(3)
N(21)-Sn(2)-O(21)	81.37(9)	C(16)-N(12)-Sn(1)	105.62(19)	C(210)-C(29)-C(212)	111.3(5)
N(21)-Sn(2)-S(21)	83.85(7)	C(18)-N(12)-Sn(1)	111.2(2)	C(210)-C(29)-C(211)	109.9(5)
O(21)-Sn(2)-S(21)	91.46(6)	C(12)-C(13)-C(14)	124.7(3)	C(212)-C(29)-C(211)	109.7(4)
N(21)-Sn(2)-N(22)	72.74(10)	O(11)-C(12)-C(13)	128.4(3)	C(210)-C(29)-S(21)	110.5(3)
O(21)-Sn(2)-N(22)	154.10(9)	O(11)-C(12)-C(11)	112.8(3)	C(212)-C(29)-S(21)	110.3(3)
S(21)-Sn(2)-N(22)	86.47(7)	C(13)-C(12)-C(11)	118.8(3)	C(211)-C(29)-S(21)	105.1(3)
C(39)-S(31)-Sn(3)	108.51(11)	N(41)-C(44)-C(43)	127.9(3)	F(41)-C(41)-F(42)	106.3(4)
C(29)-S(21)-Sn(2)	106.10(13)	N(11)-C(14)-C(13)	128.4(3)	F(41)-C(41)-F(43)	106.6(4)
C(49)-S(41)-Sn(4)	105.74(11)	O(41)-C(42)-C(43)	127.8(3)	F(42)-C(41)-F(43)	104.6(4)
C(19)-S(11)-Sn(1)	105.02(13)	O(41)-C(42)-C(41)	113.6(3)	F(41)-C(41)-C(42)	112.2(3)
C(12)-O(11)-Sn(1)	124.37(19)	C(43)-C(42)-C(41)	118.6(3)	F(42)-C(41)-C(42)	111.9(3)
C(42)-O(41)-Sn(4)	125.7(2)	N(31)-C(34)-C(33)	128.3(3)	F(43)-C(41)-C(42)	114.6(3)
C(22)-O(21)-Sn(2)	125.1(2)	N(22)-C(26)-C(25)	110.0(3)	C(112)-C(19)-C(111)	111.9(4)
C(32)-O(31)-Sn(3)	125.6(2)	C(311)-C(39)-C(312)	110.2(3)	C(112)-C(19)-C(110)	108.8(4)
C(14)-N(11)-C(15)	117.3(3)	C(311)-C(39)-C(310)	110.1(3)	C(111)-C(19)-C(110)	108.9(4)
C(14)-N(11)-Sn(1)	125.8(2)	C(312)-C(39)-C(310)	110.3(3)	C(112)-C(19)-S(11)	106.3(3)
C(15)-N(11)-Sn(1)	116.6(2)	C(311)-C(39)-S(31)	111.1(2)	C(111)-C(19)-S(11)	111.1(3)
C(24)-N(21)-C(25)	117.7(3)	C(312)-C(39)-S(31)	105.2(2)	C(110)-C(19)-S(11)	109.7(3)
C(24)-N(21)-Sn(2)	125.6(2)	C(310)-C(39)-S(31)	110.0(2)	F(22)-C(21)-F(21)	106.4(3)
C(25)-N(21)-Sn(2)	116.3(2)	C(32)-C(33)-C(34)	124.4(3)	F(22)-C(21)-F(23)	107.0(3)
C(44)-N(41)-C(45)	116.6(3)	N(21)-C(24)-C(23)	128.3(3)	F(21)-C(21)-F(23)	105.7(3)
C(44)-N(41)-Sn(4)	126.1(2)	O(31)-C(32)-C(33)	127.9(3)	F(22)-C(21)-C(22)	114.3(3)
C(45)-N(41)-Sn(4)	117.06(19)	O(31)-C(32)-C(31)	113.0(3)	F(21)-C(21)-C(22)	111.7(3)
C(34)-N(31)-C(35)	117.4(3)	C(33)-C(32)-C(31)	119.1(3)	F(23)-C(21)-C(22)	111.2(3)
C(34)-N(31)-Sn(3)	125.2(2)	C(42)-C(43)-C(44)	125.2(3)	F(31)-C(31)-F(33)	110.3(4)
C(35)-N(31)-Sn(3)	117.1(2)	N(41)-C(45)-C(46)	110.4(3)	F(31)-C(31)-F(32)	104.2(5)
C(36)-N(32)-C(37)	110.8(3)	N(21)-C(25)-C(26)	110.9(3)	F(33)-C(31)-F(32)	100.5(4)
C(36)-N(32)-C(38)	112.9(3)	O(21)-C(22)-C(23)	128.3(3)	F(31)-C(31)-C(32)	114.5(3)
C(37)-N(32)-C(38)	109.0(3)	O(21)-C(22)-C(21)	112.6(3)	F(33)-C(31)-C(32)	116.0(3)
C(36)-N(32)-Sn(3)	106.09(19)	C(23)-C(22)-C(21)	119.0(3)	F(32)-C(31)-C(32)	109.7(4)

Table C.10: Anisotropic displacement parameters ($\text{Å}^2 * 10^3$) for [Sn(SBu^t)(tfb-$dmeda$)] (**2a**). The anisotropic displacement factor exponent takes the form: $-2\pi^2[h^2a^2 * U^{11} + ... + h^2k^2a^2 * b^2 * U^{12}]$.

	U^{11}	U^{22}	U^{33}	U^{23}	U^{13}	U^{12}
Sn(1)	36(1)	35(1)	28(1)	9(1)	4(1)	18(1)
Sn(2)	38(1)	40(1)	37(1)	20(1)	4(1)	13(1)
Sn(3)	32(1)	31(1)	34(1)	8(1)	8(1)	13(1)
Sn(4)	35(1)	36(1)	30(1)	9(1)	7(1)	19(1)
S(31)	32(1)	29(1)	40(1)	9(1)	10(1)	11(1)
S(21)	45(1)	32(1)	29(1)	8(1)	2(1)	11(1)
S(41)	34(1)	35(1)	46(1)	11(1)	9(1)	16(1)
S(11)	44(1)	33(1)	35(1)	8(1)	−2(1)	17(1)
O(11)	35(1)	49(1)	30(1)	14(1)	6(1)	22(1)
O(41)	39(1)	53(1)	34(1)	10(1)	2(1)	25(1)
O(21)	40(1)	45(1)	43(1)	18(1)	4(1)	18(1)
O(31)	38(1)	51(1)	40(1)	12(1)	5(1)	23(1)
F(12)	45(1)	103(2)	45(1)	19(1)	16(1)	23(1)
F(23)	49(1)	85(2)	119(2)	51(2)	16(1)	36(1)
F(22)	49(1)	102(2)	72(2)	41(2)	20(1)	21(1)
F(21)	45(1)	74(2)	85(2)	−1(1)	3(1)	0(1)
N(11)	34(1)	34(1)	30(1)	4(1)	−1(1)	16(1)
F(43)	79(2)	120(2)	40(1)	−14(1)	−13(1)	53(2)
N(21)	39(1)	30(1)	41(2)	8(1)	−3(1)	14(1)
N(41)	33(1)	34(1)	33(1)	10(1)	6(1)	15(1)
F(13)	58(1)	65(2)	94(2)	−11(1)	17(1)	-3(1)
N(31)	34(1)	30(1)	38(1)	14(1)	7(1)	12(1)
F(11)	39(1)	133(2)	114(2)	84(2)	8(1)	31(1)
N(32)	41(1)	31(1)	33(1)	9(1)	3(1)	12(1)
N(42)	45(2)	40(1)	29(1)	8(1)	1(1)	20(1)
N(22)	36(1)	45(2)	52(2)	26(1)	10(1)	11(1)
N(12)	36(1)	48(2)	43(2)	11(1)	8(1)	17(1)
F(41)	77(2)	160(3)	74(2)	29(2)	−27(2)	−36(2)
C(13)	41(2)	38(2)	30(2)	7(1)	5(1)	17(1)
C(12)	38(2)	34(2)	32(2)	10(1)	6(1)	19(1)
F(33)	104(2)	242(5)	39(2)	−3(2)	−6(2)	106(3)
C(44)	37(2)	40(2)	36(2)	13(1)	11(1)	17(1)
C(14)	50(2)	37(2)	27(2)	4(1)	−1(1)	20(1)
C(42)	46(2)	35(2)	32(2)	8(1)	−1(1)	20(1)
C(34)	41(2)	38(2)	45(2)	20(1)	16(1)	18(1)
C(26)	36(2)	42(2)	53(2)	17(2)	−1(2)	14(1)
C(39)	35(2)	31(2)	43(2)	11(1)	7(1)	6(1)
C(33)	51(2)	42(2)	33(2)	14(1)	10(1)	25(2)
F(42)	147(3)	146(3)	85(2)	−26(2)	−57(2)	117(3)
C(24)	49(2)	35(2)	35(2)	6(1)	−3(1)	18(1)
C(32)	50(2)	35(2)	36(2)	9(1)	2(1)	23(1)
C(43)	46(2)	49(2)	29(2)	9(1)	6(1)	23(2)

Table C.11: *Continuation of previous table* Anisotropic displacement parameters ($\text{Å}^2 * 10^3$) for [Sn(SBu^t)(*tfb-dmeda*)] (**2a**). The anisotropic displacement factor exponent takes the form: $-2\pi^2[h^2a^2 * U^{11} + ... + h^2k^2a^2 * b^2 * U^{12}]$.

	U^{11}	U^{22}	U^{33}	U^{23}	U^{13}	U^{12}
F(31)	137(3)	201(4)	89(2)	−59(2)	−63(2)	138(3)
C(45)	32(2)	43(2)	41(2)	10(1)	2(1)	14(1)
C(25)	43(2)	42(2)	49(2)	4(2)	−8(2)	13(2)
C(22)	39(2)	32(2)	46(2)	15(1)	5(1)	13(1)
C(35)	32(2)	39(2)	49(2)	18(2)	3(1)	8(1)
C(36)	37(2)	42(2)	42(2)	12(1)	2(1)	13(1)
C(23)	50(2)	40(2)	41(2)	12(1)	7(2)	19(2)
C(11)	41(2)	51(2)	34(2)	14(2)	3(1)	17(2)
C(15)	38(2)	48(2)	41(2)	−4(2)	−8(1)	18(2)
C(46)	42(2)	46(2)	39(2)	7(1)	0(1)	24(2)
C(16)	37(2)	56(2)	48(2)	11(2)	−1(2)	22(2)
C(47)	61(2)	47(2)	40(2)	3(2)	2(2)	24(2)
C(37)	58(2)	45(2)	38(2)	17(2)	3(2)	14(2)
C(49)	38(2)	39(2)	52(2)	18(2)	8(2)	14(1)
C(311)	32(2)	50(2)	67(2)	17(2)	2(2)	10(2)
C(29)	53(2)	43(2)	39(2)	2(2)	3(2)	10(2)
C(41)	45(2)	64(2)	43(2)	7(2)	−1(2)	26(2)
C(38)	53(2)	44(2)	44(2)	0(2)	−4(2)	16(2)
C(19)	63(2)	40(2)	53(2)	−5(2)	−17(2)	26(2)
C(48)	62(2)	59(2)	41(2)	20(2)	1(2)	24(2)
F(32)	191(5)	94(3)	125(3)	12(2)	−87(3)	−25(3)
C(21)	45(2)	47(2)	58(2)	18(2)	7(2)	13(2)
C(27)	50(2)	66(2)	61(2)	17(2)	16(2)	28(2)
C(310)	54(2)	62(2)	58(2)	31(2)	17(2)	11(2)
C(312)	58(2)	33(2)	76(3)	4(2)	14(2)	12(2)
C(18)	49(2)	85(3)	62(3)	5(2)	10(2)	39(2)
C(31)	56(2)	57(2)	46(2)	−3(2)	−4(2)	31(2)
C(17)	45(2)	77(3)	85(3)	41(3)	12(2)	14(2)
C(111)	81(3)	63(3)	78(3)	−17(2)	−43(3)	37(2)
C(211)	81(3)	40(2)	112(4)	−14(2)	−31(3)	25(2)
C(28)	50(2)	67(3)	102(4)	56(3)	25(2)	15(2)
C(212)	85(3)	50(2)	101(4)	−6(3)	−49(3)	21(2)
C(112)	110(4)	36(2)	113(4)	2(2)	−37(3)	18(2)
C(110)	114(4)	99(4)	56(3)	−17(3)	4(3)	56(3)
C(410)	65(3)	42(3)	255(9)	50(4)	41(4)	15(2)
C(412)	33(2)	169(6)	234(9)	155(7)	−8(4)	4(3)
C(411)	167(7)	104(5)	105(5)	17(4)	91(5)	−16(4)
C(210)	158(7)	162(7)	46(3)	−36(4)	41(4)	−48(5)
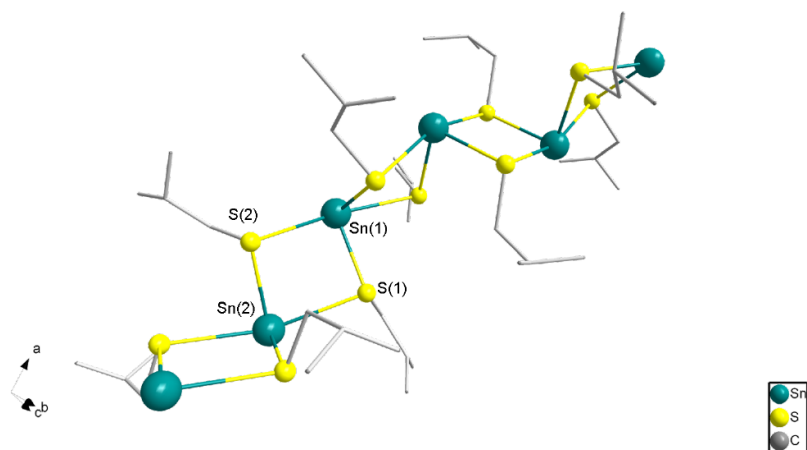
Figure C.1: View on the crystal structure of $[\mathrm{Sn}(\mathrm{SBu}^i)_2]_n$ (**2c**). The tin and sulfur atoms of the asymmetric unit are numbered, and the hydrogen atoms omitted for clarity.
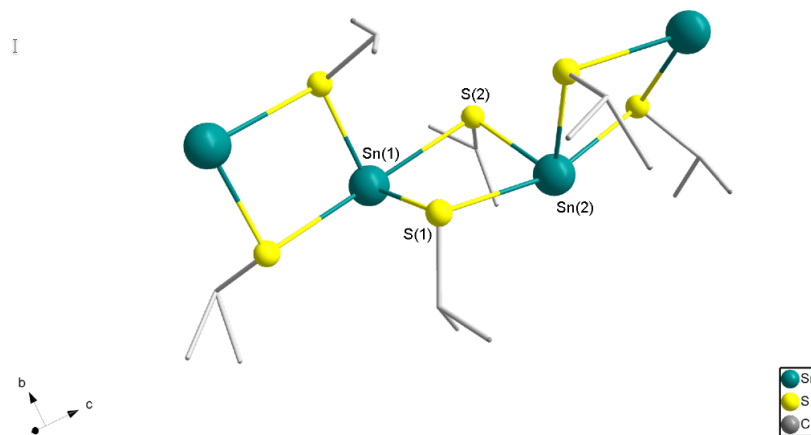
Figure C.2: View on the crystal structure of $[\mathrm{Sn}(\mathrm{SPr}^i)_2]_n$ (**2b**). The tin and sulfur atoms of the asymmetric unit are numbered, and the hydrogen atoms omitted for clarity.

Table C.12: Crystallographic information table for (**2b**) and (**2c**).

	$[\text{Sn}(\text{SPr}^i)_2]_n$ (**2b**)	$[\text{Sn}(\text{SBu}^i)_2]_n$ (**2c**)
CCDC number		
Empirical formula	$[\text{Sn}(\text{SPr}^i)_2]_n$	$[\text{Sn}(\text{SBu}^i)_2]_n$
Moiety Formula	$C_{18}H_{42}S_6Sn_3$	$C_{24}H_{54}SSn_3$
Formula weight	261.01	297.03
Temperature / K	293(2)	170(2)
Crystal system	monoclinic	monoclinic
Space group (number)	$C\,2/c$ (15)	$C\,2/c$ (15)
a / Å	14.565(5)	19.1182(8)
b / Å	11.254(5)	19.2165(7)
c / Å	19.386(5)	10.5825(4)
α / °	90.000(5)	90
β / °	107.242(5)	102.230(3)
γ / °	90.000(5)	90
Volume / Å^3	3034.8(19)	3799.6(3)
Z	4	4
ρ_{calc} / gcm^{-3}	1.766	1.558
μ / mm^{-1}	2.867	2.298
$F(000)$	1584	1776
Crystal size / mm^3	$0.5*0.4*0.2$	$0.4*0.4*0.2$
Crystal color	yellow	yellow
Crystal shape	needle	block
Radiation	Mo-K$_\alpha$ ($\lambda = 0.71073$ Å)	Mo-K$_\alpha$ ($\lambda = 0.71073$ Å)
2θ range / °	4.40 to 53.49 (0.79 Å)	4.24 to 53.63 (0.77 Å)
Index ranges	$-18 \leq h \leq 18$	$-24 \leq h \leq 24$
	$-14 \leq k \leq 14$	$-24 \leq k \leq 24$
	$-24 \leq l \leq 24$	$-13 \leq l \leq 13$
Reflections collected	22619	28421
Independent reflections	3229	4039
	$R_{int} = 0.0525$	$R_{int} = 0.0602$
	$R_{sigma} = 0.0251$	$R_{sigma} = 0.0257$
Completeness to	100.0 %	100 %
$\theta = 25.242°$:		
Data / Restraints / Parameters	3229/0/152	4039/0/150
Goodness-of-fit on F^2	1.028	1.065
Final R indexes	$R_1 = 0.0256$	$R_1 = 0.0290$
$[I \geq 2\sigma(I)]$	$wR_2 = 0.0621$	$wR_2 = 0.0859$
Final R indexes	$R_1 = 0.0302$	$R_1 = 0.0324$
[all data]	$wR_2 = 0.0644$	$wR_2 = 0.0882$
Largest peak/hole /eÅ^{-3}	$0.45/-0.88$	$1.22/-0.51$

Table C.13: Atomic coordinates and U_{eq}/ Å^2 for [Sn(SPr^i)$_2$]$_n$ (**2b**).

Atom	x	y	z	U_{eq}[a)]
Sn(1)	0.58168(2)	0.40812(2)	0.08521(2)	0.03785(8)
Sn(2)	0.5	0.27584(3)	0.25	0.04436(9)
S(3)	0.61291(5)	0.44054(7)	0.23814(4)	0.03874(16)
S(1)	0.51604(6)	0.61858(6)	0.06719(4)	0.03910(16)
S(2)	0.42707(5)	0.31476(7)	0.09485(4)	0.03843(16)
C(11)	0.4282(2)	0.6433(3)	0.11747(17)	0.0439(7)
C(12A)	0.3326(9)	0.6659(14)	0.0713(7)	0.090(4)
C(12B)	0.3244(9)	0.6052(8)	0.0741(7)	0.046(2)
C(13A)	0.4674(6)	0.7266(8)	0.1791(5)	0.060(3)
C(13B)	0.4259(7)	0.7813(6)	0.1270(5)	0.064(3)
C(21)	0.4267(3)	0.1676(3)	0.05298(16)	0.0493(8)
C(22)	0.3381(4)	0.1016(4)	0.0571(3)	0.0859(16)
C(23)	0.5168(3)	0.0984(3)	0.0855(2)	0.0683(11)
C(31)	0.7338(3)	0.3759(5)	0.2689(3)	0.0933(17)
C(32)	0.8020(4)	0.4626(7)	0.2510(5)	0.142(3)
C(33A)	0.7772(6)	0.3490(16)	0.3368(5)	0.148(7)
C(33B)	0.7366(6)	0.2461(8)	0.2619(5)	0.061(3)

[a)] $U_{eq.}$ is defined as $\frac{1}{3}$ of the trace of the orthogonalized U_{ij} tensor.

Table C.14: Bond lengths and bond angles $[Sn(SPr^i)_2]_n$ (**2b**).

Atom–Atom[a)]	Bond Length / pm	Atom-Atom-Atom[a)]	Bond Angle /°
Sn(1)-S(1)	253.93(13)	S(1)-Sn(1)-S(2)	95.17(3)
Sn(1)-S(2)	254.15(11)	S(1)-Sn(1)-S(3)	87.80(2)
Sn(1)-S(3)	288.64(10)	S(2)-Sn(1)-S(3)	81.38(2)
Sn(1)-S(1)#1	288.99(10)	S(1)-Sn(1)-S(1)#1	84.56(3)
Sn(2)-S(3)	253.32(11)	S(2)-Sn(1)-S(1)#1	81.58(3)
Sn(2)-S(3)#2	253.33(11)	S(3)-Sn(1)-S(1)#1	160.59(2)
Sn(2)-S(2)#2	291.08(10)	S(3)-Sn(2)-S(3)#2	85.94(5)
Sn(2)-S(2)	291.09(10)	S(3)-Sn(2)-S(2)#2	86.32(2)
S(3)-C(31)	183.4(4)	S(3)#2-Sn(2)-S(2)#2	81.03(2)
S(1)-C(11)	184.5(3)	S(3)-Sn(2)-S(2)	81.03(2)
S(2)-C(21)	184.4(3)	S(3)#2-Sn(2)-S(2)	86.32(2)
C(11)-C(12A)	143.8(13)	S(2)#2-Sn(2)-S(2)	162.69(3)
C(11)-C(13A)	149.3(8)	C(31)-S(3)-Sn(2)	105.49(19)
C(11)-C(12B)	155.7(13)	C(31)-S(3)-Sn(1)	97.3(2)
C(11)-C(13B)	156.6(7)	Sn(2)-S(3)-Sn(1)	95.27(2)
C(21)-C(23)	149.6(5)	C(11)-S(1)-Sn(1)	111.07(11)
C(21)-C(22)	151.2(6)	C(11)-S(1)-Sn(1)#1	110.32(11)
C(31)-C(33A)	131.7(9)	Sn(1)-S(1)-Sn(1)#1	95.45(3)
C(31)-C(33B)	146.9(10)	C(21)-S(2)-Sn(1)	103.06(12)
C(31)-C(32)	150.5(9)	C(21)-S(2)-Sn(2)	105.80(10)
		Sn(1)-S(2)-Sn(2)	94.49(3)
		C(12A)-C(11)-C(13A)	117.2(7)
		C(12B)-C(11)-C(13B)	106.6(5)
		C(12A)-C(11)-S(1)	113.2(6)
		C(13A)-C(11)-S(1)	110.9(4)
		C(12B)-C(11)-S(1)	112.8(5)
		C(13B)-C(11)-S(1)	104.7(3)
		C(23)-C(21)-C(22)	112.3(3)
		C(23)-C(21)-S(2)	113.3(2)
		C(22)-C(21)-S(2)	108.0(3)
		C(33A)-C(31)-C(32)	103.1(7)
		C(33B)-C(31)-C(32)	125.9(6)
		C(33A)-C(31)-S(3)	123.1(6)
		C(33B)-C(31)-S(3)	114.5(4)
		C(32)-C(31)-S(3)	107.7(4)

[a)] Symmetry transformation to generate equivalent atoms: #1: $-x+1$, $-y+1$, $-z$; #2: $-x+1$, y, $z+\frac{1}{2}$.

Table C.15: Anisotropic displacement parameters ($\text{Å}^2 * 10^3$) for $[\text{Sn}(\text{SPr}^i)_2]_n$ (**2b**). The anisotropic displacement factor exponent takes the form: $-2\pi^2[h^2a^2 * U^{11} + ... + h^2k^2a^2 * b^2 * U^{12}]$.

	U^{11}	U^{22}	U^{33}	U^{23}	U^{13}	U^{12}
Sn(1)	42(1)	44(1)	30(1)	−1(1)	14(1)	2(1)
Sn(2)	70(1)	36(1)	30(1)	0	20(1)	0
S(3)	43(1)	46(1)	27(1)	−5(1)	10(1)	3(1)
S(1)	53(1)	38(1)	29(1)	2(1)	16(1)	−3(1)
S(2)	41(1)	44(1)	30(1)	0(1)	9(1)	−2(1)
C(11)	57(2)	42(2)	38(2)	−3(1)	22(1)	1(1)
C(12A)	54(5)	152(13)	67(6)	−25(10)	21(4)	13(9)
C(12B)	49(5)	48(4)	47(4)	1(4)	22(4)	7(4)
C(13A)	66(5)	70(6)	50(5)	−21(4)	24(4)	0(4)
C(13B)	89(6)	44(4)	68(6)	−11(3)	36(5)	6(3)
C(21)	69(2)	46(2)	28(1)	−3(1)	5(1)	−11(2)
C(22)	74(3)	52(2)	117(4)	5(2)	7(3)	−19(2)
C(23)	78(3)	54(2)	68(3)	−23(2)	16(2)	7(2)
C(31)	47(2)	93(3)	111(4)	−16(3)	−23(2)	9(2)
C(32)	52(3)	158(6)	197(8)	−56(6)	7(4)	−22(4)
C(33A)	44(4)	340(20)	55(5)	76(9)	13(4)	51(8)
C(33B)	48(4)	71(5)	61(5)	11(4)	13(4)	27(4)

Table C.16: Atomic coordinates and U_{eq}/ Å^2 $[\text{Sn}(\text{SBu}^i)_2]_n$ (**2c**).

Atom	x	y	z	U_{eq}[a]
Sn(1)	0.5	0.34334(2)	0.75	0.04358(10)
Sn(2)	0.30331(2)	0.29329(2)	0.65772(2)	0.04397(9)
S(2)	0.39270(4)	0.32845(4)	0.52100(8)	0.04210(18)
S(1)	0.43115(5)	0.24636(5)	0.83001(8)	0.0473(2)
S(3)	0.29378(5)	0.16940(4)	0.57558(10)	0.0501(2)
C(21)	0.3701(2)	0.42101(17)	0.5000(3)	0.0484(8)
C(31)	0.3772(2)	0.1516(2)	0.5237(5)	0.0668(12)
C(11)	0.4139(3)	0.2778(3)	0.9827(4)	0.0683(11)
C(22)	0.3664(4)	0.4470(3)	0.3658(5)	0.0905(17)
C(32)	0.3930(4)	0.0753(3)	0.5125(8)	0.104(2)
C(23)	0.3415(5)	0.5239(3)	0.3620(7)	0.134(3)
C(12)	0.3854(8)	0.2229(7)	1.0558(9)	0.211(7)
C(24)	0.4256(6)	0.4383(5)	0.3125(10)	0.172(5)
C(33)	0.3404(5)	0.0380(4)	0.4146(11)	0.162(4)
C(14)	0.3464(11)	0.1723(5)	1.0139(14)	0.304(12)
C(34)	0.4098(7)	0.0433(6)	0.6319(12)	0.221(7)
C(13)	0.3710(11)	0.2573(12)	1.1733(11)	0.380(17)

[a] U_{eq} is defined as $\frac{1}{3}$ of the trace of the orthogonalized U_{ij} tensor.

Table C.17: Bond lengths and bond angles $[\text{Sn}(\text{SBu}^i)_2]_n$ (**2c**).

Atom-Atom[a]	Bond Length / pm	Atom-Atom-Atom[a]	Bond Angle /°
Sn(1)-S(1)#1	252.88(9)	S(1)#1-Sn(1)-S(1)	85.05(4)
Sn(1)-S(1)	252.88(9)	S(1)#1-Sn(1)-S(2)#1	83.00(3)
Sn(1)-S(2)#1	283.84(8)	S(1)-Sn(1)-S(2)#1	88.46(3)
Sn(1)-S(2)	283.84(8)	S(1)#1-Sn(1)-S(2)	88.46(3)
Sn(2)-S(3)	252.77(9)	S(1)-Sn(1)-S(2)	83.01(3)
Sn(2)-S(2)	255.30(9)	S(2)#1-Sn(1)-S(2)	168.42(4)
Sn(2)-S(3)#2	284.83(9)	S(3)-Sn(2)-S(2)	93.59(3)
Sn(2)-S(1)	286.76(9)	S(3)-Sn(2)-S(3)#2	87.29(3)
S(2)-C(21)	183.3(3)	S(2)-Sn(2)-S(3)#2	80.43(3)
S(1)-C(11)	182.0(4)	S(3)-Sn(2)-S(1)	84.95(3)
S(3)-C(31)	182.6(5)	S(2)-Sn(2)-S(1)	82.00(3)
C(21)-C(22)	149.3(6)	S(3)#2-Sn(2)-S(1)	160.29(3)
C(31)-C(32)	150.7(6)	C(21)-S(2)-Sn(2)	99.00(13)
C(11)-C(12)	147.8(10)	C(21)-S(2)-Sn(1)	96.61(11)
C(22)-C(24)	137.7(10)	Sn(2)-S(2)-Sn(1)	89.56(2)
C(22)-C(23)	155.0(8)	C(11)-S(1)-Sn(1)	104.94(16)
C(32)-C(34)	138.0(12)	C(11)-S(1)-Sn(2)	99.75(17)
C(32)-C(33)	146.8(10)	Sn(1)-S(1)-Sn(2)	89.39(3)
C(12)-C(14)	124.8(14)	C(31)-S(3)-Sn(2)	106.04(13)
C(12)-C(13)	148.5(16)	C(31)-S(3)-Sn(2)#2	103.70(17)
		Sn(2)-S(3)-Sn(2)#2	92.71(3)
		C(22)-C(21)-S(2)	113.7(3)
		C(32)-C(31)-S(3)	114.1(4)
		C(12)-C(11)-S(1)	112.5(5)
		C(24)-C(22)-C(21)	118.1(6)
		C(24)-C(22)-C(23)	112.4(6)
		C(21)-C(22)-C(23)	107.2(5)
		C(34)-C(32)-C(33)	114.9(9)
		C(34)-C(32)-C(31)	111.9(7)
		C(33)-C(32)-C(31)	114.3(5)
		C(14)-C(12)-C(11)	129.0(9)
		C(14)-C(12)-C(13)	116.1(10)
		C(11)-C(12)-C(13)	105.9(11)

[a] Symmetry transformation to generate equivalent atoms: #1: $-x + 1$, y, $-z + \frac{3}{2}$; #2: $-x + \frac{1}{2}$, $-y + \frac{1}{2}$, $-z + 1$.

Table C.18: Anisotropic displacement parameters ($\text{Å}^2 * 10^3$)for $[\text{Sn}(\text{SBu}^i)_2]_n$ (**2c**). The anisotropic displacement factor exponent takes the form: $-2\pi^2[h^2a^2*U^{11} + ... + h^2k^2a^2*b^2*U^{12}]$.

	U^{11}	U^{22}	U^{33}	U^{23}	U^{13}	U^{12}
Sn(1)	41(1)	42(1)	43(1)	0	−2(1)	0
Sn(2)	41(1)	39(1)	50(1)	2(1)	5(1)	0(1)
S(2)	43(1)	39(1)	40(1)	5(1)	1(1)	−1(1)
S(1)	47(1)	49(1)	42(1)	4(1)	0(1)	−2(1)
S(3)	41(1)	34(1)	67(1)	6(1)	−7(1)	−2(1)
C(21)	54(2)	38(2)	49(2)	5(1)	0(2)	−4(1)
C(31)	47(2)	43(2)	104(3)	−9(2)	3(2)	8(2)
C(11)	80(3)	80(3)	43(2)	1(2)	11(2)	−8(2)
C(22)	146(5)	62(3)	66(3)	29(2)	30(3)	22(3)
C(32)	96(4)	47(3)	160(6)	−11(3)	6(4)	19(3)
C(23)	238(10)	73(4)	97(4)	42(3)	49(5)	53(5)
C(12)	283(14)	279(15)	100(6)	−60(7)	107(8)	−196(13)
C(24)	254(12)	119(6)	185(9)	81(6)	141(9)	58(7)
C(33)	161(8)	85(5)	238(12)	−62(6)	36(8)	5(5)
C(14)	610(30)	100(7)	306(16)	−32(9)	340(20)	−124(13)
C(34)	295(16)	138(8)	207(12)	54(8)	5(11)	113(10)
C(13)	510(30)	560(30)	137(10)	−147(15)	205(16)	−350(30)

Table C.19: Crystallographic information table for $\mathrm{Pb(SBu}^{t})_2$ (**3a**) and $\mathrm{Pb(SBu}^{i})_2$ (**3c**)

	(**3a**)	(**3c**)
CCDC number		
Empirical formula	$\mathrm{Pb(SBu}^{t})_2$	$\mathrm{Pb(SBu}^{i})_2$
Moiety Formula	$[\mathrm{Pb}_3(\mu\text{-}\mathrm{SBu}^{t})_6]$	$[\mathrm{Pb}_5(\mu\text{-}\mathrm{SBu}^{i})_4(\mathrm{SBu}^{i})_6]$
Formula weight	1156.6	1925.65
Temperature / K	173(2)	170(2)
Crystal system	triclinic	monoclinic
Space group (number)	$P\bar{1}$ (2)	Cc (9)
a / Å	11.5071(9)	17.1585(18)
b / Å	15.4292(11)	22.5050(19)
c / Å	17.7239(15)	17.7875(19)
α / °	111.890(6)	90
β / °	105.781(6)	113.396(8)
γ / °	98.909(6)	90
Volume / Å^3	2691.7(4)	6304.0(11)
Z	3	4
ρ_{calc} / gcm^{-3}	2.141	2.029
μ / mm^{-1}	14.4	13.663
$F(000)$	1620	3592
Crystal size / mm^3	$0.7*0.4*0.2$	$0.4*0.4*0.2$
Crystal color	yellow	yellow
Crystal shape	plate	plate
Radiation	Mo-K$_\alpha$ ($\lambda = 0.71073\,\text{Å}$)	Mo-K$_\alpha$ ($\lambda = 0.71073\,\text{Å}$)
2θ range / °	3.80 to 53.71 (0.79 Å)	3.16 to 54.64 (0.77 Å)
Index ranges	$-14 \leq h \leq 14$	$-21 \leq h \leq 22$
	$-19 \leq k \leq 19$	$-26 \leq k \leq 28$
	$-22 \leq l \leq 22$	$-22 \leq l \leq 22$
Reflections collected	35160	29545
Independent reflections	11413	13360
	$R_{int} = 0.2055$	$R_{int} = 0.0740$
	$R_{sigma} = 0.1523$	$R_{sigma} = 0.0779$
Completeness to	99.80 %	100.00 %
$\theta = 25.242°$		
Data / Restraints / Parameters	11413/216/448	13360/193/496
Goodness-of-fit on F^2	0.97	1.062
Final R indexes	$R_1 = 0.0855$	$R_1 = 0.0497$
$[I \geq 2\sigma(I)]$	$wR_2 = 0.2196$	$wR_2 = 0.1027$
Final R indexes	$R_1 = 0.1340$	$R_1 = 0.0989$
[all data]	$wR_2 = 0.2642$	$wR_2 = 0.1363$
Largest peak/hole /eÅ^{-3}	$7.75/-3.10$	$1.61/-2.01$
Flack X parameter		$-0.034(7)$
Extinction coefficient		0.00029(3)

Table C.20: Crystallographic information table for $[\mathrm{Pb_{12}O_6(SPr^{\mathit{i}})_{12}\cdot C_6H_6}]$ (**3d**) and $[\mathrm{Pb_{12}O_6(SBu^{\mathit{t}})_{12}}]\cdot 6\,(\mathrm{NC_5H_5})$ (**3e**).

	(**3d**)	(**3e**)
CCDC number		
Empirical formula	$[\mathrm{Pb_{12}O_6(SPr^{\mathit{i}})_{12}\cdot C_6H_6}]$	$[\mathrm{Pb_{12}O_6(SBu^{\mathit{t}})_{12}}]\cdot 6\,(\mathrm{NC_5H_5})$
Formula weight	3562.13	4126.94
Temperature / K	170(2)	150(2)
Crystal system	triclinic	triclinic
Space group (number)	$P\bar{1}$ (2)	$P\bar{1}$ (2)
a / Å	9.9462(4)	10.5178(7)
b / Å	13.2531(6)	14.8897(9)
c / Å	16.5961(8)	19.5541(12)
α / °	66.962(3)	66.543(5)
β / °	71.444(3)	78.750(5)
γ / °	76.593(3)	82.244(5)
Volume / Å^3	1894.03(16)	2749.7(3)
Z	1	1
ρ_{calc} / gcm^{-3}	3.123	2.492
μ / mm^{-1}	26.922	18.565
$F(000)$	1566	1872
Crystal size / mm^3	$0.4*0.4*0.4$	$0.7*0.4*0.1$
Crystal color	yellow	yellow
Crystal shape	block	plate
Radiation	Mo-K$_\alpha$ ($\lambda = 0.71073\,\text{Å}$)	Mo-K$_\alpha$ ($\lambda = 0.71073\,\text{Å}$)
2θ range / °	3.36 to 53.54 (0.79 Å)	3.96 to 53.70 (0.79 Å)
Index ranges	$-12 \le h \le 12$	$-13 \le h \le 11$
	$-15 \le k \le 16$	$-18 \le k \le 18$
	$-20 \le l \le 20$	$-24 \le l \le 24$
Reflections collected	26021	23858
Independent reflections	8018	11191
	$R_{int} = 0.0752$	$R_{int} = 0.1193$
	$R_{sigma} = 0.0529$	$R_{sigma} = 0.1636$
Completeness to $\theta = 25.242°$	100.00 %	96.20 %
Data / Restraints / Parameters	8018/0/316	11191/72/514
Goodness-of-fit on F^2	0.958	0.802
Final R indexes $[I \ge 2\sigma(I)]$	$R_1 = 0.0307$ $wR_2 = 0.0725$	$R_1 = 0.0517$ $wR_2 = 0.0986$
Final R indexes [all data]	$R_1 = 0.0417$ $wR_2 = 0.0782$	$R_1 = 0.1317$ $wR_2 = 0.1228$
Largest peak/hole /eÅ^{-3}	2.40/−1.58	1.77/−2.21
Extinction coefficient	0.00077(4)	

Table C.21: Atomic coordinates and $U_{eq}/\text{Å}^2$ Pb(SBu^t)$_2$ (**3a**).

Atom	x	y	z	U_{eq} [a]
Pb(1)	0.07654(6)	0.95991(4)	0.15964(4)	0.03610(19)
S(1)	0.1709(4)	0.8887(3)	0.0371(3)	0.0394(8)
Pb(2)	0.32627(6)	0.82948(4)	0.16430(4)	0.03578(19)
S(2)	0.0637(4)	0.7955(3)	0.1754(3)	0.0403(9)
Pb(3)	0.58915(6)	0.71531(4)	0.17312(4)	0.03761(19)
S(3)	0.3087(4)	1.0236(3)	0.2723(3)	0.0370(8)
Pb(4)	0.26103(6)	0.38303(4)	0.50427(5)	0.0407(2)
S(4)	0.5893(4)	0.8884(3)	0.1748(3)	0.0412(9)
Pb(5)	0	0.5	0.5	0.0361(2)
S(5)	0.3662(4)	0.6457(3)	0.0460(3)	0.0392(9)
S(6)	0.4764(4)	0.7580(3)	0.2878(3)	0.0389(8)
S(7)	0.1442(4)	0.4322(3)	0.3824(3)	0.0433(9)
S(8)	0.2681(5)	0.5535(3)	0.6215(3)	0.0425(9)
S(9)	0.0364(5)	0.3133(3)	0.5048(3)	0.0440(10)
C(11)	0.0414(18)	0.7861(12)	−0.0619(11)	0.043(3)
C(12)	−0.082(2)	0.802(2)	−0.0642(19)	0.090(8)
C(13)	0.067(2)	0.7930(14)	−0.1377(13)	0.065(5)
C(14)	0.051(2)	0.6909(13)	−0.0620(15)	0.064(6)
C(21)	0.0638(18)	0.8155(11)	0.2856(13)	0.044(3)
C(22)	−0.018(2)	0.7219(15)	0.2760(15)	0.062(5)
C(23)	0.1935(19)	0.8357(15)	0.3453(11)	0.055(4)
C(24)	0.004(3)	0.8972(16)	0.3171(15)	0.066(6)
C(31)	0.3976(17)	1.1333(10)	0.2695(10)	0.036(3)
C(32)	0.335(3)	1.2116(15)	0.298(2)	0.084(7)
C(33)	0.527(2)	1.163(2)	0.332(2)	0.095(8)
C(34)	0.400(3)	1.1136(17)	0.1825(16)	0.087(8)
C(41)	0.6073(18)	0.8825(14)	0.0723(14)	0.050(4)
C(42)	0.665(2)	0.8034(15)	0.0334(13)	0.057(4)
C(43)	0.4810(18)	0.8702(14)	0.0090(12)	0.051(4)
C(44)	0.6993(18)	0.9826(14)	0.0983(13)	0.054(4)
C(51)	0.2736(19)	0.5336(10)	0.0452(11)	0.045(4)
C(52)	0.188(2)	0.5620(14)	0.0969(13)	0.058(4)
C(53)	0.202(2)	0.4657(14)	−0.0496(11)	0.062(5)
C(54)	0.362(2)	0.4869(13)	0.0830(14)	0.063(5)
C(61)	0.5968(17)	0.8571(12)	0.3947(12)	0.042(3)
C(62)	0.559(2)	0.8335(15)	0.4631(12)	0.056(5)
C(63)	0.7280(17)	0.8528(14)	0.4004(12)	0.050(4)
C(64)	0.5809(18)	0.9543(12)	0.4032(13)	0.049(4)
C(71)	0.255(2)	0.5283(14)	0.3788(13)	0.050(4)
C(72)	0.215(4)	0.522(3)	0.2914(19)	0.138(14)
C(73)	0.385(2)	0.524(3)	0.409(3)	0.126(11)
C(74)	0.247(4)	0.6256(18)	0.432(2)	0.123(11)
C(81)	0.288(2)	0.5457(12)	0.7277(12)	0.051(4)
C(82)	0.330(3)	0.4571(18)	0.7257(15)	0.084(7)
C(83)	0.161(3)	0.532(2)	0.7373(16)	0.078(6)
C(84)	0.383(3)	0.6359(18)	0.7980(16)	0.111(10)
C(91)	−0.0512(19)	0.2034(10)	0.4007(12)	0.044(4)
C(92)	−0.122(3)	0.1300(14)	0.4224(16)	0.075(7)
C(93)	−0.142(2)	0.2283(15)	0.3385(15)	0.061(5)
C(94)	0.042(2)	0.1608(14)	0.3602(13)	0.057(4)

[a] $U_{eq.}$ is defined as $\frac{1}{3}$ of the trace of the orthogonalized U_{ij} tensor.

Table C.22: Bond lengths Pb(SBu^t)$_2$ (**3a**).

Atom-Atom[a]	Bond Length / pm	Atom-Atom[a]	Bond Length / pm
Pb(1)-S(3)	262.9(4)	S(9)-C(91)	185.0(18)
Pb(1)-S(2)	264.1(4)	C(11)-C(12)	147(3)
Pb(1)-S(1)	264.1(4)	C(11)-C(13)	149(3)
S(1)-C(11)	189.3(18)	C(11)-C(14)	149(2)
S(1)-Pb(2)	299.4(4)	C(21)-C(23)	148(3)
Pb(2)-S(4)	295.5(5)	C(21)-C(22)	152(2)
Pb(2)-S(3)	296.6(4)	C(21)-C(24)	152(2)
Pb(2)-S(5)	302.4(4)	C(31)-C(34)	147(3)
Pb(2)-S(6)	305.4(4)	C(31)-C(33)	147(3)
Pb(2)-S(2)	305.8(5)	C(31)-C(32)	150(3)
S(2)-C(21)	185.8(19)	C(41)-C(43)	151(3)
Pb(3)-S(6)	263.6(4)	C(41)-C(42)	151(2)
Pb(3)-S(5)	264.8(4)	C(41)-C(44)	155(2)
Pb(3)-S(4)	265.9(4)	C(51)-C(54)	149(3)
S(3)-C(31)	186.3(14)	C(51)-C(53)	151(2)
Pb(4)-S(9)	264.5(5)	C(51)-C(52)	153(3)
Pb(4)-S(7)	264.6(4)	C(61)-C(64)	150(2)
Pb(4)-S(8)	264.7(4)	C(61)-C(63)	150(3)
S(4)-C(41)	186(2)	C(61)-C(62)	154(2)
Pb(5)-S(7)	299.8(5)	C(71)-C(72)	145(3)
Pb(5)-S(7)#1	299.8(5)	C(71)-C(73)	147(3)
Pb(5)-S(9)	300.3(4)	C(71)-C(74)	148(3)
Pb(5)-S(9)#1	300.3(4)	C(81)-C(84)	148(3)
Pb(5)-S(8)	301.8(5)	C(81)-C(82)	151(3)
Pb(5)-S(8)#1	301.8(5)	C(81)-C(83)	151(3)
S(5)-C(51)	187.8(17)	C(91)-C(93)	151(3)
S(6)-C(61)	189.8(19)	C(91)-C(92)	152(2)
S(7)-C(71)	183.2(19)	C(91)-C(94)	154(3)
S(8)-C(81)	188.4(19)		

[a] Symmetry transformation to generate equivalent atoms: #1: $-x$, $-y + 1$, $-z + 1$.

Table C.23: Bond angles Pb(SBu^t)$_2$ (**3a**).

Atom-Atom-Atom[a]	Bond Angle /°	Atom-Atom-Atom[a]	Bond Angle /°
S(3)-Pb(1)-S(2)	86.64(13)	C(81)-S(8)-Pb(4)	108.7(6)
S(3)-Pb(1)-S(1)	86.89(13)	C(81)-S(8)-Pb(5)	116.1(7)
S(2)-Pb(1)-S(1)	87.46(12)	Pb(4)-S(8)-Pb(5)	82.19(12)
C(11)-S(1)-Pb(1)	108.4(6)	C(91)-S(9)-Pb(4)	108.3(6)
C(11)-S(1)-Pb(2)	115.5(5)	C(91)-S(9)-Pb(5)	114.1(5)
Pb(1)-S(1)-Pb(2)	83.32(11)	Pb(4)-S(9)-Pb(5)	82.51(11)
S(4)-Pb(2)-S(3)	98.72(11)	C(12)-C(11)-C(13)	109(2)
S(4)-Pb(2)-S(1)	106.62(11)	C(12)-C(11)-C(14)	113(2)
S(3)-Pb(2)-S(1)	74.88(11)	C(13)-C(11)-C(14)	109.8(17)
S(4)-Pb(2)-S(5)	75.11(12)	C(12)-C(11)-S(1)	110.1(14)
S(3)-Pb(2)-S(5)	172.42(11)	C(13)-C(11)-S(1)	104.8(13)
S(1)-Pb(2)-S(5)	102.39(11)	C(14)-C(11)-S(1)	109.4(13)
S(4)-Pb(2)-S(6)	74.88(11)	C(23)-C(21)-C(22)	108.7(16)
S(3)-Pb(2)-S(6)	107.58(11)	C(23)-C(21)-C(24)	113.1(18)
S(1)-Pb(2)-S(6)	177.01(10)	C(22)-C(21)-C(24)	109.0(17)
S(5)-Pb(2)-S(6)	75.38(11)	C(23)-C(21)-S(2)	110.2(12)
S(4)-Pb(2)-S(2)	172.06(11)	C(22)-C(21)-S(2)	107.2(13)
S(3)-Pb(2)-S(2)	73.74(11)	C(24)-C(21)-S(2)	108.4(13)
S(1)-Pb(2)-S(2)	74.19(11)	C(34)-C(31)-C(33)	110(2)
S(5)-Pb(2)-S(2)	112.60(11)	C(34)-C(31)-C(32)	110.4(19)
S(6)-Pb(2)-S(2)	104.70(11)	C(33)-C(31)-C(32)	110(2)
C(21)-S(2)-Pb(1)	109.8(5)	C(34)-C(31)-S(3)	112.1(12)
C(21)-S(2)-Pb(2)	114.2(6)	C(33)-C(31)-S(3)	106.9(12)
Pb(1)-S(2)-Pb(2)	82.09(11)	C(32)-C(31)-S(3)	107.4(13)
S(6)-Pb(3)-S(5)	89.38(13)	C(43)-C(41)-C(42)	111.9(18)
S(6)-Pb(3)-S(4)	87.26(13)	C(43)-C(41)-C(44)	109.6(15)
S(5)-Pb(3)-S(4)	86.76(13)	C(42)-C(41)-C(44)	108.2(16)
C(31)-S(3)-Pb(1)	110.1(5)	C(43)-C(41)-S(4)	109.2(12)
C(31)-S(3)-Pb(2)	118.8(5)	C(42)-C(41)-S(4)	112.4(13)
Pb(1)-S(3)-Pb(2)	84.08(11)	C(44)-C(41)-S(4)	105.4(14)
S(9)-Pb(4)-S(7)	87.26(14)	C(54)-C(51)-C(53)	108.6(15)
S(9)-Pb(4)-S(8)	87.32(14)	C(54)-C(51)-C(52)	111.2(17)
S(7)-Pb(4)-S(8)	87.77(13)	C(53)-C(51)-C(52)	112.9(18)
C(41)-S(4)-Pb(3)	106.8(6)	C(54)-C(51)-S(5)	109.4(14)
C(41)-S(4)-Pb(2)	115.1(6)	C(53)-C(51)-S(5)	105.3(12)
Pb(3)-S(4)-Pb(2)	82.95(11)	C(52)-C(51)-S(5)	109.2(11)
S(7)-Pb(5)-S(7)#1	180	C(64)-C(61)-C(63)	111.5(15)
S(7)-Pb(5)-S(9)	74.95(11)	C(64)-C(61)-C(62)	109.6(15)
S(7)#1-Pb(5)-S(9)	105.05(11)	C(63)-C(61)-C(62)	112.4(15)
S(7)-Pb(5)-S(9)#1	105.05(11)	C(64)-C(61)-S(6)	109.3(12)
S(7)#1-Pb(5)-S(9)#1	74.95(11)	C(63)-C(61)-S(6)	110.8(12)
S(9)-Pb(5)-S(9)#1	180.0(2)	C(62)-C(61)-S(6)	102.8(12)
S(7)-Pb(5)-S(8)	75.16(12)	C(72)-C(71)-C(73)	113(3)
S(7)#1-Pb(5)-S(8)	104.84(12)	C(72)-C(71)-C(74)	103(3)
S(9)-Pb(5)-S(8)	74.70(12)	C(73)-C(71)-C(74)	110(3)
S(9)#1-Pb(5)-S(8)	105.30(12)	C(72)-C(71)-S(7)	109.4(18)
S(7)-Pb(5)-S(8)#1	104.84(12)	C(73)-C(71)-S(7)	111.3(15)
S(7)#1-Pb(5)-S(8)#1	75.16(12)	C(74)-C(71)-S(7)	110.6(17)
S(9)-Pb(5)-S(8)#1	105.30(12)	C(84)-C(81)-C(82)	111(2)
S(9)#1-Pb(5)-S(8)#1	74.70(12)	C(84)-C(81)-C(83)	113(2)
S(8)-Pb(5)-S(8)#1	180	C(82)-C(81)-C(83)	106.9(19)
C(51)-S(5)-Pb(3)	109.2(6)	C(84)-C(81)-S(8)	107.7(14)
C(51)-S(5)-Pb(2)	112.0(6)	C(82)-C(81)-S(8)	110.2(14)
Pb(3)-S(5)-Pb(2)	81.81(11)	C(83)-C(81)-S(8)	108.0(14)
C(61)-S(6)-Pb(3)	107.5(5)	C(93)-C(91)-C(92)	110.5(19)
C(61)-S(6)-Pb(2)	115.5(5)	C(93)-C(91)-C(94)	110.3(17)
Pb(3)-S(6)-Pb(2)	81.44(11)	C(92)-C(91)-C(94)	109.4(15)
C(71)-S(7)-Pb(4)	109.8(7)	C(93)-C(91)-S(9)	110.2(11)
C(71)-S(7)-Pb(5)	115.9(6)	C(92)-C(91)-S(9)	106.6(13)
Pb(4)-S(7)-Pb(5)	82.59(11)	C(94)-C(91)-S(9)	109.9(14)

[a] Symmetry transformation to generate equivalent atoms: #1: $-x$, $-y + 1$, $-z + 1$.

Table C.24: Anisotropic displacement parameters ($\mathring{A}^2 * 10^3$) for Pb(SBu^t)$_2$ (**3a**). The anisotropic displacement factor exponent takes the form: $-2\pi^2[h^2a^2 * U^{11} + ... + h^2k^2a^2 * b^2 * U^{12}]$.

	U^{11}	U^{22}	U^{33}	U^{23}	U^{13}	U^{12}
Pb(1)	41(1)	35(1)	35(1)	16(1)	17(1)	11(1)
S(1)	49(2)	39(2)	27(2)	13(2)	16(2)	6(2)
Pb(2)	40(1)	33(1)	36(1)	15(1)	16(1)	10(1)
S(2)	53(2)	34(2)	29(2)	13(2)	16(2)	2(2)
Pb(3)	42(1)	38(1)	36(1)	18(1)	16(1)	13(1)
S(3)	46(2)	34(2)	24(2)	12(2)	10(2)	1(2)
Pb(4)	44(1)	37(1)	44(1)	18(1)	18(1)	13(1)
S(4)	52(2)	36(2)	34(2)	16(2)	17(2)	4(2)
Pb(5)	40(1)	34(1)	34(1)	14(1)	14(1)	9(1)
S(5)	55(2)	32(2)	22(2)	10(2)	9(2)	1(2)
S(6)	44(2)	35(2)	27(2)	8(2)	11(2)	0(2)
S(7)	52(3)	42(2)	31(2)	18(2)	14(2)	0(2)
S(8)	62(3)	36(2)	23(2)	14(2)	10(2)	6(2)
S(9)	59(3)	35(2)	31(2)	10(2)	20(2)	0(2)
C(11)	54(9)	40(7)	25(7)	13(7)	5(7)	2(7)
C(12)	46(11)	94(17)	74(17)	-4(14)	3(10)	9(11)
C(13)	98(16)	45(9)	34(10)	9(8)	20(10)	−4(10)
C(14)	73(13)	35(8)	58(13)	23(9)	0(10)	−18(8)
C(21)	53(9)	30(7)	49(10)	14(7)	28(7)	5(6)
C(22)	70(12)	60(9)	55(12)	33(10)	25(10)	−11(9)
C(23)	62(9)	69(11)	24(9)	23(8)	9(7)	2(8)
C(24)	109(16)	72(11)	59(13)	41(11)	61(13)	47(12)
C(31)	53(9)	20(6)	28(7)	7(6)	13(6)	−1(6)
C(32)	98(16)	41(10)	110(20)	24(12)	55(16)	15(11)
C(33)	43(10)	109(18)	104(17)	66(17)	−10(10)	−38(10)
C(34)	130(20)	66(12)	50(10)	20(10)	50(11)	−26(13)
C(41)	44(9)	54(9)	57(11)	27(9)	25(7)	8(7)
C(42)	69(12)	64(9)	38(10)	11(9)	38(9)	16(9)
C(43)	58(9)	59(10)	38(10)	28(8)	17(7)	3(7)
C(44)	49(9)	58(8)	50(11)	24(8)	24(8)	−11(8)
C(51)	66(11)	17(6)	24(7)	−5(5)	3(6)	−4(6)
C(52)	80(13)	51(10)	33(9)	18(8)	19(9)	−4(9)
C(53)	67(12)	52(10)	15(7)	-2(7)	−9(7)	−33(9)
C(54)	97(14)	39(9)	41(10)	21(8)	7(9)	9(9)
C(61)	48(8)	49(8)	36(9)	25(8)	18(7)	8(7)
C(62)	73(12)	67(11)	24(9)	30(8)	10(8)	2(10)
C(63)	41(8)	61(10)	30(9)	14(8)	1(7)	2(8)
C(64)	52(10)	38(8)	50(11)	24(8)	13(8)	−4(7)
C(71)	62(10)	52(9)	44(10)	28(8)	24(8)	12(9)
C(72)	180(30)	120(20)	49(12)	45(13)	−10(16)	−60(20)
C(73)	47(12)	140(20)	210(30)	130(30)	31(15)	−6(14)
C(74)	190(30)	49(12)	120(20)	21(13)	80(20)	3(15)
C(81)	69(11)	33(7)	38(9)	19(7)	4(8)	0(7)
C(82)	140(20)	83(12)	40(12)	36(10)	14(13)	56(15)
C(83)	89(12)	103(17)	49(13)	41(13)	24(11)	25(12)
C(84)	160(20)	70(11)	33(12)	10(10)	−9(14)	−50(15)
C(91)	68(11)	22(6)	45(9)	12(6)	29(8)	10(7)
C(92)	118(19)	40(9)	57(13)	14(9)	46(13)	−11(11)
C(93)	63(12)	50(10)	63(13)	23(9)	21(10)	5(9)
C(94)	70(12)	49(10)	38(10)	4(8)	20(9)	15(9)

Table C.25: Atomic coordinates and $U_{eq}/$ Å^2 Pb(SBu^i)$_2$ (**3c**).

Atom	x	y	z	U_{eq} $^{a)}$
Pb(1)	0.1094(10)	−0.11152(5)	1.21735(6)	0.0458(3)
Pb(2)	0.2425(10)	0.02839(5)	1.20353(6)	0.0510(3)
Pb(3)	0.1452(10)	0.07070(5)	0.95963(6)	0.0445(3)
Pb(4)	0.3255(10)	0.17665(5)	1.10639(6)	0.0478(3)
Pb(5)	0.4759(10)	0.27408(5)	1.28077(6)	0.0486(3)
S(1)	0.1746(11)	−0.1742(3)	1.3566(5)	0.0485(17)
C(11)	0.267(3)	−0.2120(16)	1.356(3)	0.086(11)
C(12)	0.286(4)	−0.266(2)	1.382(4)	0.133(14)
C(13)	0.375(4)	−0.290(3)	1.367(4)	0.17(3)
C(14)	0.266(3)	−0.3013(16)	1.428(3)	0.093(12)
S(2)	0.1645(11)	−0.0024(4)	1.3036(5)	0.0521(17)
C(21)	0.077(3)	0.0494(17)	1.284(3)	0.106(14)
C(22)	0.112(3)	0.116(2)	1.315(3)	0.128(16)
C(23)	0.173(4)	0.123(3)	1.390(4)	0.19(3)
C(24)	0.025(4)	0.150(2)	1.291(4)	0.16(2)
S(3)	0.2980(11)	−0.0807(4)	1.2427(6)	0.064(2)
C(31)	0.307(4)	−0.108(2)	1.151(3)	0.128(16)
C(32)	0.369(5)	−0.150(3)	1.149(5)	0.18(2)
C(33)	0.406(5)	−0.191(3)	1.213(5)	0.19(2)
C(34)	0.450(4)	−0.095(3)	1.186(4)	0.17(2)
S(4)	0.1148(11)	−0.0147(3)	1.0613(4)	0.0525(18)
C(41)	0.013(2)	0.0185(14)	1.0521(18)	0.060(8)
C(42)	−0.059(2)	0.0107(17)	0.968(2)	0.077(9)
C(43)	−0.084(3)	−0.0552(19)	0.951(2)	0.091(11)
C(44)	−0.134(2)	0.0465(18)	0.970(2)	0.094(12)
S(5)	0.3059(11)	0.0463(3)	1.0438(4)	0.0501(17)
C(51)	0.361(2)	0.0627(19)	0.9743(19)	0.074(11)
C(52)	0.447(3)	0.037(2)	1.003(2)	0.087(13)
C(53)	0.421(6)	−0.037(4)	0.978(5)	0.24(5)
C(54)	0.494(3)	0.065(3)	0.962(4)	0.15(2)
S(6)	0.1611(11)	0.1501(3)	1.0859(4)	0.0461(16)
C(61)	0.111(2)	0.2187(16)	1.0346(19)	0.064(8)
C(62)	0.037(3)	0.239(2)	1.045(3)	0.107(12)
C(63)	−0.010(4)	0.209(3)	1.076(5)	0.17(3)
C(64)	0.004(4)	0.294(2)	1.001(3)	0.127(18)
S(7)	0.4085(11)	0.1360(4)	1.2551(5)	0.0545(18)
C(71)	0.480(3)	0.079(2)	1.236(2)	0.113(16)
C(72)	0.571(3)	0.086(3)	1.296(3)	0.126(15)
C(73)	0.5837	0.0772	1.384(2)	0.137(19)
C(74)	0.618(4)	0.033(3)	1.272(4)	0.20(3)
S(8)	0.3053(11)	0.2768(4)	1.1917(5)	0.0538(18)
C(81)	0.270(2)	0.2522(15)	1.274(2)	0.063(8)
C(82)	0.252(2)	0.3063(16)	1.317(2)	0.075(8)
C(83)	0.177(3)	0.345(2)	1.261(3)	0.115(14)
C(84)	0.238(3)	0.287(2)	1.390(3)	0.112(13)
S(9)	0.4866(11)	0.2745(4)	1.1363(5)	0.0535(18)
C(91)	0.559(3)	0.2154(18)	1.140(3)	0.084(10)
C(92)	0.628(3)	0.226(2)	1.112(3)	0.115(13)
C(93)	0.681(3)	0.173(2)	1.117(3)	0.124(17)
C(94)	0.583(5)	0.248(3)	1.022(4)	0.19(3)
S(10)	0.4763(11)	0.3989(3)	1.2700(4)	0.0483(16)
C(95)	0.390(2)	0.4168(15)	1.1722(16)	0.057(8)
C(96)	0.314(2)	0.4480(16)	1.185(2)	0.062(8)
C(97)	0.332(2)	0.5069(18)	1.218(2)	0.084(11)
C(98)	0.238(2)	0.451(2)	1.107(3)	0.110(16)

$^{a)}$ $U_{eq.}$ is defined as $\frac{1}{3}$ of the trace of the orthogonalized U_{ij} tensor.

Table C.26: Bond lengths Pb(SBu^i)$_2$ (**3c**).

Atom-Atom$^{a)}$	Bond Length / pm	Atom-Atom$^{a)}$	Bond Length / pm
Pb(1)-S(1)	267.8(8)	S(4)-C(41)	185(3)
Pb(1)-S(10)#1	280.2(7)	C(41)-C(42)	152(4)
Pb(1)-S(2)	285.0(8)	C(42)-C(44)	154(5)
Pb(2)-S(3)	262.5(9)	C(42)-C(43)	154(5)
Pb(2)-S(2)	270.7(8)	S(5)-C(51)	186(3)
Pb(2)-S(4)	278.2(7)	C(51)-C(52)	148(5)
Pb(3)-S(5)	262.1(7)	C(52)-C(54)	144(6)
Pb(3)-S(6)	279.7(7)	C(52)-C(53)	175(9)
Pb(3)-S(4)	282.7(8)	S(6)-C(61)	182(3)
Pb(3)-S(1)#2	312.6(7)	C(61)-C(62)	144(5)
Pb(4)-S(7)	262.1(8)	C(62)-C(63)	132(6)
Pb(4)-S(6)	276.1(7)	C(62)-C(64)	146(5)
Pb(4)-S(8)	281.4(8)	S(7)-C(71)	189(4)
Pb(4)-S(5)	310.8(7)	C(71)-C(72)	152(5)
Pb(5)-S(9)	264.8(8)	C(72)-C(73)	150(6)
Pb(5)-S(8)	272.0(7)	C(72)-C(74)	159(7)
Pb(5)-S(10)	281.5(7)	S(8)-C(81)	187(3)
S(1)-C(11)	180(4)	C(81)-C(82)	154(5)
C(11)-C(12)	130(5)	C(82)-C(84)	148(5)
C(12)-C(14)	129(6)	C(82)-C(83)	154(6)
C(12)-C(13)	173(6)	S(9)-C(91)	180(4)
S(2)-C(21)	182(4)	C(91)-C(92)	147(6)
C(21)-C(22)	162(6)	C(92)-C(93)	149(6)
C(22)-C(23)	134(7)	C(92)-C(94)	156(7)
C(22)-C(24)	157(6)	S(10)-C(95)	183(3)
S(3)-C(31)	181(4)	C(95)-C(96)	157(4)
C(31)-C(32)	144(7)	C(96)-C(97)	143(5)
C(32)-C(33)	141(8)	C(96)-C(98)	147(5)
C(32)-C(34)	178(10)		

$^{a)}$ Symmetry transformation to generate equivalent atoms: #1: $x - \frac{1}{2}$, $y - \frac{1}{2}$, z; #2: x, $-y$, $z + \frac{1}{2}$; #3: x, $-y$, $z + \frac{1}{2}$; #4: $x + \frac{1}{2}$, $y + \frac{1}{2}$, z.

Table C.27: Bond angles Pb(SBu^i)$_2$ (**3c**).

Atom-Atom-Atom	Bond Angle /°	Atom-Atom-Atom	Bond Angle /°
S(1)-Pb(1)-S(10)#1	80.3(2)	C(42)-C(41)-S(4)	114(3)
S(1)-Pb(1)-S(2)	91.6(2)	C(41)-C(42)-C(44)	106(3)
S(10)#1-Pb(1)-S(2)	83.6(2)	C(41)-C(42)-C(43)	111(3)
S(3)-Pb(2)-S(2)	78.9(2)	C(44)-C(42)-C(43)	110(3)
S(3)-Pb(2)-S(4)	89.3(3)	C(51)-S(5)-Pb(3)	105.8(10)
S(2)-Pb(2)-S(4)	95.3(2)	C(51)-S(5)-Pb(4)	92.3(14)
S(5)-Pb(3)-S(6)	86.0(2)	Pb(3)-S(5)-Pb(4)	86.9(2)
S(5)-Pb(3)-S(4)	84.9(2)	C(52)-C(51)-S(5)	113(3)
S(6)-Pb(3)-S(4)	84.6(2)	C(54)-C(52)-C(51)	110(4)
S(5)-Pb(3)-S(1)#2	96.5(2)	C(54)-C(52)-C(53)	114(4)
S(6)-Pb(3)-S(1)#2	90.4(2)	C(51)-C(52)-C(53)	99(4)
S(4)-Pb(3)-S(1)#2	174.7(2)	C(61)-S(6)-Pb(4)	97.8(11)
S(7)-Pb(4)-S(6)	100.1(2)	C(61)-S(6)-Pb(3)	105.2(11)
S(7)-Pb(4)-S(8)	82.5(2)	Pb(4)-S(6)-Pb(3)	90.8(2)
S(6)-Pb(4)-S(8)	84.6(2)	C(62)-C(61)-S(6)	118(3)
S(7)-Pb(4)-S(5)	88.3(2)	C(63)-C(62)-C(61)	128(4)
S(6)-Pb(4)-S(5)	77.8(2)	C(63)-C(62)-C(64)	119(4)
S(8)-Pb(4)-S(5)	158.4(2)	C(61)-C(62)-C(64)	112(3)
S(9)-Pb(5)-S(8)	84.7(2)	C(71)-S(7)-Pb(4)	100.7(13)
S(9)-Pb(5)-S(10)	85.8(2)	C(72)-C(71)-S(7)	112(3)
S(8)-Pb(5)-S(10)	88.3(2)	C(73)-C(72)-C(71)	113(4)
C(11)-S(1)-Pb(1)	106.6(14)	C(73)-C(72)-C(74)	108(4)
C(11)-S(1)-Pb(3)#3	134.7(16)	C(71)-C(72)-C(74)	103(4)
Pb(1)-S(1)-Pb(3)#3	92.6(2)	C(81)-S(8)-Pb(5)	98.3(11)
C(12)-C(11)-S(1)	123(3)	C(81)-S(8)-Pb(4)	109.3(11)
C(14)-C(12)-C(11)	135(4)	Pb(5)-S(8)-Pb(4)	87.8(2)
C(14)-C(12)-C(13)	113(4)	C(82)-C(81)-S(8)	110(2)
C(11)-C(12)-C(13)	111(4)	C(84)-C(82)-C(83)	111(4)
C(21)-S(2)-Pb(2)	107.3(18)	C(84)-C(82)-C(81)	110(3)
C(21)-S(2)-Pb(1)	112.2(14)	C(83)-C(82)-C(81)	114(3)
Pb(2)-S(2)-Pb(1)	90.6(2)	C(91)-S(9)-Pb(5)	106.0(13)
C(22)-C(21)-S(2)	111(3)	C(92)-C(91)-S(9)	120(3)
C(23)-C(22)-C(24)	120(5)	C(91)-C(92)-C(93)	114(5)
C(23)-C(22)-C(21)	118(5)	C(91)-C(92)-C(94)	106(4)
C(24)-C(22)-C(21)	100(4)	C(93)-C(92)-C(94)	110(4)
C(31)-S(3)-Pb(2)	103.4(16)	C(95)-S(10)-Pb(1)#4	99.4(10)
C(32)-C(31)-S(3)	125(5)	C(95)-S(10)-Pb(5)	105.1(11)
C(33)-C(32)-C(31)	121(6)	Pb(1)#4-S(10)-Pb(5)	87.9(2)
C(33)-C(32)-C(34)	97(6)	C(96)-C(95)-S(10)	111.7(19)
C(31)-C(32)-C(34)	91(5)	C(97)-C(96)-C(98)	108(3)
C(41)-S(4)-Pb(2)	108.3(10)	C(97)-C(96)-C(95)	114(3)
C(41)-S(4)-Pb(3)	94.3(10)	C(98)-C(96)-C(95)	111(3)
Pb(2)-S(4)-Pb(3)	93.8(2)		

$^{a)}$ Symmetry transformation to generate equivalent atoms: #1: $x - \frac{1}{2}$, $y - \frac{1}{2}$, z; #2: x, $-y$, $z + \frac{1}{2}$; #3: x, $-y$, $z + \frac{1}{2}$; #4: $x + \frac{1}{2}$, $y + \frac{1}{2}$, z.

Table C.28: Anisotropic displacement parameters ($\text{Å}^2 * 10^3$)for cePb(SBu^i)2 (**3c**). The anisotropic displacement factor exponent takes the form: $-2\pi^2[h^2a^2*U^{11}+...+h^2k^2a^2*b^2*U^{12}]$.

	U^{11}	U^{22}	U^{33}	U^{23}	U^{13}	U^{12}
Pb(1)	44(1)	44(1)	50(1)	0(1)	19(1)	1(1)
Pb(2)	48(1)	52(1)	48(1)	4(1)	13(1)	−10(1)
Pb(3)	40(1)	50(1)	41(1)	0(1)	13(1)	−3(1)
Pb(4)	43(1)	51(1)	50(1)	−4(1)	18(1)	−4(1)
Pb(5)	45(1)	54(1)	46(1)	−5(1)	17(1)	−7(1)
S(1)	46(4)	47(4)	54(4)	0(3)	21(3)	6(3)
C(11)	80(20)	60(20)	130(30)	20(20)	70(20)	9(16)
C(12)	170(30)	110(30)	180(30)	80(20)	130(30)	80(20)
C(13)	190(50)	210(50)	190(50)	140(40)	140(40)	140(40)
C(14)	100(30)	50(20)	140(40)	40(20)	60(30)	40(20)
S(2)	47(4)	54(4)	52(4)	0(3)	16(3)	2(3)
C(21)	120(30)	65(19)	100(30)	−20(20)	10(20)	29(19)
C(22)	130(30)	70(20)	140(30)	−40(20)	10(20)	40(20)
C(23)	160(50)	120(40)	180(50)	−80(40)	−20(30)	20(30)
C(24)	150(40)	90(30)	210(50)	−10(40)	50(40)	70(30)
S(3)	49(4)	72(6)	73(5)	18(4)	25(4)	12(4)
C(31)	210(40)	120(30)	130(30)	30(30)	140(30)	40(30)
C(32)	220(50)	140(40)	200(40)	10(30)	110(40)	80(30)
C(33)	230(60)	180(40)	260(60)	90(40)	220(50)	90(30)
C(34)	200(40)	140(40)	220(60)	50(40)	130(50)	80(30)
S(4)	48(4)	54(4)	51(4)	−2(3)	14(3)	−3(3)
C(41)	50(13)	53(17)	60(16)	8(13)	3(12)	−13(12)
C(42)	49(15)	83(18)	71(18)	18(17)	−5(13)	−10(14)
C(43)	90(30)	100(20)	80(20)	−30(20)	40(20)	−42(18)
C(44)	46(14)	90(20)	130(30)	30(20)	9(17)	−12(14)
S(5)	49(4)	49(4)	48(4)	−6(3)	14(3)	8(3)
C(51)	62(19)	120(30)	43(16)	−4(19)	28(15)	20(20)
C(52)	70(20)	130(40)	80(30)	0(20)	60(20)	20(20)
C(53)	370(120)	230(90)	290(100)	130(80)	300(100)	170(80)
C(54)	80(30)	160(50)	210(70)	20(50)	70(40)	-10(30)
S(6)	42(3)	45(4)	52(4)	0(3)	19(3)	1(3)
C(61)	58(16)	80(20)	51(17)	3(16)	18(14)	14(14)
C(62)	100(20)	130(30)	130(30)	70(20)	80(20)	57(19)
C(63)	130(40)	150(50)	290(70)	110(40)	140(40)	60(30)
C(64)	170(40)	120(30)	140(40)	70(30)	120(30)	90(30)
S(7)	47(4)	56(4)	53(4)	−5(4)	12(3)	2(3)
C(71)	80(20)	150(40)	64(18)	−30(20)	−21(17)	50(20)
C(72)	80(20)	180(40)	77(19)	−10(20)	−13(18)	60(20)
C(73)	100(30)	180(50)	69(17)	0(30)	-38(18)	20(30)
C(74)	110(30)	270(70)	160(40)	−60(50)	-30(30)	120(40)
S(8)	42(4)	58(5)	63(5)	−6(4)	24(3)	−6(3)
C(81)	55(16)	60(17)	90(20)	−5(15)	42(16)	−4(13)
C(82)	72(18)	80(20)	90(20)	−24(15)	47(16)	−25(14)
C(83)	100(30)	90(30)	170(40)	−20(30)	70(30)	30(20)
C(84)	140(30)	110(30)	130(30)	−40(20)	100(30)	−50(30)
S(9)	50(4)	58(5)	55(4)	−8(4)	24(3)	−3(3)
C(91)	90(20)	80(20)	100(20)	10(20)	60(20)	19(19)
C(92)	120(30)	140(30)	120(20)	10(30)	90(20)	40(20)
C(93)	100(30)	160(40)	130(40)	−20(30)	60(30)	40(30)
C(94)	260(60)	260(60)	140(30)	60(40)	150(40)	130(50)
S(10)	37(3)	56(4)	49(4)	−6(3)	13(3)	1(3)
C(95)	49(16)	80(20)	32(14)	4(14)	5(12)	3(15)
C(96)	39(15)	80(20)	62(19)	1(17)	13(14)	10(15)
C(97)	70(20)	100(30)	80(20)	−10(20)	20(19)	20(20)
C(98)	41(18)	140(40)	120(30)	30(30)	0(20)	10(20)

Table C.29: Atomic coordinates and $U_{eq}/\text{Å}^2$ for $[Pb_{12}O_6(SPr^i)_{12} \cdot (C_6H_6)]$ (**3d**).

Atom	x	y	z	U_{eq} [a]
Pb(2)	0.46193(3)	0.28490(2)	0.68942(2)	0.02799(8)
S(2)	0.2397(2)	0.40905(17)	0.77785(15)	0.0347(4)
O(2)	0.2772(5)	0.3234(4)	0.6242(3)	0.0217(10)
Pb(3)	0.48660(3)	0.56495(2)	0.67375(2)	0.02614(8)
S(3)	0.6807(2)	0.39294(16)	0.75767(15)	0.0362(5)
O(3)	0.2966(5)	0.4097(4)	0.4350(3)	0.0223(10)
Pb(4)	0.70188(3)	0.48709(2)	0.47608(2)	0.02190(7)
S(4)	0.58977(19)	0.26667(13)	0.49711(14)	0.0263(4)
Pb(5)	0.29891(3)	0.22925(2)	0.52998(2)	0.02534(8)
S(5)	−0.0062(2)	0.30407(14)	0.57573(14)	0.0275(4)
Pb(6)	0.12419(3)	0.45534(2)	0.36430(2)	0.02855(8)
S(6)	0.2657(2)	0.28532(17)	0.31811(17)	0.0409(5)
C(11)	0.1750(13)	-0.0389(7)	0.8128(8)	0.058(3)
C(12)	0.0710(16)	-0.0283(11)	0.8966(9)	0.084(4)
C(13)	0.2928(16)	-0.1328(8)	0.8318(9)	0.080(4)
C(21)	0.2217(12)	0.3741(10)	0.8980(7)	0.057(3)
C(22)	0.1034(19)	0.3053(13)	0.9546(10)	0.099(5)
C(23)	0.1886(16)	0.4793(13)	0.9209(9)	0.087(4)
C(31)	0.6313(17)	0.3916(15)	0.8711(10)	0.100(5)
C(32)	0.718(3)	0.435(2)	0.8924(18)	0.164(9)
C(33)	0.643(3)	0.272(2)	0.936(2)	0.191(11)
C(41)	0.6864(8)	0.1374(5)	0.4798(6)	0.0299(17)
C(42)	0.6447(10)	0.0400(6)	0.5628(7)	0.043(2)
C(43)	0.6607(10)	0.1287(7)	0.3986(7)	0.043(2)
C(51)	−0.0956(8)	0.1823(6)	0.6035(6)	0.0302(17)
C(52)	−0.1536(10)	0.1281(7)	0.7064(7)	0.043(2)
C(53)	0.0016(9)	0.0996(6)	0.5624(7)	0.041(2)
C(61)	0.1570(18)	0.244(2)	0.2712(17)	0.144(10)
C(62)	0.0121(17)	0.2833(14)	0.2826(13)	0.106(6)
C(63)	0.242(2)	0.2082(14)	0.1947(11)	0.115(6)
Pb(1)	0.07848(3)	0.27461(2)	0.73507(2)	0.02910(8)
S(1)	0.2553(2)	0.08754(15)	0.74222(15)	0.0360(5)
O(1)	0.4944(5)	0.4586(4)	0.5934(3)	0.0207(10)
C(1)	0.4715(16)	-0.0086(11)	0.0888(8)	0.074(4)
C(2)	0.3687(16)	0.0355(14)	0.0441(11)	0.094(5)
C(3)	0.5999(17)	-0.0477(11)	0.0475(10)	0.081(4)

[a] $U_{eq.}$ is defined as $\frac{1}{3}$ of the trace of the orthogonalized U_{ij} tensor.

Table C.30: Bond lengths $[Pb_{12}O_6(SPr^i)_{12} \cdot (C_6H_6)]$ (**3d**).

Atom-Atom[a]	Bond Length / pm	Atom-Atom[a]	Bond Length / pm
Pb(2)-O(1)	225.5(4)	S(4)-C(41)	184.0(7)
Pb(2)-O(2)	228.1(4)	S(4)-Pb(5)	289.18(18)
Pb(2)-S(2)	280.8(2)	Pb(5)-S(5)	291.49(19)
Pb(2)-S(4)	312.1(2)	Pb(5)-Pb(1)	360.48(5)
Pb(2)-Pb(4)#1	366.05(4)	S(5)-C(51)	185.2(7)
Pb(2)-Pb(1)	366.87(4)	S(5)-Pb(1)	288.3(2)
Pb(2)-Pb(3)	367.82(4)	Pb(6)-S(6)	261.6(2)
S(2)-C(21)	181.9(11)	S(6)-C(61)	179.4(14)
S(2)-Pb(1)	304.8(2)	C(11)-C(12)	148.2(18)
O(2)-Pb(1)	224.9(5)	C(11)-C(13)	150.8(15)
O(2)-Pb(5)	228.9(5)	C(11)-S(1)	181.9(10)
O(2)-Pb(4)#1	242.3(4)	C(21)-C(22)	149.0(17)
Pb(3)-O(1)	226.4(5)	C(21)-C(23)	152.3(17)
Pb(3)-O(3)#1	232.5(5)	C(31)-C(32)	133(3)
Pb(3)-S(3)	283.7(2)	C(31)-C(33)	153(3)
Pb(3)-S(4)#1	303.80(18)	C(41)-C(42)	149.3(12)
Pb(3)-Pb(6)#1	368.13(4)	C(41)-C(43)	150.0(12)
Pb(3)-Pb(4)	368.31(4)	C(51)-C(53)	150.9(11)
S(3)-C(31)	178.2(16)	C(51)-C(52)	154.0(13)
S(3)-Pb(6)#1	283.4(2)	C(61)-C(62)	139(2)
O(3)-Pb(6)	221.9(4)	C(61)-C(63)	147(2)
O(3)-Pb(5)	229.1(4)	Pb(1)-S(1)	267.1(2)
O(3)-Pb(4)#1	237.8(5)	C(1)-C(3)	133.5(19)
Pb(4)-O(1)	232.8(5)	C(1)-C(2)	134.2(19)
Pb(4)-O(1)#1	240.6(4)	C(2)-C(3)#2	140(2)

[a] Symmetry transformation to generate equivalent atoms: #1: $-x+1$, $-y+1$, $-z+1$; #2: $-x+1$, $-y$, $-z$.

Table C.31: Bond angles [Pb$_{12}$O$_6$(SPr^i)$_{12}$ · (C$_6$H$_6$)] (**3d**).

Atom-Atom-Atom[a]	Bond Angle /°	Atom-Atom-Atom[a]	Bond Angle /°	Atom-Atom-Atom[a]	Bond Angle /°
O(1)-Pb(2)-O(2)	80.04(16)	Pb(2)-Pb(3)-Pb(4)	64.837(8)	S(6)-Pb(6)-Pb(3)#1	66.50(5)
O(1)-Pb(2)-S(2)	78.65(13)	Pb(6)#1-Pb(3)-Pb(4)	65.109(8)	S(3)#1-Pb(6)-Pb(3)#1	49.57(4)
O(2)-Pb(2)-S(2)	73.23(13)	C(31)-S(3)-Pb(6)#1	114.1(7)	C(61)-S(6)-Pb(6)	108.1(5)
O(1)-Pb(2)-S(4)	74.31(13)	C(31)-S(3)-Pb(3)	103.9(5)	C(12)-C(11)-C(13)	112.6(11)
O(2)-Pb(2)-S(4)	72.50(13)	Pb(6)#1-S(3)-Pb(3)	80.96(5)	C(12)-C(11)-S(1)	112.0(8)
S(2)-Pb(2)-S(4)	139.24(5)	Pb(6)-O(3)-Pb(5)	110.50(19)	C(13)-C(11)-S(1)	108.5(8)
O(1)-Pb(2)-Pb(4)#1	39.75(11)	Pb(6)-O(3)-Pb(3)#1	108.2(2)	C(22)-C(21)-C(23)	107.9(11)
O(2)-Pb(2)-Pb(4)#1	40.34(11)	Pb(5)-O(3)-Pb(3)#1	110.08(19)	C(22)-C(21)-S(2)	111.4(8)
S(2)-Pb(2)-Pb(4)#1	70.04(4)	Pb(6)-O(3)-Pb(4)#1	119.0(2)	C(23)-C(21)-S(2)	109.7(9)
S(4)-Pb(2)-Pb(4)#1	69.63(3)	Pb(5)-O(3)-Pb(4)#1	105.58(19)	C(32)-C(31)-C(33)	101.1(18)
O(1)-Pb(2)-Pb(1)	104.12(12)	Pb(3)#1-O(3)-Pb(4)#1	103.08(17)	C(32)-C(31)-S(3)	116.0(16)
O(2)-Pb(2)-Pb(1)	35.62(13)	O(1)-Pb(4)-O(3)#1	73.92(16)	C(33)-C(31)-S(3)	109.6(17)
S(2)-Pb(2)-Pb(1)	54.19(4)	O(1)-Pb(4)-O(1)#1	73.37(19)	C(42)-C(41)-C(43)	111.8(7)
S(4)-Pb(2)-Pb(1)	104.06(3)	O(3)#1-Pb(4)-O(1)#1	115.77(16)	C(42)-C(41)-S(4)	110.8(6)
Pb(4)#1-Pb(2)-Pb(1)	67.757(8)	O(1)-Pb(4)-O(2)#1	115.82(16)	C(43)-C(41)-S(4)	109.9(5)
O(1)-Pb(2)-Pb(3)	35.60(12)	O(3)#1-Pb(4)-O(2)#1	72.78(16)	C(53)-C(51)-C(52)	111.1(7)
O(2)-Pb(2)-Pb(3)	99.50(11)	O(1)#1-Pb(4)-O(2)#1	74.31(15)	C(53)-C(51)-S(5)	111.6(6)
S(2)-Pb(2)-Pb(3)	56.93(4)	O(1)-Pb(4)-Pb(2)#1	96.26(11)	C(52)-C(51)-S(5)	111.6(6)
S(4)-Pb(2)-Pb(3)	108.49(3)	O(3)#1-Pb(4)-Pb(2)#1	96.30(11)	C(62)-C(61)-C(63)	122.7(16)
Pb(4)#1-Pb(2)-Pb(3)	63.900(8)	O(1)#1-Pb(4)-Pb(2)#1	36.82(11)	C(62)-C(61)-S(6)	120.6(12)
Pb(1)-Pb(2)-Pb(3)	104.767(10)	O(2)#1-Pb(4)-Pb(2)#1	37.54(10)	C(63)-C(61)-S(6)	112.1(13)
C(21)-S(2)-Pb(2)	116.3(4)	O(1)-Pb(4)-Pb(3)	36.08(11)	O(2)-Pb(1)-S(1)	74.12(12)
C(21)-S(2)-Pb(1)	114.4(4)	O(3)#1-Pb(4)-Pb(3)	37.94(12)	O(2)-Pb(1)-S(5)	77.68(12)
Pb(2)-S(2)-Pb(1)	77.46(5)	O(1)#1-Pb(4)-Pb(3)	93.10(12)	S(1)-Pb(1)-S(5)	97.82(6)
Pb(1)-O(2)-Pb(2)	108.2(2)	O(2)#1-Pb(4)-Pb(3)	93.91(12)	O(2)-Pb(1)-S(2)	68.80(12)
Pb(1)-O(2)-Pb(5)	105.20(18)	Pb(2)#1-Pb(4)-Pb(3)	95.760(10)	S(1)-Pb(1)-S(2)	103.17(6)
Pb(2)-O(2)-Pb(5)	115.82(19)	C(41)-S(4)-Pb(5)	100.0(2)	S(5)-Pb(1)-S(2)	133.16(6)
Pb(1)-O(2)-Pb(4)#1	121.91(19)	C(41)-S(4)-Pb(3)#1	111.9(3)	O(2)-Pb(1)-Pb(5)	37.78(12)
Pb(2)-O(2)-Pb(4)#1	102.13(17)	Pb(5)-S(4)-Pb(3)#1	79.24(4)	S(1)-Pb(1)-Pb(5)	59.48(5)
Pb(5)-O(2)-Pb(4)#1	104.21(19)	C(41)-S(4)-Pb(2)	122.3(3)	S(5)-Pb(1)-Pb(5)	51.95(4)
O(1)-Pb(3)-O(3)#1	76.15(16)	Pb(5)-S(4)-Pb(2)	80.07(5)	S(2)-Pb(1)-Pb(5)	106.23(4)
O(1)-Pb(3)-S(3)	85.80(12)	Pb(3)#1-S(4)-Pb(2)	124.36(6)	O(2)-Pb(1)-Pb(2)	36.21(11)
O(3)#1-Pb(3)-S(3)	76.54(12)	O(2)-Pb(5)-O(3)	76.93(17)	S(1)-Pb(1)-Pb(2)	61.97(5)
O(1)-Pb(3)-S(4)#1	77.27(12)	O(2)-Pb(5)-S(4)	77.17(12)	S(5)-Pb(1)-Pb(2)	112.81(4)
O(3)#1-Pb(3)-S(4)#1	75.01(12)	O(3)-Pb(5)-S(4)	78.55(12)	S(2)-Pb(1)-Pb(2)	48.34(4)
S(3)-Pb(3)-S(4)#1	149.61(6)	O(2)-Pb(5)-S(5)	76.42(12)	Pb(5)-Pb(1)-Pb(2)	64.311(9)
O(1)-Pb(3)-Pb(2)	35.45(12)	O(3)-Pb(5)-S(5)	79.89(13)	C(11)-S(1)-Pb(1)	115.3(4)
O(3)#1-Pb(3)-Pb(2)	97.72(11)	S(4)-Pb(5)-S(5)	148.99(5)	Pb(2)-O(1)-Pb(3)	108.9(2)
S(3)-Pb(3)-Pb(2)	63.77(4)	O(2)-Pb(5)-Pb(1)	37.01(12)	Pb(2)-O(1)-Pb(4)	118.83(19)
S(4)#1-Pb(3)-Pb(2)	109.90(3)	O(3)-Pb(5)-Pb(1)	98.41(13)	Pb(3)-O(1)-Pb(4)	106.63(18)
O(1)-Pb(3)-Pb(6)#1	96.33(12)	S(4)-Pb(5)-Pb(1)	110.81(4)	Pb(2)-O(1)-Pb(4)#1	103.43(17)
O(3)#1-Pb(3)-Pb(6)#1	34.94(11)	S(5)-Pb(5)-Pb(1)	51.16(4)	Pb(3)-O(1)-Pb(4)#1	112.47(18)
S(3)-Pb(3)-Pb(6)#1	49.48(4)	C(51)-S(5)-Pb(1)	106.3(3)	Pb(4)-O(1)-Pb(4)#1	106.63(19)
S(4)#1-Pb(3)-Pb(6)#1	107.13(4)	C(51)-S(5)-Pb(5)	105.2(2)	C(3)-C(1)-C(2)	119.8(13)
Pb(2)-Pb(3)-Pb(6)#1	99.234(9)	Pb(1)-S(5)-Pb(5)	76.88(4)	C(1)-C(2)-C(3)#2	119.7(14)
O(1)-Pb(3)-Pb(4)	37.28(12)	O(3)-Pb(6)-S(6)	79.68(13)	C(1)-C(3)-C(2)#2	120.3(13)
O(3)#1-Pb(3)-Pb(4)	38.98(11)	O(3)-Pb(6)-S(3)#1	78.22(13)		
S(3)-Pb(3)-Pb(4)	81.08(5)	S(6)-Pb(6)-S(3)#1	96.22(7)		
S(4)#1-Pb(3)-Pb(4)	70.13(4)	O(3)-Pb(6)-Pb(3)#1	36.87(13)		

[a] Symmetry transformation to generate equivalent atoms: #1: $-x+1, -y+1, -z+1$; #2: $-x+1, -y, -z$.

Table C.32: Anisotropic displacement parameters ($\text{Å}^2 * 10^3$) for $[Pb_{12}O_6(SPr^i)_{12} \cdot (C_6H_6)]$ (**3d**). The anisotropic displacement factor exponent takes the form: $-2\pi^2[h^2a^2 * U^{11} + ... + h^2k^2a^2 * b^2 * U^{12}]$.

	U^{11}	U^{22}	U^{33}	U^{23}	U^{13}	U^{12}
Pb(2)	28(1)	24(1)	32(1)	−4(1)	−13(1)	−6(1)
S(2)	33(1)	41(1)	34(1)	−19(1)	−3(1)	−11(1)
O(2)	20(2)	23(2)	29(3)	−11(2)	−11(2)	−3(2)
Pb(3)	26(1)	28(1)	29(1)	−14(1)	−6(1)	−5(1)
S(3)	32(1)	33(1)	39(1)	−4(1)	−12(1)	−7(1)
O(3)	24(3)	20(2)	28(3)	−9(2)	−12(2)	−6(2)
Pb(4)	20(1)	20(1)	28(1)	−10(1)	−7(1)	−3(1)
S(4)	22(1)	22(1)	39(1)	−13(1)	−11(1)	−1(1)
Pb(5)	25(1)	21(1)	33(1)	−11(1)	−9(1)	−4(1)
S(5)	23(1)	26(1)	36(1)	−11(1)	−11(1)	−4(1)
Pb(6)	25(1)	28(1)	39(1)	−14(1)	−14(1)	−1(1)
S(6)	44(1)	35(1)	54(1)	−26(1)	−18(1)	1(1)
C(11)	76(8)	30(4)	63(7)	−1(4)	−23(6)	−16(4)
C(12)	102(11)	79(8)	50(7)	3(7)	−3(7)	−38(8)
C(13)	139(13)	31(5)	79(9)	−5(5)	−57(9)	−10(6)
C(21)	47(6)	91(8)	41(6)	−29(6)	−7(5)	−18(5)
C(22)	137(14)	104(11)	61(9)	−15(8)	−19(9)	−58(10)
C(23)	88(10)	136(13)	64(8)	−70(9)	3(7)	−30(9)
C(31)	79(10)	132(14)	59(9)	−7(9)	−23(8)	7(9)
C(41)	21(4)	24(3)	50(5)	−17(3)	−15(4)	4(3)
C(42)	37(5)	25(4)	71(7)	−18(4)	−19(5)	1(3)
C(43)	34(5)	44(5)	65(6)	−37(5)	−15(5)	4(4)
C(51)	18(4)	24(3)	52(5)	−12(3)	−16(4)	−2(3)
C(52)	39(5)	37(4)	49(6)	−9(4)	−10(4)	−12(4)
C(53)	39(5)	31(4)	56(6)	−20(4)	−7(4)	−7(3)
C(61)	82(11)	220(20)	240(30)	−190(20)	−80(14)	28(12)
C(62)	90(11)	127(13)	139(16)	−60(12)	−61(11)	−16(9)
C(63)	189(19)	119(12)	98(12)	−82(11)	−59(13)	−17(12)
Pb(1)	25(1)	30(1)	31(1)	−10(1)	−5(1)	−7(1)
S(1)	39(1)	28(1)	38(1)	−6(1)	−11(1)	−6(1)
O(1)	21(2)	22(2)	25(2)	−9(2)	−8(2)	−6(2)
C(1)	87(10)	91(9)	42(6)	−28(6)	−15(6)	−3(7)
C(2)	65(9)	132(13)	85(11)	−48(10)	−14(8)	−2(8)
C(3)	99(11)	78(9)	75(9)	−31(7)	−38(9)	0(7)

Table C.33: Atomic coordinates and $U_{eq}/\text{Å}^2$ for $[\text{Pb}_{12}\text{O}_6(\text{SBu}^t)_{12} \cdot 6\,(\text{NC}_5\text{H}_5)]$ (**3e**).

Atom	x	y	z	U_{eq} [a]
Pb(1)	0.64282(7)	0.46057(6)	0.55290(4)	0.03166(18)
O(1)	0.5098(10)	0.4072(9)	0.4946(7)	0.030(3)
N(1)	0.9217(19)	0.0091(14)	0.7684(11)	0.059(5)
C(1)	0.032(4)	0.531(2)	0.856(2)	0.098(12)
Pb(2)	0.41974(7)	0.27644(6)	0.58648(4)	0.03445(18)
S(2)	0.4746(5)	0.1122(4)	0.7661(3)	0.0441(12)
O(2)	0.5577(12)	0.3154(9)	0.6481(6)	0.033(3)
N(2)	1.110(2)	0.2935(17)	0.9837(15)	0.082(7)
C(2)	0.954(2)	-0.0769(19)	0.7580(14)	0.063(7)
Pb(3)	0.60097(7)	0.37092(6)	0.39342(4)	0.03543(19)
S(3)	0.3649(5)	0.2945(4)	0.4246(3)	0.0364(11)
O(3)	0.5322(11)	0.4968(8)	0.6606(7)	0.031(3)
N(3)	0.050(3)	0.587(3)	0.7780(19)	0.112(10)
C(3)	1.022(3)	0.0677(19)	0.7548(13)	0.061(6)
Pb(4)	0.44801(7)	0.35414(6)	0.74377(4)	0.03491(18)
S(4)	0.6994(4)	0.3316(4)	0.7764(3)	0.0356(11)
C(4)	1.144(3)	0.045(3)	0.7293(17)	0.089(10)
Pb(5)	0.65217(7)	0.54470(6)	0.72476(4)	0.03638(19)
S(5)	0.4096(5)	0.5550(4)	0.7901(3)	0.0429(12)
C(5)	1.171(2)	-0.042(3)	0.7185(15)	0.076(9)
Pb(6)	0.69753(7)	0.18111(6)	0.68815(4)	0.03732(19)
S(6)	0.6762(4)	0.1586(4)	0.5573(3)	0.0418(12)
C(6)	1.079(3)	-0.103(2)	0.7316(16)	0.073(8)
S(7)	0.7315(4)	0.5716(4)	0.3771(3)	0.0342(11)
C(8)	1.036(3)	0.229(3)	1.0327(19)	0.090(11)
C(9)	1.039(3)	0.133(3)	1.0389(18)	0.099(12)
C(10)	−0.058(4)	0.562(5)	0.900(2)	0.14(2)
C(11)	−0.139(3)	0.641(4)	0.868(3)	0.105(14)
C(12)	−0.130(3)	0.686(2)	0.795(2)	0.077(9)
C(13)	−0.043(3)	0.659(3)	0.7540(17)	0.095(11)
C(14)	1.126(3)	0.115(3)	0.983(2)	0.103(11)
C(16)	1.189(3)	0.272(3)	0.9328(18)	0.089(10)
C(17)	1.202(3)	0.177(3)	0.9301(18)	0.086(10)
C(21)	0.5083(19)	-0.0158(17)	0.8274(11)	0.048(5)
C(22)	0.573(3)	-0.0714(19)	0.7767(17)	0.081(9)
C(23)	0.377(2)	-0.053(2)	0.8697(15)	0.072(8)
C(24)	0.592(2)	-0.023(2)	0.8844(13)	0.071(8)
C(31)	0.3793(19)	0.1719(16)	0.4194(11)	0.042(5)
C(32)	0.272(2)	0.1714(18)	0.3776(13)	0.053(5)
C(33)	0.5092(19)	0.1505(17)	0.3815(12)	0.049(5)
C(34)	0.3529(19)	0.0953(15)	0.5006(12)	0.044(4)
C(41)	0.704(2)	0.2810(17)	0.8797(13)	0.052(5)
C(42)	0.562(2)	0.257(2)	0.9211(12)	0.075(7)
C(43)	0.760(3)	0.350(2)	0.8999(14)	0.072(7)
C(44)	0.784(2)	0.1859(17)	0.9002(12)	0.050(5)
C(51)	0.396(2)	0.6047(16)	0.8630(12)	0.046(4)
C(52)	0.346(3)	0.522(2)	0.9406(13)	0.072(7)
C(53)	0.293(2)	0.6930(18)	0.8478(14)	0.057(6)
C(54)	0.522(2)	0.6334(19)	0.8694(13)	0.061(6)
C(61)	0.8516(17)	0.1664(15)	0.5101(10)	0.038(5)
C(62)	0.9347(18)	0.0857(14)	0.5630(12)	0.043(5)
C(63)	0.8560(17)	0.1472(17)	0.4404(13)	0.048(6)
C(64)	0.8969(18)	0.2624(14)	0.4952(11)	0.037(5)
C(71)	0.9021(18)	0.6104(15)	0.3475(12)	0.040(5)
C(72)	0.9876(19)	0.5139(18)	0.3710(14)	0.052(6)
C(73)	0.918(2)	0.6681(17)	0.2619(11)	0.054(6)
C(74)	0.9233(19)	0.6675(17)	0.3870(12)	0.050(6)

[a] $U_{eq.}$ is defined as $\frac{1}{3}$ of the trace of the orthogonalized U_{ij} tensor.

Table C.34: Bond lengths $[Pb_{12}O_6(SBu^t)_{12} \cdot 6\,(NC_5H_5)]$ **(3e)**.

Atom-Atom[a]	Bond Length / pm	Atom-Atom[a]	Bond Length / pm
Pb(1)-O(1)	235.2(11)	Pb(4)-Pb(5)	364.60(12)
Pb(1)-O(1)#1	236.4(12)	S(4)-C(41)	186(2)
Pb(1)-O(2)	236.8(12)	S(4)-Pb(5)	292.5(5)
Pb(1)-O(3)	242.1(11)	C(4)-C(5)	138(4)
Pb(1)-Pb(2)	362.69(11)	Pb(5)-S(5)	263.6(5)
Pb(1)-Pb(3)#1	364.45(10)	S(5)-C(51)	182.5(19)
O(1)-Pb(2)	222.7(12)	C(5)-C(6)	134(4)
O(1)-Pb(3)	225.8(11)	Pb(6)-S(6)	276.4(5)
N(1)-C(2)	136(3)	S(6)-C(61)	189.1(18)
N(1)-C(3)	137(3)	S(7)-C(71)	187(2)
C(1)-C(10)	131(5)	C(8)-C(9)	138(5)
C(1)-N(3)	141(4)	C(9)-C(14)	138(4)
Pb(2)-O(2)	231.6(13)	C(10)-C(11)	136(6)
Pb(2)-S(7)#1	283.3(5)	C(11)-C(12)	132(4)
Pb(2)-S(6)	309.8(5)	C(12)-C(13)	122(4)
Pb(2)-Pb(6)	366.11(11)	C(14)-C(17)	130(4)
Pb(2)-Pb(3)	368.14(11)	C(16)-C(17)	141(4)
S(2)-C(21)	183(2)	C(21)-C(23)	151(3)
S(2)-Pb(6)	262.4(5)	C(21)-C(24)	152(3)
O(2)-Pb(4)	223.6(10)	C(21)-C(22)	154(3)
O(2)-Pb(6)	227.6(12)	C(31)-C(33)	148(3)
N(2)-C(8)	127(4)	C(31)-C(32)	152(3)
N(2)-C(16)	129(3)	C(31)-C(34)	154(3)
C(2)-C(6)	138(3)	C(41)-C(43)	146(3)
Pb(3)-O(3)#1	226.6(12)	C(41)-C(44)	149(3)
Pb(3)-S(3)	273.0(5)	C(41)-C(42)	157(3)
Pb(3)-Pb(5)#1	363.24(11)	C(51)-C(54)	148(3)
S(3)-C(31)	185(2)	C(51)-C(53)	155(3)
S(3)-Pb(5)#1	296.9(5)	C(51)-C(52)	157(3)
O(3)-Pb(4)	226.6(12)	C(61)-C(64)	147(3)
O(3)-Pb(5)	229.0(12)	C(61)-C(63)	149(3)
N(3)-C(13)	135(4)	C(61)-C(62)	153(3)
C(3)-C(4)	133(4)	C(71)-C(74)	142(3)
Pb(4)-S(4)	278.5(4)	C(71)-C(73)	153(3)
Pb(4)-S(7)#1	307.8(5)	C(71)-C(72)	154(3)

[a] Symmetry transformation to generate equivalent atoms: #1: $-x+1$, $-y+1$, $-z+1$.

Table C.35: Bond angles [Pb$_{12}$O$_6$(SBu^t)$_{12}$ · 6 (NC$_5$H$_5$)] (**3e**).

Atom-Atom-Atom$^{a)}$	Bond Angle /°	Atom-Atom-Atom$^{a)}$	Bond Angle /°	Atom-Atom-Atom$^{a)}$	Bond Angle /°
O(1)-Pb(1)-O(1)#1	73.8(5)	O(3)#1-Pb(3)-Pb(5)#1	37.4(3)	S(6)-Pb(6)-Pb(2)	55.57(10)
O(1)-Pb(1)-O(2)	75.1(4)	S(3)-Pb(3)-Pb(5)#1	53.38(11)	C(61)-S(6)-Pb(6)	100.4(6)
O(1)#1-Pb(1)-O(2)	116.3(4)	O(1)-Pb(3)-Pb(1)#1	39.0(3)	C(61)-S(6)-Pb(2)	145.5(6)
O(1)-Pb(1)-O(3)	115.0(4)	O(3)#1-Pb(3)-Pb(1)#1	40.5(3)	Pb(6)-S(6)-Pb(2)	77.05(11)
O(1)#1-Pb(1)-O(3)	74.3(4)	S(3)-Pb(3)-Pb(1)#1	72.28(10)	C(5)-C(6)-C(2)	118(2)
O(2)-Pb(1)-O(3)	71.0(4)	Pb(5)#1-Pb(3)-Pb(1)#1	67.60(2)	C(71)-S(7)-Pb(2)#1	106.0(6)
O(1)-Pb(1)-Pb(2)	36.4(3)	O(1)-Pb(3)-Pb(2)	34.6(3)	C(71)-S(7)-Pb(4)#1	117.7(7)
O(1)#1-Pb(1)-Pb(2)	93.5(3)	O(3)#1-Pb(3)-Pb(2)	99.8(3)	Pb(2)#1-S(7)-Pb(4)#1	78.98(12)
O(2)-Pb(1)-Pb(2)	38.7(3)	S(3)-Pb(3)-Pb(2)	58.21(10)	N(2)-C(8)-C(9)	125(3)
O(3)-Pb(1)-Pb(2)	92.5(3)	Pb(5)#1-Pb(3)-Pb(2)	103.64(2)	C(14)-C(9)-C(8)	113(3)
O(1)-Pb(1)-Pb(3)#1	96.6(3)	Pb(1)#1-Pb(3)-Pb(2)	63.12(2)	C(1)-C(10)-C(11)	120(4)
O(1)#1-Pb(1)-Pb(3)#1	36.9(3)	C(31)-S(3)-Pb(3)	112.0(7)	C(12)-C(11)-C(10)	121(3)
O(2)-Pb(1)-Pb(3)#1	95.9(3)	C(31)-S(3)-Pb(5)#1	112.0(7)	C(13)-C(12)-C(11)	119(3)
O(3)-Pb(1)-Pb(3)#1	37.4(3)	Pb(3)-S(3)-Pb(5)#1	79.07(14)	C(12)-C(13)-N(3)	126(3)
Pb(2)-Pb(1)-Pb(3)#1	95.72(2)	Pb(3)#1-O(3)-Pb(5)	105.7(4)	C(17)-C(14)-C(9)	125(4)
Pb(2)-O(1)-Pb(3)	110.3(5)	Pb(4)-O(3)-Pb(5)	106.3(5)	N(2)-C(16)-C(17)	123(3)
Pb(2)-O(1)-Pb(1)	104.7(5)	Pb(3)#1-O(3)-Pb(1)	102.0(5)	C(14)-C(17)-C(16)	115(3)
Pb(3)-O(1)-Pb(1)	118.6(5)	Pb(4)-O(3)-Pb(1)	104.9(4)	C(23)-C(21)-C(24)	108.4(19)
Pb(2)-O(1)-Pb(1)#1	113.2(4)	Pb(5)-O(3)-Pb(1)	118.4(5)	C(23)-C(21)-C(22)	112(2)
Pb(3)-O(1)-Pb(1)#1	104.1(5)	C(13)-N(3)-C(1)	115(3)	C(24)-C(21)-C(22)	112(2)
Pb(1)-O(1)-Pb(1)#1	106.2(5)	C(4)-C(3)-N(1)	123(3)	C(23)-C(21)-S(2)	105.3(16)
C(2)-N(1)-C(3)	117(2)	O(2)-Pb(4)-O(3)	76.3(4)	C(24)-C(21)-S(2)	111.2(17)
C(10)-C(1)-N(3)	118(4)	O(2)-Pb(4)-S(4)	80.0(3)	C(22)-C(21)-S(2)	107.8(16)
O(1)-Pb(2)-O(2)	78.5(4)	O(3)-Pb(4)-S(4)	77.8(3)	C(33)-C(31)-C(32)	111.9(17)
O(1)-Pb(2)-S(7)#1	79.8(3)	O(2)-Pb(4)-S(7)#1	74.8(3)	C(33)-C(31)-C(34)	110.3(17)
O(2)-Pb(2)-S(7)#1	78.9(3)	O(3)-Pb(4)-S(7)#1	76.8(3)	C(32)-C(31)-C(34)	108.4(18)
O(1)-Pb(2)-S(6)	86.6(3)	S(4)-Pb(4)-S(7)#1	147.72(13)	C(33)-C(31)-S(3)	111.9(16)
O(2)-Pb(2)-S(6)	77.3(3)	O(2)-Pb(4)-Pb(5)	97.6(3)	C(32)-C(31)-S(3)	106.4(14)
S(7)#1-Pb(2)-S(6)	154.57(14)	O(3)-Pb(4)-Pb(5)	37.1(3)	C(34)-C(31)-S(3)	107.7(13)
O(1)-Pb(2)-Pb(1)	38.8(3)	S(4)-Pb(4)-Pb(5)	52.04(11)	C(43)-C(41)-C(44)	110(2)
O(2)-Pb(2)-Pb(1)	39.8(3)	S(7)#1-Pb(4)-Pb(5)	111.57(10)	C(43)-C(41)-C(42)	113(2)
S(7)#1-Pb(2)-Pb(1)	73.91(9)	C(41)-S(4)-Pb(4)	112.5(7)	C(44)-C(41)-C(42)	107(2)
S(6)-Pb(2)-Pb(1)	82.01(10)	C(41)-S(4)-Pb(5)	108.5(7)	C(43)-C(41)-S(4)	110.2(18)
O(1)-Pb(2)-Pb(6)	97.6(3)	Pb(4)-S(4)-Pb(5)	79.31(12)	C(44)-C(41)-S(4)	108.9(15)
O(2)-Pb(2)-Pb(6)	36.8(3)	C(3)-C(4)-C(5)	118(3)	C(42)-C(41)-S(4)	107.4(15)
S(7)#1-Pb(2)-Pb(6)	113.11(10)	O(3)-Pb(5)-S(5)	74.7(3)	C(54)-C(51)-C(53)	110.8(19)
S(6)-Pb(2)-Pb(6)	47.38(9)	O(3)-Pb(5)-S(4)	74.5(3)	C(54)-C(51)-C(52)	107.6(19)
Pb(1)-Pb(2)-Pb(6)	66.17(2)	S(5)-Pb(5)-S(4)	99.67(15)	C(53)-C(51)-C(52)	108.5(19)
O(1)-Pb(2)-Pb(3)	35.1(3)	O(3)-Pb(5)-S(3)#1	71.2(3)	C(54)-C(51)-S(5)	113.3(15)
O(2)-Pb(2)-Pb(3)	99.2(3)	S(5)-Pb(5)-S(3)#1	99.47(15)	C(53)-C(51)-S(5)	109.3(14)
S(7)#1-Pb(2)-Pb(3)	111.49(10)	S(4)-Pb(5)-S(3)#1	134.27(13)	C(52)-C(51)-S(5)	107.2(15)
S(6)-Pb(2)-Pb(3)	63.95(10)	O(3)-Pb(5)-Pb(3)#1	36.9(3)	C(64)-C(61)-C(63)	113.4(17)
Pb(1)-Pb(2)-Pb(3)	65.68(2)	S(5)-Pb(5)-Pb(3)#1	61.76(12)	C(64)-C(61)-C(62)	109.1(17)
Pb(6)-Pb(2)-Pb(3)	98.14(2)	S(4)-Pb(5)-Pb(3)#1	110.62(9)	C(63)-C(61)-C(62)	109.3(16)
C(21)-S(2)-Pb(6)	107.1(6)	S(3)#1-Pb(5)-Pb(3)#1	47.55(10)	C(64)-C(61)-S(6)	110.0(12)
Pb(4)-O(2)-Pb(6)	112.0(5)	O(3)-Pb(5)-Pb(4)	36.6(3)	C(63)-C(61)-S(6)	106.1(13)
Pb(4)-O(2)-Pb(2)	111.6(5)	S(5)-Pb(5)-Pb(4)	63.36(11)	C(62)-C(61)-S(6)	108.9(13)
Pb(6)-O(2)-Pb(2)	105.7(5)	S(4)-Pb(5)-Pb(4)	48.65(9)	C(74)-C(71)-C(73)	112.5(19)
Pb(4)-O(2)-Pb(1)	107.7(5)	S(3)#1-Pb(5)-Pb(4)	107.49(10)	C(74)-C(71)-C(72)	109.8(19)
Pb(6)-O(2)-Pb(1)	117.8(5)	Pb(3)#1-Pb(5)-Pb(4)	65.37(2)	C(73)-C(71)-C(72)	113.7(16)
Pb(2)-O(2)-Pb(1)	101.5(4)	C(51)-S(5)-Pb(5)	111.5(7)	C(74)-C(71)-S(7)	109.7(13)
C(8)-N(2)-C(16)	119(3)	C(6)-C(5)-C(4)	122(2)	C(73)-C(71)-S(7)	106.1(13)
N(1)-C(2)-C(6)	123(2)	O(2)-Pb(6)-S(2)	78.1(3)	C(72)-C(71)-S(7)	104.8(14)
O(1)-Pb(3)-O(3)#1	79.4(4)	O(2)-Pb(6)-S(6)	85.4(3)		
O(1)-Pb(3)-S(3)	79.7(3)	S(2)-Pb(6)-S(6)	97.52(16)		
O(3)#1-Pb(3)-S(3)	76.4(3)	O(2)-Pb(6)-Pb(2)	37.5(3)		
O(1)-Pb(3)-Pb(5)#1	102.7(3)	S(2)-Pb(6)-Pb(2)	65.18(12)		

$^{a)}$ Symmetry transformation to generate equivalent atoms: #1: $-x+1, -y+1, -z+1$.

Table C.36: Anisotropic displacement parameters ($\text{Å}^2 * 10^3$) for $[\text{Pb}_{12}\text{O}_6(\text{SBu}^t)_{12} \cdot 6\,(\text{NC}_5\text{H}_5)]$ (**3e**). The anisotropic displacement factor exponent takes the form: $-2\pi^2[h^2a^2 * U^{11} + ... + h^2k^2a^2 * b^2 * U^{12}]$.

	U^{11}	U^{22}	U^{33}	U^{23}	U^{13}	U^{12}
Pb(1)	27(1)	35(1)	34(1)	-14(1)	-5(1)	-1(1)
O(1)	24(6)	34(8)	35(7)	-15(6)	-5(5)	-4(5)
N(1)	69(13)	35(12)	66(13)	-19(11)	1(10)	7(9)
C(1)	120(30)	50(20)	140(30)	-30(20)	-90(30)	-10(18)
Pb(2)	34(1)	34(1)	36(1)	-12(1)	-7(1)	-5(1)
S(2)	46(3)	37(3)	44(3)	-12(3)	-3(2)	0(2)
O(2)	45(7)	32(8)	14(6)	-3(6)	4(5)	-3(6)
N(2)	58(14)	47(15)	103(19)	-1(14)	10(13)	0(11)
C(2)	82(17)	49(17)	78(18)	-26(15)	-54(14)	-4(13)
Pb(3)	31(1)	39(1)	39(1)	-19(1)	-6(1)	3(1)
S(3)	40(3)	36(3)	37(3)	-18(2)	-10(2)	1(2)
O(3)	40(7)	10(7)	45(8)	-12(6)	-5(6)	-5(5)
N(3)	100(20)	140(30)	110(20)	-70(20)	-50(19)	20(20)
C(3)	85(19)	40(16)	52(14)	-6(12)	-17(13)	-9(13)
Pb(4)	33(1)	39(1)	33(1)	-14(1)	-3(1)	-4(1)
S(4)	29(2)	42(3)	38(3)	-16(2)	-9(2)	0(2)
C(4)	65(19)	100(30)	80(20)	-2(19)	0(15)	-18(17)
Pb(5)	33(1)	40(1)	39(1)	-17(1)	-8(1)	-3(1)
S(5)	42(3)	48(4)	47(3)	-28(3)	-8(2)	1(2)
C(5)	33(13)	120(30)	61(17)	-25(18)	-11(11)	29(15)
Pb(6)	34(1)	36(1)	41(1)	-14(1)	-8(1)	2(1)
S(6)	32(2)	50(4)	48(3)	-26(3)	-2(2)	-3(2)
C(6)	67(18)	70(20)	90(20)	-47(18)	-34(15)	41(15)
S(7)	28(2)	41(3)	38(3)	-19(2)	-4(2)	-5(2)
C(8)	68(19)	140(40)	90(20)	-70(30)	-4(16)	-30(20)
C(9)	70(20)	110(30)	80(20)	20(20)	-22(17)	-40(20)
C(10)	70(20)	290(70)	60(20)	-50(30)	15(18)	-50(30)
C(11)	57(19)	170(40)	140(40)	-120(30)	-10(20)	-30(20)
C(12)	60(17)	80(20)	90(20)	-31(19)	-17(16)	32(14)
C(13)	54(17)	140(30)	67(19)	0(20)	-23(15)	-30(18)
C(14)	80(20)	90(30)	110(30)	-20(20)	-10(20)	12(19)
C(16)	73(19)	90(30)	90(20)	-40(20)	12(16)	-2(17)
C(17)	49(16)	100(30)	90(20)	-30(20)	11(14)	-1(16)
C(21)	38(11)	49(15)	38(11)	8(10)	-11(9)	-12(9)
C(22)	120(20)	33(16)	90(20)	-34(16)	7(17)	-16(14)
C(23)	51(15)	100(20)	67(17)	-29(17)	-7(12)	-14(14)
C(24)	65(16)	90(20)	56(15)	-9(14)	-21(12)	-40(14)
C(31)	45(10)	43(13)	36(9)	-15(8)	-8(7)	6(9)
C(32)	55(10)	53(15)	64(12)	-36(12)	-12(10)	-5(10)
C(33)	45(9)	50(15)	53(12)	-22(11)	1(8)	-10(9)
C(34)	40(10)	29(12)	63(10)	-10(9)	-8(8)	-26(8)
C(41)	66(12)	38(12)	48(13)	-15(11)	-9(9)	5(8)
C(42)	62(11)	110(20)	31(12)	-6(13)	-10(10)	17(10)
C(43)	108(17)	70(15)	62(15)	-45(14)	-43(13)	18(12)
C(44)	51(11)	53(12)	51(13)	-22(12)	-20(10)	9(9)
C(51)	66(11)	39(12)	42(10)	-21(9)	-24(9)	11(8)
C(52)	105(19)	61(15)	48(13)	-22(9)	-6(12)	-1(12)
C(53)	50(11)	56(13)	70(15)	-36(11)	-8(11)	9(10)
C(54)	62(11)	68(18)	55(14)	-26(13)	-19(10)	13(9)
C(61)	38(10)	30(12)	33(10)	-3(9)	1(8)	12(8)
C(62)	39(11)	18(12)	60(13)	1(10)	-16(9)	2(8)
C(63)	23(9)	60(16)	72(15)	-40(13)	-7(9)	1(9)
C(64)	50(11)	22(11)	33(10)	-8(9)	-10(8)	22(9)
C(71)	46(11)	28(12)	50(12)	-24(10)	-1(9)	0(8)
C(72)	40(12)	63(17)	68(15)	-34(14)	-16(10)	-8(10)
C(73)	43(12)	48(15)	46(13)	8(11)	7(10)	-29(10)
C(74)	38(11)	68(17)	52(13)	-26(12)	10(9)	-41(10)

Erklärung zur Dissertation

Hiermit versichere ich an Eides statt, dass ich die vorliegende Dissertation selbstständig und ohne die Benutzung anderer als der angegebenen Hilfsmittel und Literatur angefertigt habe. Alle Stellen, die wörtlich oder sinngemäß aus veröffentlichten und nicht veröffentlichten Werken dem Wortlaut oder dem Sinn nach entnommen wurden, sind als solche kenntlich gemacht. Ich versichere an Eides statt, dass diese Dissertation noch keiner anderen Fakultät oder Universität zur Prüfung vorgelegen hat; dass sie - abgesehen von unten angegebenen Teilpublikationen und eingebundenen Artikeln und Manuskripten - noch nicht veröffentlicht worden ist sowie, dass ich eine Veröffentlichung der Dissertation vor Abschluss der Promotion nicht ohne Genehmigung des Promotionsausschusses vornehmen werde. Die Bestimmungen dieser Ordnung sind mir bekannt. Darüber hinaus erkläre ich hiermit, dass ich die Ordnung zur Sicherung guter wissenschaftlicher Praxis und zum Umgang mit wissenschaftlichem Fehlverhalten der Universität zu Köln gelesen und sie bei der Durchführung der Dissertation zugrundeliegenden Arbeiten und der schriftlich verfassten Dissertation beachtet habe und verpflichte mich hiermit, die dort genannten Vorgaben bei allen wissenschaftlichen Tätigkeiten zu beachten und umzusetzen. Ich versichere, dass die eingereichte elektronische Fassung der eingereichten Druckfassung vollständig entspricht.

Teilpublikationen:

U. Atamtürk, E. Jung, T. Fischer, S. Mathur, *Chem. Mater.* **2022**, *34* (16), 7344–7356.

U. Atamtürk, V. Brune, S. Mishra, S. Mathur *Molecules*, **2021**, *26* (17), 5367.

Kapitel 5 und 6 (Chapter 5 and Chapter 6) sind jeweils Zusammenfassungen der, im Sinne der obigen Erklärung, eigenen Ergebnisse, welche von mir in Manuskript-Form geschrieben wurden. Diese wurden bisher weder veröffentlicht, noch einem Journal zur Veröffentlichung eingereicht.

Datum, Name und Unterschrift:

5. Oktober 2022, Ufuk Atamtürk.